University of Alberta

MODELING THE SUPPRESSION OF MOTONEURONAL HYPEREXCITABILITY FOLLOWING SPINAL CORD INJURY

By

Sherif M. ElBasiouny 

A thesis submitted to the Faculty of Graduate Studies and Research in partial fulfillment of the requirements for the degree of Doctor of Philosophy

in

Medical Sciences – Biomedical Engineering

Edmonton, Alberta
Spring 2007

Your file Votre référence
ISBN: 978-0-494-29669-1
Our file Notre référence
ISBN: 978-0-494-29669-1

In the name of ALLAH, the most gracious, the most merciful:

"[1] Did we not cool your temper?
[2] And we unloaded your load (of sins).
[3] One that burdened your back.
[4] We exalted you to an honorable position.
[5] With pain there is gain.
[6] Indeed, with pain there is gain.
[7] Whenever possible you shall strive.
[8] Seeking only your Lord"

The Holy Quran, chapter 94

This thesis work is dedicated to individuals with disabilities resulting from spasticity. It represents one step in our efforts to help alleviate this motor disorder.

ABSTRACT

The long-term goal of this research project is to develop rehabilitation interventions for reducing the intensity of spasticity in individuals with spinal cord injury (SCI). Weeks after SCI, spasms, involving exaggerated long-lasting reflexes and muscle contractions, develop in response to brief sensory stimuli in muscles innervated below the level of the lesion. These involuntarily sustained contractures are usually painful, and reduce the functional outcome of the residual voluntary drive in individuals with incomplete SCI. Activation of low-threshold persistent inward currents (PICs), particularly those mediated by dendritic L-type calcium channels ($Ca_v1.3$ type), in motoneurons below the injury may be responsible for the activation of the long-lasting reflexes and muscle spasms. Despite the development of an animal model of spasticity, direct recordings of PICs from the dendrites of motoneurons are unfeasible experimentally. The objectives of this thesis work were to develop a morphologically-realistic computer model of a spinal motoneuron to study the properties of the dendritic Ca^{+2} PIC (e.g., spatial distribution of channels and mode of activation) and its role in dendritic processing of synaptic inputs (enhancement of individual inputs and integration of multiple inputs). The developed model was also used to design electrical stimulation-based techniques to modulate the gating of voltage-sensitive ion channels mediating the dendritic Ca^{+2} PIC and those generating action potentials (e.g., fast Na^{+} channels). Our simulations demonstrated that the dendritic spatial distribution of $Ca_v1.3$ channels is similar to that of synaptic contacts delivering sensory inputs to motoneurons. This finding explained the effectiveness of sensory inputs in activating the dendritic Ca^{+2} PIC and triggering muscle spasms. Our simulations also supported the linear activation of the Ca^{+2} PIC in proportion to the level of synaptic inputs (i.e., graded activation) during normal cell firing. This finding resolved the dichotomy of the mode of activation of the PIC and its role in the dendritic processing of synaptic inputs. The graded activation of the voltage-gated PIC suggested that electrical stimulation may modulate the magnitude of the PIC, thereby regulating the motoneuronal firing behavior and muscle activity after injury. Various modes of electrical stimulation were examined in the model to suppress the motoneuronal hyperexcitability following injury. Application of electrical fields was shown to modulate primarily the magnitude of the dendritic Ca^{+2} PIC, whereas injection of electrical pulses was shown to hyperpolarize

the first node(s) of Ranvier and reduce axonal conduction. In sum, results of this thesis work provide specifications for novel potential clinical therapies to alleviate spasticity following injury.

ACKNOWLEDGEMENTS

Above all, praise and thanks to ALLAH. I thank him for giving me the strength and diligence to do this work.

I would like to thank my wife, Nermin, for her encouragement and support. It would not have been possible to accomplish this work without her support. I would also like to thank my children, Mahmoud and Sarah. Playing with them and looking at their eyes provided me with hope during the frustration time. I also want to thank my parents who believed in me and provided me with continuous encouragement and motivation.

I would like to thank my supervisors, Dr. Vivian Mushahwar for her support and the opportunities that she has provided me with, and Dr. David Bennett for his amazing insightful discussions. I would also like to thank my committee members, Drs. David Collins, K. Ming Chan, Monica Gorassini, and Richard Stein, for their expert comments on my research work and my dissertation. I truly feel proud of my supervisory committee. To them all I am truly grateful. Special thanks to Dr. Kelvin Jones for introducing me to the world of computer modeling and for having excellent discussions whenever we meet. I would also like to express my deep appreciation to Dr. Locksley McGann, Associate Dean of Faculty of Graduate Studies and Research, for the exceptional support that he provided to me and for attending my final oral defense.

Above all, I am greatly indebted to Dr. Robert Burrell, Chair of the Department of Biomedical Engineering, for the exceptional personal support that he provided to me, and for his words of wisdom and guidance. He provided me with help when there was no hope. He created a path to me through the difficulties, and he was exceptionally generous in giving me his valuable time. To him I truly say from the heart "Thank You. I will never forget that".

Special thanks to Maisie Goh for her advice and support, and helping me to overcome any problem throughout my program. I would also like to acknowledge all my fellow graduate students for their comments on my talks. I sincerely thank Lisa Guevremont for her support before my candidacy exam and Dr. Jonathan Norton for his words of encouragement at all times. I also thank Andrew Ganton and Jason Dyck who have made the workplace an enjoyable place to be. I also want to thank Atiyah Yahya for her continuous support and words of encouragement.

I would like to thank Alberta Heritage Foundation for Medical Research (AHFMR) and the Faculty of Medicine and Dentistry, University of Alberta for their support and funding of my work throughout my doctoral program.

TABLE OF CONTENTS

List of Tables

List of Figures

List of Abbreviations

Action potential	AP
Afterhyperpolarization	AHP
Alternating current	AC
Axon hillock	AH
Calcium-activated potassium channels	K(Ca)
Calcium persistent inward current	Ca^{+2} PIC
Current-voltage	I-V
Delayed rectifier potassium channels	Kdr
Direct current	DC
Fast sodium channels	Naf
Fatigue-resistant	FR
Frequency-Current	F-I
Horseradish peroxidase	HRP
Ia effective synaptic current	Ia I_N
Initial segment	IS
Low voltage-activated	LVA
N-type calcium channels	CaN
Norepinephrine	NE
Negative slope region	NSR
Persistent inward currents	PICs
Persistent sodium channels	Nap
Serotonin	5-HT
Sodium persistent inward current	Na^{+} PIC
Spinal cord	SC
Spinal cord injury	SCI
Tetrodotoxin	TTX
Three-dimensional	3D
Threshold	T

Chapter 1: Introduction

1.1 CLINICAL SPASTICITY

Spasticity is one of the features of the upper motor neuron syndrome, and is a major cause of disability in individuals with a variety of neurological disorders (e.g., spinal cord injury, stroke, cerebral palsy, multiple sclerosis). Spasticity is defined as "a velocity-dependent increase in the tonic stretch reflex (muscle tone) with exaggerated tendon jerks, resulting from the hyperexcitability of the stretch reflex" (Lance 1980). It is also characterized by clonus, clasp-knife response, long-lasting cutaneous reflexes and muscle spasms evoked by brief non-noxious stimuli (Lance and Burke 1974; Young 1994). Spasticity affects over 500,000 people in the United States every year and over 12 million people world wide (Vanek 2005). Furthermore, more than 80% of people with spinal cord injury (SCI) live with spasticity and about 36% to 38% of people with stroke develop spasticity during the first year post-stroke (Levi et al. 1995; Watkins et al. 2002). The large number of individuals affected by spasticity, spasticity-related disabilities, and the required health care costs indicate the need for effective treatments of this neurological disorder.

Spasticity usually develops several months after injury. Immediately following SCI, the spinal cord becomes areflexic for a period of time that lasts for weeks (Nacimiento and Noth 1999). This period is called spinal shock and is characterized by loss of tendon reflexes below the level of the lesion, muscle paralysis, and flaccid muscle tone (Bastian 1890). Several weeks after injury, various muscle reflexes such as the tendon reflex, the flexor withdrawal reflex, and the Babinski sign recover gradually (Hiersemenzel et al. 2000). The threshold of the flexor reflexes, which are usually evoked by cutaneous stimulation, decreases over time to the point that a brief stimulation of the foot plantar surface becomes capable of generating long-lasting strong contraction of the flexor muscles (Ashby and McCrea 1987; Kuhn and Macht 1948). Extensor reflexes, which are usually evoked by proprioceptive stimuli, recover later than the flexor reflexes, and

sometimes flexor/extensor muscle co-contractions, causing rigidity, can occur and can last for several seconds (Ashby and McCrea 1987; Kuhn and Macht 1948). Furthermore, intense muscle spasms lasting for several seconds can be triggered by various other stimuli such as heat/cold sensation and bladder distention (Little et al. 1989). Interestingly, extensor spasms in the leg muscles which make the leg rigid can at times provide assistance in dressing or walking (Barnes 2001). Nonetheless, these spasms are usually painful and sustained contractures may cause deformation in the limb. This led to the taxonomy of spasticity in which spastic contractures that sustain postural tone are termed 'useful' spasticity, whereas contractures that produce abnormal posture are termed 'harmful' spasticity (Mertens and Sindou 2001). In individuals with incomplete SCI spasticity can reduce the functional outcome of the residual voluntary drive; thus, compromising rehabilitation efforts. This makes spasticity one of the most debilitating side effects of spinal cord injury (Delwaide and Pennisi 1994; Little et al. 1989).

1.2 CURRENT TREATMENTS OF SPASTICITY

Current clinical management of spasticity involves a wide variety of therapies ranging from non-invasive (e.g., oral administration of antispastic drugs, physiotherapy) to invasive procedures (e.g., intrathecal injection of baclofen, surgical rhizotomy). The type and rate of treatment depends on the levels of spread (diffuse versus focal spasticity) and disability (mild versus severe spasticity) caused by spasticity (Barnes 2001). The common techniques for clinical management of spasticity are summarized below:

1.2.1 Physiotherapy

A characteristic feature of spasticity is that the muscle tone is dependent on the velocity of muscle stretch (Lance 1980). Therefore, spasticity resists muscle stretch which, in turn, causes the spastic muscles to remain shortened for a long duration of time. The implication of this prolonged muscle shortening is that changes in the properties of the muscle fibers develop (Barnes 2001). Another consequence is that voluntary movements resulting from residual descending drive in individuals with incomplete SCI are restricted. Physiotherapy is thus the first choice of treatment that could be conducted in

companion with other procedures to minimize those side effects. Daily passive muscle stretching is usually recommended to reduce muscle tone and maintain mobility and range of motion. Orthoses and cast devices can also be used to position and hold the limb in a normal position and resist spastic contractures. Strengthening exercises are also performed to strengthen the spastic and surrounding muscles (Boyd and Ada 2001).

1.2.2 Oral antispastic medications

Because oral medications produce systemic effects, they are usually used in patients with diffuse spasticity. The most commonly used antispastic drugs are baclofen, benzodiazepine, dantrolene sodium, clonidine, and tizanidine (Ward and Ko Ko 2001). These drugs could be used alone or in combination to obtain a desired effect. Given that these medications are formed of non-specific pharmacological agents, their major side effect is general suppression of the neuronal activity in individuals already suffering from a reduced voluntary drive. Other common side effects of oral drugs are vomiting, constipation, muscle weakness, and dizziness (Ward and Ko Ko 2001).

Baclofen

Baclofen is the most popular drug in the treatment of spasticity. It has been used as an antispastic drug for more than 30 years (Ward and Ko Ko 2001). Baclofen, which is a $GABA_B$ receptor agonist, is thought to exert its action primarily presynaptically because $GABA_B$ receptors are distributed extensively on the presynaptic terminals of the primary sensory afferents (Price et al. 1984; Yang et al. 2001). Therefore, baclofen likely acts by binding to the presynaptic $GABA_B$ receptors and decreasing neurotransmitter release from presynaptic terminals by reducing Ca^{+2} influx to the cell (Bussieres and El Manira 1999; Miller 1998). Other studies also showed postsynaptic effects of baclofen in turtle motoneurons through reduction of the elevated Ca^{+2} persistent inward current (PIC) (Russo et al. 1998; Svirskis and Hounsgaard 1998). The Ca^{+2} PIC causes a sustained depolarization in the membrane potential which facilitates prolonged motoneuronal firing and activation of long-lasting reflexes during spasticity (Li et al. 2004a; Li et al. 2004b). However, in motoneurons of spastic rats with chronic SCI, baclofen reduced the

prolonged monosynaptic EPSPs without changing the amplitude of the PIC (Li et al. 2004c).

Benzodiazepines

Benzodiazepines act through $GABA_A$ receptors by increasing the binding of GABA to $GABA_A$ receptors (Guidotti et al. 1978; Skerritt and Johnston 1983). This initiates opening of chloride ion channels and cause inhibition of the postsynaptic cell. Therefore, benzodiazepines may act by increasing presynaptic inhibition at spinal and supraspinal sites (Schlosser 1971).

Dantrolene sodium

Dantrolene sodium acts peripherally on muscle fibers by decreasing the release of Ca^{+2} from the sarcoplasmic reticulum; thus, reducing muscle force during contractions (Ellis and Carpenter 1974). This effect is seen on both intrafusal and extrafusal muscle fibers (Monster et al. 1974).

Clonidine

The mechanism of action of clonidine is not fully understood. However, it is thought that clonidine, which is an α_2-adrenergic receptor agonist, has an inhibitory action through the enhancement of presynaptic inhibition of sensory afferents and suppression of polysynaptic reflexes (Schomburg and Steffens 1988; Tremblay and Bedard 1986). Li et al. (2004b) showed that clonidine's antispastic action appears to be due to the blockade of the prolonged polysynaptic EPSPs that activate the PICs.

Tizanidine

Tizanidine is an α_2-adrenergic receptor agonist (Coward 1994). Its mechanism of action is also not fully understood. It may act presynaptically to reduce the release of excitatory neurotransmitters (e.g., glutamate and aspartate) of interneurons (Davies et al. 1983).

1.2.3 Chemical neurolysis

Chemical neurolysis refers to the destruction or blockage of peripheral nerves innervating spastic muscles using chemical substances like phenol or alcohol solutions. These solutions cause destruction of the nerve tissue, mainly myelin, and their effects are proportional to their concentrations (Bakheit 2001). Reactions start as inflammation for some hours, followed by nerve degeneration over weeks (Nathan et al. 1965). Aqueous phenol is also used for motor point injection in spastic muscles. Chemical neurolysis techniques are usually used in individuals with focal spasticity or in those who want to assess the functional gain or effectiveness of future surgical treatments before operation. The motor point injection procedure is easy and safe, and could target specific muscles; however, the effectiveness of injection diminishes over time and repeated injections are needed (Bakheit et al. 1996). The common complication is treatment failure due to poor localization of the nerve or inadequate dosage (Bakheit 2001).

1.2.4 Botulinum toxin

The botulinum toxin is a poisonous substance that acts on the neuromuscular junction to inhibit the release of acetylcholine (Burgen et al. 1949). The toxin causes chemical denervation of intrafusal and extrafusal muscle fibers, and its effect is reversible (Rosales et al. 1996). It is available commercially under the names Botox® (Allergan) and Dysport® (Ipsen). The clinical effect of the toxin appears after 24 to 72 hours, and the duration of the effect is from two to six months depending on the dosage of the toxin (Davis and Barnes 2001). The treatment using botulinum toxin is effective in reducing pain and muscle spasms. The major side effect is excessive weakness of the treated muscle. At times an immune response to the toxin can develop (Zuber et al. 1993). The combination of muscle injection of the botulinum toxin with electrical stimulation leads to improvement in the treatment results (Hesse et al. 1998). The uptake of the toxin may be improved by electrical stimulation; hence, lower dosages could be used.

1.2.5 Intrathecal injection of baclofen

This refers to the injection of baclofen directly to the space around the spinal canal (subarachnoid space). Because baclofen bypasses the blood brain barrier and diffuses into the cerebrospinal fluid, clinical benefits could be obtained at doses 100 to 1000 times less than that used orally (Rushton 2001). This technique is very effective in the treatment of diffuse spasticity; however, it is expensive, invasive, and requires pump maintenance (pump refill, pump replacement, etc). Different types of pumps are used such as manual pumps, constant infusion pumps, and programmable pumps (Medtronics pump). The common problems are catheter failure and leakage of the cerebrospinal fluid into the pump (Brindley et al. 1986).

1.2.6 Surgical procedures

Surgical procedures are commonly used when spasticity can not be managed by any of the aforementioned techniques. They involve the ablation of motor nerves and/or rhizotomy of the sensory spinal roots to interrupt the sensory input (Foerster 1913; Gros et al. 1967). Ablation of motor nerves is effective when spasticity is focal in muscles innervated by the same nerve. In this case, ablation is usually selective to suppress spasticity without causing excessive muscle weakening. Keeping 25% of the motor fibers is necessary to preserve the muscle tone (Mertens and Sindou 2001). On the other hand, the main disadvantage of surgical procedures is that they are irreversible.

1.2.7 Electrical stimulation techniques

Various modalities of electrical stimulation have been used to reduce the level of spasticity. These modalities ranged from surface electrical stimulation of muscles to electrical stimulation of the peripheral and central (e.g., epidural electrical stimulation) nerves.

Electrical stimulation of muscles

Surface electrical stimulation for the reduction of spasticity involved stimulation of the spastic muscles (Vodovnik et al. 1984) as well as their antagonists (Alfieri 1982). In the former case, reduction of spasticity was attributed to the electrical stimulation of the

cutaneous afferents (Bajd et al. 1985; Dewald et al. 1996) which is thought to suppress the motoneuronal excitability through the depression of the propriospinal system (Dewald and Given 1994; Dewald et al. 1996). With this protocol, the reduction in spasticity was maintained for at least 30 min after stimulation (Dewald et al. 1996). Reduction of spasticity was attributed to the effect of electrical stimulation in activating the Ia-reciprocal inhibition pathway which, in turn, reduces the amplitude of the motoneuronal PIC (Kuo et al. 2003).

Electrical stimulation of peripheral nerves

Electrical stimulation of peripheral nerves to block the unwanted motor nerve activity in spasticity was examined in animal models. Application of DC electrical stimulation (Bhadra and Kilgore 2004) or high-frequency stimulation of various waveforms (e.g., sinusoidal and rectangular pulses) were shown to induce conduction block in peripheral nerves (Bhadra and Kilgore 2005; Kilgore and Bhadra 2004; Williamson and Andrews 2005). This conduction block was complete and reversible.

Epidural electrical stimulation

Electrical stimulation of the dorsal columns of the spinal cord through epiduarlly placed electrodes was also used for the reduction of spasticity (Kanaka and Kumar 1990; Pinter et al. 2000). Epidural stimulation was initially used to alleviate pain. Its analgesic action in reducing pain was explained by the "gate theory" in which activity induced in low-threshold afferents is thought to inhibit nociceptive neurons by the effect of their shared inhibitory interneurons (Melzack and Wall 1984; Wall 1964). Epidural stimulation can be effective in reducing mild spasticity (Barolat et al. 1995). Stimulation of the lumbar part of the spinal cord was used to reduce spasticity in the lower limbs, whereas stimulation of the cervical part of the spinal cord was used to reduce spasticity in the upper limbs (Pinter et al. 2000). The efficacy of stimulation in reducing spasticity was found to be dependent on the location of the electrodes on the cord and the parameters (e.g., amplitude, frequency, and pulse width) of the stimulation waveform (Pinter et al. 2000; Waltz et al. 1987). The clinical effect of epidural stimulation may be achieved by activating inhibitory networks in the spinal cord (Pinter et al. 2000), increasing the level of

presynaptic inhibition (Hunter and Ashby 1994), or activating inhibitory networks within the dorsal column-brainstem-spinal loop (Saade et al. 1984). However, other studies showed that epidural stimulation of the dorsal column lacks long-term efficacy in reducing spasticity, pain, and muscle spasms after SCI (Midha and Schmitt 1998).

1.3 MECHANISMS UNDERLYING SPASTICITY

The mechanisms underlying spasticity are still unclear; however, some mechanisms have been proposed.

1.3.1 Fusimotor hyperexcitability

The common characteristics between human spasticity and animal rigidity after intercollicular decerebration led to the assumption that the same spinal mechanisms are contributing to the exaggeration of the stretch reflex in the two conditions. These common features involve more pronounced reflexes with faster movements particularly in the anti-gravity muscles (Pierrot-Deseilligny and Burke 2005). For decerebrate animal rigidity, the exaggerated stretch reflex is due to the hyperactivity of gamma motor neurons (γ- motoneurons) that control the sensitivity of muscle spindles and set the gain of the spinal stretch reflex (Rushworth 1960). This hyperactivity of γ- motoneurons contributes to the hyperexcitability of the stretch reflex (for review see Rothwell 1994). The hypothesis on the role of muscle spindle hypersensitivity in spasticity was disproved later by direct recordings from muscle spindles in humans during spasticity which showed no increase in spindle activity (Hagbarth et al. 1973). Furthermore, despite the resemblance between spasticity and decerebrate animal rigidity, there are critical differences in the time course of development of each. Spasticity develops weeks after injury, whereas decerebrate animal rigidity appears almost immediately, usually within 1 hour, after decerebration (Pierrot-Deseilligny and Burke 2005). This prolonged duration for the development of spasticity supports the contribution of plastic changes in other spinal pathways after injury to spasticity (see below).

1.3.2 Axonal sprouting

Another mechanism for spasticity was proposed by McCouch et al. (1958). Following spinal cord injury, terminals of the damaged axons on spinal neurons (both motoneurons and interneurons) degenerate. After nearly 2 to 3 weeks of injury, the remaining afferent terminals sprout new synaptic terminals in the vacated space and enhance the efficacy of the spinal connections. The proposed mechanism of axonal sprouting was attractive as it provided an explanation for the temporal changes in behavior after injury. This mechanism may contribute to spasticity after SCI by strengthening existing spinal circuits and/or increasing synaptic inputs to interneurons (Calancie et al. 2002; Krenz and Weaver 1998).

1.3.3 Alterations in other spinal mechanisms

Many spinal pathways, both excitatory and inhibitory, converge onto the motoneuron and are involved in the modulation of the excitability of the stretch reflex (e.g., Ia-reciprocal inhibition, recurrent inhibition, presynaptic inhibition, interneurons, etc). Theoretically, malfunctions that cause enhancement of the excitability of an excitatory pathway or suppression of the excitability of an inhibitory pathway would increase the excitability of the stretch reflex (Pierrot-Deseilligny and Burke 2005). Experimental evidence demonstrated that a reduction in the excitability of various inhibitory pathways, in addition to an enhancement in the excitability of motoneurons and interneurons exists after SCI or stroke.

Reduction in presynaptic inhibition

Presynaptic inhibition evoked by tendon vibration was found to be reduced in spastic individuals with stroke (Delwaide 1973; Delwaide and Pennisi 1994) and SCI (Faist et al. 1994). The magnitude of the H-reflex and tendon jerks were reduced when vibration of the homonymous muscle or tendon was applied (Delwaide 1973). However, this response was influenced by the effect of post-activation depression activated by the applied vibration as well (Crone and Nielsen 1989; Katz et al. 1977).

Reduction in post-activation depression

Post-activation depression measured at rest was reduced in spastic animals with midthoracic contusion injury regardless of the level of lesion, but not changed on the side contralateral to the lesion (Hultborn and Nielsen 1998; Thompson et al. 1998). However, when muscles ipsilateral to the lesion were activated, post-activation depression was found to be reduced significantly; thus, its contribution to spasticity is uncertain (Stein and Thompson 2006).

Reduction in Ia reciprocal inhibition

Contradictory results have been obtained regarding the role of Ia reciprocal inhibition in spasticity. Ia reciprocal inhibition was found to be reduced in spastic patients diagnosed with multiple sclerosis (Morita et al. 2001). Similarly, individuals with spasticity after incomplete SCI could not suppress their H-reflex by activating their antagonist muscle, and showed abnormal coactivation of their muscles during isometric muscle contractions (Boorman et al. 1996). Conversely, Crone et al. (2003) reported Ia reciprocal facilitation between antagonistic muscles after SCI.

Enhancement in the excitability of interneurons

Spasticity could result from an abnormality not only in the components of the stretch reflex (e.g., the motoneuron, Ia-motoneuron synapse, etc), but also in other pathways converging onto those components (e.g., interneurons, Ia-reciprocal inhibition, etc). Evidence supporting an increase in the excitability of spinal interneurons in spasticity has been reported. Flexor reflexes mediated by polysynaptic pathways were increased in magnitude in individuals with spasticity after SCI (Hiersemenzel et al. 2000). Moreover, Mailis and Ashby (1990) showed an enhanced transmission through polysynaptic pathways from Ia afferents to motoneurons after SCI. This was indicated by late facilitation of Ia excitatory post synaptic potentials (EPSPs). More recently, Kitzman (2006, 2007) used immunohistochemical techniques to study the temporal changes in excitatory and inhibitory inputs during the development of spasticity (arising from myelinated sensory afferents and spinal interneuronal sources) to motoneurons. He showed that during spasticity there is an increase in the ratio of excitatory to inhibitory

inputs; however, the increased excitation appears to originate predominantly from spinal interneurons and not from Ia afferents.

Enhancement in the excitability of motoneurons

An increase in the excitability of spinal motoneurons as a potential mechanism underlying spasticity was initially suggested to account for spasticity (Landau and Clare 1964). The excitability of motoneurons is usually assessed through waveforms elicited from the direct activation of Ia-afferents (H-wave), the direct activation of motor axons (M-wave), and the antidromic activation of motoneurons (F-wave) in response to electrical stimulation of the nerve. In stroke patients with spasticity, an increase in the ratio of H_{max}/M_{max} was observed (Delwaide 1985; Landau and Clare 1964). Furthermore, an increase in the amplitude and persistence of F-wave was shown in individuals with spasticity after SCI (Hiersemenzel et al. 2000). Alteration in the intrinsic membrane properties (e.g., activation of PICs, depolarization of resting membrane potential, etc) in motoneurons of spastic rats after chronic SCI have been shown to contribute to the increased excitability of motoneurons during spasticity (Li et al. 2004a; Li et al. 2004b).

In sum, spasticity appears to be the result of malfunction in one or more of the spinal pathways involved in regulating the excitability of the stretch reflex and its components. Therefore, a rehabilitation scheme that suppresses the excitability of any of the excitatory pathways and/or enhances the excitability of any of the inhibitory pathways could alleviate spasticity. Interestingly, when the intensity of spasticity, as assessed on the Ashworth scale, was examined versus the level of aberration in the various spinal pathways (e.g., motoneuron hyperexcitability, reduction in presynaptic inhibition, Ia reciprocal inhibition, etc), no statistically significant correlation was found (Faist et al. 1994; Hiersemenzel et al. 2000; Marque et al. 2001; Pierrot-Deseilligny and Burke 2005). Therefore, the intensity of spasticity is not a function of one specific abnormality.

1.4 ACTIVATION OF PICs DURING SPASTICITY AFTER SCI

Schwindt and Crill (1977) were the first to discover PICs in spinal motoneurons. A PIC is a depolarizing current that does not inactivate with prolonged membrane depolarization. In the mid 1980s, Hultborn and colleagues (the Copenhagen group) suggested that the long-lasting exaggerated reflexes and muscle spasms seen during spasticity could be partly due to changes in the voltage-dependent intrinsic membrane properties of spinal motoneurons and activation of PICs after injury (for review see Eken et al. 1989; Powers and Binder 2001). The activation of PICs changed the response of motoneurons to a brief volley of Ia input from a short-lasting firing activity in the anaesthetized preparation to a long-lasting firing activity (i.e., self-sustained firing) in the decerebrate preparation (Hounsgaard et al. 1988; Hounsgaard et al. 1984). Therefore, activation of PICs caused a maintained increase in the motoneuronal excitability. The activation of PICs was found to be contingent upon the level of monoaminergic input (mainly NE and 5-HT) from the brainstem to motoneurons (Conway et al. 1988; Hounsgaard et al. 1988; Hounsgaard and Kiehn 1985). Immediately following SCI (acute injury), the monoaminergic drive from the brainstem to motoneurons is lost leading to immediate reduction of the PICs, suppression of the motoneuronal excitability, and depression of spinal reflexes (spinal shock). Weeks after injury (chronic injury), motoneurons below the level of the lesion regain their capacity to generate a near-normal level of PICs and self-sustained firing (Li et al. 2004a). Activation of the PICs after SCI in the absence of the monoaminergic inputs to motoneurons from the brainstem is due to the supersensitivity of motoneuron receptors after long-term injury to the residual monoamines (5-HT and NE) below the level of the lesion from the autonomic system and blood vessels (Harvey et al. 2006a, b; Li et al. 2007). However, the activation of the PICs in chronic injury is no longer under the control of the brainstem leading to uncontrolled motoneuronal firing evoked by synaptic inputs (Li et al. 2004a).

1.4.1 Ionic channels mediating PICs in motoneurons

In spinal motoneurons, PICs are mediated by two distinct types of channels with distinctive properties: Low voltage-activated (LVA) L-type calcium channels ($Ca_V1.3$

type; Hounsgaard and Kiehn 1985, 1993; Schwindt and Crill 1980) and persistent sodium channels (Hsiao et al. 1998; Lee and Heckman 2001; Li and Bennett 2003). The Ca^{+2} PIC, which has little or no time-dependent inactivation, appears to be responsible for the long-lasting reflexes seen in spasticity (Gorassini et al. 2004; Li et al. 2004a). The Ca^{+2} PIC has an activation threshold range of -45 to -55 mV (Hounsgaard and Kiehn 1989), nearly ± 5 mV relative to the spike threshold (Li and Bennett 2003), and has slow activation/deactivation kinetics (Perrier et al. 2002). The Ca^{+2} PIC is very hysteretic (Li and Bennett 2003) and its mediating channels are of dendritic origin (Hounsgaard and Kiehn 1993). The Ca^{+2} PIC also plays a role in amplification of synaptic inputs (Bennett et al. 1998; Lee and Heckman 2000).

On the other hand, Na^{+} PIC, which has partial inactivation with time, appears to be responsible for the initiation of the spontaneous firing commonly seen after a muscle spasm or voluntary contraction (Gorassini et al. 2004; Li et al. 2004a). The Na^{+} PIC has an activation threshold of 7 mV below the spike threshold (Li and Bennett 2003), and has fast activation/inactivation kinetics (Hsiao et al. 1998; Li and Bennett 2003). Given that the Na^{+} PIC is not hysteretic (Li and Bennett 2003), its mediating channels are thought to be located primarily at the soma and proximal dendrites. The Na^{+} PIC plays an essential role in initiation of action potentials (APs) during rhythmic firing (Lee and Heckman 2001). Motor unit recordings in patients with spasticity after long-term injury to the spinal cord suggest that spasticity in humans involves the same ionic mechanisms reported in animal models (Gorassini et al. 2004; Kiehn and Eken 1997).

1.4.2 Effect of monoamines on motoneurons

The monoaminergic drive from the brainstem to the spinal cord forms a control system to regulate the excitability of spinal neurons for different motor tasks (Baldissera et al. 1981). A number of neuromodulators have been shown to influence motoneurons such as 5-HT, NE, acetylcholine, thyroid releasing hormone, substance P, and adenosine; however, 5-HT and NE were the most extensively studied monoaminergic inputs to spinal motoneurons. Axons that release 5-HT and NE from the brainstem originate from the raphe nucleus and the locus ceruleus nucleus, respectively (Maxwell et al. 1996; Patel

et al. 1997). Interestingly, monoamines have differential effects on the ventral versus dorsal horn. For the ventral horn, monoamines have excitatory effects on motoneurons and low-threshold muscle afferents (Hammar and Jankowska 2003). Furthermore, 5-HT and NE have been shown to enhance the activation of PICs (Lee and Heckman 1999), reduce the resting leak conductance (Elliott and Wallis 1992), induce membrane depolarization (Hsiao et al. 1997), enhance hyperpolarization-activated inward current (Hsiao et al. 1997), and decrease the amplitude of the medium duration afterhyperpolarization (Berger et al. 1992). Collectively, these effects increase the excitability of the cell, increase the slope of the frequency-current relationship (Berger et al. 1992; Heckman et al. 2005), reduce the amount of synaptic current required to recruit the motoneuron or to generate self-sustained firing (Lindsay and Feldman 1993).

Conversely, monoamines inhibit, through presynaptic inhibition, sensory inputs to motoneurons (Jacobs and Fornal 1997) such as cutaneous inputs (Clarke et al. 2002) and high-threshold muscle afferents (groups III and IV) (Cleland and Rymer 1990; Jankowska 1992; Miller et al. 1995). They also suppress inputs to deep dorsal horn interneurons from high-threshold afferents (groups III and IV) (Garraway and Hochman 2001). The mechanism of this differential control of the monoaminergic drive on the spinal cord is attained through the effect of the different monoamine receptors. For example, PIC facilitation in motoneurons is achieved through 5-HT_2 (Perrier and Hounsgaard 2003) and NE α_1 receptors (Lee and Heckman 1999), whereas inhibition of cutaneous inputs and high-threshold muscle afferent inputs is achieved through 5-$HT1_{b/d}$ and NE α_2 receptors (Bras et al. 1990; Miller et al. 1995).

Immediately following SCI (acute injury), the loss of the monoaminergic drive reduces the excitability of motoneurons in the ventral horn, but increases the size and duration of the polysynaptic EPSPs of sensory inputs mediated through the dorsal horn, due to loss of inhibition (Bennett et al. 2004). Long-lasting reflexes are not activated during this stage due to the reduced excitability of motoneurons. Conversely, in chronic injury, motoneurons become highly sensitive to monoamines. This supersensitivity of receptors allows the residual monoamines available below the level of the lesion to reactivate the

PICs after injury and restore the motoneuronal excitability (Harvey et al. 2006a, b; Li et al. 2007). At this stage, prolonged EPSPs generated by sensory stimuli can activate the PIC and trigger long-lasting reflexes and muscle spasms (Bennett et al. 2004).

1.5 WORK OBJECTIVES AND DISSERTATION OUTLINE

The long-term goal of this project is to develop a rehabilitation intervention for reducing the level of spasticity after chronic SCI. For the present thesis work, the objective was to develop a detailed computer model of a spinal motoneuron that could be used to study the dendritic spatial distribution of Ca^{+2} PIC-mediating channels, and investigate activation properties of PICs which are responsible for generating long-lasting reflexes and muscle spasms after injury. Given that it is experimentally unfeasible to record currents directly from the very small and extensive dendrites of real motoneurons during synaptically-evoked cell firing, computer simulations were chosen for conducting this work. The developed model was also used to design novel electrical stimulation paradigms to suppress the enhanced excitability of spinal motoneurons after chronic SCI. To achieve this objective, four studies were conducted which appear in the present thesis in the following order:

Chapter 2. Simulation of Dendritic $Ca_V1.3$ Channels in Cat Lumbar Motoneurons: Spatial Distribution

This study had two primary objectives: 1) to develop a three-dimensional morphologically-detailed compartmental model of a spinal α-motoneuron that accurately represents the firing behavior of spinal motoneurons in a reduced preparation (i.e., anaesthetized preparation in which PICs are suppressed), 2) to study the dendritic spatial distribution of $Ca_V1.3$ channels that mediate Ca^{+2} PIC and match electrical and firing properties of spinal motoneurons in a decerebrate preparation (i.e., preparation in which the PICs are active). The lack of neuromodulatory control of the Ca^{+2} PIC activation through the brainstem after SCI is responsible for the long-lasting reflexes seen in spasticity. Although the $Ca_V1.3$ channels were thought to be of dendritic origin, their dendritic spatial distribution is

still unknown. The distribution of these channels is critical because it has a direct influence on the activation/deactivation properties of the Ca^{+2} PIC; hence, the properties (e.g., duration) of the generated long-lasting reflexes after injury. Our hypothesis was that dendritic $Ca_V1.3$ channels would have a similar distribution to that of dendritic synaptic contacts delivering sensory inputs to motoneurons. Results of this study supported our hypothesis and the developed model was able to match multiple sets of experimental data with that distribution. A version of this chapter has been published (ElBasiouny SM, Bennett DJ, and Mushahwar VK, *J. Neurophysiol.* 94: 3961-74, 2005 'used with permission').

Chapter 3. Simulation of Ca^{+2} Persistent Inward Currents in Spinal Motoneurons: Mode of Activation and Integration of Synaptic Inputs

The objective of this study was to perform direct measurements of the dendritic Ca^{+2} PIC during simulations of synaptically-evoked cell firing to examine the nature of activation of the Ca^{+2} PIC by sensory stimuli (graded versus all-or-none activation). The role of the dendritic Ca^{+2} PIC in dendritic processing of synaptic inputs to motoneurons (e.g., amplification of individual inputs and integration of multiple inputs) was also investigated. This study demonstrated that during normal cell firing the Ca^{+2} PIC is activated linearly in proportion to the level of synaptic input (graded activation). Graded activation of the Ca^{+2} PIC with increasing synaptic input resulted in a graded (linear) enhancement and linear summation of synaptic inputs. When the PIC reached its full activation level, additional increase in the level of synaptic input resulted in minimal changes in the Ca^{+2} PIC which became saturated. The saturated Ca^{+2} PIC enhanced synaptic inputs by a constant amount (constant current), and caused less-than linear summation of multiple synaptic inputs. These findings resolve the discrepancies in experimental reports regarding the mode of activation of the PIC and its role in the enhancement and integration of synaptic inputs. A version of this chapter has been published (ElBasiouny SM, Bennett DJ, and Mushahwar VK, *J. Physiol. (Lond)* 570 (2): 355-74, 2006 'used with permission').

Chapter 4. Suppressing the Excitability of Spinal Motoneurons by Extracellularly-applied Electrical Fields: Insights from Computer Simulations

The objective of this study was to examine the efficacy of applied electrical fields as a rehabilitation intervention for the reduction of spasticity in chronic SCI. Our hypothesis was that the applied electrical field would modulate the magnitude of the dendritic Ca^{+2} PIC and suppress the increased excitability of spinal motoneurons after injury. This study supported our proposal to apply AC and DC electrical fields to suppress motoneuronal excitability. A version of this chapter has been submitted for publication in the Journal of Applied Physiology.

Chapter 5. Modulation of Motoneuronal Firing Behavior after Spinal Cord Injury using Intraspinal Microstimulation Current Pulses: A Modeling Study

The objective of this study was to examine the efficacy of extracellularly-injected current pulses with various waveforms in modulating the firing activity of spinal motoneurons following SCI. Our hypothesis was that high-frequency current pulses would inactivate the Na^{+} channels and prohibit the propagation of APs through the axon, whereas biphasic charge-imbalanced pulses would induce differential polarization in the different structures of the motoneuron and reduce the axonal firing activity. Results of this study supported our hypothesis and suggested that suprathreshold high-frequency AC pulses and subthreshold biphasic imbalanced pulses can reduce the firing activity of motoneurons. A version of this chapter has been published (ElBasiouny SM and Mushahwar VK, *J. Applied Physiol.* , in press, 2007 'used with permission').

In conclusion, the work of the present thesis supports the hypothesis that electrical stimulation-based techniques could reduce spasticity in chronic SCI by suppressing the hyperexcitability of spinal motoneurons.

1.6 REFERENCES

Alfieri V. Electrical treatment of spasticity. Reflex tonic activity in hemiplegic patients and selected specific electrostimulation. *Scand J Rehabil Med* 14: 177-182, 1982.

Ashby P and McCrea D. Neurophysiology of spinal spasticity. In: *Handbook of the spinal cord*, edited by Davidoff RA. New York: Marcel Dekker Inc, 1987, p. 120-143.

Bajd T, Gregoric M, Vodovnik L, and Benko H. Electrical stimulation in treating spasticity resulting from spinal cord injury. *Arch Phys Med Rehabil* 66: 515-517, 1985.

Bakheit A. Chemical neurolysis in the management of spasticity. In: *Upper Motor Neurone Syndrome and Spasticity. Clinical Management and Neurophysiology*, edited by Barnes MP and Johnson GR: Cambridge University Press, 2001, p. 188-205.

Bakheit A, Badwan D, and McLellan D. The effectiveness of chemical neurolysis in the treatment of lower limb muscle spasticity. *Clin Rehabil* 10: 40-43, 1996.

Baldissera F, Hultborn H, and Illert M. Integration in spinal neuronal systems. In: *Handbook of Physiology. The Nervous System. Motor Control.*, edited by Brooks V. Bethesda, MD: American Physiological Society, 1981, p. 509-595.

Barnes MP. An overview of the clinical management of spasticity. In: *Upper Motor Neurone Syndrome and Spasticity. Clinical Management and Neurophysiology*, edited by Barnes MP and Johnson GR: Cambridge University Press, 2001, p. 1-11.

Barolat G, Singh-Sahni K, Staas WJ, Shatin D, Ketcik B, and Allen K. Epidural spinal cord stimulation in the management of spasms in spinal cord injury: a prospective study. *Stereotact Funct Neurosurg* 64: 153-164, 1995.

Bastian H. On the symptomatology of total transverse lesions of the spinal cord, with special reference to the condition of the various reflexes. *Med-Chir Trans Lond* 73: 151-217, 1890.

Bennett DJ, Hultborn H, Fedirchuk B, and Gorassini MA. Synaptic Activation of Plateaus in Hindlimb Motoneurons of Decerebrate Cats. *J Neurophysiol* 80: 2023-2037, 1998.

Bennett DJ, Sanelli L, Cooke CL, Harvey PJ, and Gorassini MA. Spastic Long-Lasting Reflexes in the Awake Rat After Sacral Spinal Cord Injury. *J Neurophysiol* 91: 2247-2258, 2004.

Berger A, Bayliss D, and Viana F. Modulation of neonatal rat hypoglossal motoneuron excitability by serotonin. *Neurosci Lett* 143: 164-168, 1992.

Bhadra N and Kilgore KL. Block of mammalian motor nerve conduction using high frequency alternating current. *10th Annual conference of the international FES society*: 165-167, 2005.

Bhadra N and Kilgore KL. Direct current electrical conduction block of peripheral nerve. *IEEE Trans Neural Syst Rehabil Eng* 12: 313-324, 2004.

Boorman GI, Lee RG, Becker WJ, and Windhorst UR. Impaired "natural reciprocal inhibition" in patients with spasticity due to incomplete spinal cord injury. *Electroencephalogr Clin Neurophysiol* 101: 84-92., 1996.

Boyd RN and Ada L. Physiotherapy management of spasticity. In: *Upper Motor Neurone Syndrome and Spasticity. Clinical Management and Neurophysiology*, edited by Barnes MP and Johnson GR: Cambridge University Press, 2001, p. 96-121.

Bras H, Jankowska E, Noga B, and Skoog B. Comparison of Effects of Various Types of NA and 5-HT Agonists on Transmission from Group II Muscle Afferents in the Cat. *Eur J Neurosci* 2: 1029-1039, 1990.

Brindley G, Polkey C, Rushton D, and Cardozo L. Sacral anterior root stimulators for bladder control in paraplegia: the first 50 cases. *J Neurol Neurosurg Psychiatry* 49: 1104-1114, 1986.

Burgen A, Dickens F, and Zatman L. The action of botulinum toxin on the neuro-muscular junction. *J Physiol* 109: 10-24, 1949.

Bussieres N and El Manira A. GABAB receptor activation inhibits N- and P/Q-type calcium channels in cultured lamprey sensory neurons. *Brain Research* 847: 175-185, 1999.

Calancie B, Molano MR, and Broton JG. Interlimb reflexes and synaptic plasticity become evident months after human spinal cord injury. *Brain* 125: 1150-1161, 2002.

Clarke RW, Eves S, Harris J, Peachey JE, and Stuart E. Interactions between cutaneous afferent inputs to a withdrawal reflex in the decerebrated rabbit and their control by descending and segmental systems. *Neuroscience* 112: 555-571, 2002.

Cleland CL and Rymer WZ. Neural mechanisms underlying the clasp-knife reflex in the cat. I. Characteristics of the reflex. *J Neurophysiol* 64: 1303-1318, 1990.

Conway BA, Hultborn H, Kiehn O, and Mintz I. Plateau potentials in alpha-motoneurones induced by intravenous injection of L-dopa and clonidine in the spinal cat. *J Physiol* 405: 369-384, 1988.

Coward D. Tizanidine: neuropharmacology and mechanism of action. *Neurology* 44: S6-10; discussion S10-11, 1994.

Crone C, Johnsen LL, Biering-Sorensen F, and Nielsen JB. Appearance of reciprocal facilitation of ankle extensors from ankle flexors in patients with stroke or spinal cord injury. *Brain* 126: 495-507, 2003.

Crone C and Nielsen J. Methodological implications of the post activation depression of the soleus H-reflex in man. *Exp Brain Res* 78: 28-32, 1989.

Davies J, Johnston S, and Lovering R. Inhibition by DS 103-282 of D-(3H) aspartate release from spinal cord slices. *Br J Pharmacol* 78: 2P, 1983.

Davis EC and Barnes MP. The use of botulinum toxin in spasticity. In: *Upper Motor Neurone Syndrome and Spasticity. Clinical Management and Neurophysiology*, edited by Barnes MP and Johnson GR: Cambridge University Press, 2001, p. 206-222.

Delwaide P. Electrophysiological testing of spastic patients: its potential usefulness and limitation. In: *Clinical Neurophysiology in spasticity*, edited by Delwaide J and Young R. Amsterdam: Elsevier, 1985, p. 185-203.

Delwaide P. Human monosynaptic reflexes and presynaptic inhibition. In: *New developments in electromyography and clinical neurophysiology*, edited by Desmedt J. Basel: Karger, 1973, p. 508-522.

Delwaide P and Pennisi G. Tizanidine and electrophysiologic analysis of spinal control mechanisms in humans with spasticity. *Neurology* 44: S21-27; discussion S27-28, 1994.

Dewald J and Given J. Electrical stimulation and spasticity reduction: fact or fiction? *Phys Med Rehab - State of the art reviews* 8: 507-522, 1994.

Dewald J, Given J, and Rymer W. Long-lasting reductions of spasticity induced by skin electrical stimulation. *IEEE Trans Rehabil Eng* 4: 231-242, 1996.

Eken T, Hultborn H, and Kiehn O. Possible functions of transmitter-controlled plateau potentials in alpha motoneurones. *Prog Brain Res* 80: 257-267; discussion 239-242, 1989.

Elliott P and Wallis DI. Serotonin andl-norepinephrine as mediators of altered excitability in neonatal rat motoneurons studied in vitro. *Neuroscience* 47: 533-544, 1992.

Ellis K and Carpenter J. Mechanism of control of skeletal-muscle contraction by dantrolene sodium. *Arch Phys Med Rehabil* 55: 362-369, 1974.

Faist M, Mazevet D, Dietz V, and Pierrot-Deseilligny E. A quantitative assessment of presynaptic inhibition of la afferents in spastics: Differences in hemiplegics and paraplegics. *Brain* 117: 1449-1455, 1994.

Foerster O. On the indications and results of the excision of posterior spinal nerve root in men. *Surg Gynecol Obstet* 16: 463-474, 1913.

Garraway SM and Hochman S. Modulatory Actions of Serotonin, Norepinephrine, Dopamine, and Acetylcholine in Spinal Cord Deep Dorsal Horn Neurons. *J Neurophysiol* 86: 2183-2194, 2001.

Gorassini MA, Knash ME, Harvey PJ, Bennett DJ, and Yang JF. Role of motoneurons in the generation of muscle spasms after spinal cord injury. *Brain* 127: 2247-2258, 2004.

Gros C, Ouaknine G, Vlahovitch B, and Frerebeau P. [Selective posterior radicotomy in the neurosurgical treatment of pyramidal hypertension]. *Neurochirurgie* 13: 505-518, 1967.

Guidotti A, Toffano G, and Costa E. An endogenous protein modulates the affinity of GABA and benzodiazepine receptors in rat brain. *Nature* 275: 553-555, 1978.

Hagbarth KE, Wallin G, and Lofstedt L. Muscle spindle responses to stretch in normal and spastic subjects. *Scand J Rehabil Med* 5: 156-159, 1973.

Hammar I and Jankowska E. Modulatory Effects of alpha 1-,alpha 2-, and beta -Receptor Agonists on Feline Spinal Interneurons with Monosynaptic Input from Group I Muscle Afferents. *J Neurosci* 23: 332-338, 2003.

Harvey PJ, Li X, Li Y, and Bennett DJ. 5-HT2 Receptor Activation Facilitates a Persistent Sodium Current and Repetitive Firing in Spinal Motoneurons of Rats With and Without Chronic Spinal Cord Injury. *J Neurophysiol* 96: 1158-1170, 2006a.

Harvey PJ, Li X, Li Y, and Bennett DJ. Endogenous Monoamine Receptor Activation Is Essential for Enabling Persistent Sodium Currents and Repetitive Firing in Rat Spinal Motoneurons. *J Neurophysiol* 96: 1171-1186, 2006b.

Heckman C, Gorassini M, and Bennett D. Persistent inward currents in motoneuron dendrites: Implications for motor output. *Muscle Nerve* 31: 135-156, 2005.

Hesse S, Reiter F, Konrad M, and Jahnke MT. Botulinum toxin type A and short-term electrical stimulation in the treatment of upper limb flexor spasticity after stroke: a randomized, double-blind, placebo-controlled trial. *Clinical Rehabilitation* 12: 381-388, 1998.

Hiersemenzel L-P, Curt A, and Dietz V. From spinal shock to spasticity: Neuronal adaptations to a spinal cord injury. *Neurology* 54: 1574-1582, 2000.

Hounsgaard J, Hultborn H, Jespersen B, and Kiehn O. Bistability of alpha-motoneurones in the decerebrate cat and in the acute spinal cat after intravenous 5-hydroxytryptophan. *J Physiol* 405: 345-367., 1988.

Hounsgaard J, Hultborn H, Jespersen B, and Kiehn O. Intrinsic membrane properties causing a bistable behaviour of alpha-motoneurones. *Exp Brain Res* 55: 391-394, 1984.

Hounsgaard J and Kiehn O. Ca++ dependent bistability induced by serotonin in spinal motoneurons. *Exp Brain Res* 57: 422-425., 1985.

Hounsgaard J and Kiehn O. Calcium spikes and calcium plateaux evoked by differential polarization in dendrites of turtle motoneurones in vitro. *J Physiol* 468: 245-259, 1993.

Hounsgaard J and Kiehn O. Serotonin-induced bistability of turtle motoneurones caused by a nifedipine-sensitive calcium plateau potential. *J Physiol* 414: 265-282., 1989.

Hsiao C-F, Negro CAD, Trueblood PR, and Chandler SH. Ionic Basis for Serotonin-Induced Bistable Membrane Properties in Guinea Pig Trigeminal Motoneurons. *J Neurophysiol* 79: 2847-2856, 1998.

Hsiao CF, Trueblood PR, Levine MS, and Chandler SH. Multiple Effects of Serotonin on Membrane Properties of Trigeminal Motoneurons In Vitro. *J Neurophysiol* 77: 2910-2924, 1997.

Hultborn H and Nielsen J. Modulation of transmitter release from Ia afferents by their preceding activity - a 'postactivation depression'. In: *Presynaptic inhibition and neural control*, edited by Rudomin P, Romo R and Mendell LM. New York: Oxford University Press, 1998, p. 178-191.

Hunter JP and Ashby P. Segmental effects of epidural spinal cord stimulation in humans. *J Physiol* 474: 407-419, 1994.

Jacobs BL and Fornal CA. Serotonin and motor activity. *Current Opinion in Neurobiology* 7: 820-825, 1997.

Jankowska E. Interneuronal relay in spinal pathways from proprioceptors. *Progress in Neurobiology* 38: 335-378, 1992.

Kanaka T and Kumar M. Neural stimulation for spinal spasticity. *Paraplegia* 28: 399-405, 1990.

Katz R, Morin C, Pierrot-Deseilligny E, and Hibino R. Conditioning of H reflex by a preceding subthreshold tendon reflex stimulus. *J Neurol Neurosurg Psychiatry* 40: 575-580, 1977.

Kiehn O and Eken T. Prolonged Firing in Motor Units: Evidence of Plateau Potentials in Human Motoneurons? *J Neurophysiol* 78: 3061-3068, 1997.

Kilgore K and Bhadra N. Nerve conduction block utilising high-frequency alternating current. *Med Biol Eng Comput* 42: 394-406, 2004.

Kitzman P. Changes in vesicular glutamate transporter 2, vesicular GABA transporter and vesicular acetylcholine transporter labeling of sacrocaudal motoneurons in the spastic rat. *Experimental Neurology* 197: 407-419, 2006.

Kitzman P. VGLUT1 and GLYT2 labeling of sacrocaudal motoneurons in the spinal cord injured spastic rat. *Experimental Neurology* In Press, Corrected Proof, 2007.

Krenz NR and Weaver LC. Sprouting of primary afferent fibers after spinal cord transection in the rat. *Neuroscience* 85: 443-458, 1998.

Kuhn R and Macht M. Some manifestations of reflex activity in spinal man with particular reference to the occurrence of extensor spasm. *Bull Johns Hopkins Hosp* 84: 43-85, 1948.

Kuo JJ, Lee RH, Johnson MD, Heckman HM, and Heckman C. Active Dendritic Integration of Inhibitory Synaptic Inputs In Vivo. *J Neurophysiol* 90: 3617-3624, 2003.

Lance J. Pathophysiology of spasticity and clinical experience with Baclofen. In: *Spasticity: Disordered motor control*, edited by Lance J, Feldman R, Young R and Koella W. Chicago: Yearbook, 1980, p. 185 – 204.

Lance J and Burke D. Mechanisms of spasticity. *Arch Phys Med Rehabil* 55: 332-337, 1974.

Landau W and Clare M. Fusimotor function. Vi. H reflex, tendon jerk, and reinforcement in hemiplegia. *Arch Neurol* 10: 128-134, 1964.

Lee RH and Heckman CJ. Adjustable Amplification of Synaptic Input in the Dendrites of Spinal Motoneurons In Vivo. *J Neurosci* 20: 6734-6740, 2000.

Lee RH and Heckman CJ. Enhancement of Bistability in Spinal Motoneurons In Vivo by the Noradrenergic alpha 1 Agonist Methoxamine. *J Neurophysiol* 81: 2164-2174, 1999.

Lee RH and Heckman CJ. Essential Role of a Fast Persistent Inward Current in Action Potential Initiation and Control of Rhythmic Firing. *J Neurophysiol* 85: 472-475, 2001.

Levi R, Hultling C, and Seiger A. The Stockholm Spinal Cord Injury Study: 2. Associations between clinical patient characteristics and post-acute medical problems. *Paraplegia* 33: 585-594, 1995.

Li X, Murray K, Harvey PJ, Ballou EW, and Bennett DJ. Serotonin Facilitates a Persistent Calcium Current in Motoneurons of Rats With and Without Chronic Spinal Cord Injury. *J Neurophysiol* 97: 1236-1246, 2007.

Li Y and Bennett DJ. Persistent Sodium and Calcium Currents Cause Plateau Potentials in Motoneurons of Chronic Spinal Rats. *J Neurophysiol* 90: 857-869, 2003.

Li Y, Gorassini MA, and Bennett DJ. Role of Persistent Sodium and Calcium Currents in Motoneuron Firing and Spasticity in Chronic Spinal Rats. *J Neurophysiol* 91: 767-783, 2004a.

Li Y, Harvey PJ, Li X, and Bennett DJ. Spastic Long-Lasting Reflexes of the Chronic Spinal Rat Studied In Vitro. *J Neurophysiol* 91: 2236-2246, 2004b.

Li Y, Li X, Harvey PJ, and Bennett DJ. Effects of Baclofen on Spinal Reflexes and Persistent Inward Currents in Motoneurons of Chronic Spinal Rats With Spasticity. *J Neurophysiol* 92: 2694-2703, 2004c.

Lindsay A and Feldman J. Modulation of respiratory activity of neonatal rat phrenic motoneurones by serotonin. *J Physiol* 461, 1993.

Little J, Micklesen P, Umlauf R, and Britell C. Lower extremity manifestations of spasticity in chronic spinal cord injury. *Am J Phys Med Rehabil* 68: 32-36, 1989.

Mailis A and Ashby P. Alterations in group Ia projections to motoneurons following spinal lesions in humans. *J Neurophysiol* 64: 637-647, 1990.

Marque P, Simonetta-Moreau M, Maupas E, and Roques CF. Facilitation of transmission in heteronymous group II pathways in spastic hemiplegic patients. *J Neurol Neurosurg Psychiatry* 70: 36-42, 2001.

Maxwell L, Maxwell DJ, Neilson M, and Kerr R. A confocal microscopic survey of serotoninergic axons in the lumbar spinal cord of the rat: co-localization with glutamate decarboxylase and neuropeptides. *Neuroscience* 75: 471-480, 1996.

McCouch GP, Austin GM, Liu CN, and Liu CY. Sprouting as a cause of spasticity. *J Neurophysiol* 21: 205-216, 1958.

Melzack R and Wall P. Acupuncture and transcutaneous electrical nerve stimulation. *Postgrad Med J* 60: 893-896, 1984.

Mertens P and Sindou M. Surgical management of spasticity. In: *Upper Motor Neurone Syndrome and Spasticity. Clinical Management and Neurophysiology*, edited by Barnes MP and Johnson GR: Cambridge University Press, 2001, p. 239-265.

Midha M and Schmitt J. Epidural spinal cord stimulation for the control of spasticity in spinal cord injury patients lacks long-term efficacy and is not cost-effective. *Spinal Cord* 36: 190-192, 1998.

Miller JF, Paul KD, Rymer WZ, and Heckman CJ. 5-HT1B/1D agonist CGS-12066B attenuates clasp knife reflex in the cat. *J Neurophysiol* 74: 453-456, 1995.

Miller RJ. Presynaptic receptors. *Annual Review of Pharmacology and Toxicology* 38: 201-227, 1998.

Monster A, Tamai Y, and McHenry J. Dantrolene sodium: its effect on extrafusal muscle fibers. *Arch Phys Med Rehabil* 55: 355-362, 1974.

Morita H, Crone C, Christenhuis D, Petersen NT, and Nielsen JB. Modulation of presynaptic inhibition and disynaptic reciprocal Ia inhibition during voluntary movement in spasticity. *Brain* 124: 826-837, 2001.

Nacimiento W and Noth J. What, If Anything, Is Spinal Shock? *Arch Neurol* 56: 1033-1035, 1999.

Nathan P, Sears T, and Smith M. Effects of phenol solutions on the nerve roots of the cat: an electrophysiological and histological study. *J Neurol Sci* 2: 7-29, 1965.

Patel R, Kerr R, and Maxwell DJ. Absence of co-localized glutamic acid decarboxylase and neuropeptides in noradrenergic axons of the rat spinal cord. *Brain Research* 749: 164-169, 1997.

Perrier J-F, Alaburda A, and Hounsgaard J. Spinal plasticity mediated by postsynaptic L-type Ca2+ channels. *Brain Research Reviews* 40: 223-229, 2002.

Perrier J-F and Hounsgaard J. 5-HT2 Receptors Promote Plateau Potentials in Turtle Spinal Motoneurons by Facilitating an L-Type Calcium Current. *J Neurophysiol* 89: 954-959, 2003.

Pierrot-Deseilligny E and Burke D. *The Circuitry of the Human Spinal Cord: Its Role in Motor Control and Movement Disorders*. New York: Cambridge University Press, 2005.

Pinter M, Gerstenbrand F, and Dimitrijevic M. Epidural electrical stimulation of posterior structures of the human lumbosacral cord: 3. Control Of spasticity. *Spinal Cord* 38: 524-531, 2000.

Powers RK and Binder MD. Input-output functions of mammalian motoneurons. *Rev Physiol Biochem Pharmacol* 143: 137-263, 2001.

Price G, Wilkin G, Turnbull M, and Bowery N. Are baclofen-sensitive GABAB receptors present on primary afferent terminals of the spinal cord? *Nature* 307: 71-74, 1984.

Rosales R, Arimura K, Takenaga S, and Osame M. Extrafusal and intrafusal muscle effects in experimental botulinum toxin-A injection. *Muscle Nerve* 19: 488-496, 1996.

Rothwell J. *Control of human voluntary movement.* London: Chapman & Hall, 1994.

Rushton DN. Intrathecal baclofen for control of spinal and supraspinal spasticity. In: *Upper Motor Neurone Syndrome and Spasticity. Clinical Management and Neurophysiology*, edited by Barnes MP and Johnson GR: Cambridge University Press, 2001, p. 223-238.

Rushworth G. Spasticity and rigidity: an experimental study and review. *J Neurol Neurosurg Psychiatry* 23: 99-118, 1960.

Russo RE, Nagy F, and Hounsgaard J. Inhibitory control of plateau properties in dorsal horn neurones in the turtle spinal cord in vitro. *J Physiol (Lond)* 506: 795-808, 1998.

Saade NE, Tabet MS, Atweh SF, and Jabbur SJ. Modulation of segmental mechanisms by activation of a dorsal column brainstem spinal loop. *Brain Research* 310: 180-184, 1984.

Schlosser W. Action of diazepam on the spinal cord. *Arch Int Pharmacodyn Ther* 194: 93-102, 1971.

Schomburg E and Steffens H. The effect of DOPA and clonidine on reflex pathways from group II muscle afferents to alpha-motoneurones in the cat. *Exp Brain Res* 71: 442-446, 1988.

Schwindt PC and Crill WE. A persistent negative resistance in cat lumbar motoneurons. *Brain Res* 120: 173-178, 1977.

Schwindt PC and Crill WE. Role of a persistent inward current in motoneuron bursting during spinal seizures. *J Neurophysiol* 43: 1296-1318, 1980.

Skerritt J and Johnston G. Enhancement of GABA binding by benzodiazepines and related anxiolytics. *Eur J Pharmacol* 89: 193-198, 1983.

Stein R and Thompson A. Muscle reflexes in motion: how, what, and why? *Exerc Sport Sci Rev* 34: 145-153, 2006.

Svirskis G and Hounsgaard J. Transmitter Regulation of Plateau Properties in Turtle Motoneurons. *J Neurophysiol* 79: 45-50, 1998.

Thompson F, Parmer R, and Reier P. Alteration in rate modulation of reflexes to lumbar motoneurons after midthoracic spinal cord injury in the rat. I. Contusion injury. *J Neurotrauma* 15: 495-508, 1998.

Tremblay L and Bedard P. Effect of clonidine on motoneuron excitability in spinalized rats. *Neuropharmacology* 25: 41-46, 1986.

Vanek Z. 'Spasticity'. *wwwemedicinecom/neuro/topic706htm*, 2005.

Vodovnik L, Bowman B, and Hufford P. Effects of electrical stimulation on spinal spasticity. *Scand J Rehabil Med* 16: 29-34, 1984.

Wall P. Presynaptic control of impulses at the first central synapse in the cutaneous pathway. *Prog Brain Res* 12: 92-118, 1964.

Waltz J, Andreesen W, and Hunt D. Spinal cord stimulation and motor disorders. *Pacing Clin Electrophysiol* 10: 180-204, 1987.

Ward AB and Ko Ko C. Pharmacological management of spasticity. In: *Upper Motor Neurone Syndrome and Spasticity. Clinical Management and Neurophysiology*, edited by Barnes MP and Johnson GR: Cambridge University Press, 2001, p. 165-187.

Watkins C, Leathley M, Gregson J, Moore A, Smith T, and Sharma A. Prevalence of spasticity post stroke. *Clinical Rehabilitation* 16: 515 – 522, 2002.

Williamson R and Andrews B. Localized electrical nerve blocking. *IEEE Trans Biomed Eng* 52: 362-370, 2005.

Yang K, Wang D, and Li Y-Q. Distribution and depression of the GABAB receptor in the spinal dorsal horn of adult rat. *Brain Research Bulletin* 55: 479-485, 2001.

Young RR. Spasticity: a review. *Neurology* 44: S12-20, 1994.

Zuber M, Sebald M, Bathien N, De Recondo J, and Rondot P. Botulinum antibodies in dystonic patients treated with type A botulinum toxin: frequency and significance. *Neurology* 43: 1715-1718, 1993.

Chapter 2: Simulation of Dendritic $Ca_V1.3$ Channels in Cat Lumbar Motoneurons: Spatial Distribution †

2.1 INTRODUCTION

Since their discovery by Schwindt and Crill in cat motoneurons, persistent inward currents (PICs) were suggested to be mediated by calcium ions (Schwindt and Crill 1980b). Recent evidence showed that PICs in spinal motoneurons of various species are mediated by two main classes of channels: low voltage-activated (LVA) L-type Ca^{+2} (specifically $Ca_V1.3$, Schwindt and Crill 1980b; Hounsgaard and Kiehn 1989) and persistent sodium (Nap) (Li and Bennett 2003) channels.

In their early work Schwindt and Crill (1980a) suggested that PICs were generated near or at the soma. However, different experimental protocols (Hounsgaard and Kiehn 1993; Lee and Heckman 1996; Bennett et al. 1998), anatomical localization of channels (Carlin et al. 2000a; Simon et al. 2003), and computer simulations (Gutman 1991; Booth et al. 1997; Carlin et al. 2000b) emphasized the dendritic origin of PICs. Furthermore, measurements of Ca^{+2} PIC under voltage clamp conditions in spinal motoneurons showed that they exhibit hysteresis in the current-voltage (I-V) relationship. The hysteresis is due to the distal location of the channels mediating this current relative to the soma, suggesting again a dendritic origin of the L-type Ca^{+2} channels where they cannot be fully voltage-clamped (Lee and Heckman 1998b; Li and Bennett 2003; Carlin et al. 2000b). The factors influencing this hysteresis are mainly the dendritic location of the $Ca_V1.3$ channels relative to the soma, and the intrinsic activation/inactivation properties of these channels.

Upon activation of $Ca_V1.3$ channels, a strong PIC is triggered that overcomes potassium-mediated outward currents resulting in the formation of a negative slope region in the

† A revised version of this chapter has been published (ElBasiouny SM, Bennett DJ, and Mushahwar VK, *J. Neurophysiol.* 94: 3961-74, 2005 'used with permission').

steady state I-V relationship. Sustained depolarization (plateau potentials) and long-lasting self-sustained firing (bistability) can therefore be seen if the cell is sufficiently depolarized by intracellular current injection or excitatory synaptic input (Conway et al. 1988; Crone et al. 1988; Hounsgaard et al. 1988; Lee and Heckman 1998a).

Schwindt and Crill (1980b) suggested that synaptic currents do not sustain spontaneous bursts of motoneuronal activity and postulated an interaction of synaptic and membrane mechanisms that allows PICs to dominate the neural behavior. This interaction was confirmed experimentally where it was observed that the somatic voltage threshold for generating plateau potentials can be altered by background synaptic activity (Bennett et al. 1998). Dendritic channels mediating PICs amplify the synaptic input and enhance the delivery of synaptic current to the soma (Binder et al. 1996; Johnston et al. 1996; Yuste and Tank 1996). These channels receive neuromodulatory monoaminergic inputs originating from the brain stem (Hounsgaard et al. 1988; Takahashi and Berger 1990; Wang and Dun 1990; White et al. 1991; Binder et al. 1996). Therefore, information on the dendritic spatial distribution of these channels, which is currently sparse, is important to predict the effects of neuromodulators on dendritic processing. The goal of this study was to investigate the dendritic spatial distribution of $Ca_V1.3$ channels in spinal motoneurons. Our hypothesis was that the dendritic spatial distribution of these channels overlaps with that of synaptic inputs from multiple origins, and this overlap results in the functional interactions seen experimentally between these two systems.

To test this hypothesis we developed a compartmental cable model of a spinal motoneuron based on the detailed morphology of fatigue-resistant (FR) cat α-motoneuron, and included realistic distribution of Ia-afferent synapses (Cullheim et al. 1987; Segev et al. 1990; Brannstrom 1993; Burke and Glenn 1996). The model was tuned to match the intrinsic properties of cat motoneurons with passive dendrites, and it was then used to predict the most likely dendritic spatial distribution of $Ca_V1.3$ channels that would match the firing behavior of motoneurons with active dendrites. Different spatial distributions of the $Ca_V1.3$ channels over the dendritic tree were tested, and the resulting model behavior was compared to experimental data. Our results suggest that the dendritic

spatial distribution of $Ca_V1.3$ channels is similar to that of Ia-synaptic contacts, and that these channels are primarily localized within the synaptic territory region (dendritic region with highest Ia-synaptic population). Part of this work was previously presented in abstract form (ElBasiouny and Mushahwar 2004).

2.2 MATERIALS AND METHODS

2.2.1 Model morphology, biophysical properties and verification

We developed a computer-based cable model of an adult cat α-motoneuron using NEURON simulation environment (Hines and Carnevale 1997). The model had full representation of the α-motoneuron structure, and consisted of soma, axon hillock (AH), initial segment (IS), and dendritic tree. The dendritic tree was based on the three-dimensional (3D) detailed morphology for type-identified triceps surae α-motoneuron (FR type, medial gastrocnemius (MG) motoneuron, identified as cell 43/5), labeled intracellularly with horseradish peroxidase (HRP). The total dendritic arbor was incorporated into the program, and was modeled with 731 compartments representing 11 root dendrites and 165 terminations (Fig. 2-1A; Cullheim et al. 1987).

The soma was modeled as a single spherical compartment of diameter 48.8 μm (Cullheim et al. 1987). The AH was represented as a series of 11 tapered cylindrical compartments of total length 20 μm (Kellerth et al. 1979), with a base diameter at the soma side of 13 μm, and diameter at the IS side of 3 μm (Conradi 1969; Kellerth et al. 1979). The IS was represented as a series of 3 cylindrical compartments of total length 30 μm and a constant diameter of 3.3 μm (Kellerth et al. 1979).

The passive parameters determining the cable properties of the motoneuron were set according to the values reported by Fleshman et al. (1988) for the same 43/5 FR motoneuron. The specific membrane resistance, R_m, was set to 225 $\Omega.cm^2$ for the soma, AH, and IS, and 11000 $\Omega.cm^2$ for the dendrites. The values of R_m for the soma, AH, and IS took into consideration the leak current induced by electrode penetration into the soma. The specific membrane capacitance, C_m, was set to 1 $\mu F/cm^2$ and the specific axial resistance, R_a, to 70 $\Omega.cm$ for all the compartments in the model (Fleshman et al. 1988; Clements and Redman 1989; Segev et al. 1990).

The model included voltage-dependent ion channels previously identified and described experimentally in cat α-motoneurons (Schwindt and Crill 1977; Barrett et al. 1980;

Barrett and Crill 1980), as well as N-type calcium channels described in turtle spinal motoneurons (Hounsgaard and Mintz 1988). The soma included conductances representing nonlinear fast sodium (Naf), delayed rectifier potassium (Kdr), calcium-activated potassium (K(Ca)), and N-type calcium (CaN, CaV2.2) channels. The AH and IS included conductances representing Nap, Naf and Kdr channels (Table 2-1). The parameters describing the kinetics of these channels were adapted from McIntyre and Grill (2002), and are shown in the Appendix 1.

The Naf and Kdr channels are responsible for the generation of the action potential (AP) spike. The voltage-dependent activation curves of the Naf channels in the AH and IS are more hyperpolarized than those in the soma. This makes the IS the site of initiation of the AP in the cell. Nap channels in the AH and IS are responsible for regulation of the cell rhythmic firing (Lee and Heckman 2001). Their density is < 1% of the Naf channels, and their activation curves are more hyperpolarized than those of the Naf channels (Crill 1996). The CaN channels allow for calcium influx during AP, and also regulate the K(Ca) conductances, which are responsible for shaping the membrane trajectory during the afterhyperpolarization (AHP) following the AP spike (Booth et al. 1997).

The model was verified by comparing its properties to experimental data from *in vivo* and *in vitro* measurements. Since experimental measurements were obtained from anaesthetized cats (Fleshman et al. 1988; Hochman and McCrea 1994a,b), the model properties were measured with a passive dendritic tree. The model variables were tuned to have properties within the 95% confidence range of experimental data. The cell input resistance (R_{in}) and membrane time constant (τ) were adjusted to experimental values for the 43/5 FR motoneuron (Cullheim et al. 1987). The model excitability was assessed by measuring the rheobase current (I_{rheo}), short-pulse current threshold (SPCT), and the firing voltage threshold (V_{th}). The model generated AP and AHP with properties very close to experimental recordings. Table 2-2 shows values of the different model properties as compared to experimental data. All experimental data are presented as mean ± SD. Moreover, the model exhibited adaptation of firing rate that was similar to

experimental recordings (Sawczuk et al., 1995) in response to somatic injection of long current pulses (Fig. 2-2).

2.2.2 $Ca_V1.3$ channels

Experimental data demonstrated that PICs in spinal motoneurons are evenly mediated by Nap and nimodipine-sensitive LVA L-type Ca^{+2} ($Ca_V1.3$ type) channels (Li and Bennett 2003). Nap PIC was found to activate and deactivate rapidly with apparent somatic activation potential of 7 mV below the spike threshold, and show significant inactivation (Li and Bennett 2003). On the other hand, Ca^{+2} PIC was found to activate and deactivate slowly with apparent somatic activation potential of ±5 mV of the spike threshold, and show no inactivation (Li and Bennett 2003). In the present study, we focused on the $Ca_V1.3$ channels given that our interest was on determining their most likely spatial distribution over the dendritic tree.

After matching the intrinsic properties of cat motoneurons under anesthesia (with passive dendrites), $Ca_V1.3$ channels were added to the dendritic tree to simulate the PICs and firing behavior of a motoneuron with active dendrites. The parameters describing the kinetics of the $Ca_V1.3$ channels were adapted from Carlin et al. (2000b), and based on experimental recordings in mice and rat (Carlin et al. 2000a; Xu and Lipscombe 2001). The activation time constant of the channels was adapted to fit tail currents which are seen experimentally at the termination of somatic long voltage pulses (Li and Bennett 2003). Since the apparent somatic activation potential of PICs in cat spinal motoneurons is about 10-30 mV positive to the resting membrane potential (Schwindt and Crill 1980b), the half-activation potential was adjusted to activate the $Ca_V1.3$ channels within this range as seen from the soma (half-activation potential = -43 mV) and allow plateau activation within the observed experimental values.

The experimental measurements of Ca^{+2} PIC were based on recordings done by Lee and Heckman (1999) in cat motoneurons after injection of the lidocaine derivative, QX-314, and Li and Bennett (2003) in rat motoneurons after injection of tetrodotoxin (TTX), to

block Na^+ channels. Measurements of Ca^{+2} PIC in the model were done under voltage clamp conditions after leak current subtraction. Leak current was estimated from the subthreshold region by fitting a regression line (Fig. 2-3B). A slow triangular voltage command of slope 4 mV/s was used. The soma was perfectly clamped over the voltage range for activation of the Ca^{+2} PIC (from -70 mV to -30 mV).

In the model, we only included $Ca_V1.3$ channels over the dendritic tree. However, there are undoubtedly other dendritic active conductances some of which might mediate outward currents that counteract the Ca^{+2} PIC (Powers and Binder 2000). Given that Ca^{+2} PIC measurements from the model were compared to experimental data in which no channel blockers, except for Na^+, were used, the inward current in this study represents the 'effective' Ca^{+2} PIC which includes the contribution of outward conductances.

2.2.3 Dendritic synaptic inputs

The monosynaptic Ia-afferent system was represented in the model (Fig. 2-1B). The dendritic spatial distribution of Ia-afferent synapses was based on the realistic distribution of group Ia afferent-to-motoneuron contacts labeled intracellularly with HRP from cat FR motoneurons (Burke et al. 1979; Glenn et al. 1982; Burke and Glenn 1996). The total number of Ia-afferent boutons was 300 based on the data from Segev et al. (1990). Two patterns of Ia-afferent activation were simulated in this study: sustained muscle stretch resulting in tonic input, and tendon vibration. For tonic input, the synapses were activated at a high frequency that resulted in a smooth somatic membrane potential. The synapse conductances were set such that the somatic membrane potential was subthreshold for firing (Bennett et al. 1998). To simulate the effects of tendon vibration, the Ia-afferents were activated at 180 Hz and the synapse conductances were set such that the Ia effective synaptic current (Ia I_N), which is the amount of Ia current reaching the soma, was approximately 4.8 nA with the soma clamped at the resting potential. This is the value of Ia I_N seen experimentally in MG motoneurons in the decerebrate cat that had received the noradrenergic $\alpha 1$ agonist, methoxamine (Lee and Heckman 2000). Given the variation in conduction velocity in Ia-afferent fibers (80-110 m/s in cat), synchronous activation of their axons through vibration in the periphery leads to asynchronous activation of their

synaptic terminations (Segev et al. 1990). We simulated this temporal dispersion among the Ia-synapses by dividing them in 4 groups that were activated asynchronously. Synapses were randomly assigned to a group and the synaptic distribution in each group was similar to that of Fig. 2-1B. All groups were activated at the vibration frequency but with a 25% phase shift. The parameters of the Ia-afferent synapses (reversal potential and time-to-peak) were chosen based on previous experimental and modeling studies (Segev et al. 1990; Jones and Bawa 1997).

2.2.4 Distributions of the $Ca_V1.3$ channels

Four different spatial distributions of the $Ca_V1.3$ channels over the dendritic tree were tested in the model. For each distribution, the density of channels was uniform with respect to the membrane area and was adjusted such that the magnitudes of Ca^{+2} PIC (depth of initial peak, I_{in}, and sustained peak, I_{sus}; Fig. 2-3B) were within the experimental range (Table 2-3). To verify our results, simulations were run under different model conditions, and the model behavior was compared to different experimental measurements from cat motoneurons. The frequency-current (F-I) relationship was obtained with the use of all channels in the model, while Ia I_N enhancement and V-I relationships were obtained with only the $Ca_V1.3$ channels active. Moreover, an independent method based on a technique used by Rose et al. (2002, 2003) was used (see customized distribution) to validate the $Ca_V1.3$ channel distribution that resulted in the best matching of motoneuron behavior to experimental data.

a) *Whole uniform density distribution:* $Ca_V1.3$ channels covered the whole motoneuronal dendritic tree ($0.78 \pm 0.49\lambda$; median: 0.72λ; λ is the space constant; Fig. 2-3A).
b) *Middle uniform density distribution:* $Ca_V1.3$ channels covered dendritic segments with dendritic path distance of 500 μm from the soma and higher ($1.0 \pm 0.41\lambda$; median: 0.93λ; Fig. 2-4A).
c) *Distal uniform density distribution:* $Ca_V1.3$ channels covered dendritic segments with dendritic path distance of 1000 μm from the soma and higher ($1.47 \pm 0.33\lambda$; median: 1.4λ; Fig. 2-5A).

d) *Wide band distribution:* $Ca_V1.3$ channels covered dendritic segments with dendritic path distance between 300 μm and 850 μm (0.62 ± 0.21λ; median: 0.61λ) from the soma, which is the dendritic region mostly covered by the Ia-afferent synapses (Fig. 2-6A). Note that synaptic inputs from other systems appear to have similar distribution to that of Ia-afferents (see section 2.4).

e) *Customized distribution:* In this distribution, the location of $Ca_V1.3$ channels was determined from the position that matched two experimental conditions: somatic plateau thresholds during rest (-50.6 mV) and during synaptic excitation (-56 mV; Bennett et al., 1998). Using the technique of Rose et al. (2002, 2003) with only $Ca_V1.3$ channels active, the soma was clamped at -50.6 mV (synapses silent) and the membrane potential was directly measured and plotted versus the dendritic path distance from the soma along each root dendrite (Fig. 2-8A – *Rest* condition). The process was repeated with the soma clamped at -56 mV with the Ia-afferent synapses tonically active (Fig. 2-8A – *Excitation* condition). Assuming that the threshold for activation of the $Ca_V1.3$ channels is the same throughout the neuronal architecture, the intersection of the two relationships for each root dendrite indicates the location of the $Ca_V1.3$ channels as it satisfies both rest and active conditions of the cell. Channels were then placed in regions centered around the average intersection site on each root dendrite (Fig. 2-8A). This was repeated in 98 paths to the terminal dendrites (of a total of 165 terminal dendrites). The intersection sites of these 98 paths were assumed to represent an average location of the $Ca_V1.3$ channels on the dendritic tree.

2.2.5 Evaluation of $Ca_V1.3$ channel distributions

The criterion used for evaluating the various distributions was to match three different and independent sets of experimental measurements from cat motoneurons innervating the MG muscle. These measurements were: a) properties of Ca^{+2} PIC and F-I relationship; b) changes in the somatic plateau threshold and F-I relationship due to background synaptic activity, and c) enhancement of Ia synaptic current.

a) Properties of Ca^{+2} PIC and F-I relationship

Properties of the Ca^{+2} PIC obtained from the model were compared to those obtained experimentally from decerebrate cats that had received QX-314 and methoxamine (Lee and Heckman 1999). Since QX-314 reduces Ca^{+2} currents in addition to blocking Na^{+} currents (Talbot and Sayer 1996; Lee and Heckman 1999) the amplitude of experimentally measured Ca^{+2} PIC from motoneurons may be underestimated. However, the magnitude of the Ca^{+2} PIC measured by Lee and Heckman (1999) was found to form nearly 50% of I_{in} and about 61% of I_{sus} of the total PICs. This contribution of Ca^{+2} PIC is similar to that observed experimentally in rat spinal motoneurons in the presence of TTX, a selective blocker of Na^{+} channels, in which Ca^{+2} PIC contributed approximately 50% of the initial peak (I_{in}) and 67% of the sustained peak (I_{sus}) of the total PICs (Li and Bennett 2003).

The F-I relationship was obtained when no channels were blocked and measuring the instantaneous firing rate at the soma during intracellular injection of slow triangular current ramps of slope 4 nA/s (Fig. 2-3C). This was compared to the results of Bennett et al. (1998) on medial and lateral gastrocnemius-soleus motoneurons in the decerebrate cat preparation.

b) Changes in the somatic plateau threshold and F-I relationship due to background synaptic activity

To study the effect of tonic synaptic activation on the somatic threshold of plateau activation and on the properties of the F-I relationship, simulations were done with and without synaptic activation and responses were compared to each other (Fig. 2-7, A and B). Synaptic excitation was produced by tonic activation of the Ia-afferent synapses (Bennett et al. 1998). The V-I relationship was obtained with only $Ca_V1.3$ channels present, by measuring the somatic membrane potential while injecting a slow increasing current ramp of 4 nA/s at the soma. The injected current ranged from 0 to 20 nA. Table 2-3 shows the experimental values for both F-I and V-I relationship properties.

c) Enhancement of Ia synaptic current

The magnitude of Ca^{+2} PIC was adjusted to be within the experimental range for the decerebrate cat that had received methoxamine (Lee and Heckman 2000), and properties of Ia synaptic current enhancement (peak Ia I_N and hyperpolarized Ia I_N: which is the effective synaptic current measured at the resting potential) were compared to those from the same preparation (Table 2-3). The Ia I_N was computed as the difference between the I-V relationships obtained during no synaptic activity (at rest) and during tendon vibration at 180 Hz (Lee and Heckman 2000).

2.3 RESULTS

The primary goal of this study was to determine the most likely dendritic distribution of the $Ca_V1.3$ channels mediating Ca^{+2} PIC in cat spinal motoneurons. We used the amount of hysteresis, which is represented by the difference between the Ca^{+2} PIC activation and deactivation potentials seen at the soma, seen experimentally in Ca^{+2} PIC to predict the dendritic distribution of these channels. Channel properties were maintained constant in all the tested distributions.

One of the advantages for using computer simulations is that they can overcome some limitations that face experimental techniques. One of these limitations when using the voltage clamp technique is the knowledge of which parts of the cell are well clamped and which parts are not. Moreover, it is difficult to know experimentally which portions of the dendritic tree are active and contributing to the obtained measurements. The present model provided a unique opportunity to predict the spatial distribution of the $Ca_V1.3$ channels over the motoneuron dendritic tree by combining realistic 3D morphology of the motoneuron dendritic tree, realistic dendritic distribution of the Ia-afferents, and experimental electrophysiological recordings from the same motoneurons after blocking Na^+ PIC. Simulation results were compared to different and independent sets of experimental electrophysiological measurements (properties of Ca^{+2} PIC and F-I relationship, changes in the somatic plateau threshold and F-I relationship due to background synaptic activity, and voltage-dependent enhancement of the synaptic current). Four different distributions were tested, and their results were compared to experimental data and validated by the use of an independent technique described by Rose et al. (2002, 2003).

2.3.1 Whole uniform density distribution

In this distribution, the density of the $Ca_V1.3$ channels was uniform throughout the dendritic tree ($0.78 \pm 0.49\lambda$; median: 0.72λ; Fig. 2-3A). The density of channels (0.06 mS/cm^2) was adjusted such that the amplitude of Ca^{+2} PIC was within the experimental

range. Figure 2-3A shows the number of the $Ca_V1.3$ channels at various distances from the soma normalized to the maximum number of channels over the dendritic tree, and was calculated from the number of channels and membrane surface area at various distances from the soma. The relative number of $Ca_V1.3$ channels was compared to the number of synaptic contacts over the dendritic tree. The measured Ca^{+2} PIC showed very little hysteresis ($V_{on} - V_{off}$ = 2.3 mV; Fig. 2-3B). This was also reflected in the F-I relationship by a complete overlap of the F-I segments during the ascending and descending phases of the injected ramp current (i.e., no bistability behavior is observed; no difference in firing rates is seen at the same injected current level; Fig. 2-3C).

These results could be explained by the strong influence of the proximal dendrites on the soma. In this distribution, the $Ca_V1.3$ channels cover the whole dendritic tree (both proximal and distal dendritic branches). Ca^{+2} PIC from proximal dendrites is not hysteretic as these dendrites are too close to the soma and are well voltage-clamped. Ca^{+2} PIC from the distal dendrites is hysteretic due to the distal location of these dendrites relative to the soma and hence are voltage-clamped imperfectly. Therefore, the proximal dendrites, which are electrotonically close to the soma, dominate the cell behavior causing the non-hysteretic Ca^{+2} PIC to dominate the total PIC seen at the soma. This proposed dominance of proximal dendrites was tested in the model by placing the $Ca_V1.3$ channels only on the proximal dendrites (from the soma till a dendritic path distance of 500 μm). We found that there was no bistability in the F-I relationship and there was a complete overlap of the upward and downward segments of the F-I relationship (data not shown) confirming that proximal dendrites were dominating the behavior seen from the *whole uniform density distribution*. Therefore, these results suggest that the $Ca_V1.3$ channels should be located more distally in order to produce the proper amount of hysteresis in the measured Ca^{+2} PIC.

2.3.2 Middle uniform density distribution

In this distribution, the density of the $Ca_V1.3$ channels was uniform in the region of the dendritic tree starting from 500 μm dendritic path distance from the soma ($1.0 \pm 0.41\lambda$;

median: 0.93λ; Fig. 2-4A). The channel density (0.125 mS/cm^2) was adjusted such that the amplitude of Ca^{+2} PIC was within the experimental range. The measured Ca^{+2} PIC showed an appropriate amount of hysteresis ($V_{on} - V_{off}$ = 14.7 mV; Fig. 2-4B). However, the effect of Ca^{+2} PIC was too strong on the soma firing behavior causing the cell to fire at very high non-physiological rates (Fig. 2-4C). Bistability was also seen in the F-I relationship, but the difference between firing rates at the same injected current was larger (about 50 imp/s) than that seen experimentally (usually from 5 to 15 imp/s). Despite our best efforts to match the physiological firing rates by reducing channel density to reduce Ca^{+2} PIC, we could not achieve physiological firing rates while maintaining the magnitude of Ca^{+2} PIC within the experimental range.

In order to further assess the effect of Ca^{+2} PIC on the cell behavior, we measured the Ia I_N reaching the soma at different membrane potentials (Fig. 2-4D). The Ia I_N enhancement profile was similar to that seen experimentally, but the Ia I_N peak value (about 18.5 nA) was high, indicating a strong effect of Ca^{+2} PIC (compare Fig. 2-4D to Fig. 3A in Lee and Heckman 2000). This peak Ia I_N is considered high, even though its absolute value is within the acceptable confidence range of experimental data. This is because the measured Ia I_N enhancement in the model is only due to the contribution of Ca^{+2} PIC, while the experimental Ia I_N enhancement is due to the contribution of both Na^+ and Ca^{+2} PICs.

The proper amount of hysteresis in Ca^{+2} PIC in this distribution of the $Ca_V1.3$ channels indicates that the channels are placed approximately around the correct location. However, the strong effect of Ca^{+2} PIC on the cell firing behavior indicates that the PIC reaching the soma should be lowered by either localizing the channels over a limited middle region or placing the channels more distally on the dendritic tree.

2.3.3 Distal uniform density distribution

In this distribution, the density of the $Ca_V1.3$ channels was uniform (0.4 mS/cm^2) in the region of the dendritic tree starting from 1 mm dendritic path distance (1.47 ± 0.33λ;

median: 1.4λ; Fig. 2-5A) from the soma. The measured Ca^{+2} PIC (I_{in} and I_{sus}) was small in magnitude and very hysteretic (Fig. 2-5B). $Ca_V1.3$ channels were activated at low hyperpolarized somatic potentials (at -68.5 mV, indicated by the dotted line in Fig. 2-5B), and deactivated at much lower hyperpolarized somatic potentials (-127 mV, indicated by the arrow in Fig. 2-5B) relative to experimental values (Table 2-3). With this distribution, we could not achieve Ca^{+2} PIC with features similar to those of experimental measurements regardless of our best attempts at modifying the $Ca_V1.3$ channel density. Activation of Ca^{+2} PIC at a potential lower than the recruitment threshold (-55.5 mV) caused the cell to start firing at relatively high rates which normally correspond to the secondary segment of the F-I relationship, and the cell could not produce bistability (Fig. 2-5C). The peak Ia I_N was also found to be shifted closer to the resting potential and occurred at a potential corresponding to that at which Ca^{+2} PIC was fully activated (Fig. 2-5D, compare to Fig. 3A in Lee and Heckman 2000). These results suggested that the majority of the $Ca_V1.3$ channels cannot be located at such distal locations from the soma, and should be located more proximally.

2.3.4 Wide band distribution

Results from the *middle uniform density distribution* suggested that the $Ca_V1.3$ channels may be localized over a limited middle region or be placed more distally. However, results from the *distal uniform density distribution* showed that the $Ca_V1.3$ channels cannot be located too distally from the soma. Our hypothesis was that there is an overlap between the dendritic spatial distribution of the $Ca_V1.3$ channels and that of the Ia-afferent synapses, based on the functional interaction seen experimentally between the dendritic active conductances and synaptic inputs from the Ia-afferents (Bennett et al. 1998; Lee and Heckman 2000). The $Ca_V1.3$ channels were therefore placed over the dendritic region covered most by the Ia-afferent synapses at dendritic path distance between 300 μm and 850 μm (0.62 ± 0.21λ; median: 0.61λ; Fig. 2-6A) from the soma. The density of the channels was uniform (0.14 mS/cm^2) and was adjusted to give Ca^{+2} PIC of magnitude within the experimental range (Table 2-3). The measured Ca^{+2} PIC matched all the features seen experimentally and showed a proper amount of hysteresis

(Fig. 2-6B; Table 2-3). The F-I relationship also had properties that agreed with experimental recordings (Fig. 2-6C; Table 2-3). Furthermore, the effect of Ca^{+2} PIC on the cell firing behavior was appropriate as the maximum firing rate and the difference in firing rates at the same injected current levels (bistability range) were within physiological ranges. Figure 2-6D shows the Ia I_N enhancement profile. The hyperpolarized Ia I_N was within the experimental range, while the peak Ia I_N was within the expected range of synaptic current that is only enhanced by Ca^{+2} PIC (Table 2-3). Figures 2-7, A and B, respectively, illustrate the changes in the properties of F-I and V-I relationships due to tonic synaptic activation of Ia-afferent synapses. Tonic excitation of the Ia-afferent synapses lowered the transition frequency by 8 Hz, and the activation threshold of the plateau potential at the soma by 3.4 mV relative to the rest condition, in accordance to experimental findings (Bennett et al. 1998).

Moreover, Ca^{+2} PIC measured under voltage clamp conditions using long voltage pulses showed activation profile very similar to experimental data (Fig. 2-7C). Ca^{+2} PIC was activated slowly during the pulse onset with half-activation time of 271 ms (experimental data ranges from 300 ± 120 ms at 50 mV; Fig. 7D in Li and Bennett 2003) and full-activation time of 1 sec (Li and Bennett 2003). It was deactivated slowly as well at the termination of the pulse producing tail current that lasted for 1 sec (Fig. 2-7C, compare to Fig. 7C in Li and Bennett 2003). The tail current, as seen from the soma, results from the distal location of the $Ca_V1.3$ channels over the dendritic tree relative to the soma, and is considered to be a significant indicator of the location of these channels relative to the soma. We also investigated the changes in the shape of AHP seen after the activation of plateau potentials (Bennett et al. 1998). Figure 2-7D shows the shape of AHP before (1) and after (2) activation of plateau potentials by intracellular current injection obtained from the model. Comparison of interspike intervals of equal duration showed that there was a reduction in the size of AHP and the appearance of afterdepolarization (indicated by the arrow) in the same manner reported from *in vivo* measurements (Bennett et al. 1998). The results from this distribution were consistent with the three different and independent sets of experimental measurements, suggesting that the $Ca_V1.3$ channels are

distributed over that middle range of the motoneuron dendritic tree where the Ia-afferents form the majority of their contacts.

2.3.5 Customized distribution

In order to verify that the $Ca_V1.3$ channels are located at the wide band distribution, we reversed the question by obtaining the channel locations while clamping the soma at the observed experimental values for both the 'rest' and 'synaptic excitation' conditions as described by Rose et al. (2002, 2003). The membrane potential was directly measured from each compartment in the model, and the relationship between the membrane potential and the distance along each root dendrite was plotted for both the 'rest' and 'synaptic excitation' conditions, and the intersection of the two plots represented the location of channels that satisfied both experimental conditions. The channels were then placed with uniform density in a region centered around the average intersection site on each root dendrite.

Investigation of 98 terminal dendrites with maximum dendritic lengths varying from 400 μm to 1800 μm was completed, and the intersection of their plots was obtained (only 73 showed intersections). The location of the channels was found to be at dendritic path distance of 551.9 ± 159.7 μm from the soma. This location was common on most of the root dendrites as the median was 510.6 μm showing little scatter in the data from all terminal dendrites. This is the center of the region covered by the majority of Ia-afferent synapses, and is the same region that was previously described in the wide band distribution.

Terminal dendrites that did not show intersection of plots were characterized by having the Ia-synapses located primarily proximal to the soma (up to 500 μm from the soma). This localization of the Ia-synapses caused the membrane potential trace along the dendritic length during the *Excitation* condition to decay before crossing the trace during the *Rest* condition. Conversely, figure 2-8A shows the intersection sites of the membrane potential profiles along the dendritic length for two different dendritic segments that showed intersection of their plots. The distribution of synapses along the dendritic

segment is indicated by the black dots at the top of each graph. The intersection site for each dendrite was dependent on the synaptic distribution on that dendrite. Figure 2-8B compares the distribution of Ia-afferent synapses (same data in Fig. 2-1B) and the distribution of the $Ca_V1.3$ channel locations obtained from the intersection method. The distribution of the $Ca_V1.3$ channels corresponds to the synaptic distribution on the dendritic tree, and is primarily localized to an intermediate wide band at dendritic path distances from 300 μm to 900 μm from the soma. The normal distribution of the channel locations (indicated by the thin line in Fig. 2-8B) is similar to that of the Ia-synapse locations (indicated by the thick black line in Fig. 2-8B). Both distributions peak at a dendritic distance of 500 μm from the soma.

The spatial width of the $Ca_V1.3$ channel regions was varied around the intersection site on each root dendrite in order to obtain proper amplitude of Ca^{+2} PIC. It was only possible to obtain acceptable magnitudes of Ca^{+2} PIC when the width of the region containing the $Ca_V1.3$ channels was at least 300 μm centered around the average intersection site for each root dendrite (0.235 mS/cm^2) in the model of our MG motoneuron. With this distribution, the measured Ca^{+2} PIC showed a proper amount of hysteresis (Fig. 2-8C) and was very similar to that measured from the wide band distribution (Fig. 2-6B).

2.3.6 Spatiotemporal measurements of Ca^{+2} current

The wide band distribution was then used to study the spatiotemporal characteristics of the membrane potential (Fig. 2-9B - upper graph) and Ca^{+2} current (Fig. 2-9B - lower graph) along the length of a dendritic branch and at different points in time during repetitive cell firing in response to excitation of the Ia-afferent synapses (Fig. 2-9A). Ca^{+2} current had its maximum amplitude during the repolarization phase of the AP (Fig. 2-9B - lower graph - trace *c*), and not the peak of AP at which maximum depolarization of the soma membrane takes place. This could explain the appearance of afterdepolarization and reduction of the AHP seen after the activation of plateau potentials (Fig. 6D-2; Bennett et al. 1998).

2.4 DISCUSSION

2.4.1 Distribution of $Ca_V1.3$ channels over the dendritic tree

Our results suggest that the $Ca_V1.3$ channels located on the dendrites of spinal motoneurons do not uniformly cover the whole dendritic tree. Rather, they are preferentially localized within the Ia-synaptic territory, a region that lies approximately 300 μm to 850 μm (about 0.6λ) from the somata of MG motoneurons. This finding provides a very likely explanation for the functional interaction seen experimentally between the dendritic active conductances and synaptic inputs. Bennett and colleagues (1998) showed that motoneuron excitation through synaptic activation, as opposed to intracellular current injection, alters the somatic threshold of plateau potentials. Measurements of Ia I_N in the decerebrate preparation, which has tonic activity in the monoaminergic axons originating from the brain stem (Baldissera et al. 1981; Lee and Heckman 1998a), revealed strong enhancement of the synaptic current by PICs (Lee and Heckman 2000; Powers and Binder 2000; Kuo et al. 2003). The strong influence of synaptic inputs on the activation threshold of PICs as seen from the soma supports the spatial overlap between the dendritic distributions of the PIC-mediating channels and the synaptic inputs suggested by the present study.

Different dendritic distributions of $Ca_V1.3$ channels were tested in the model. For each distribution, the model behavior was compared to experimental data. However, the tested distributions were of uniform channel densities; the realistic distribution of these channels might be non-uniform. Uniform distribution of channels was used as a first approximation to predict their region of highest density over the motoneuron dendritic tree. Therefore, the suggested distribution represents a regional distribution of these channels rather than a detailed one. The distribution of the $Ca_V1.3$ channels within the Ia-synaptic territory might be non-uniform (Gaussian, ramp, punctuate, etc.), and can only be confirmed by immunohistochemical labeling of these channels. A non-uniform distribution of channels is not expected to cause major changes in behavior as seen at the soma. This is due to the remote electrotonic location of the dendritic wide band (nearly

0.6λ) from the soma. Thus, the soma will not be affected greatly by the channel distribution within that band, but will be affected primarily by the total current reaching it. Accordingly, the channel density will be the only variable affected by the type of distribution as it determines the proper magnitude of the Ca^{+2} PIC that is obtained. Moreover, our results do not reject the presence of the $Ca_V1.3$ channels in both proximal and distal dendrites, but confirm that their highest density appears to be within the Ia-synaptic territory region. Hence, our main finding is that the distribution of the $Ca_V1.3$ channels is similar to that of Ia-synaptic inputs, and these channels are primarily localized within the Ia-synaptic territory.

Simulations done by Rose et al. (2002, 2003) on reconstructed spinal motoneurons innervating the neck extensor muscles of the adult cat suggested that $Ca_V1.3$ channels are localized in a single 100 μm aggregation, termed 'hot spot', on each dendritic branch. These 'hot spots' were found to start at dendritic distances between 150 to 400 μm from the soma. The $Ca_V1.3$ channels at these locations mimicked the change in threshold for plateau potentials caused by tonic synaptic excitation. This localization has recently been implemented in a model by Taylor and Enoka (2004a,b) focused on assessing the patterns of motor unit discharge. The technique described by Rose et al. (2002, 2003) was used as an independent validation tool for the findings of the present model. However, a number of differences between the present model and that of Rose et al. (2002, 2003) should be noted. Only $Ca_V1.3$ channels were used in the aforementioned model, and the distribution of Ia-synapses was uniform throughout the dendritic tree. In the current study we extended the investigation by: 1) incorporating other channels to examine the model firing behavior, 2) using realistic distribution of Ia-afferent synapses, and 3) comparing the results to several different and independent sets of experimental data. Our results showed that the technique of using intersections of the membrane potential profiles along the length of dendritic segments during 'rest' and 'synaptic excitation' for localizing the $Ca_V1.3$ channels is not adequate for determining the location of these channels, and is contingent upon the pattern of synaptic distribution over the dendritic tree. Some dendritic segments did not show intersection of their plots due to the distribution of the

Ia-synapses on their segments. The membrane potential profile along the dendritic length under the 'rest' condition was in general similar in all the dendrites. But the dendritic depolarization under the 'synaptic excitation' condition was dependent on the distribution of synapses over that dendrite (see Fig. 2-8A). Having a realistic distribution of synapses over the motoneuron dendritic tree is essential for obtaining correct results using this technique.

Our results are also in agreement with previous modeling and experimental studies, which suggested that $Ca_V1.3$ channels should be included distally on the dendritic tree in order to reproduce experimental observations. In a model with only L-type Ca^{+2} channels and no synapses, Carlin et al. (2000b) were unable to achieve late-onset and hysteretic Ca^{+2} currents close to what is seen experimentally unless the $Ca_V1.3$ channels were placed distally starting from the third branch point (which varies between 15-1600 μm from the soma). Bennett et al. (1998) predicted that inward currents underlying the plateau potentials in MG motoneurons should arise at locations around 0.5λ from the soma in order to be consistent with their measurements. The average location of Ia-afferent synapses is $0.57 \pm 0.36\lambda$, while the suggested wide band of the $Ca_V1.3$ channels in this study is located at $0.62 \pm 0.21\lambda$. Finally, using antibody labeling in turtle motoneurons Simon et al. (2003) observed that $Ca_V1.3$ channels were always located at synaptic sites, but not all synapses were associated with these channels. However, with immunohistochemical labeling techniques, it is usually difficult to differentiate between channels related to the motoneuronal structure and those located around them in presynaptic terminals.

2.4.2 Distribution of synaptic inputs over the dendritic tree

One could argue that the model represents only synaptic input from the monosynaptic Ia-afferent system, and that the dendritic tree may be widely covered by synaptic contacts from other systems resulting in a uniform distribution of synaptic input. The overall distribution of group Ia-boutons does not cover the entire dendritic tree of motoneurons but is confined to a roughly rectangular 3D region (the Ia-synaptic territory). This region represents the intersection of Ia-collateral trajectories and the radially organized

motoneuron dendrites, and contains 95% of the identified Ia-contacts (Segev et al. 1990; Burke and Glenn 1996). However, multiple studies suggest that synaptic contacts, in general, do follow the profile formed by the Ia inputs. The overall spatial distribution of the inhibitory synapses from Renshaw cells on the dendritic tree of cat lumbar motoneurons was found to be between 65 and 706 μm from the soma which closely resembles the distribution of excitatory Ia-afferent synapses (Fyffe 1991). Furthermore, results from ultrastructural studies on quantitative synaptology in different types of cat MG motoneurons showed that the total number of synaptic boutons from all different inputs is larger at 300 μm than at 100 μm and 700 μm from the soma in all motoneuron types (Brannstrom 1993). More strikingly, serotonergic contacts on the dendrites of spinal motoneurons have their maximum number in the same region as that suggested for the $Ca_V1.3$ channels in the present study (see Fig. 4B in Alvarez et al. 1998) which is consistent with their modulatory effects on these channels (Hounsgaard and Kiehn 1989; Berger and Takahashi 1990). This shows that the spatial distribution of all synaptic contacts mimics that of the Ia-afferents' and peaks within the suggested location for the $Ca_V1.3$ channels. Therefore, Ca^{+2} PIC would equally enhance synaptic inputs from various systems resulting in near-linear summation, as has been observed experimentally (Powers and Binder 2000; Prather et al. 2001). Distal synaptic inputs, which appear to be much fewer in number, would get 'boosted' by the Ca^{+2} PIC once they reach the location of the $Ca_V1.3$ channels.

2.4.3 Model considerations

One could contend that the modeling parameters have been adjusted so that a reference set of experimental data was mimicked. Hence, the suggested distribution of the $Ca_V1.3$ channels in this study is not the only solution as other parameters may equally mimic experimental data. However, the technique used in the customized distribution to predict the location of the $Ca_V1.3$ channels provided an independent validation method of the predicted results. Single intersection sites of the membrane potential profiles were found on each dendritic branch indicating only one location of those channels on that branch that could satisfy experimental data. Moreover, the model behavior was compared to

multiple independent sets of experimental measurements. Therefore, we believe that the suggested distribution of $Ca_V1.3$ channels is reasonably accurate, but has to be directly confirmed by appropriate labeling of these channels.

2.4.4 Concluding remarks

In summary, computer simulations in the present study allowed testing various dendritic spatial distributions of the $Ca_V1.3$ channels in spinal motoneurons. Our results point out the strong correlation between the spatial distribution of $Ca_V1.3$ channels and synaptic inputs over the dendritic tree of motoneurons. This overlap may result in the functional interactions seen experimentally between these two systems. The detailed role of $Ca_V1.3$ channels in generating plateau potentials and in enhancing and integrating synaptic inputs is currently under investigation.

2.5 TABLES

Table 2-1. Conductance of ion channels in different structures of the model

Soma	g_{Naf}	0.06 S/cm^2
	g_{Kdr}	0.80 S/cm^2
	$g_{K(Ca)}$	0.02 S/cm^2
	g_{CaN}	0.01 S/cm^2
Axon Hillock and Initial Segment	g_{Naf}	1.34 S/cm^2
	g_{Nap}	0.033 mS/cm^2
	g_{Kdr}	0.17 S/cm^2

Table 2-2. Model properties

Property	Model Results	Experimental Data
Membrane Resting Potential, V_{rest} [mV]	-70.0	-70 ± 7.0‡
Input Resistance, R_{in} [MΩ]	1.33	1.4†
Time constant, τ [ms]	7.0	6.8†
Rheobase, I_{rheo} [nA]	10.5	13.4 ± 7.9‡
Single Pulse Current Threshold, SPCT [nA]	46.0	37.7 ± 17.1‡
Voltage Threshold, V_{th} [mV]	14.5	11.6 ± 3.4‡
AP Height, [mV]	77.42	81.8 ± 9.3§
AHP Depth, [mV]	3.01	3.27 ± 1.53‡
AHP Duration, [ms]	94.21	86.3 ± 26.7‡
AHP Half Decay Time, [ms]	21.9	22.1 ± 8.5‡

Values are in means ± SD. ‡Hochman and McCrea (1994a); †Fleshman et al. (1988); §Hochman and McCrea (1994b).

Table 2-3. Electrophysiological recordings obtained from the model using the *wide band distribution* of $Ca_V1.3$ channels compared to experimental data.

	Property	Model Results	Experimental Data
Ca^{+2} PIC Properties	Initial Peak (I_{in}), nA	16.0	8.4 ± 7.9†
	Sustained Peak (I_{sus}), nA	16.22	6.8 ± 5.0†
	Onset Potential (V_{on}), mV	-53.5	-46.5 ± 5.1†
	Offset Potential (V_{off}), mV	-59.6	-57.3 ± 8.4†
	$V_{on} - V_{off}$, mV	6.1	10.9 ± 6.3†
	$I_{in} - I_{sus}$, nA	-0.22	1.6 ± 4.1†
F-I Relationship Properties	Initial Firing Rate, Hz	13.9	13.0 ± 4.0§
	Primary Slope, Hz/nA	2.6	1.7 ± 0.7§
	Secondary Slope, Hz/nA	7.0	7.5 ± 4.1§
	EPSP Effect, Hz	-8.0	-12.3 ± 7.2§
V-I Relationship Properties	Primary Slope, mV/nA	1.63	1.6 ± 0.5§
	Plateau Threshold, mV	-50.5	-50.6 ± 6.6§
	EPSP Effect, mV	-3.4	-5.8 ± 4.5§
	Peak Ia I_N, nA	11.36*	17.0 ± 2.7‡

Ia I_N Properties	Peak Ia I_N, nA	11.36*	17.0 ± 2.7‡
	Hyperpolarized Ia I_N, nA	4.8	4.8 ± 1.6‡

Values are in means ± SD. *This value includes only the contribution of Ca^{+2} PIC to the enhancement of Ia I_N, whereas experimental data include the contribution of both Na^{+} and Ca^{+2} PICs. †Lee and Heckman (1999); §Bennett et al. (1998); ‡Lee and Heckman (2000).

2.6 FIGURES

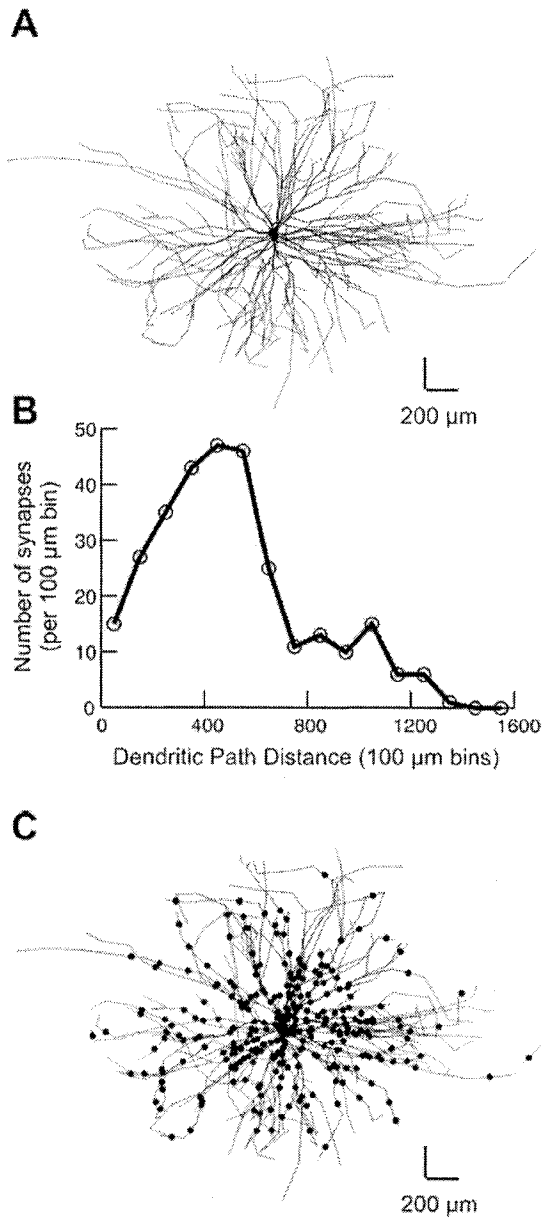

Figure 2-1. Model morphology. **A**: Detailed 3D morphology of the dendritic tree of FR cat α-motoneuron identified as cell 43/5 by Cullheim et al. (1987). **B**: Realistic distribution of group Ia afferent-to-motoneuron contacts for the modeled cat FR motoneuron along the dendritic path from the soma to terminations (Segev et al. 1990). **C**: The dendritic tree with Ia-synapses distributed as shown in **B**.

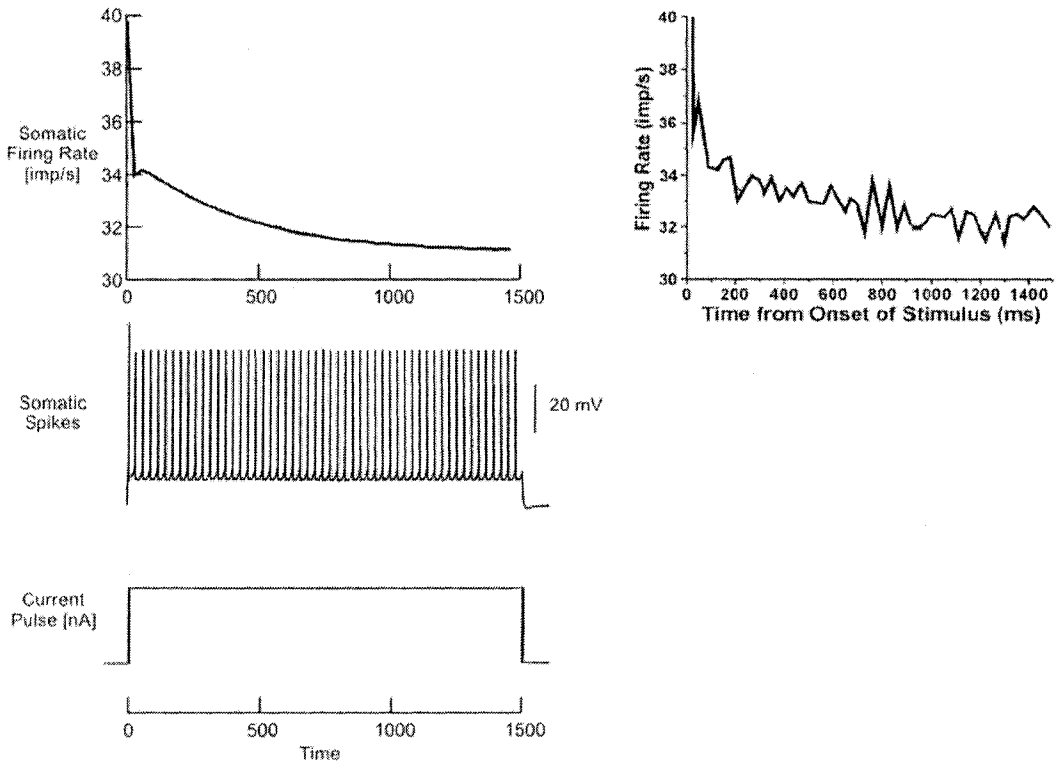

Figure 2-2. Adaptation of somatic firing rate. Instantaneous firing rate (left upper panel) as measured from the somatic spikes (left middle panel) in response to the injection of a current pulse (left lower panel) of amplitude 18 nA at the soma in a model with passive dendrites. Experimental data (right upper panel) from Sawczuk et. al. (1995) in which firing rates were obtained from anaesthetized animals. Figure of experimental data was adapted from fig. 3B in McIntyre and Grill (2002).

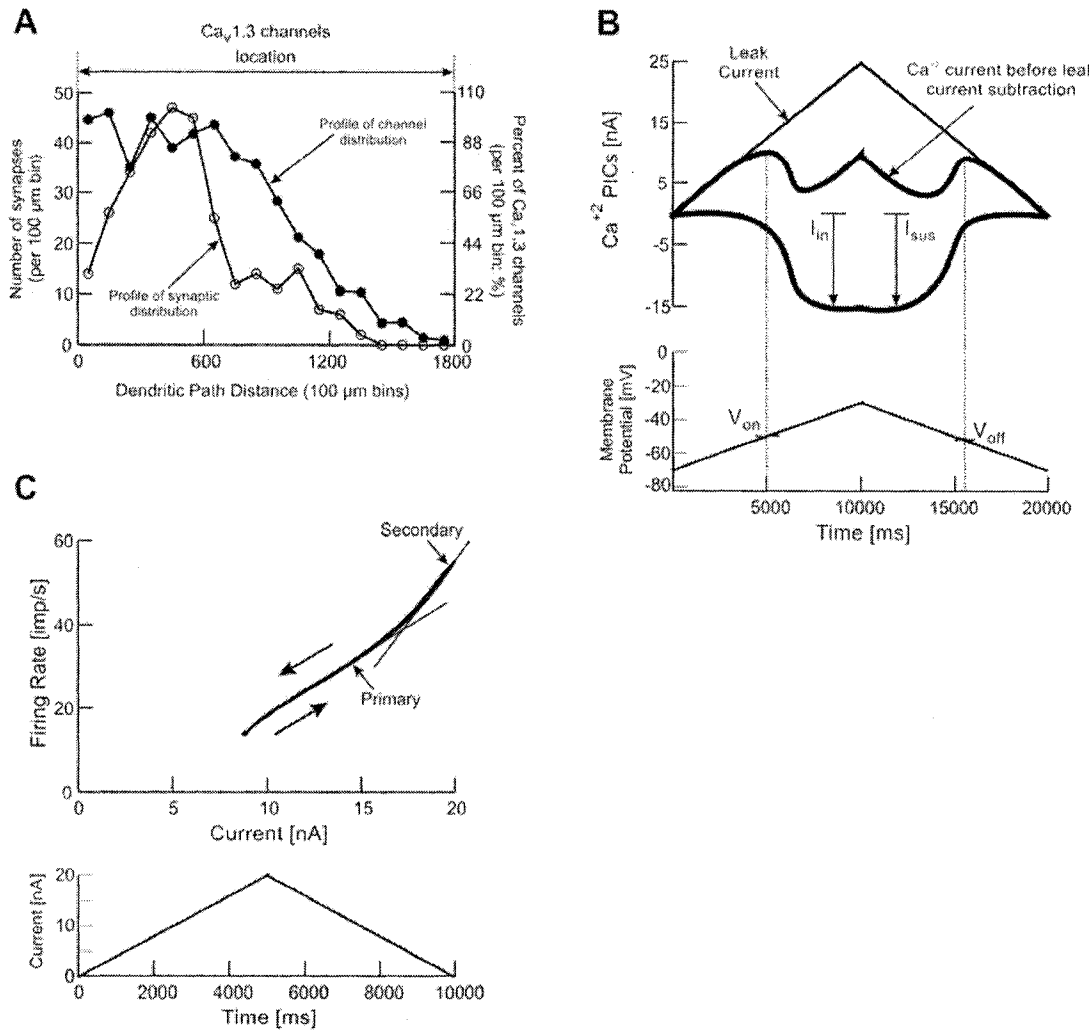

Figure 2-3. Whole uniform density distribution. **A**: Tested spatial distribution of $Ca_V1.3$ channels (between the two vertical dashed lines). Number of channels per 100 µm bins (filled circles), normalized to the maximum number of channels over the dendritic tree, compared to that of Ia-synaptic contacts (open circles). **B**: Ca^{+2} PIC measurements during voltage clamp with a triangular voltage command of slope 4 mV/s. Leak current was subtracted from the measured Ca^{+2} current. V_{on}, the onset potential, and V_{off}, the offset potential, are the potentials of the first and last zero-slope points on the current trace before leak current subtraction, respectively. I_{in}, the depth of the initial peak, and I_{sus}, the depth of the sustained peak, are measured after leak current subtraction (Lee and Heckman 1999). **C**: F-I relationship obtained by intracellular injection of a triangular

current ramp of slope 4 nA/s at the soma. Thin lines indicate the primary and secondary segments of the F-I relationship. Arrows show firing rates during the ascending (indicated by the upward arrow) and descending (indicated by the downward arrow) phases of the injected current. Note that minimal hysteresis and no bistability are seen with this distribution.

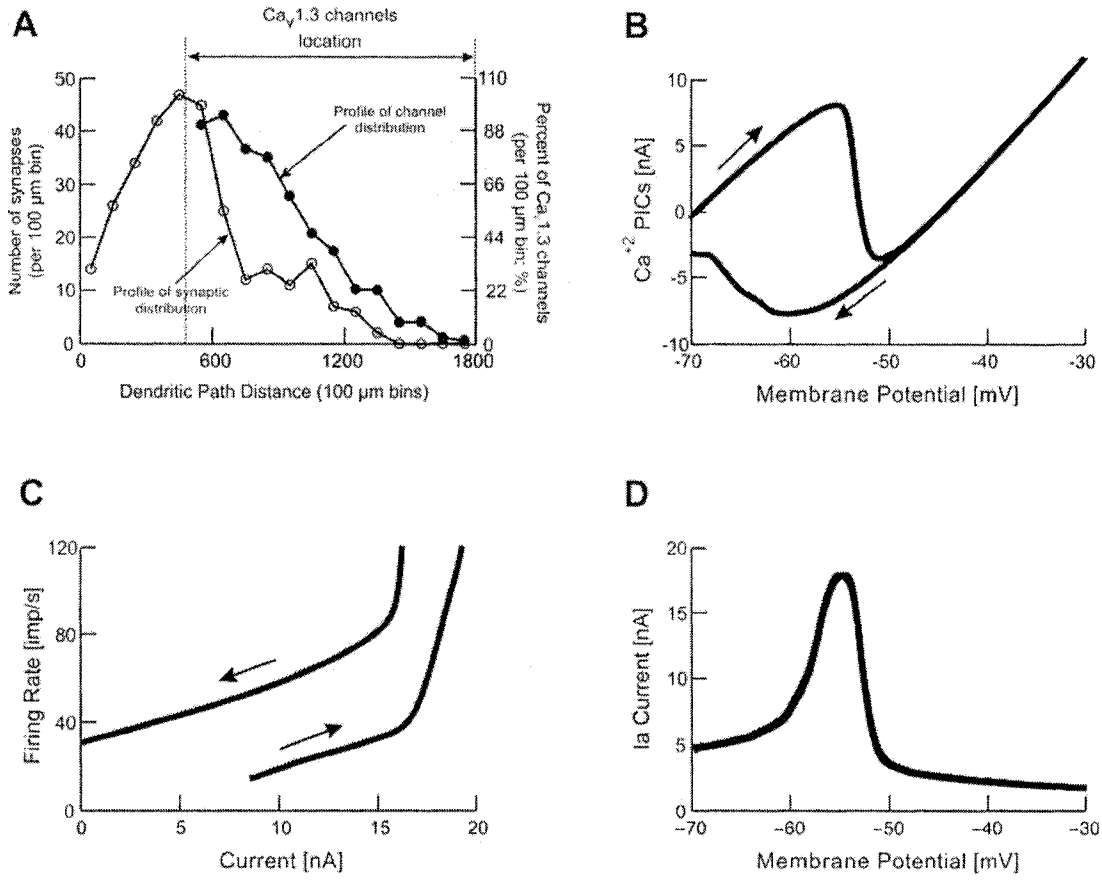

Figure 2-4. Middle uniform density distribution. **A**: Tested spatial distribution of $Ca_V1.3$ channels (between the two vertical dashed lines). Number of channels per 100 µm bins (filled circles), normalized to the maximum number of channels over the dendritic tree, compared to that of Ia-synaptic contacts (open circles). **B**: I-V relationship with the down phase of the command voltage ramp (indicated by the lower arrow) reversed and superimposed on the up phase (indicated by the upper arrow). **C**: F-I relationship obtained as described in Fig. 2-3C. Firing rates over 120 Hz were clipped. Arrows show firing rates during the ascending (indicated by the upward arrow) and descending (indicated by the downward arrow) phases of the injected current. **D**: Enhancement of Ia I_N was obtained from the difference between the I-V relations with no synaptic activity (at rest), and during tendon vibration at 180 Hz. Note the presence of hysteresis in the

Ca^{+2} PIC. However, an unusually strong effect of Ca^{+2} PIC is seen in the high firing rates and the high peak value of Ia I_N.

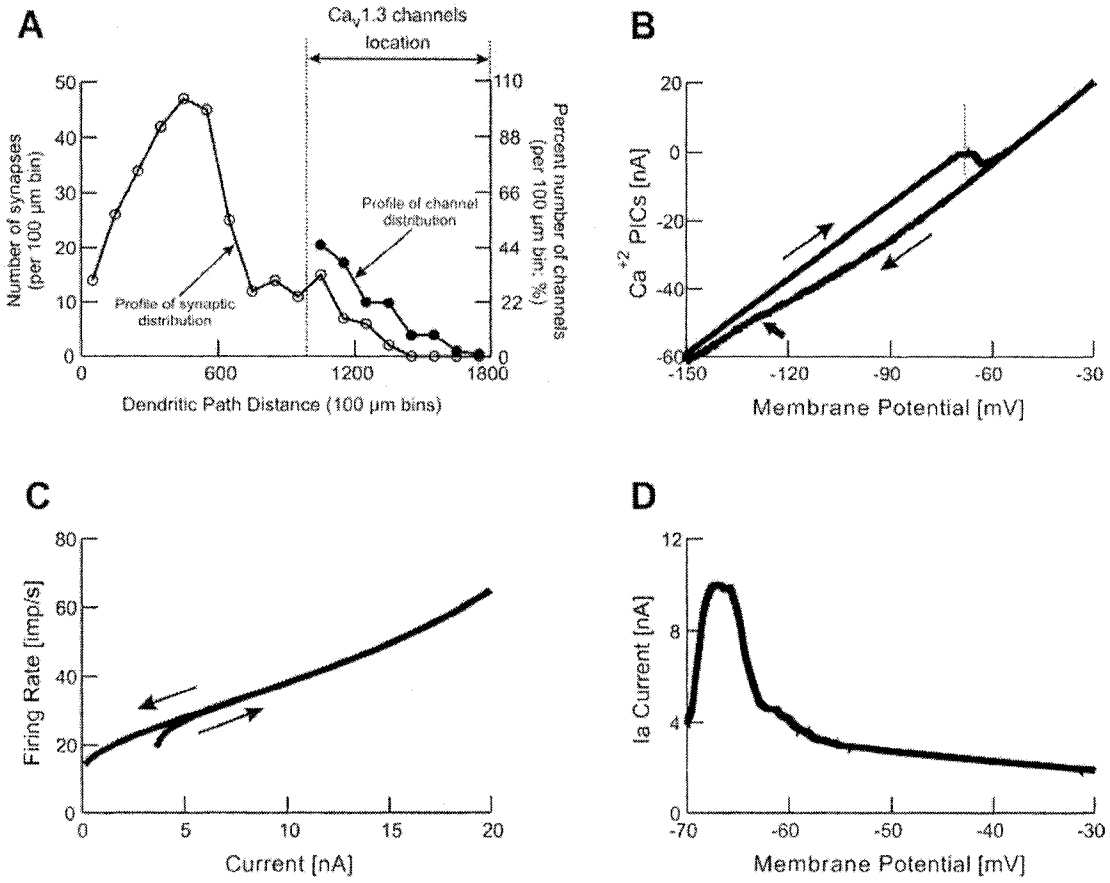

Figure 2-5. Distal uniform density distribution. **A**: Tested spatial distribution of $Ca_V1.3$ channels (between the two vertical dashed lines). Number of channels per 100 µm bins (filled circles), normalized to the maximum number of channels over the dendritic tree, compared to that of Ia-synaptic contacts (open circles). **B**: I-V relationship with the down phase of the command voltage ramp (indicated by the lower arrow) reversed and superimposed on the up phase (indicated by the upper arrow). Dotted line indicates the apparent somatic activation threshold of Ca^{+2} PIC, which is equal to -68.5 mV. Arrow indicates the apparent somatic deactivation threshold of Ca^{+2} PIC, which is equal to -127 mV. **C**: F-I relationship obtained as described in Fig. 2-3C. Arrows show firing rates during the ascending (indicated by the upward arrow) and descending (indicated by the downward arrow) phases of the injected current. **D**: Enhancement of Ia I_N obtained as described in Fig. 2-4D. Note the large hysteresis in the Ca^{+2} PIC and the lack of

bistability in the F-I relationship. The peak of Ia I_N occurred very close to the resting potential.

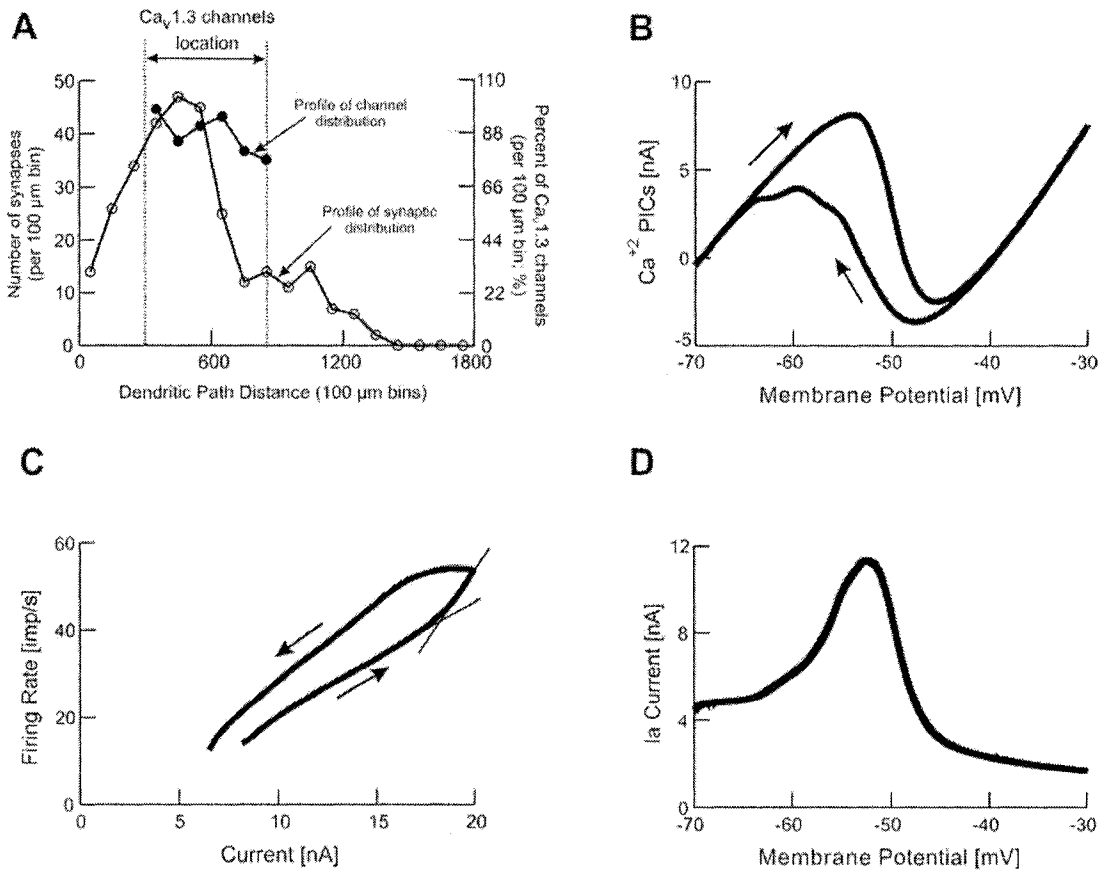

Figure 2-6. Wide band distribution. **A**: Tested spatial distribution of $Ca_V1.3$ channels (between the two vertical dashed lines). Number of channels per 100 µm bins (filled circles), normalized to the maximum number of channels over the dendritic tree, compared to that of Ia-synaptic contacts (open circles). **B**: I-V relationship with the down phase of the command voltage ramp (indicated by the lower arrow) reversed and superimposed on the up phase (indicated by the upper arrow). **C**: F-I relation obtained as described in Fig. 2-3C. Thin lines indicate the primary and secondary segments of the F-I relationship. Arrows show firing rates during the ascending (indicated by the upward arrow) and descending (indicated by the downward arrow) phases of the injected current. **D**: Voltage-dependent enhancement of Ia I_N obtained as described in Fig. 2-4D. See Table 2-3 for a complete list of parameter values.

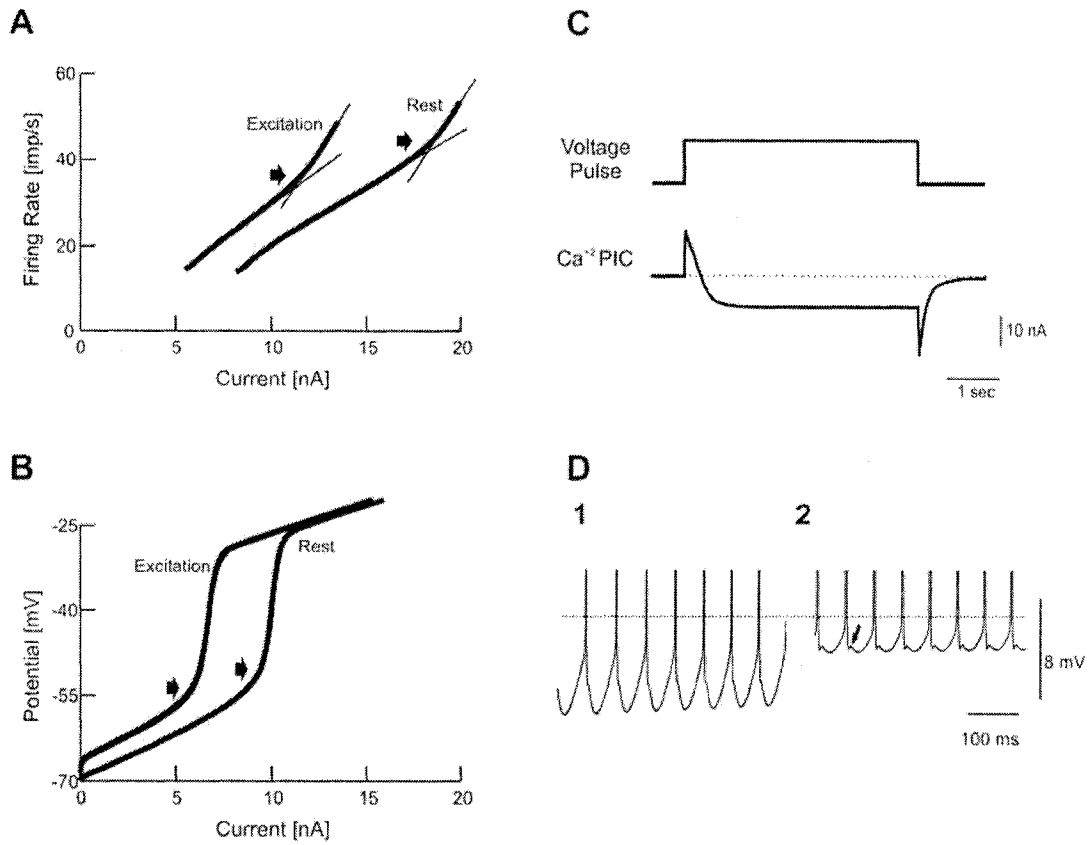

Figure 2-7. Wide band distribution. **A**: Effects of tonic synaptic activation of Ia-afferent synapses on the transition frequency from primary to secondary ranges. Arrows show the transition frequency. Tonic Ia-afferent excitation lowered the transition frequency by 8 Hz. **B**: Effects of tonic synaptic activation of Ia-afferent synapses on the somatic plateau threshold. Arrows show the somatic plateau threshold. Tonic Ia-afferent excitation lowered the somatic plateau threshold by 3.4 mV. *Rest* shows the response when no synaptic activation was present. *Excitation* shows the response during tonic activation of Ia-afferent synapses. Compare **A** and **B** to figures 2B and 4B in Bennett et al. (1998), respectively. **C**: Activation of Ca^{+2} PIC during a long suprathreshold (-50 mV) voltage pulse under voltage clamp conditions. Compare to Fig. 7C in Li and Bennett (2003). **D**: Changes in properties of AHP after activation of plateau potentials. Shown are model results of AHP before plateau activation (1), and after plateau activation with intracellular current injection (2). Arrow shows the appearance of afterdepolarization. Note the reduction in the size of the AHP and appearance of afterdepolarization after plateau activation (compare to Fig. 3B in Bennett et al. 1998).

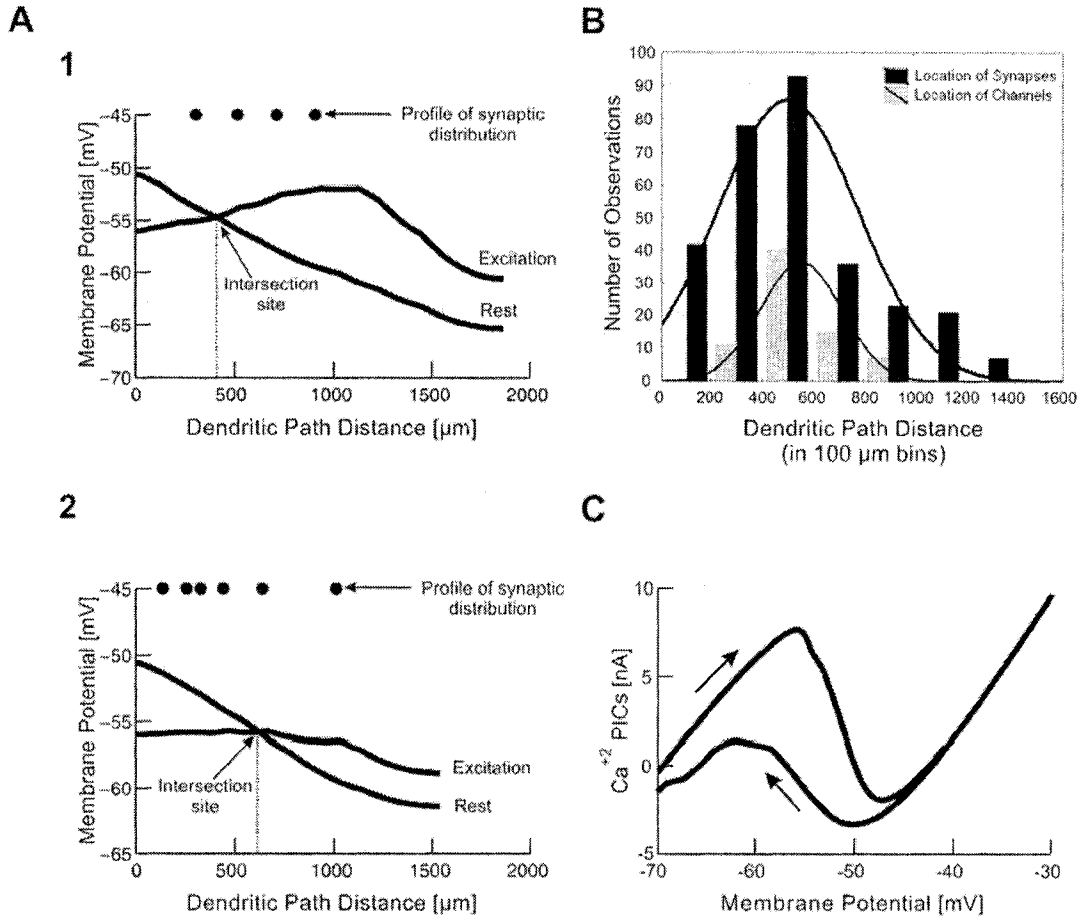

Figure 2-8. Customized distribution. **A**: Relationships between membrane potential and the distance along the dendritic path from the soma obtained at 'rest' and 'synaptic excitation' conditions for two terminal dendrites (1 and 2) with different synaptic distributions along their segments and different intersection sites. The intersection of the two plots was used to place the $Ca_V1.3$ channels in regions centered around the average intersection site on that root dendrite. *Rest* and *Excitation* are as defined in Fig. 2-7. The distribution of synapses along the dendritic segment is indicated by the black dots at the top of each graph. **B**: Comparison of the $Ca_V1.3$ channels and Ia-afferent synapse distributions over the dendritic tree. Black bars represent the distribution of Ia-afferent synapses (same data in Fig. 2-1B). The upper thick line represents the normal distribution of the synapse locations over the dendritic tree. Gray bars represent the overall distribution of the $Ca_V1.3$ channels over the dendritic tree, and the thin line represents the

normal distribution of channel locations over the dendritic tree. Note that both the synapses and channels have very similar normal distributions. **C**: Measured Ca^{+2} PIC from channels centered around the average intersection site of each root dendrite with region width of 300 μm. Ca^{+2} PIC was measured as described in Fig. 2-3B with the down phase of the command voltage ramp (indicated by the lower arrow) reversed and superimposed on the up phase (indicated by the upper arrow). Note the similarity between Ca^{+2} PICs measured from the customized and wide band distributions (compare Fig. 2-8C to 2-6B).

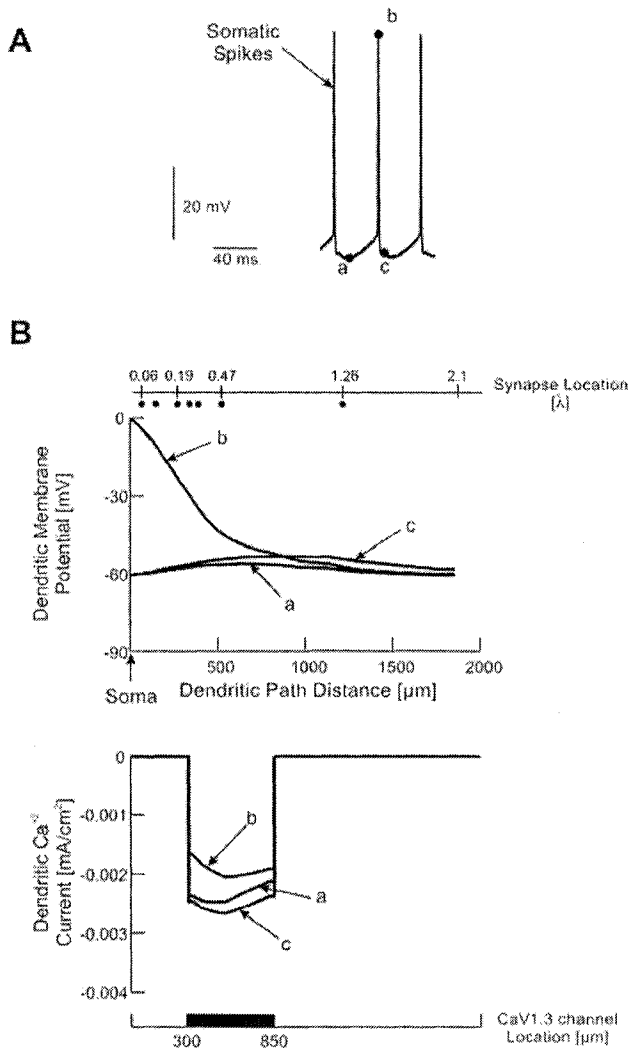

Figure 2-9. Spatiotemporal measurements of membrane potential and Ca^{+2} current. **A**: Spike train evoked by excitation of Ia-afferent synapses. Points *a*, *b* and *c* show different points in time during AHP, peak of AP, and repolarization phase of AP, respectively. **B**: Dendritic membrane potential (upper graph) and Ca^{+2} current (lower graph) along the dendritic path distance from the soma at different points in time. Location of Ia-afferent synapses in λ is represented as black dots on the upper ordinate and $Ca_V1.3$ channels in μm on that dendritic branch is shown on the lower ordinate.

2.7 REFERENCES

Alvarez FJ, Pearson JC, Harrington D, Dewey D, Torbeck L, and Fyffe RE. Distribution of 5-hydroxytryptamine-immunoreactive boutons on alpha-motoneurons in the lumbar spinal cord of adult cats. *J Comp Neurol* 393: 69-83, 1998.

Baldissera F, Hultborn H, and Illert M. Integration in spinal neuronal systems. In: *Handbook of Physiology. The Nervous System. Motor Control.*, edited by Brooks V. Bethesda, MD: American Physiological Society, 1981, p. 509-595.

Barrett EF, Barrett JN, and Crill WE. Voltage-sensitive outward currents in cat motoneurones. *J Physiol* 304: 251-276., 1980.

Barrett JN and Crill WE. Voltage clamp of cat motoneurone somata: properties of the fast inward current. *J Physiol* 304: 231-249., 1980.

Bennett DJ, Hultborn H, Fedirchuk B, and Gorassini MA. Synaptic Activation of Plateaus in Hindlimb Motoneurons of Decerebrate Cats. *J Neurophysiol* 80: 2023-2037, 1998.

Berger AJ and Takahashi T. Serotonin enhances a low-voltage-activated calcium current in rat spinal motoneurons. *J Neurosci* 10: 1922-1928, 1990.

Binder MD, Heckman CJ, and Powers RK. The Physiological control of motoneuron activity. In: *Section 12: Exercise: Regulation and Integration of Multiple Systems.* New York: Oxford Univ Press, 1996, p. 3-53 , 89-127.

Booth V, Rinzel J, and Kiehn O. Compartmental Model of Vertebrate Motoneurons for Ca2+-Dependent Spiking and Plateau Potentials Under Pharmacological Treatment. *J Neurophysiol* 78: 3371-3385, 1997.

Brannstrom T. Quantitative synaptology of functionally different types of cat medial gastrocnemius alpha-motoneurons. *J Comp Neurol* 330: 439-454, 1993.

Burke RE and Glenn LL. Horseradish peroxidase study of the spatial and electrotonic distribution of group Ia synapses on type-identified ankle extensor motoneurons in the cat. *J Comp Neurol* 372: 465-485., 1996.

Burke RE, Walmsley B, and Hodgson JA. HRP anatomy of group Ia afferent contacts on alpha motoneurones. *Brain Res* 160: 347-352., 1979.

Carlin KP, Jiang Z, and Brownstone RM. Characterization of calcium currents in functionally mature mouse spinal motoneurons. *Eur J Neurosci* 12: 1624-1634., 2000a.

Carlin KP, Jones KE, Jiang Z, Jordan LM, and Brownstone RM. Dendritic L-type calcium currents in mouse spinal motoneurons: implications for bistability. *Eur J Neurosci* 12: 1635-1646, 2000b.

Clements JD and Redman SJ. Cable properties of cat spinal motoneurones measured by combining voltage clamp, current clamp and intracellular staining. *J Physiol* 409: 63-87., 1989.

Conradi S. Observations on the ultrastructure of the axon hillock and initial axon segment of lumbosacral motoneurons in the cat. *Acta Physiol Scand Suppl* 332: 65-84., 1969.

Conway BA, Hultborn H, Kiehn O, and Mintz I. Plateau potentials in alpha-motoneurones induced by intravenous injection of L-dopa and clonidine in the spinal cat. *J Physiol* 405: 369-384, 1988.

Crill WE. Persistent sodium current in mammalian central neurons. *Annu Rev Physiol* 58: 349-362., 1996.

Crone C, Hultborn H, Kiehn O, Mazieres L, and Wigstrom H. Maintained changes in motoneuronal excitability by short-lasting synaptic inputs in the decerebrate cat. *J Physiol* 405: 321-343, 1988.

Cullheim S, Fleshman JW, Glenn LL, and Burke RE. Membrane area and dendritic structure in type-identified triceps surae alpha motoneurons. *J Comp Neurol* 255: 68-81, 1987.

ElBasiouny SM and Mushahwar VK. Spatial distribution of low voltage-activated L-type calcium channels in the dendrites of cat lumbar motoneurons. *2004 Abstract Viewer/Itinerary Planner, Washington, DC: Society for Neuroscience, Online.* Program No. 875.7, 2004.

Fleshman JW, Segev I, and Burke RE. Electrotonic architecture of type-identified alpha-motoneurons in the cat spinal cord. *J Neurophysiol* 60: 60-85, 1988.

Fyffe RE. Spatial distribution of recurrent inhibitory synapses on spinal motoneurons in the cat. *J Neurophysiol* 65: 1134-1149, 1991.

Glenn LL, Burke RE, Fleshman JW, and Lev-Tov A. Estimates of electrotonic distance of group Ia contacts on cat a-motoneurons: An HRP-morphological study. *Soc Neurosci Abstr* 8: 995, 1982.

Gustafsson B and Pinter MJ. An investigation of threshold properties among cat spinal alpha-motoneurones. *J Physiol* 357: 453-483, 1984.

Gutman AM. Bistability of dendrites. *Int J Neural Sys* 1: 291-304, 1991.

Helmchen F, Imoto K, and Sakmann B. Ca2+ buffering and action potential-evoked Ca2+ signaling in dendrites of pyramidal neurons. *Biophys J* 70: 1069-1081., 1996.

Hines M and Carnevale T. The NEURON simulation environment. *Neural Comput* 9: 1179-1209, 1997.

Hochman S and McCrea DA. Effects of chronic spinalization on ankle extensor motoneurons. II. Motoneuron electrical properties. *J Neurophysiol* 71: 1468-1479, 1994a.

Hochman S and McCrea DA. Effects of chronic spinalization on ankle extensor motoneurons. III. Composite Ia EPSPs in motoneurons separated into motor unit types. *J Neurophysiol* 71: 1480-1490, 1994b.

Hounsgaard J, Hultborn H, Jespersen B, and Kiehn O. Bistability of alpha-motoneurones in the decerebrate cat and in the acute spinal cat after intravenous 5-hydroxytryptophan. *J Physiol* 405: 345-367., 1988.

Hounsgaard J and Kiehn O. Calcium spikes and calcium plateaux evoked by differential polarization in dendrites of turtle motoneurones in vitro. *J Physiol* 468: 245-259, 1993.

Hounsgaard J and Kiehn O. Serotonin-induced bistability of turtle motoneurones caused by a nifedipine-sensitive calcium plateau potential. *J Physiol* 414: 265-282., 1989.

Hounsgaard J and Mintz I. Calcium conductance and firing properties of spinal motoneurones in the turtle. *J Physiol* 398: 591-603., 1988.

Johnston D, Magee JC, Colbert CM, and Cristie BR. Active properties of neuronal dendrites. *Annu Rev Neurosci* 19: 165-186, 1996.

Jones KE and Bawa P. Computer Simulation of the Responses of Human Motoneurons to Composite 1A EPSPS: Effects of Background Firing Rate. *J Neurophysiol* 77: 405-420, 1997.

Kellerth JO, Berthold CH, and Conradi S. Electron microscopic studies of serially sectioned cat spinal alpha-motoneurons. III. Motoneurons innervating fast-twitch (type FR) units of the gastrocnemius muscle. *J Comp Neurol* 184: 755-767., 1979.

Kuo JJ, Lee RH, Johnson MD, Heckman HM, and Heckman CJ. Active Dendritic Integration of Inhibitory Synaptic Inputs In Vivo. *J Neurophysiol* 90: 3617-3624, 2003.

Lee RH and Heckman CJ. Influence of voltage-sensitive dendritic conductances on bistable firing and effective synaptic current in cat spinal motoneurons in vivo. *J Neurophysiol* 76: 2107-2110., 1996.

Lee RH and Heckman CJ. Bistability in Spinal Motoneurons In Vivo: Systematic Variations in Rhythmic Firing Patterns. *J Neurophysiol* 80: 572-582, 1998a.

Lee RH and Heckman CJ. Bistability in Spinal Motoneurons In Vivo: Systematic Variations in Persistent Inward Currents. *J Neurophysiol* 80: 583-593, 1998b.

Lee RH and Heckman CJ. Paradoxical Effect of QX-314 on Persistent Inward Currents and Bistable Behavior in Spinal Motoneurons In Vivo. *J Neurophysiol* 82: 2518-2527, 1999.

Lee RH and Heckman CJ. Adjustable Amplification of Synaptic Input in the Dendrites of Spinal Motoneurons In Vivo. *J Neurosci* 20: 6734-6740, 2000.

Lee RH and Heckman CJ. Essential Role of a Fast Persistent Inward Current in Action Potential Initiation and Control of Rhythmic Firing. *J Neurophysiol* 85: 472-475, 2001.

Li Y and Bennett DJ. Persistent Sodium and Calcium Currents Cause Plateau Potentials in Motoneurons of Chronic Spinal Rats. *J Neurophysiol* 90: 857-869, 2003.

McIntyre CC and Grill WM. Extracellular Stimulation of Central Neurons: Influence of Stimulus Waveform and Frequency on Neuronal Output. *J Neurophysiol* 88: 1592–1604, 2002.

Powers RK and Binder MD. Summation of Effective Synaptic Currents and Firing Rate Modulation in Cat Spinal Motoneurons. *J Neurophysiol* 83: 483-500, 2000.

Powers RK and Binder MD. Persistent Sodium and Calcium Currents in Rat Hypoglossal Motoneurons. *J Neurophysiol* 89: 615-624, 2003.

Prather JF, Powers RK, and Cope TC. Amplification and Linear Summation of Synaptic Effects on Motoneuron Firing Rate. *J Neurophysiol* 85: 43-53, 2001.

Rall W. Distinguishing theoretical synaptic potentials computed for different soma-dendritic distributions of synaptic input. *J Neurophysiol* 30: 1138-1168, 1967.

Rose PK, Ter-Mikaelian M, and Bui T. Location of l-type calcium channels on spinal motoneurons: insights from compartmental models. *2002 Abstract Viewer/Itinerary Planner Washington, DC: Society for Neuroscience, Online,* Program No. 856.9., 2002.

Rose PK, Ter-Mikaelian M, Bui T, Cushing S, and Bedrossian D. Influence of L-type calcium channels on the input-output properites of spinal motoneurons: insights from compartmental models. *2003 Abstract Viewer/Itinerary Planner Washington, DC: Society for Neuroscience, Online,* Program No. 496.8., 2003.

Sawczuk A, Powers R, and Binder MD. Spike frequency adaptation studied in hypoglossal motoneurons of the rat. *J Neurophysiol* 73: 1799-1810., 1995.

Schwindt PC and Crill WE. A persistent negative resistance in cat lumbar motoneurons. *Brain Res* 120: 173-178, 1977.

Schwindt PC and Crill WE. Properties of a persistent inward current in normal and TEA-injected motoneurons. *J Neurophysiol* 43: 1700-1724., 1980a.

Schwindt PC and Crill WE. Role of a persistent inward current in motoneuron bursting during spinal seizures. *J Neurophysiol* 43: 1296-1318, 1980b.

Segev I, Fleshman JW, and Burke RE. Computer simulation of group Ia EPSPs using morphologically realistic models of cat alpha-motoneurons. *J Neurophysiol* 64: 648-660, 1990.

Simon M, Perrier J-F, and Hounsgaard J. Subcellular distribution of L-type Ca²⁺ channels responsible for plateau potentials in motoneurons from the lumbar spinal cord of the turtle. *Eur J Neurosci* 18: 258-266, 2003.

Takahashi T and Berger AJ. Direct excitation of rat spinal motoneurones by serotonin. *J Physiol* 423: 63-76, 1990.

Talbot MJ and Sayer RJ. Intracellular QX-314 inhibits calcium currents in hippocampal CA1 pyramidal neurons. *J Neurophysiol* 76: 2120-2124, 1996.

Taylor AM and Enoka RM. Optimization of input patterns and neuronal properties to evoke motor neuron synchronization. *J Comput Neurosci* 16: 139-157, 2004.

Taylor AM and Enoka RM. Quantification of the Factors That Influence Discharge Correlation in Model Motor Neurons. *J Neurophysiol* 91: 796-814, 2004.

Wang MY and Dun NJ. 5-Hydroxytryptamine responses in neonate rat motoneurones in vitro. *J Physiol* 430: 87-103, 1990.

White SR, Fung SJ, and Barnes CD. Norepinephrine effects on spinal motoneurons. *Prog Brain Res* 88: 343-350, 1991.

Xu W and Lipscombe D. Neuronal CaV1.3{alpha}1 L-Type Channels Activate at Relatively Hyperpolarized Membrane Potentials and Are Incompletely Inhibited by Dihydropyridines. *J Neurosci* 21: 5944-5951, 2001.

Yuste R and Tank D. Dendritic integration in mammalian neurons, a century after Cajal. *Neuron* 16: 701-716, 1996.

Chapter 3: Simulation of Ca^{+2} Persistent Inward Currents in Spinal Motoneurons: Mode of Activation and Integration of Synaptic Inputs [†]

3.1 INTRODUCTION

The finding of voltage-gated ion channels on the dendritic tree of spinal motoneurons has changed the classical view of dendrites being passive structures. This classical view was supported by the linear summation of synaptic inputs reported from early motoneuron experimental recordings obtained from anesthetized animal preparations (Granit et al. 1966a). Instead, dendrites of motoneurons are active structures that have ionic conductances which play a fundamental role in shaping the motor output. The ionic conductances, especially those mediating persistent inward currents (PICs), when activated generate sustained depolarization of the membrane causing plateau potentials (Hounsgaard et al. 1988). They also amplify synaptic currents by three to six fold at potentials close to the voltage threshold for firing (Lee et al. 2003). The enhancement of synaptic currents by these PIC-mediating channels explains the inconsistency between the strength of synaptic current reaching the soma and the resulting motoneuron firing rates (Rose and Cushing 1999; Powers and Binder 2001).

The question of whether PICs and plateau potentials are activated in a graded or all-or-none manner has recently received much attention (for example: Hultborn et al. 2003; Lee et al. 2003); however, the answer to this question remains unclear. The difficulty in inferring the mode of activation of the dendritic PIC comes from the discrepancies in experimental results leading to inconsistent explanations of the behavior of the PIC. For example, synaptic input provided by smooth muscle stretch caused a graded increase in motoneuron firing rate before saturation (Lee et al. 2003) suggesting graded activation of

[†] A revised version of this chapter has been published (ElBasiouny SM, Bennett DJ, and Mushahwar VK, *J. Physiol. (Lond)* 570 (2): 355-74, 2006 'used with permission'). This article was ranked by the *Journal of Physiology (Lond)* among the Top Ten Research Papers published in that journal issue based on the number of electronic access and downloads.

the PIC. However, in the same study, a step increase in firing rate was also seen in some motoneurons suggesting all-or-none activation of the PIC (Lee et al. 2003). In current-clamp experiments where the spikes were blocked, the membrane potential was found to jump abruptly into a state of sustained depolarization (plateau potentials) when the PIC was activated, suggesting an all-or-none activation of the PIC as well (Hounsgaard et al. 1988; Bennett et al. 1998; Lee and Heckman 1999).

Discrepancies have also been reported regarding the role of the PIC in enhancing and integrating synaptic inputs. In examining the enhancement of synaptic currents by the effect of PIC, Hultborn et al. (2003) reported graded (variable) enhancement of synaptic inputs as the PIC is activated in experimental recordings obtained from decerebrate cat motoneurons. Prather et al. (2001), on the other hand, reported constant enhancement of synaptic inputs by the PIC (indicated by a vertical shift in the frequency-current (F-I) relationship relative to that predicted when the synaptic input was applied) in decerebrate cat motoneurons as well. Because of the effect of the dendritic PIC on the enhancement of synaptic inputs, non-linear summation of multiple synaptic inputs was expected (Powers and Binder 2001). However, linear summation (Burke 1967; Prather et al. 2001), less-than linear summation (Kuno and Miyahara 1969), and even occasionally greater-than linear summation (Powers and Binder 2000) of synaptic inputs have been reported.

The primary reason for the existence of these unresolved discrepancies in experimental reports is the inability to record directly the dendritic currents in experimental setups. Thus, the goal of the present study is to examine the mode of activation of the Ca^{+2} PIC in spinal motoneurons using computer simulations, and examine its role in the production of cell firing, and in the enhancement and summation of synaptic inputs. For the purposes of this paper, we define all-or-none activation as an abrupt transition from a state of no PIC activation to a state of full PIC activation in response to a small increase in synaptic current (in steady-state). In other words, a discontinuity in the activation profile of the PIC will be seen with respect to the change in synaptic current. In contrast, graded activation is defined as small increases in PIC activation in response to successive small increases in synaptic current. To quantify the F-I relationship, we use the classical

nomenclature for describing the different piece-wise linear ranges of cell firing in response to current injection at the soma (primary, secondary, and tertiary ranges), as originally defined by Kernell (1965a,b). We also extend the use of this nomenclature to describe the piece-wise linear firing ranges in response to *synaptic* activation (Granit et al. 1966a,b; Heckman and Binder 1988).

A compartmental cable model of a cat α-motoneuron comprising the dendritic low voltage-activated (LVA) L-type calcium ($Ca_V1.3$ type) channels and the realistic dendritic distribution of Ia-afferent synapses, which was previously developed and verified (ElBasiouny et al. 2005b), was used to examine these behaviors. This made the evaluation of the dendritic Ca^{+2} PIC possible since dendritic recordings are generally difficult in real motoneurons. The synaptic input to the motoneuron was linearly increased while cell firing, somatic and dendritic membrane potentials, dendritic $Ca_V1.3$ channel conductance, and dendritic Ca^{+2} PIC were simultaneously measured. The modes of activation of the Ca^{+2} PIC were investigated under three conditions: 1) during spike blockage; 2) under voltage-clamp conditions; and 3) during normal cell firing. The role of the Ca^{+2} PIC in the enhancement and summation of synaptic inputs was then assessed and explained in light of its distinct modes of activation. Our simulations suggest that during normal firing Ca^{+2} PIC is not activated in an all-or-none manner; rather, it is activated in two stages. The Ca^{+2} PIC is first activated in a graded fashion in response to increasing synaptic input causing the cell to fire in its secondary range. The Ca^{+2} PIC then becomes fully activated (saturated) and no additional increase in its amplitude is achieved in response to more synaptic input. This saturated stage corresponds to the tertiary range of cell firing (Li et al. 2004). No all-or-none activation of the Ca^{+2} PIC occurs during cell firing due to the subthreshold clamping effect of the post spike afterhyperpolarization (AHP) on the membrane potential, which limits the extent of Ca^{+2} PIC activation. During the graded phase of Ca^{+2} PIC activation, the PIC causes a graded (linear) enhancement of the synaptic inputs in proportion to the level of synaptic excitation, whereas when the Ca^{+2} PIC is saturated it enhances synaptic inputs by a constant amount (i.e. constant current) in proportion to the level of synaptic excitation. During the secondary range of firing where the Ca^{+2} PIC is graded, synaptic inputs sum linearly. Conversely, during the

tertiary range of firing where the Ca^{+2} PIC is saturated, synaptic inputs sum less-than linearly. Part of this work was previously presented in abstract form (ElBasiouny and Mushahwar 2004; ElBasiouny et al. 2005a).

3.2 MATERIALS AND METHODS

3.2.1 Model description

Full description of the model morphology, biophysical properties, and its verification is provided in ElBasiouny et al. (2005b). Briefly, a computer-based cable model of an adult cat α-motoneuron was developed using NEURON simulation environment (Hines and Carnevale 1997). The model had full representation of the α-motoneuron structure, and consisted of soma, axon hillock, initial segment (IS), and dendritic tree. The model dendritic tree was based on the three-dimensional (3D) detailed morphology for type-identified triceps surae α-motoneuron (fatigue-resistant (FR) type, medial gastrocnemius (MG) motoneuron, identified as cell 43/5), labeled intracellularly with horseradish peroxidase (Cullheim et al. 1987). The model *passive* properties were set based on previous studies for the same 43/5 FR motoneuron (Cullheim et al. 1987; Fleshman et al. 1988). Voltage-gated ion channels (fast Na^+, persistent Na^+, delayed rectifier K^+, Ca^{+2}-activated K^+, and N-type Ca^{+2}), were then set such that the model properties were within the 95% confidence range of experimental data, and the model generated action potential and AHP with properties similar to experimental recordings (Table 2 in ElBasiouny et al. 2005b). Furthermore, the model exhibited adaptation of firing rate that was similar to experimental data when long current pulses were injected into the soma (Sawczuk et al. 1995; not illustrated).

3.2.2 $Ca_V1.3$ channels

LVA L-type calcium ($Ca_V1.3$ type) channels were then distributed on the dendritic tree based on the *wide band distribution* previously described in ElBasiouny et al. (2005b). In this distribution, the $Ca_V1.3$ channels were localized on dendritic segments with dendritic path distance between 300 μm and 850 μm from the soma, which is the dendritic region mostly covered by the Ia-afferent synapses. With this distribution, the model matched different and independent sets of experimental measurements from cat motoneurons innervating the MG muscle. These measurements were: a) properties of Ca^{+2} PIC and F-I relationship; b) changes in the somatic plateau threshold and F-I relationship due to background synaptic activity, c) enhancement of Ia-synaptic current, d) shape and timing

of tail currents seen experimentally at the termination of long voltage pulses, and e) changes in the shape of AHP after the activation of the Ca^{+2} PIC (ElBasiouny et al. 2005b).

3.2.3 Dendritic synaptic inputs and their graded activation

The monosynaptic Ia-afferent system was represented in the model. The dendritic spatial distribution of Ia-afferent synapses was based on the realistic distribution of group Ia afferent-to-motoneuron contacts from cat FR motoneurons (Burke et al. 1979; Glenn et al. 1982; Burke and Glenn 1996). Noteworthy, synaptic inputs from other systems appear to have similar distribution to that of Ia-afferents (Segev et al. 1990; Fyffe 1991; Brannstrom 1993; Burke and Glenn 1996). Tendon vibration was simulated by activating the Ia-afferent synapses at 180 Hz while adjusting the synapse conductances to give Ia effective synaptic current (Ia I_N) of 4.8 nA at resting potential, which is the experimental value reported by Lee and Heckman (2000). This provided the effective synaptic conductance associated with the Ia I_N. The synapses were activated asynchronously as detailed by ElBasiouny et al. (2005b).

To allow for systematic gradation of the synaptic input, the total number of Ia-synapses was divided into 8 nearly-equal groups, randomly distributed on the dendrites (ElBasiouny et al. 2005b). The Ia-synaptic groups were sequentially activated (from 14% to 100%) such that the maximum magnitude of Ia I_N was equal to that obtained experimentally when all Ia-synapses were activated (Ia I_N = 4.8 nA at 100% of synaptic excitation). This synaptic input resulted in a linear increase in the Ia I_N (measured at resting potential, -70 mV; Heckman and Binder 1988) reaching the soma as more synapses were activated (Fig. 3-1). Given that the distribution of all synaptic inputs appears to be effectively similar (for discussion see ElBasiouny et al. 2005b), synaptic input from systems other than the Ia-afferents was simulated by increasing the synapse conductances to generate higher synaptic currents (over 100% of synaptic excitation), and this again resulted in a linear increase in the Ia I_N reaching the soma (Fig. 3-1).

3.2.4 Measurement of dendritic Ca^{+2} PIC and its conductance

While plateau potentials are commonly seen experimentally in a variety of motoneurons, their mode of activation and level of gradability have been difficult to assess. To address this question, simulations were run under three conditions: 1) during spike blockage; 2) under voltage-clamp conditions; and 3) during normal cell firing. For each condition, we systematically increased the level of synaptic activation (as described above) and then measured, from the soma, the somatic membrane potential, firing rate, and the leak-subtracted Ca^{+2} PIC as seen from the soma under voltage-clamp conditions (e.g. Fig. 3-3). We also calculated the average/filtered somatic membrane potential during firing by applying a low pass filter (LPF; corner frequency = 1 Hz) which effectively provides the level of somatic membrane potential without spikes, i.e. potential seen due to the slow Ca^{+2} PIC (e.g. Fig. 3-4B). The dendritic Ca^{+2} PIC flowing in the $Ca_V1.3$ channels of a dendritic compartment located 695.9 μm (0.52 λ) from the soma (e.g. Fig. 3-2A and 3-4D) and the dendritic membrane potential of the same compartment (e.g. Fig. 3-2A and 3-4C) were directly measured in the model. We also assessed the level of activation of the $Ca_V1.3$ channels by measuring the overall conductance of the $Ca_V1.3$ channels on the dendritic tree (G_{Ca}; e.g. Fig. 3-4E). This overall conductance was computed as follows:

$$G_{Ca} = 1/n \times \sum_{i=1}^{n} g_{Cai}$$

where n is the number of compartments that have the $Ca_V1.3$ channels, and g_{Cai} is the conductance of the $Ca_V1.3$ channels in compartment number i.

3.2.5 Enhancement of synaptic inputs

Enhancement of synaptic current by the Ca^{+2} PIC was examined under voltage-clamp conditions. The synaptic current was computed as the difference between the current-voltage (I-V) relationships during no synaptic activity and during synaptic excitation. At the resting membrane potential (-70 mV), the difference between the I-V relationships was called the 'hyperpolarized Ia I_N', and represented the raw synaptic current with no Ca^{+2} PIC activation. The difference between the I-V relationships was maximum near threshold (-55 mV). This was called the 'peak Ia I_N', and represented the synaptic current enhanced by the Ca^{+2} PIC (Lee and Heckman 2000). The difference between the peak Ia

I_N and hyperpolarized Ia I_N provided the amount of augmentation in synaptic current caused by the activation of Ca^{+2} PIC at different levels of synaptic excitation (e.g. Fig. 3-6D).

3.2.6 Summation of synaptic inputs

We investigated the influence of activating multiple synaptic inputs on the activation level of the Ca^{+2} PIC, and how these inputs summed. The cell was initially induced to fire with a bias current to produce a steady low background firing level. Two different approaches were used to activate the cell to obtain background firing: synaptic activation (Fig. 3-8A), and intracellular current injection at the soma as in Prather et al. (2001; Fig. 3-8D). Two additional synaptic inputs (test synaptic inputs, termed A and B) were then applied. The magnitude of the two test synaptic inputs A and B was increased incrementally. Summation was then investigated by comparing the change in firing rate (relative to background) evoked by the concurrent activation of the two test synaptic inputs to the linear sum of changes in firing rates evoked by the individual activation of each test synaptic input (following the methods of Prather et al. 2001). The change in firing rate was computed as the difference between the background firing rate and the *steady-state* firing rate during activation of the test synaptic inputs.

Synapses on the dendritic tree were divided into three groups to provide the small synaptic bias current and the two test synaptic inputs (A and B). Each group had a dendritic distribution similar to that of the Ia-afferent system. Synapses of each group were activated at 180 Hz in order to provide synaptic excitation as described earlier, and their conductance was sequentially increased to provide an increasing effective synaptic current at the soma.

3.3 RESULTS

The primary goal of this study was to investigate the nature of activation of the Ca^{+2} PIC, and assess its role in the generation of cell firing, and the enhancement and summation of synaptic inputs. Our previous simulation studies (ElBasiouny et al. 2005b) suggested that the $Ca_V1.3$ channels are primarily localized within the region of synaptic territory. This raised questions about the degree of dependence of Ca^{+2} PIC on the level of synaptic excitation, and whether Ca^{+2} PIC is activated in a graded or all-or-none manner. Furthermore, the resultant effect of PIC activation on synaptic current enhancement was in question.

3.3.1 Effective synaptic current

To address these questions, we systematically increased the level of synaptic excitation through Ia-afferent terminals by sequential activation of the Ia-synapses, as described in section 3.2. This synaptic input resulted in a linear increase in the Ia I_N reaching the soma as more synapses were activated (Fig. 3-1). The Ia I_N was measured with the somatic membrane potential clamped at -70 mV under voltage-clamp conditions, so that the PIC could not be activated, thus this current represents the raw synaptic current without activation of the Ca^{+2} PIC. Given that synaptic inputs from other systems appear to have a similar distribution to that of Ia-afferents (for discussion see ElBasiouny et al. 2005b), synaptic input up to 100% in Fig. 3-1 represented the input from the Ia-afferent system, whereas synaptic input over 100% represented the input from the many other presynaptic systems converging on motoneurons (Powers and Binder 2000).

3.3.2 Activation of the Ca^{+2} PIC during spike blockage

We first examined the activation of the Ca^{+2} PIC in the model with the sodium spikes blocked since real motoneurons have been extensively studied in the presence of sodium channel blockers, such as tetrodotoxin (TTX), (e.g. Hounsgaard and Kiehn 1989; Li and Bennett 2003), and the lidocaine derivative QX-314 (e.g. Lee and Heckman 1999). In current-clamp mode, we simultaneously measured the dendritic Ca^{+2} PIC, the somatic and dendritic membrane potential, and the overall conductance of the $Ca_V1.3$ channels

(G_{Ca}) at different levels of synaptic excitation (Fig. 3-2). $Ca_V1.3$ channels were found to be activated in two stages during increasing synaptic input. In the first stage, the channels were gradually activated in response to the level of synaptic excitation resulting in a gradual change in G_{Ca}, Ca^{+2} PIC and membrane potential (traces *a* to *b* in Fig. 3-2A and B). The range of voltage over which the grading occurred corresponded to the range of voltage in the I-V relationship that was subthreshold to when a negative slope region (NSR) occurred (i.e. membrane potentials < V_{on}). Once an adequate amount of synaptic excitation was reached, an all-or-none activation of the $Ca_V1.3$ channels took place, and resulted in a step increase in G_{Ca} (jump) and the generation of plateau potentials (see the jump from *b* to *c* in Fig. 3-2A and B). After that jump, G_{Ca} was saturated at its maximum value causing sustained depolarization in the membrane potential (plateau potentials; traces *c* to *d* in Fig. 3-2A and B). A minimum effective synaptic current of 5.4 nA was needed to trigger plateau potentials (vertical dashed line in Fig. 3-2B). Higher levels of synaptic excitation resulted in a faster activation of plateau potentials (Fig. 3-2A). The change in magnitude of G_{Ca} with respect to the increase in synaptic current showed an abrupt transition indicating an all-or-none activation of the Ca^{+2} PIC (Fig. 3-2B – lower graph). At the soma, this all-or-none activation corresponded to the jump in membrane potential from the 1st zero-slope point (V_{on}) on the I-V relationship to point *c* (in Fig. 3-2C) which allowed it to cross the unstable NSR created by the Ca^{+2} PIC (Schwindt and Crill 1977). In summary, without spiking an increasing synaptic input initially activates the Ca^{+2} PIC in a graded manner, followed by an all-or-none increase to a level at which the Ca^{+2} PIC becomes saturated. This results in all-or-none generation of plateau potentials.

3.3.3 Activation of the Ca^{+2} PIC under voltage-clamp conditions

We next investigated the mode of activation of the Ca^{+2} PIC under conditions where the spiking mechanism was unblocked, but the somatic membrane potential was controlled with a voltage-clamp at the soma. Such voltage-clamp has been extensively used to measure the PICs directly (e.g. Lee and Heckman 1998b), but is not equivalent to the physiological situation where the cell is free to fire. Two voltage-clamp commands are

usually used for experimental measurement of PICs: 1) long voltage pulses (1 second or more); and 2) a slow ramp voltage command. Long voltage pulses provide steady-state current responses, but require a relatively long time to obtain the recordings, whereas with a slow voltage ramp command (of slope around 4 mV/s) current measurements are relatively close to steady-state values and are obtained in a much shorter period. Figure 3-3A (upper graph) illustrates the difference between the I-V relationships obtained by using these two voltage commands in our model. With long voltage pulses, the activation threshold of the Ca^{+2} PIC was hyperpolarized by 2 mV, on average, from that measured during a ramp voltage command. Under these voltage-clamp conditions, $Ca_V1.3$ channels were found to be activated in a graded manner. In other words, with long voltage pulses of increasing amplitude steady-state current responses were obtained in the NSR of the I-V relationship (Fig. 3-3A – filled circles), and no abrupt activation of $Ca_V1.3$ channels occurred within that range. G_{Ca} and leak-subtracted Ca^{+2} PIC measurements from the model also showed incremental increases in magnitude within the NSR, and saturated afterwards (Fig. 3-3A – middle and lower graphs).

The graded activation of the Ca^{+2} PIC with increasing somatic voltage was maintained when a steady synaptic input was provided during the voltage-clamp simulations (*a* to *d* in Fig. 3-3B). When the steady synaptic input was gradually increased, the voltage threshold for activating the Ca^{+2} PIC from the soma gradually decreased (horizontal line in Fig. 3-3B), and the Ca^{+2} PIC amplitude at a given holding potential gradually increased (vertical line in Fig. 3-3B). The graded activation of Ca^{+2} PIC at a fixed potential occurred even when the membrane was in the unstable NSR of the steady-state I-V relationship. Correspondingly, the change in magnitude of G_{Ca} at different membrane potentials was always graded and no abrupt change in G_{Ca} occurred, further (Fig. 3-3C) suggesting that under voltage-clamp conditions, the Ca^{+2} PIC could remain partially activated by synaptic inputs, despite the presence of a NSR. In summary, when the somatic membrane is voltage-clamped at a given potential and the synaptic input is increased, the Ca^{+2} PIC is always activated in a graded manner even when the potential is in the NSR of the I-V relationship.

3.3.4 Activation of the Ca^{+2} PIC during normal cell firing

Activation of the Ca^{+2} PIC was then investigated under physiological conditions where the spike was not blocked and the cell was free to fire (with no current injected into the soma) in response to increasing synaptic input. We measured the magnitude of the dendritic Ca^{+2} PIC, dendritic G_{Ca}, cell firing rate, and membrane potential from the soma and a dendritic compartment at different levels of synaptic excitation applied for 2 seconds during normal firing (Fig. 3-4). The cell firing behavior was found to be greatly affected by the activation of the $Ca_V1.3$ channels. For a given level of synaptic excitation, the dendritic $Ca_V1.3$ channels were gradually activated (Fig. 3-4E) causing a gradual increase in the magnitude of the Ca^{+2} PIC (Fig. 3-4D) that resulted in subthreshold depolarization (Fig. 3-4B and C) and early acceleration of cell firing rate just after recruitment (Fig. 3-4A). Note that adaptation in firing rate is not seen at relatively high synaptic inputs due to the activation of the Ca^{+2} PIC which tends to increase the firing rate. Given that the Ia I_N for the Ia-afferent system is 4.8 nA and cell firing starts at 4.9 nA (100% in Fig. 3-4B), the Ia-afferent system on its own is barely able to recruit FR motoneurons, as expected (Bennett et al. 1998; Lee and Heckman 1998a; Powers and Binder 2000). Firing rates at synaptic excitation levels larger than 100% represent the effect of synaptic input from systems other than the Ia-afferents. Note that the relatively high firing rates seen in Fig. 3-4A are attributable to the fact that the modeled cell is an FR motoneuron.

The acceleration in cell firing rate (Fig. 3-4A) had a time course very similar to that of the increase in dendritic G_{Ca} (Fig. 3-4E) and experienced a slow increase over the initial 800 ms. Just prior to recruitment, the G_{Ca} began to increase sharply, but upon the onset of cell firing the rate of increase of G_{Ca} was abruptly decreased (indicated by the notches in Fig. 3-4E) due to the hyperpolarization of the membrane potential during the post spike AHPs. These AHPs effectively clamped the soma membrane potential below the firing threshold (similar to the effect of voltage-clamp described above). The clamping effect of the AHP on the somatic membrane potential was also evident in Fig. 3-4B as the filtered membrane potential was reduced upon the initiation of cell firing. The filtered potential

was obtained by low-pass filtering the membrane potential at 1 Hz to remove the spikes that do not affect the slow Ca^{+2} PIC.

To demonstrate that the AHP plays a critical role in clamping the potential below the firing level, hence limiting G_{Ca}, the effect of the AHP on cell firing was further examined by blocking the calcium-activated potassium channels (K(Ca)), which are responsible for the AHP, during simulations of synaptic activation (Fig. 3-5). In response to the same level of synaptic excitation (150%), steady-state firing rate was increased from 26.4 imp/s to 197 imp/s after blocking the K(Ca) channels (Fig. 3-5C). The acceleration in firing rate was also much faster after blocking the K(Ca) channels indicating that Ca^{+2} PIC was activated more rapidly than in the presence of the K(Ca) channels. This rapid and high activation of the Ca^{+2} PIC is also evident from the profile of G_{Ca} (Fig. 3-5D). After blocking the K(Ca) channels, G_{Ca} increased steeply upon recruitment and saturated at nearly 93% of its magnitude indicating full activation of the Ca^{+2} PIC, whereas before blocking the K(Ca) channels, G_{Ca} increased more gradually upon recruitment and saturated at only 40% of its magnitude indicating partial activation of the Ca^{+2} PIC. Thus, no graded activation of the Ca^{+2} PIC occurred when the K(Ca) channels were blocked. Furthermore, the filtered somatic membrane potential was -57.5 mV before blocking the K(Ca) channels and -44.5 mV after their blockage (Fig. 3-5E). The change in magnitude of G_{Ca} with respect to synaptic current before and after blocking the K(Ca) channels at different levels of synaptic excitation (from 14% to 400%) is shown in Fig. 3-5F. Before blocking the K(Ca) channels, gradual increase in G_{Ca} was obtained in response to increasing synaptic inputs indicating a graded activation of the Ca^{+2} PIC (Fig. 3-5F – triangles), whereas an abrupt transition in G_{Ca} was obtained after blocking the K(Ca) channels indicating an all-or-none activation of the Ca^{+2} PIC (Fig. 3-5F - circles). This all-or-none activation of the Ca^{+2} PIC occurred exactly upon cell recruitment (compare Fig. 3-5F to 3-6B where cell recruitment took place at 5 nA). These results demonstrate that the AHP serves a critical role in maintaining (clamping) the membrane potential below the firing level, and preventing the Ca^{+2} PIC from being activated in an all-on-none manner. The conductance of the dendritic $Ca_V1.3$ channels (G_{Ca}) is voltage-

dependent. Therefore, the induced reduction in membrane potential during the AHP reduces G_{Ca}, hence, limiting the activation of the Ca^{+2} PIC. On the other hand, the increase in spike threshold with firing allows gradual activation of the Ca^{+2} PIC until it eventually reaches its saturation level (not illustrated).

To further investigate the mode of activation of the Ca^{+2} PIC during normal firing behavior, the input-output F-I relationship (synaptic F-I relationship) was obtained by plotting the steady-state firing rate responses of Fig. 3-4A against the effective synaptic current (hyperpolarized Ia I_N; Fig. 3-6A) and compared to the dendritic G_{Ca} profile (Fig. 3-6B). Prior to cell recruitment, the dendritic G_{Ca} gradually increased with increasing synaptic input (Fig. 3-6B). Acceleration in the rate of increase in G_{Ca} with synaptic current was seen just before recruitment reflecting the increase in magnitude of the Ca^{+2} PIC relative to that of the leak current in the voltage range before the NSR on the I-V relationship (Fig. 3-2C). Upon the onset of cell firing, the rate of increase of G_{Ca} was abruptly decreased (notch in Fig. 3-6B) due to the clamping effect of the AHP. This effect of the AHP prevented an all-or-none jump in the magnitude of G_{Ca} (as shown in Fig. 3-5F - circles) and instead forced the G_{Ca} (dendritic Ca^{+2} PIC) to be graded with increasing synaptic input (region denoted by *s* in Fig 6B). This graded increase in the Ca^{+2} PIC in response to incremental increases in the effective synaptic current resulted in a relatively steep increase in the firing rate (gain = 6 imp.s^{-1}/nA), coinciding with what is classically termed the secondary range of the F-I relation (denoted by *s* in Fig. 3-6A; Kernell 1965a,b). Additional synaptic input caused the G_{Ca} to saturate near its maximal value leading to full activation of the dendritic Ca^{+2} PIC (region denoted by *t* in Fig. 3-6B). Because of the saturated Ca^{+2} PIC, the firing rate increased more slowly with increasing synaptic current in the region classically termed the tertiary range of the F-I relationship (slope 2.6 imp.s^{-1}/nA; denoted by *t* range of Fig. 3-6A). The tertiary range had a lower gain (slope) both because of the lack of increase in the Ca^{+2} PIC, and because the added conductance of the $Ca_V1.3$ channels resulted in a reduction in the cell input resistance, thus additional synaptic input produced a smaller increase in firing rate. This firing behavior (synaptic F-I relation) closely matches that seen experimentally in spinal

motoneurons when activated synaptically as opposed to being activated through intracellular current injection (Fig. 7 in Heckman et al. 2005).

In summary, during normal firing behavior, an increasing synaptic input initially activates the Ca^{+2} PIC in a graded manner, followed by a saturation range in which the Ca^{+2} PIC is fully activated. These distinct modes of activation lead to the secondary and tertiary firing ranges, respectively, in the synaptic F-I relationship. Due to the clamping of the membrane potential by the AHP during cell firing, no all-or-none activation of the Ca^{+2} PIC takes place.

3.3.5 Intracellular versus synaptic activation

The activation of the Ca^{+2} PIC was compared during somatic intracellular current injection to that during synaptic activation. In Figure 3-7A, the F-I relationship was obtained under two conditions: intracellular injection of a slow triangular current ramp at the soma (triangles), and synaptic activation (circles). The level of activation of the $Ca_V1.3$ channels during these conditions is expressed by the G_{Ca} profile in Fig. 3-7B. With intracellular current injection, the F-I relationship exhibited the three classical ranges of firing rates: primary, secondary, and a tertiary range. In the primary range (denoted by *p* in Fig. 3-7A and B), there was low activation of the Ca^{+2} PIC indicated by the low magnitude of G_{Ca} in Fig. 3-7B. Further current injection gradually activated the Ca^{+2} PIC, indicated by the increased level of G_{Ca} in the secondary range (denoted by *s* with triangles in Fig. 3-7A and B). This increased activation of the Ca^{+2} PIC led to the steep increase in cell firing seen during the secondary range of the F-I relationship. At higher levels of current injection, Ca^{+2} PIC was fully activated, indicated by the saturation in G_{Ca}, during the tertiary range (denoted by *t* with triangles in Fig. 3-7A and B). Saturation of the Ca^{+2} PIC resulted in the reduced firing rate seen during the tertiary range of the F-I relationship. In contrast, with synaptic activation, the F-I relationship exhibited only secondary and tertiary ranges (denoted by *s* and *t* with circles in Fig. 3-7A and B). The Ca^{+2} PIC was always activated before cell recruitment, thus no primary range was seen in the synaptic F-I relationship. Note that the slight mismatch between the firing behavior and G_{Ca} (in Fig. 3-7A and B) is due to the fact that only one synaptic input (Ia-

afferent system) is represented in the model. Activation of the $Ca_V1.3$ channels is proportional to the proximity of these channels to the Ia-synapses. Given that the depolarization provided by this system is inadequate to activate all the $Ca_V1.3$ channels, the average G_{Ca} underestimates the conductance of those channels actually activated by the synaptic input and results in the seen mismatch.

The threshold for activating plateau potentials with somatic intracellular current injection was compared to that with synaptic excitation. Plateau potentials were activated at lower current and voltage thresholds with synaptic excitation alone than with intracellular current injection alone. Synaptic excitation that provided an effective synaptic current of 5.4 nA was able to activate plateau potentials, while a somatic intracellular long current pulse of 8 nA was needed to activate them (compare the vertical dashed line in Fig. 3-2B to that in Fig. 3-7C). Furthermore, the somatic voltage threshold at which plateau potentials were activated by synaptic excitation alone (-60 mV) was lower than that with intracellular current injection alone (-56 mV, compare the horizontal dashed line in Fig. 3-2B to that in Fig. 3-7C).

3.3.6 Enhancement of synaptic current

Enhancement of synaptic current by the added PIC and its resultant effect on the motoneuron firing rate was previously investigated in many studies; however, discrepancies in reports between variable (Hultborn et al. 2003) and constant (Prather et al. 2001) enhancement of synaptic current are seen. In this section, we examined enhancement of synaptic current by the Ca^{+2} PIC, and explained it based on the distinct modes of activation of the Ca^{+2} PIC. Simulations were run under voltage-clamp conditions at different levels of synaptic excitation. For each level of steady Ia-synaptic excitation, the synaptic current was computed as the difference between the I-V relationships during no synaptic activity and during synaptic excitation (Lee and Heckman 2000). The hyperpolarized Ia I_N represented the synaptic input unaugmented by the Ca^{+2} PIC, whereas the peak Ia I_N included the activation of the Ca^{+2} PIC and the hyperpolarized Ia I_N (Fig. 3-6C). The difference between the peak Ia I_N and

hyperpolarized Ia I_N represented the amount of augmentation in synaptic current (synaptic enhancement) caused by the activation of the Ca^{+2} PIC at different levels of synaptic excitation (Fig. 3-6D). Before cell recruitment, the Ca^{+2} PIC was activated in a graded manner and resulted in a linear enhancement of synaptic current in proportion to the level of synaptic excitation (from 14% to 100% of synaptic excitation; slope = 1.3, r^2=0.97 for the left regression line in Fig. 3-6D). Upon cell recruitment, activation of the Ca^{+2} PIC was limited by the clamping effect of the AHP and resulted in a shallower linear enhancement of synaptic current during the secondary range of the synaptic F-I relationship (from 100% to 200% of synaptic excitation; slope = 0.26, r^2=0.96 for the middle regression line in Fig. 3-6D). During the tertiary range, the Ca^{+2} PIC was saturated and resulted in a constant enhancement of synaptic current (for synaptic excitation >200%; slope = -0.016, r^2=0.33 for the right regression line in Fig. 3-6D).

3.3.7 Summation of synaptic inputs

Activation of the Ca^{+2} PIC by multiple synaptic inputs and its effect on summation of these inputs was also investigated. The cell was initially activated with a bias current to achieve a low background firing level. Two additional test synaptic inputs (A and B) with incremental strengths were then applied and changes in firing rate relative to the background firing rate were computed. The change in steady-state firing rate evoked from the concurrent activation of the two test synaptic inputs (A&B) was compared to the linear sum of changes in steady-state firing rates evoked from the individual activation of each test synaptic input (A+B). Two different methods were used to activate the cell to provide background cell firing: synaptic activation (Fig. 3-8A), and intracellular current injection at the soma (Fig. 3-8D). Figure 3-8B shows the F-I relationship obtained by simultaneous application of the synaptic bias current and the two test synaptic inputs, and figure 3-8C compares the changes in firing rate evoked by the concurrent activation of the two test synaptic inputs to the linear sum of their individual changes in firing rate. When the test synaptic inputs A and B individually caused the cell to fire in the secondary range, and their concurrent activation caused the cell to also fire in the secondary range (conditions *1* and *2* in Fig. 3-8B), summation of synaptic inputs was nearly equal to their linear sum (Fig. 3-8C; condition *1&2*). When either test synaptic

input A or B caused the cell to fire in the secondary range, but their concurrent activation caused the cell to fire in the tertiary range (conditions *2* and *3* in Fig. 3-8B), or when the test synaptic inputs A and B individually caused the cell to fire in the tertiary range (conditions *4* and *5* in Fig. 3-8B), summation of synaptic inputs was less-than their linear sum (Fig. 3-8C; conditions *2&3* and *4&5*). Less-than linear summation resulted from the full activation of the Ca^{+2} PIC leading to a tertiary range of shallower gain. Therefore, linear summation is seen at moderate firing rates that correspond to the range of graded activation of the Ca^{+2} PIC, whereas less-than linear summation is seen at relatively high firing rates that correspond to the saturation of the Ca^{+2} PIC.

Given that it is often difficult experimentally to induce a cell to fire throughout its range of firing with synaptic inputs alone, intracellular current injection at the soma was the experimentally used method for obtaining the background firing in studying synaptic summation in real motoneurons (e.g. Powers and Binder 2000; Prather et al. 2001). We thus also simulated this approach by injecting an intracellular bias current at the soma, followed by activation of the test synaptic inputs (Fig. 3-8D). With somatically injected bias current, the F-I relationship obtained from subsequent synaptic inputs was shifted to the right. More importantly the firing ranges were shifted upwards (secondary range occurred are higher rates) due to the greater difficulty in activating PICs from the soma compared to the dendrites, and a primary range emerged (Fig. 3-8E) as a by-product of this intracellular current injection. When either test synaptic input A or B was weak relative to the bias current thus causing the cell to fire in its primary range, but the concurrent activation of A and B caused the cell to fire in the secondary range (conditions *1* and *2* in Fig. 3-8E), summation of synaptic inputs was greater-than their linear sum. However, during the secondary and tertiary firing ranges of the F-I relationship, linear and less-than linear summation occurred, respectively (Fig. 3-8E). In Figure 3-8F, greater-than linear summation is seen at relatively low firing rates that correspond to the range before activation of the Ca^{+2} PIC, whereas less-than linear summation is seen at relatively high firing rates that correspond to the saturation of the Ca^{+2} PIC. Similar results were obtained when different magnitudes (10 nA and 12 nA) of intracellular bias current were used (Fig. 3-8F – filled circles and open squares, respectively).

3.4 DISCUSSION

3.4.1 Model predicts that dendritic PIC has a graded followed by saturated activation with increasing synaptic current

Discrepancies in experimental reports regarding the behavior of PICs make it difficult to infer their mode of activation and whether it is graded or all-or-none (see Hultborn et al. 2003; Lee et al. 2003). Disparities in the role of PICs in the enhancement and summation of synaptic inputs are also reported (Powers and Binder 2000; Prather et al. 2001; Hultborn et al. 2003). However, direct measurements of the dendritic PIC during synaptically-evoked firing to resolve these discrepancies, as we have done with our simulations, is experimentally unfeasible in real motoneurons for the following reasons: 1) it is difficult to record directly from the very small and extensive dendrites of a motoneuron; 2) it is difficult to activate sufficient numbers of synaptic inputs to activate the cell fully; and 3) the net Ca^{+2} PIC seen at the soma, which is feasible to measure under voltage-clamp, cannot be measured during natural cell firing. Thus, computer simulations were used in the present study to examine the mode of activation of the dendritic Ca^{+2} PIC during cell firing, and to elucidate its role in the enhancement and summation of synaptic inputs. Our modeling results suggest that under physiological conditions (i.e. when the cell is free to fire) an increasing synaptic input does *not* lead to an all-or-none activation of the dendritic Ca^{+2} PIC, even when steady-state responses to increasing synaptic steps are evaluated (Fig. 3-6B). Instead, the level of activation of the dendritic Ca^{+2} PIC is initially graded with increasing synaptic input until it reaches its saturation level, after which further increases in synaptic input cause minimal changes in the Ca^{+2} PIC. The range of graded activation of the Ca^{+2} PIC corresponds to the secondary range of firing (in the synaptic F-I relationship), and the range of saturated activation of the Ca^{+2} PIC corresponds to the tertiary range of firing. The results of our simulations provided an explanation for the process of dendritic Ca^{+2} PIC activation during cell firing. It also helped in resolving the discrepancies in previous experimental reports regarding the enhancement and integration of synaptic inputs, as described below.

Previous experimental measurements from rat motoneurons suggest that the secondary and tertiary ranges of firing are indeed caused by the dendritic Ca^{+2} PIC since these ranges are eliminated when the LVA L-type Ca^{+2} channels are blocked by nimodipine, leaving only a primary range (Li et al. 2004; Heckman et al. 2005). The graded activation of the Ca^{+2} PIC in the secondary range, as opposed to an all-or-none Ca^{+2} PIC activation, occurs as a result of the AHP forcing (effectively clamping) the membrane potential to remain below the firing level throughout the interspike interval. The AHP's effect on limiting the activation of the PIC has been previously proposed (Hounsgaard and Mintz 1988; Koch 1999; Li et al. 2004), but was directly confirmed in the present study by demonstrating that the all-or-none activation of the Ca^{+2} PIC for an increasing synaptic input occurs when the K(Ca) channels mediating the AHP are blocked (Fig. 3-5) or when the spikes are themselves blocked (Fig. 3-2; compare to the QX-314 data of Lee and Heckman 1999 in cat motoneurons, the TTX data of Hounsgaard and Kiehn 1989 in turtle motoneurons, and Li and Bennett 2003 in rat motoneurons). The role of the AHP in limiting the activation of the PIC could be confirmed experimentally by examining the effect of apamin (a specific SK channel blocker) on cell firing during current-clamp. Furthermore, a similar graded activation of the Ca^{+2} PIC occurs when the motoneuron is voltage-clamped (Fig. 3-3; also similar to voltage-clamp data of Lee and Heckman 1998b in cat motoneurons, Svirskis and Hounsgaard 1998 in turtle motoneurons, and Li and Bennett 2003 in rat motoneurons). Because the firing threshold gradually increases with firing rate (Schwindt and Crill 1982), the PIC becomes gradually activated as the firing rate increases in the secondary range until saturation is reached (tertiary range).

3.4.2 Experimental data supporting graded Ca^{+2} PIC activation followed by saturation

We reexamined previously published *experimental* data for rat motoneurons during current- and voltage-clamp experiments to verify the activation ranges of the Ca^{+2} PIC (data adapted from Fig. 2B and C in Li et al. 2004). The average somatic membrane potential during firing was used as the common factor for relating the experimentally-measured firing rate evoked during current-clamp to the Ca^{+2} PIC measured during the voltage-clamp experiment (Fig. 3-9). During the ascending segment of the current ramp command, the primary range of cell firing was found to correspond to the range

preceding the activation of the Ca^{+2} PIC (left range 1, green range, in Fig. 3-9). During the secondary range of cell firing, the Ca^{+2} PIC corresponded to the NSR of the I-V relationship (left range 2, left purple range, in Fig. 3-9). Activation of the Ca^{+2} PIC was graded in this region because the slope of the F-I relationship, though relatively steep, was far from vertical. Increasing current caused an increase in firing rate, further depolarization of the cell membrane and further activation of the Ca^{+2} PIC (grading). The graded or partial activation of the Ca^{+2} PIC within this range is likely due to the clamping effect of the AHP described earlier. The tertiary range, on the other hand, corresponded to the range during which the Ca^{+2} PIC was fully activated (left range 3, left blue range, in Fig. 3-9), and minimal PIC grading took place in this range. The tertiary range was maintained until the cell was nearly de-recruited on the descending segment of the current ramp command (right range 3, right blue range, in Fig. 3-9) due to the hysteresis in the Ca^{+2} PIC. Thus, it is interesting to note that *no PIC grading* occurs through most of the range of firing frequencies during the down voltage ramp.

The finding that Ca^{+2} PIC can be graded, for at least a short duration following cell recruitment (in the secondary range; Fig. 3-6A and B), has additional support in a number of experimental observations which are summarized as follows: 1) Graded synaptic activation provided by muscle stretch causes a gradual increase in firing rate. This is then followed by a shallower tertiary range during which firing rate increases only slightly with synaptic current (Heckman et al. 2005; Lee et al. 2003). 2) The steady-state firing of the secondary range has been shown to be mediated by the activation of the Ca^{+2} PIC in motoneurons (Schwindt and Crill 1982; Li et al. 2004). Moreover, Kernell (1965b) and Schwindt and Crill (1982) have shown that steady-state firing is possible in the middle of the secondary range; thus, stable partial activation of the Ca^{+2} PIC is obtainable, consistent with the concept of graded activation of the Ca^{+2} PIC in this range. 3) Voltage-dependent enhancement of synaptic current is found to be a smooth function of the holding potential (Lee and Heckman 2000). 4) Under voltage-clamp conditions, stretch-evoked synaptic current is usually graded despite the rapid acceleration in firing rate sometimes seen under unclamped conditions (Lee et al. 2003). 5) Synaptic input provided by muscle stretch causes a graded increase in firing rate prior to saturation (Lee et al.

2003). 6) Graded (variable) amplification of firing rates is seen in decerebrate cat motoneurons in response to brief intermittent synaptic activation (Hultborn et al. 2003). Conversely, all-or-none activation of plateau potentials seen in current-clamp experiments when the spikes are blocked is likely due to the absence of the AHP, which limits the activation of the PIC as shown in the present study (Fig. 3-2).

Previous experimental recordings from human motor units also support an initially graded PIC activation followed by saturation. During increasing contractions, recordings from high threshold motor units (Romaiguere et al. 1989) showed a steep increase in firing rate after recruitment, in what appeared to be a fairly long and stable secondary range of firing (as in our Fig. 3-6A). Following this, further increases in contraction produced a lesser increase in firing rate, in what appeared to be the shallower tertiary range. This behavior is consistent with the graded activation of the Ca^{+2} PIC in the secondary range, followed by its saturation in the tertiary range, as seen from the simulations in the present study.

3.4.3 Exceptions, where all-or-none PIC activation may occur

In low threshold human motor units (Romaiguere et al. 1989; Gorassini et al. 2002) as well as in many rat motor units (Bennett et al. 2001), firing accelerates only over the first few spikes after recruitment, if at all, during a slowly increasing contraction. Following that, the firing rate increases slowly in what appears to be the tertiary range. The brief acceleration in firing at recruitment does not vary with the speed of the synaptic input (or rate of rise of contraction as in Romaiguere et al. 1989), and is thus probably due to the subthreshold activation of a large Ca^{+2} PIC in an all-or-none manner due to the absence of the AHP. Shortly after cell recruitment the Ca^{+2} PIC is saturated, and firing occurs in the tertiary range. A similar behavior in which cells fire in their tertiary range shortly after recruitment is also seen in many rat motoneurons when activated with intracellular current injection (Li et al. 2004). No extensive secondary range occurs in these cells because the Ca^{+2} PIC is mostly activated at recruitment; however, the Ca^{+2} PIC still helps in recruiting these cells and maintaining firing (enabling self-sustained firing; Li et al. 2004).

Although unusual, some cat motoneurons occasionally have an abrupt increase in firing rate in response to muscle stretch that occurs somewhat *after* recruitment, unlike the motoneurons just described (Hounsgaard et al. 1988; Lee et al. 2003). This behavior appears to be unstable as it occurs only on some stretches, and suggests an all-or-none activation of the PIC during cell firing (Lee et al. 2003). If this were the case, the magnitude of the Ca^{+2} PIC must be very large in these motoneurons and activated in distal dendritic regions that are not easily affected by the clamping effect of the AHP associated with cell firing.

3.4.4 Enhancement of synaptic current

Previous experimental and modeling studies showed that the amount of synaptic current from various presynaptic systems is inadequate to cause the cell firing levels seen during natural motor activity (Powers and Binder 1995, 2001; Rose and Cushing 1999). Later, it was shown experimentally that activation of PICs enhances the synaptic input to motoneurons and results in the observed amplified firing behavior (Bennett et al. 1998; Lee and Heckman 2000; Prather et al. 2001; Hultborn et al. 2003; Lee et al. 2003). Our simulations suggest that during the graded activation of the Ca^{+2} PIC, the enhancement of synaptic input is linearly graded in proportion to the level of synaptic excitation, whereas following the saturation of the Ca^{+2} PIC, the enhancement of synaptic input is constant.

These results could provide an explanation to the discrepancy in reports regarding the magnitude of enhancement of synaptic currents by Ca^{+2} PIC. In a study by Hultborn et al. (2003) experimental recordings obtained from decerebrate cat motoneurons showed graded (variable) enhancement of synaptic inputs as the PIC was activated. This graded enhancement of synaptic inputs may be due to the relatively small injected and synaptic inputs used to activate the cell, and could have resulted in partial activation of the PIC causing the cell to fire in the secondary range of the F-I relationship. This is comparable to the range of graded Ca^{+2} PIC activation that shows linear enhancement of synaptic inputs in our results. In contrast, Prather et al. (2001) reported constant enhancement of synaptic inputs by the PIC (indicated by a vertical shift in the F-I relationship relative to

that predicted when the synaptic input was applied) also from decerebrate cat motoneurons. The constant enhancement of synaptic inputs may be due to the relatively high current injections (up to 40 nA) used to activate the motoneurons in that study, which result in full activation of the PIC and cause the cell to fire mostly in the tertiary range of the F-I relationship. This is comparable to the range of saturated Ca^{+2} PIC activation that shows constant enhancement of synaptic inputs in the present study.

3.4.5 Intracellular versus synaptic activation

Our simulations demonstrate that motoneuron activation through synaptic excitation is different from that seen through somatic current injection, which has also been shown in previous studies (Kernell 1965c; Shapovalov 1972; Brownstone et al. 1992; Bennett et al. 1998). Synaptic excitation is more efficient in exciting the motoneuron and triggering the plateau potentials than intracellular current injection. With synaptic excitation, membrane depolarization is initiated in the dendritic tree where the $Ca_V1.3$ channels are located, and then spreads to the soma and IS and causes the cell to fire. Somatic current injection, on the other hand, initiates the membrane depolarization at the soma and directly triggers cell firing without PIC activation (Fig. 3-7B and C). Membrane depolarization then spreads from the soma to the dendritic tree opposite to the natural mode of activating motoneurons. Therefore, a primary range of firing with little Ca^{+2} PIC activation is seen in the current injected F-I relationship (Heckman et al. 2005). This primary range is a by-product of injecting current into the soma (Bennett et al. 1998; Heckman et al. 2005).

3.4.6 Summation of synaptic inputs

Our modeling results can also provide an explanation to the discrepancy in reports regarding the summation of synaptic inputs in motoneurons in which greater-than (Powers and Binder 2000), less-than (Kuno and Miyahara 1969), and linear summation (Burke 1967; Prather et al. 2001) are reported. Our results suggest that under physiological conditions, in which the motoneuron is activated synaptically, no greater-than linear summation takes place. Instead, linear summation of synaptic inputs occurs during the graded phase of the Ca^{+2} PIC (during the secondary range of the F-I relationship), and less-than linear summation occurs during the saturation phase of the

Ca^{+2} PIC (during the tertiary range of the F-I relationship). Linear summation results from the existence of stable partial activation states of the PIC, while less-than linear summation results when the PIC is fully activated by synaptic inputs. We have shown that greater-than linear summation observed experimentally in previous studies (e.g. Powers and Binder 2000; Prather et al. 2001) is likely due to using intracellular current injection in these experiments to produce background cell firing prior to applying the synaptic inputs. This somatic intracellular current enables the formation of a primary range of firing, not seen with synaptic input, and when subsequent synaptic inputs produce a transition of cell firing from the primary range to the secondary range greater-than-linear summation occurs.

3.4.7 Model considerations

One could argue that saturation of the PIC is expected from a current whose steady-state activation is described by a Boltzmann function. Any ionic current that has no inactivation, like the Ca^{+2} PIC, will reach saturation when the membrane potential is sufficiently depolarized to have the underlying channels fully open. However, the question investigated in the present study is whether the PIC is activated in a graded or an all-or-none manner until it reaches its saturation level. We demonstrated that the graded activation of the Ca^{+2} PIC during cell firing is due to the clamping effect of the AHP on membrane potential. This was confirmed when an all-or-none activation of the Ca^{+2} PIC was seen during the blockade of the AHP either directly by blocking the K(Ca) channels (Fig. 3-5) or indirectly by blocking the spikes (Fig. 3-2). Moreover, the graded activation of the Ca^{+2} PIC had different slopes before and after the onset of cell firing, which cannot be described by a Boltzmann function (Fig. 3-6B).

In the present study we used a compartmental model for an FR motoneuron to study the mode of activation of the dendritic Ca^{+2} PIC. However, our results could be extended to other types of motoneurons (S- and FF-types) and neuronal cells. A probable difference in S-type motoneurons is that the Ca^{+2} PIC will be activated at a lower threshold (Bennett et al. 1998) and the secondary range of cell firing with synaptic activation will be shorter.

3.4.8 Concluding remarks

In summary, computer simulations in the present study allowed direct assessment of the dendritic Ca^{+2} PIC during synaptically-evoked cell firing. This helped in elucidating the nature of activation of the Ca^{+2} PIC and in resolving the discrepancies in previous reports regarding this question. It also allowed for the reconciliation of several conflicting experimental results on the role of PICs in the enhancement and integration of synaptic inputs.

3.5 FIGURES

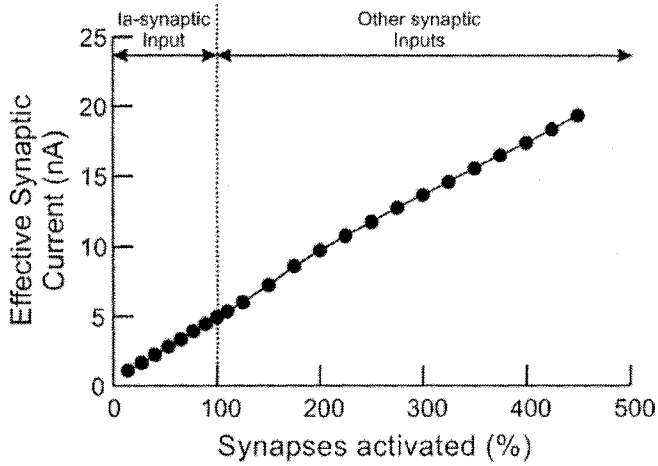

Figure 3-1. Effective synaptic current reaching the soma at different levels of synaptic excitation. Sequential activation of a larger number of Ia-synaptic groups resulted in a linear increase in the effective synaptic current reaching the soma. Synapses activated above 100% represent inputs from systems other than the Ia-afferent system.

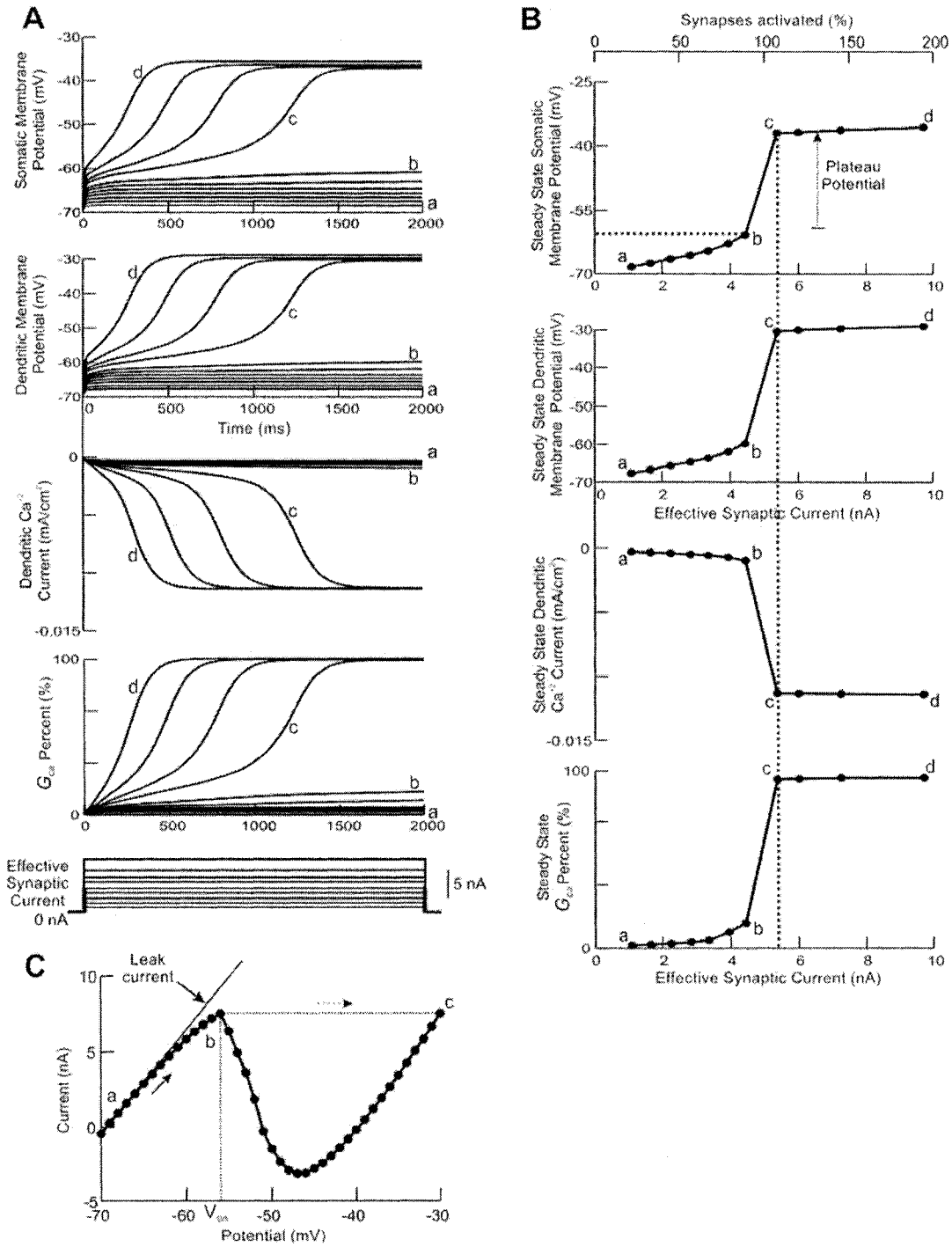

Figure 3-2. Direct measurements from the soma and a dendritic compartment during spike blockage at different levels of synaptic excitation. **A**: Simultaneous measurements from the model of the somatic (upper graph) and dendritic (2nd graph) membrane

potentials, dendritic Ca^{+2} PIC (3rd graph), and G_{Ca} (lower graph) at different levels of synaptic excitation. Traces show the responses for 14% to 200% in an ascending order of level of synaptic excitation (14%, 27%, 40%. 53%, 65%, 77%, 89%, 110%, 125%, 150%, and 200%). *a*, *b*, *c*, and *d* show the responses at 14%, 89%, 110%, and 200% of synaptic excitation, respectively. **B**: Steady state responses, measured at the end of a 2 second period of synaptic excitation in the traces shown in **A**, are plotted as a function of synaptic excitation level. The top axis shows the percent of activated synapses at each level. Vertical dashed line shows the current level at which plateau potentials were triggered by synaptic excitation, which is equal to 5.4 nA. Horizontal dashed line shows the voltage threshold at which plateau potentials were triggered by graded synaptic excitation alone, which is equal to -60 mV. **C**: Steady-state I-V relationship at the soma with a NSR created by the Ca^{+2} PIC. Thin solid line shows the leak current. Vertical dashed line shows the 1st zero-slope point, or the onset potential (V_{on}) of the Ca^{+2} PIC. Solid arrow shows the direction of change in somatic current for an increasing level of membrane potential. Dashed arrow shows the jump in membrane potential to cross the NSR.

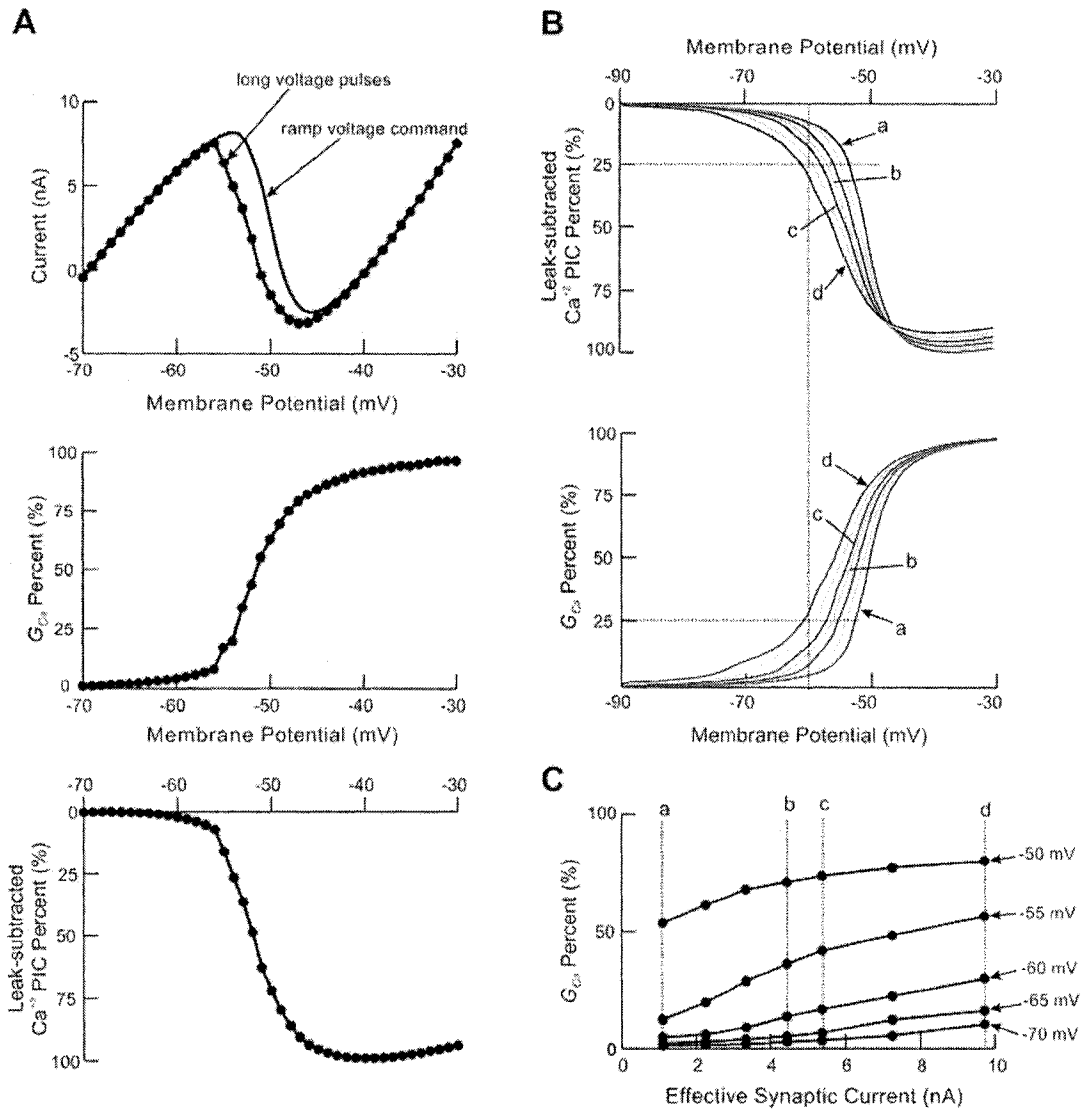

Figure 3-3. Measurements from the soma under voltage-clamp conditions for different levels of synaptic excitation. **A**: Comparison of I-V relationships (upper graph) obtained by using a ramp voltage command (solid line) and long voltage pulses (filled circles) with no synaptic activation. G_{Ca} (middle graph) and leak-subtracted Ca^{+2} PIC (lower graph) normalized to their peak values measured during long voltage pulses. **B**: Leak-subtracted Ca^{+2} PIC (upper graph) and G_{Ca} (lower graph) normalized to their peak values measured from the model during the ascending phase of the ramp voltage-clamp command at different levels of synaptic excitation. The horizontal and vertical dashed lines show the graded decrease in the PIC somatic activation threshold and graded increase in the

amplitude of Ca^{+2} PIC, respectively, as more synapses are activated. *a*, *b*, *c* and *d* are as defined in Fig. 3-2A. **C**: The change in magnitude of G_{Ca} with respect to synaptic current at different membrane potentials (-50 mV to -70 mV) under voltage-clamp conditions in **B**.

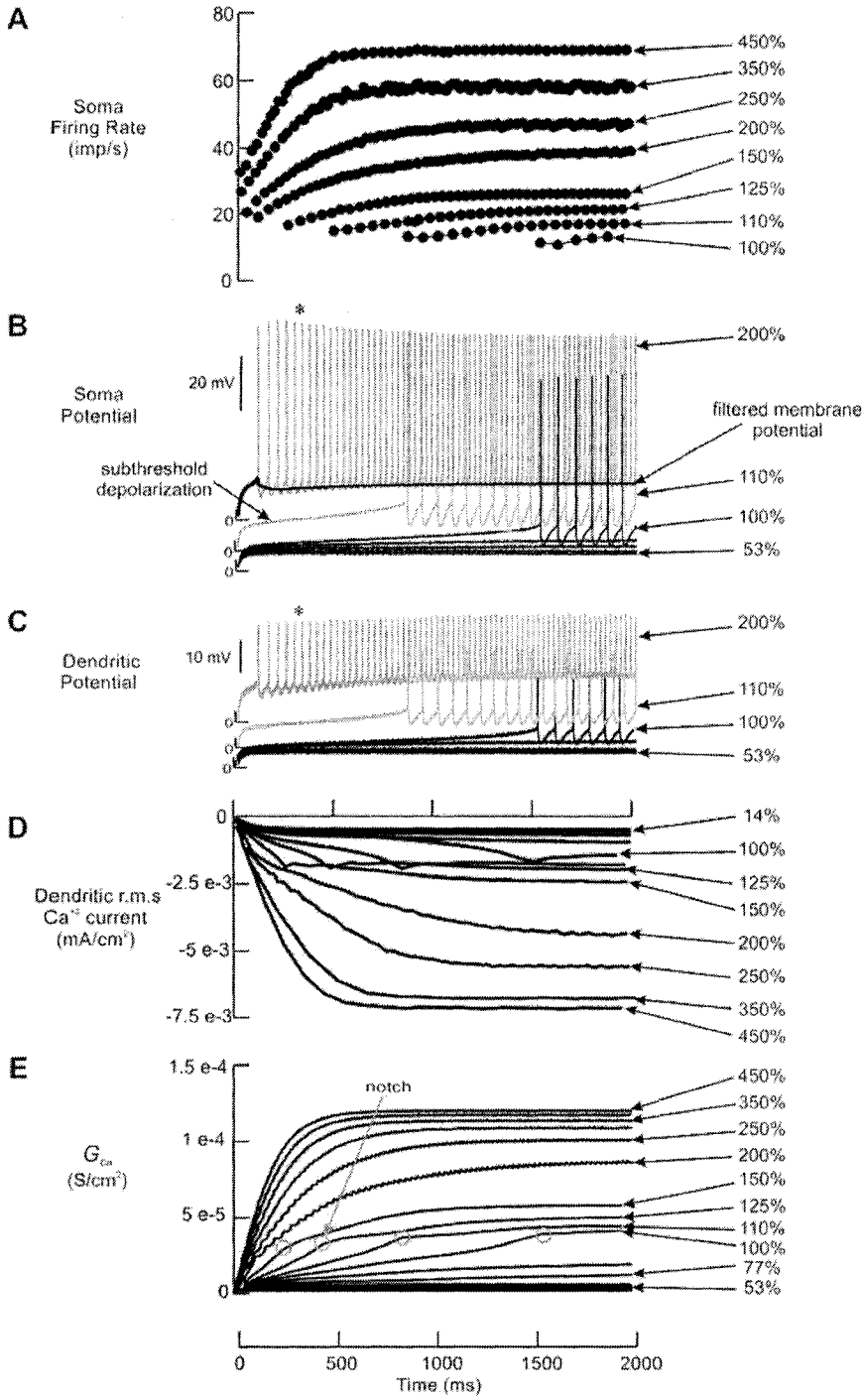

Figure 3-4. Measurements from the soma and a dendritic compartment during cell firing at different levels of synaptic excitation. For each level of synaptic excitation, the recordings show the soma firing rate (**A**), soma spikes (**B**), dendritic spikes measured

from a dendritic compartment located at 695.9 μm (0.52 λ) from the soma (**C**), dendritic root mean square Ca^{+2} current measured from the same dendritic compartment (**D**), G_{Ca} (**E**). *: traces are shifted up for clearer display and avoidance of overlap. Gray circles (notches) show the abrupt change in G_{Ca} upon firing onset. Thick black line in **B** shows the filtered somatic membrane potential during cell firing.

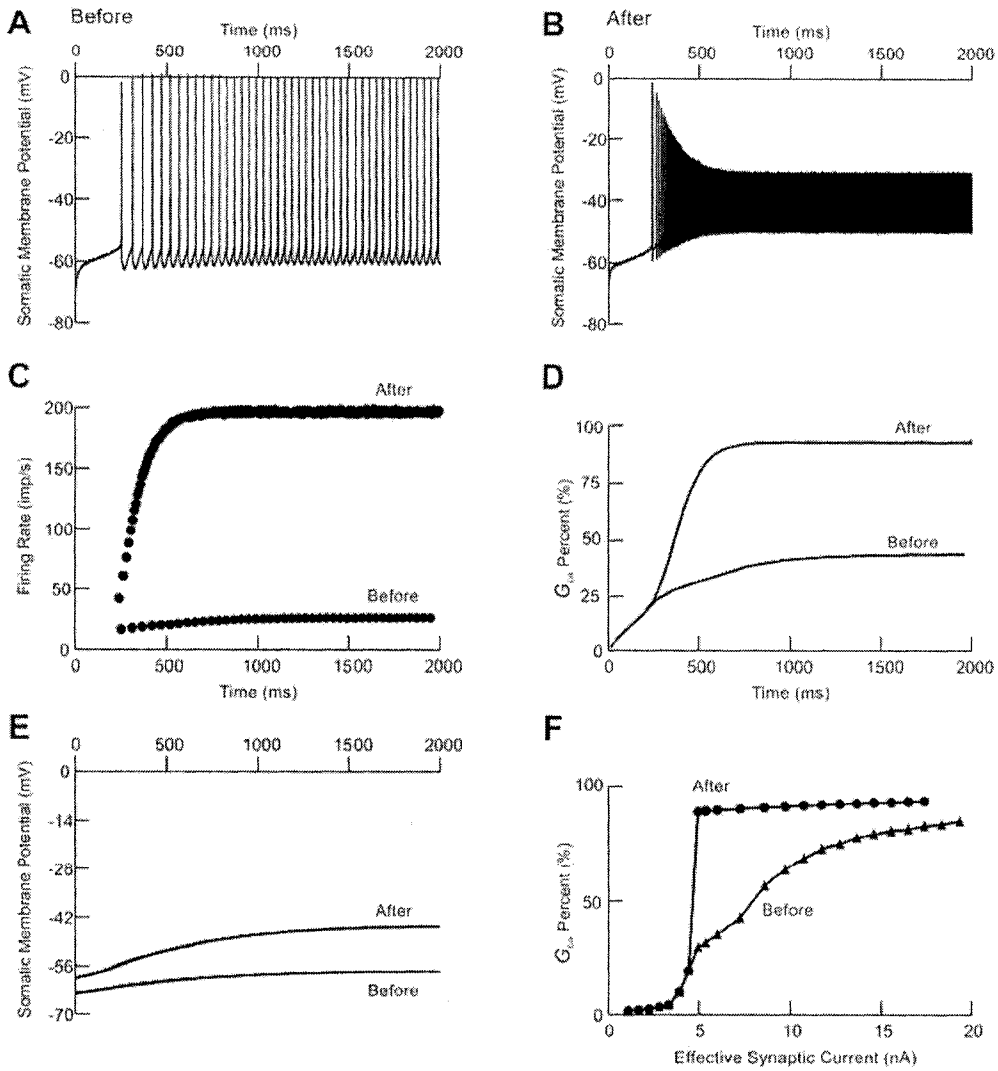

Figure 3-5. Effect of the AHP on the activation of the Ca^{+2} PIC. Somatic spikes before (**A**) and after (**B**) blocking the K(Ca) channels, cell firing rate (**C**), relative magnitude of G_{Ca} (**D**), and the filtered somatic membrane potential (**E**) in response to 150% of synaptic excitation. **F**: The change in magnitude of G_{Ca} with respect to synaptic current before and after blocking the K(Ca) channels at different levels of synaptic excitation (from 14% to 400%).

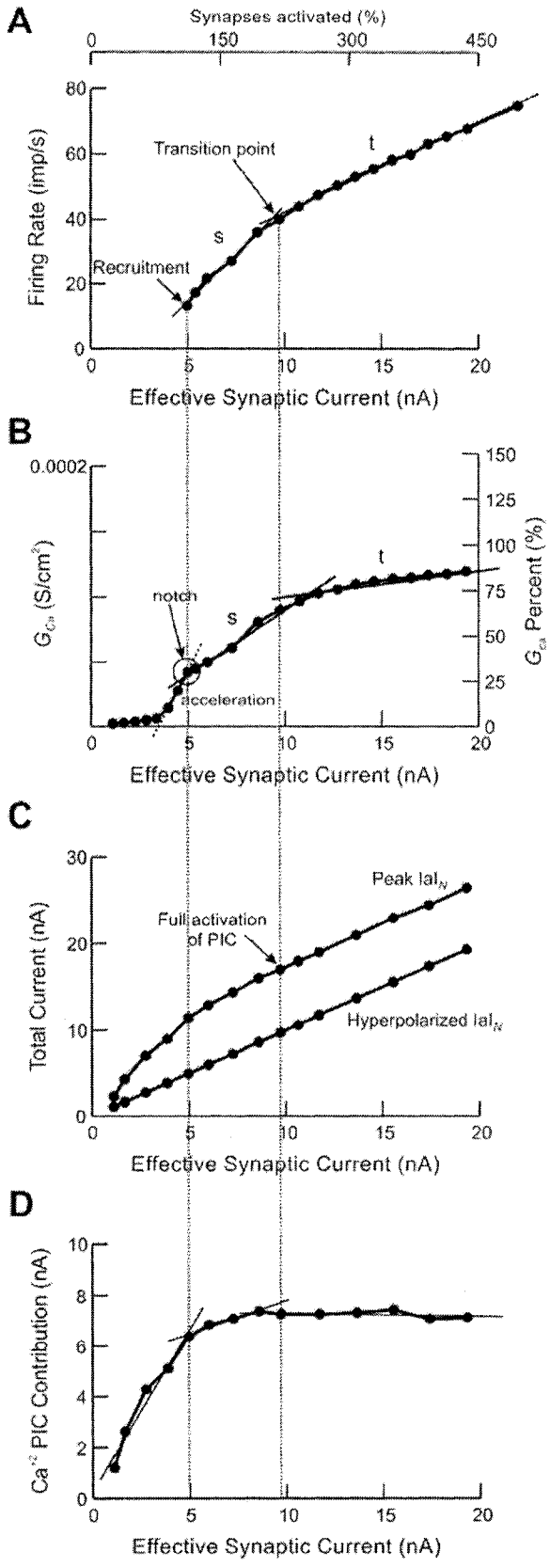

Figure 3-6. Enhancement of synaptic current. **A**: Steady-state F-I relationship evoked by synaptic excitation. The top axis shows the percent of activated synapses at each level. Thin solid lines: linear fit for secondary (s, r^2=0.995) and tertiary (t, r^2=0.994) segments. Transition point indicates change in slope between the secondary and tertiary segments. Long dashed vertical lines represent the point at which the cell is recruited and the point of full activation of Ca^{+2} PIC, respectively. The latter corresponds to the transition from the secondary to tertiary ranges on the synaptic F-I relationship. **B**: Steady-state magnitude of G_{Ca} at different levels of synaptic excitation. Right axis shows the percent increase in G_{Ca} relative to its maximum achievable value. Thin solid lines: linear fit for increase in G_{Ca} in the secondary (r^2=0.98) and tertiary (r^2=0.97) ranges. Dashed line shows the acceleration in the magnitude of G_{Ca} during the period of graded activation of Ca^{+2} PIC. Circle (notch) shows the abrupt change in G_{Ca} upon firing onset. **C**: Hyperpolarized and peak Ia I_N measurements from the model at different levels of synaptic excitation, indicated by the effective synaptic current at resting potential. At each level of synaptic excitation, the Ia I_N was computed as the difference between the I-V relationships during no synaptic activity and during tendon vibration at 180 Hz. **D**: Contribution of Ca^{+2} PIC to the synaptic current at different levels of synaptic excitation. This was computed as the difference between the peak and hyperpolarized Ia I_N traces presented in **C** at each level of synaptic excitation. Thin lines: linear fit representing PIC contribution to the enhancement of synaptic current before recruitment (slope = 1.3, r^2=0.97), during the secondary range (slope = 0.26, r^2=0.96), and during the tertiary range (slope = -0.016, r^2=0.33)).

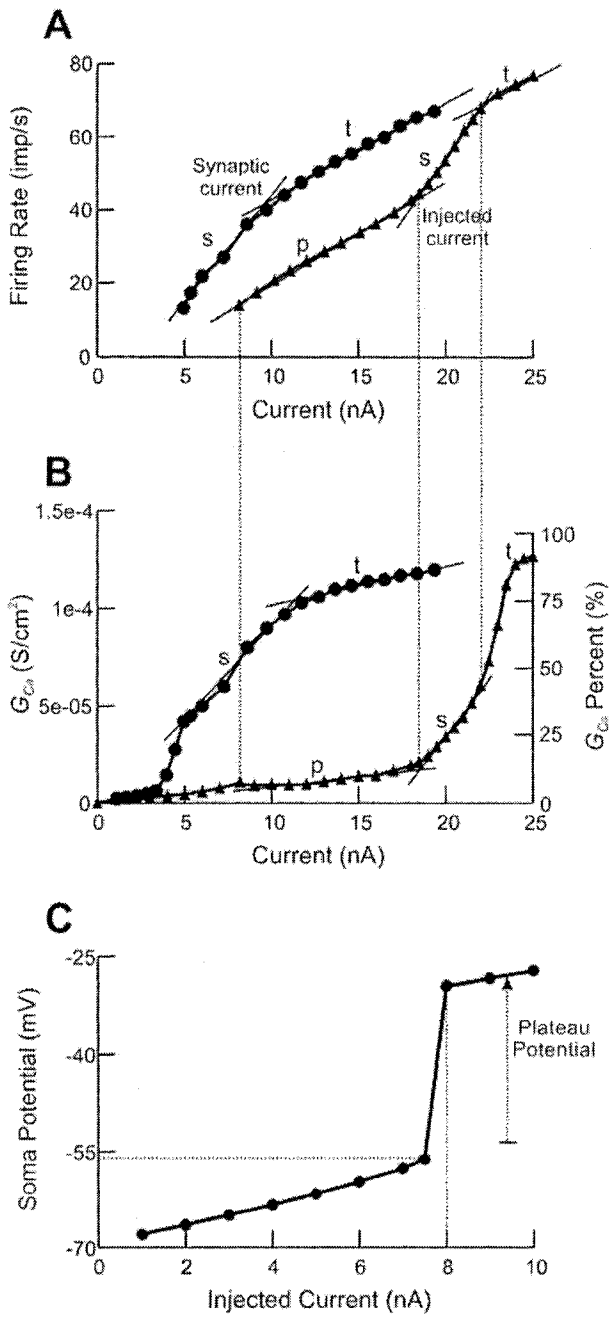

Figure 3-7. Comparison of the efficacy of intracellular current injection in activating the PIC to that of synaptic excitation. **A**: Comparison of F-I relationships evoked by synaptic activation (circles) and intracellular current injection (triangles) at the soma. **B**: Steady-state magnitude of G_{Ca} measured for the F-I relationships in **A**. Right axis shows the percent increase in G_{Ca} relative to its maximum achievable value. **C**: Steady-state somatic

membrane potential in response to intracellular long current pulses injected at the soma. Horizontal dashed line shows the somatic plateau threshold (-56 mV). Vertical dashed line shows the current level at which the somatic plateau threshold takes place (8 nA).

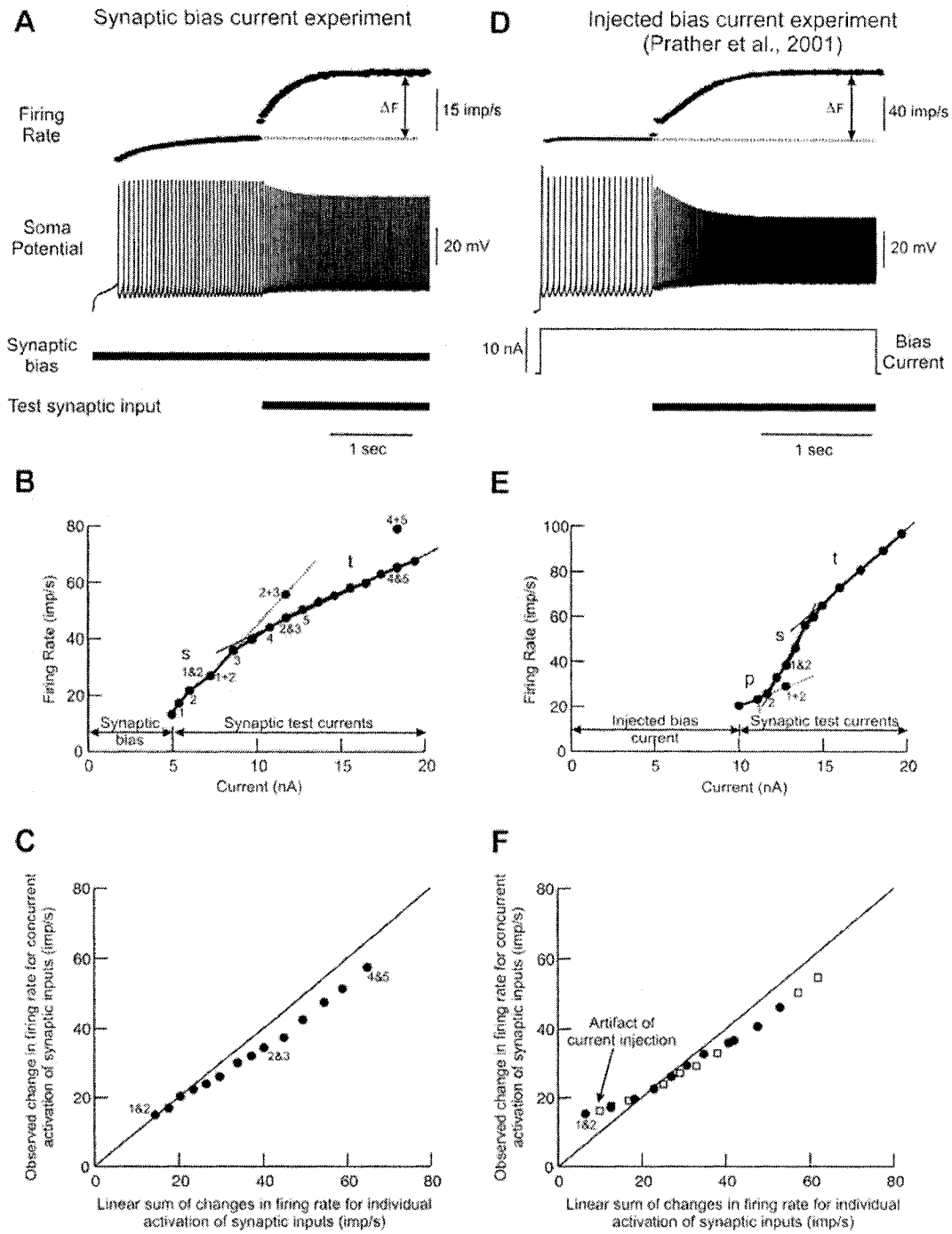

Figure 3-8. Summation of synaptic inputs investigated when using synaptic (**A-C**) and injected (**D-F**) bias currents. Measurement of change in firing rate evoked by activating one of the two test synaptic inputs when synaptic (**A**) and injected (**D**) bias currents were used. Change in firing rate (ΔF) was computed as the difference between steady-state

firing rates before and after activation of the test synaptic input. In **D**, a bias current of 10 nA was used to obtain background firing. Steady-state synaptic F-I relationships evoked from simultaneous application of the bias current and the test synaptic input when synaptic (**B**) and injected (**E**) bias currents were used. Dashed lines in **B** and **E** represent extrapolation lines to the primary and secondary segments. *1&2* represents the change in firing rate evoked by *simultaneous* activation of the two test synaptic inputs, whereas *1+2* represents the linear sum of changes in firing rate evoked by *individual* activation of the test synaptic inputs represented by points *1* and *2*. Comparison of changes in firing rate evoked by concurrent activation of the two test synaptic inputs and the linear sum of their individual changes in firing rate when synaptic (**C**) and injected (**F**) bias currents were used. Solid line represents the line of unity at which the observed firing rate is equal to the linear sum. Data presented in **F** were obtained with injected bias current of 10 nA (filled circles) and 12 nA (open squares).

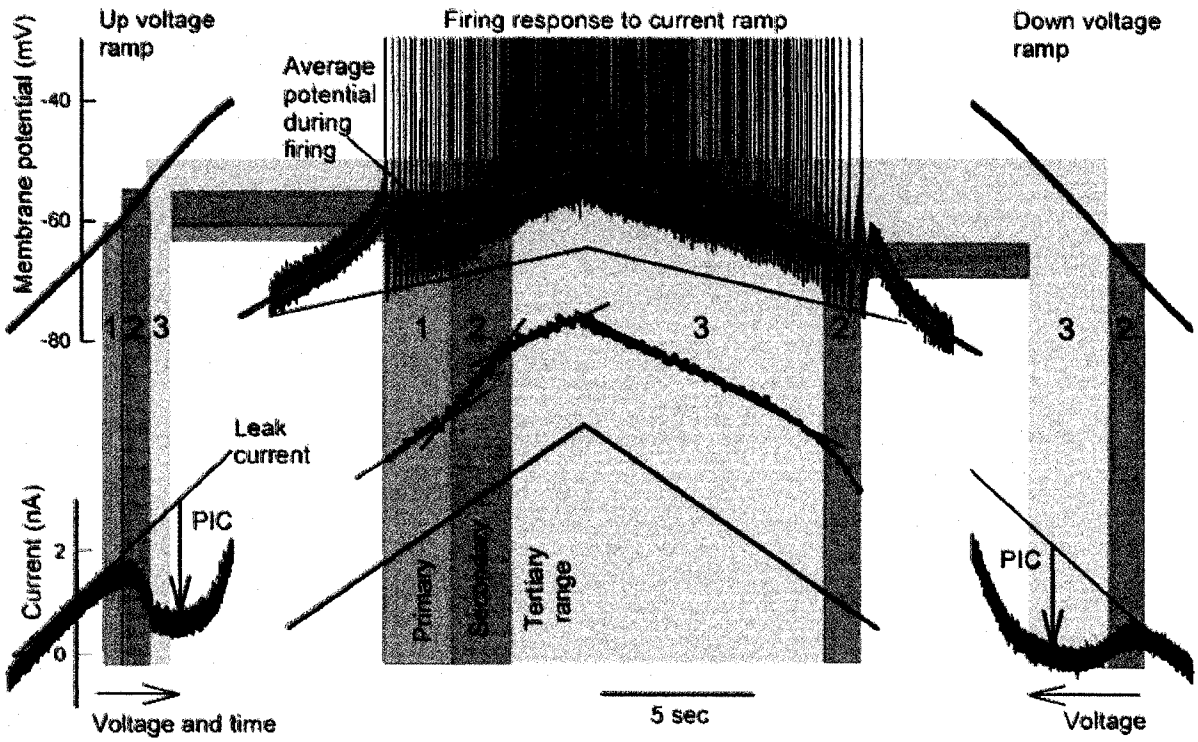

Figure 3-9. Overlay of the *experimentally-measured* firing rate (center) and Ca^{+2} PIC (both sides) during ascending and descending ramp current- and voltage-clamp experiments, respectively, from a real rat motoneuron (data adapted from Fig. 2B and C in Li et al. 2004). The regions were marked as the primary, secondary and tertiary ranges of firing, and their corresponding locations on the I-V relationship were determined by using the filtered potential during firing (red line; 2 Hz LPF raw data) corresponding to the top and bottom of each range.

3.6 REFERENCES

Bennett DJ, Hultborn H, Fedirchuk B, and Gorassini MA. Synaptic Activation of Plateaus in Hindlimb Motoneurons of Decerebrate Cats. *J Neurophysiol* 80: 2023-2037, 1998.

Bennett DJ, Li Y, and Siu M. Plateau Potentials in Sacrocaudal Motoneurons of Chronic Spinal Rats, Recorded In Vitro. *J Neurophysiol* 86: 1955-1971, 2001.

Brannstrom T. Quantitative synaptology of functionally different types of cat medial gastrocnemius alpha-motoneurons. *J Comp Neurol* 330: 439-454, 1993.

Brownstone RM, Jordan LM, Kriellaars DJ, Noga BR, and Shefchyk SJ. On the regulation of repetitive firing in lumbar motoneurones during fictive locomotion in the cat. *Exp Brain Res* 90: 441-455., 1992.

Burke RE. Composite nature of the monosynaptic excitatory postsynaptic potential. *J Neurophysiol* 30: 1114-1137, 1967.

Burke RE and Glenn LL. Horseradish peroxidase study of the spatial and electrotonic distribution of group Ia synapses on type-identified ankle extensor motoneurons in the cat. *J Comp Neurol* 372: 465-485., 1996.

Burke RE, Walmsley B, and Hodgson JA. HRP anatomy of group Ia afferent contacts on alpha motoneurones. *Brain Res* 160: 347-352., 1979.

Cullheim S, Fleshman JW, Glenn LL, and Burke RE. Membrane area and dendritic structure in type-identified triceps surae alpha motoneurons. *J Comp Neurol* 255: 68-81, 1987.

ElBasiouny SM, Bennett DJ, and Mushahwar VK. Role of persistent inward currents (PICs) in enhancement and integration of synaptic inputs in spinal motoneurons. *2005 Abstract Viewer/Itinerary Planner, Washington, DC: Society for Neuroscience, Online* Program No. 750.4, 2005a.

ElBasiouny SM, Bennett DJ, and Mushahwar VK. Simulation of Dendritic Cav1.3 Channels in Cat Lumbar Motoneurons: Spatial Distribution. *J Neurophysiol* 94: 3961-3974, 2005b.

ElBasiouny SM and Mushahwar VK. Spatial distribution of low voltage-activated L-type calcium channels in the dendrites of cat lumbar motoneurons. *2004 Abstract*

Viewer/Itinerary Planner, Washington, DC: Society for Neuroscience, Online Program No. 875.7, 2004.

Fleshman J, Segev I, and Burke R. Electrotonic architecture of type-identified alpha-motoneurons in the cat spinal cord. *J Neurophysiol* 60: 60-85, 1988.

Fyffe R. Spatial distribution of recurrent inhibitory synapses on spinal motoneurons in the cat. *J Neurophysiol* 65: 1134-1149, 1991.

Glenn L, Burke R, Fleshman J, and Lev-Tov A. Estimates of electrotonic distance of group Ia contacts on cat a-motoneurons: An HRP-morphological study. *Soc Neurosci Abstr* 8: 995, 1982.

Gorassini M, Yang JF, Siu M, and Bennett DJ. Intrinsic Activation of Human Motoneurons: Possible Contribution to Motor Unit Excitation. *J Neurophysiol* 87: 1850-1858, 2002.

Granit R, Kernell D, and Lamarre Y. Algebraical summation in synaptic activation of motoneurones firing within the 'primary range' to injected currents. *J Physiol* 187: 379-399, 1966a.

Granit R, Kernell D, and Lamarre Y. Synaptic stimulation superimposed on motoneurones firing in the 'secondary range' to injected current. *J Physiol* 187: 401-415, 1966b.

Heckman C and Binder MD. Analysis of effective synaptic currents generated by homonymous Ia afferent fibers in motoneurons of the cat. *J Neurophysiol* 60: 1946-1966., 1988.

Heckman C, Gorassini M, and Bennett D. Persistent inward currents in motoneuron dendrites: Implications for motor output. *Muscle Nerve* 31: 135-156, 2005.

Hines M and Carnevale T. The NEURON simulation environment. *Neural Comput* 9: 1179-1209, 1997.

Hounsgaard J, Hultborn H, Jespersen B, and Kiehn O. Bistability of alpha-motoneurones in the decerebrate cat and in the acute spinal cat after intravenous 5-hydroxytryptophan. *J Physiol* 405: 345-367., 1988.

Hounsgaard J and Kiehn O. Serotonin-induced bistability of turtle motoneurones caused by a nifedipine-sensitive calcium plateau potential. *J Physiol* 414: 265-282., 1989.

Hounsgaard J and Mintz I. Calcium conductance and firing properties of spinal motoneurones in the turtle. *J Physiol* 398: 591-603., 1988.

Hultborn H, Denton ME, Wienecke J, and Nielsen JB. Variable amplification of synaptic input to cat spinal motoneurones by dendritic persistent inward current. *J Physiol (Lond)* 552: 945-952, 2003.

Kernell D. The adaptation and the relation between discharge frequency and current strength of cat lumbosacral motoneurones stimulated by long-lasting injected currents. *Acta Physiol Scand* 65: 65-73, 1965a.

Kernell D. High-frequency repetitive firing of cat lumbosacral motoneurones stimulated by long-lasting injected currents. *Acta Physiol Scand* 65: 74-86, 1965b.

Kernell D. Synaptic Influence On The Repetitive Activity Elicited In Cat Lumbosacral Motoneurones By Long-Lasting Injected Currents. *Acta Physiol Scand* 63: 409-410, 1965c.

Kuno M and Miyahara JT. Non-linear summation of unit synaptic potentials in spinal motoneurones of the cat. *J Physiol* 201: 465-477, 1969.

Lee RH and Heckman CJ. Adjustable Amplification of Synaptic Input in the Dendrites of Spinal Motoneurons In Vivo. *J Neurosci* 20: 6734-6740, 2000.

Lee RH and Heckman CJ. Bistability in Spinal Motoneurons In Vivo: Systematic Variations in Persistent Inward Currents. *J Neurophysiol* 80: 583-593, 1998b.

Lee RH and Heckman CJ. Bistability in Spinal Motoneurons In Vivo: Systematic Variations in Rhythmic Firing Patterns. *J Neurophysiol* 80: 572-582, 1998a.

Lee RH and Heckman CJ. Paradoxical Effect of QX-314 on Persistent Inward Currents and Bistable Behavior in Spinal Motoneurons In Vivo. *J Neurophysiol* 82: 2518-2527, 1999.

Lee RH, Kuo JJ, Jiang MC, and Heckman CJ. Influence of Active Dendritic Currents on Input-Output Processing in Spinal Motoneurons In Vivo. *J Neurophysiol* 89: 27-39, 2003.

Li Y and Bennett DJ. Persistent Sodium and Calcium Currents Cause Plateau Potentials in Motoneurons of Chronic Spinal Rats. *J Neurophysiol* 90: 857-869, 2003.

Li Y, Gorassini MA, and Bennett DJ. Role of Persistent Sodium and Calcium Currents in Motoneuron Firing and Spasticity in Chronic Spinal Rats. *J Neurophysiol* 91: 767-783, 2004.

Powers RK and Binder MD. Effective synaptic current and motoneuron firing rate modulation. *J Neurophysiol* 74: 793-801., 1995.

Powers RK and Binder MD. Input-output functions of mammalian motoneurons. *Rev Physiol Biochem Pharmacol* 143: 137-263, 2001.

Powers RK and Binder MD. Summation of Effective Synaptic Currents and Firing Rate Modulation in Cat Spinal Motoneurons. *J Neurophysiol* 83: 483-500, 2000.

Prather JF, Powers RK, and Cope TC. Amplification and Linear Summation of Synaptic Effects on Motoneuron Firing Rate. *J Neurophysiol* 85: 43-53, 2001.

Romaiguere P, Vedel JP, Pagni S, and Zenatti A. Physiological properties of the motor units of the wrist extensor muscles in man. *Exp Brain Res* 78: 51-61, 1989.

Rose P and Cushing S. Non-linear summation of synaptic currents on spinal motoneurons: lessons from simulations of the behaviour of anatomically realistic models. *Prog Brain Res* 123: 99-107, 1999.

Sawczuk A, Powers R, and Binder MD. Spike frequency adaptation studied in hypoglossal motoneurons of the rat. *J Neurophysiol* 73: 1799-1810., 1995.

Schwindt PC and Crill WE. A persistent negative resistance in cat lumbar motoneurons. *Brain Res* 120: 173-178, 1977.

Schwindt PC and Crill WE. Factors influencing motoneuron rhythmic firing: results from a voltage-clamp study. *J Neurophysiol* 48: 875-890., 1982.

Segev I, Fleshman JW, and Burke RE. Computer simulation of group Ia EPSPs using morphologically realistic models of cat alpha-motoneurons. *J Neurophysiol* 64: 648-660, 1990.

Shapovalov AI. Extrapyramidal monosynaptic and disynaptic control of mammalian alpha-motoneurons. *Brain Research* 40: 105-115, 1972.

Svirskis G and Hounsgaard J. Transmitter Regulation of Plateau Properties in Turtle Motoneurons. *J Neurophysiol* 79: 45-50, 1998.

Chapter 4: Suppressing the Excitability of Spinal Motoneurons by Extracellularly-applied Electrical Fields: Insights from Computer Simulations [†]

4.1 INTRODUCTION

Over the past two decades experimental recordings revealed the presence of voltage-gated ion channels over the dendrites of spinal motoneurons (Carlin et al. 2000; Hounsgaard et al. 1988; Hounsgaard and Kiehn 1993; Lee and Heckman 1996; Simon et al. 2003). Some of these dendritic channels mediate a persistent inward current (PIC) which is a depolarizing current that does not inactivate with prolonged membrane depolarization. This dendritic PIC plays a fundamental role in determining the response of the motoneuron to synaptic inputs and in shaping the motor output. After spinal cord injury (SCI), activation of PICs in motoneurons is no longer under the control of descending drive (e.g., lack of inhibition) leading to increased motoneuronal excitability and firing rate, muscle spasms, and long-lasting reflexes in response to afferent inputs (Li et al. 2004a; Thomas and Ross 1997).

Electrical fields have been previously used to study the electrical properties and firing behavior of neurons in the brain (Chan and Nicholson 1986; Chan et al. 1988) and spinal cord (Baginskas et al. 1993; Delgado-Lezama et al. 1999; Delgado-Lezama et al. 1997; Hounsgaard and Kiehn 1993; Svirskis et al. 1997a; Svirskis et al. 1997b). In the present study, we investigate the application of electrical fields to reduce spasticity after SCI. The degree of differential polarization induced in different elements of a neuron exposed to an electrical field is determined by the relationship between the applied field properties (e.g., intensity, polarity, and direction) and the dendritic morphology and orientation relative to the imposed field, the internal resistance of the cell, and the spatial distribution, density, and type of dendritic voltage-gated ion channels (Hounsgaard and Kiehn 1993). The net

[†] A version of this chapter has been submitted for publication in the *J. Applied Physiol.*

effect of field-induced polarization on the firing behavior of the neuron is *critically* dependent on the positional symmetry of the soma and initial segment (sites of spike initiation) with respect to the dendrites; hence, their location relative to the neutral point (where no polarization takes place). Actively firing Pyramidal or Purkinje cells, with somata positioned asymmetrically relative to their dendrites, experience an increased firing rate during a soma-depolarizing field and a reduced firing rate during a soma-hyperpolarizing field (Bikson et al. 2004; Chan and Nicholson 1986). Spinal motoneurons, on the other hand, have dendrites that are relatively symmetric around the soma, and their spike initiation structures thus experience little polarization as compared to that of their dendrites. This suggests that their excitability could not be modulated effectively by electrical fields similarly to brain cells. However, modulation of the activation level of their dendritic voltage-gated conductances by electrical fields could provide an alternative means for regulating their excitability.

The goal of the present study was to investigate, using computer simulations, the effect of applied direct current (DC) and alternating current (AC) electrical fields on the magnitude of the dendritic PICs and the resulting excitability of spinal motoneurons. This would be beneficial in suppressing the increased excitability of motoneurons following SCI and the emergence of spasticity during which the PIC is fully activated. Our results demonstrate that application of weak DC or AC electrical fields could suppress the excitability of motoneurons and reduce their firing rate. The reduction in firing rate was due to the induced reduction in the magnitude of the dendritic PIC reaching the soma by the applied field. The reduction in PIC was achieved in both the depolarized and hyperpolarized segments of the dendrites due to the nonlinear current-voltage (I-V) relationship of the dendritic PIC-mediating channels. Results of the present study propose application of electrical fields as an effective clinical therapy to alleviate spasticity after SCI. Part of this work was previously presented in abstract form (ElBasiouny and Mushahwar 2006).

4.2 MATERIALS AND METHODS

A morphologically-detailed computer model of a spinal α-motoneuron was developed to investigate the effect of electrical fields on the excitability and firing behavior of motoneurons. This model incorporated realistic motoneuron morphology, realistic dendritic distribution of synaptic inputs, and a dendritic distribution of ionic channels that closely reproduced several electrophysiological recordings from spinal motoneurons (ElBasiouny et al. 2005).

4.2.1 Model structure

Full description of the model motoneuron morphology, biophysical properties, and verification is provided in ElBasiouny et al. (2005). Briefly, a compartmental cable model of a cat motoneuron was developed that had full representation of the α-motoneuron structure, consisting of soma, initial segment, axon hillock, dendritic tree, and a myelinated axon. The model dendritic tree was based on the three-dimensional (3D) detailed morphology for type-identified triceps surae motoneurons (fatigue-resistant (FR) type, medial gastrocnemius motoneuron, identified as cell 43/5 in Cullheim et al., 1987). The model was developed using NEURON simulation environment (Hines and Carnevale 1997). The passive parameters determining the cable properties of the motoneuron were set based on previous studies for the same 43/5 FR motoneuron (Cullheim et al. 1987; Fleshman et al. 1988). Somatic and initial segment voltage-gated ion channels determining the motoneuron active properties included fast and persistent Na^+, delayed rectifier K^+, Ca^{+2}-activated K^+, and N-type Ca^{+2} channels. Channel densities were set such that the model active properties were within the 95% confidence range of experimental measurements from cat α-motoneurons, and the model generated action potentials and afterhyperpolarizations potential with characteristics similar to empirical recordings (ElBasiouny et al. 2005).

The myelinated axon was based on the model developed by McIntyre and Grill (2002) in which nodes of Ranvier and myelin were electrically represented. The myelinated axon

had a fiber diameter of 14 μm, 10 nodes of Ranvier, and conduction velocity of 83 m/s which is comparable to that of FR motoneurons (Hochman and McCrea 1994c).

4.2.2 Dendritic channels and synaptic inputs

The dendritic low-voltage-activated L-type calcium ($Ca_V1.3$ type) channels that mediate Ca^{+2} PIC were distributed over a region between 300 μm and 850 μm from the soma. With this dendritic distribution, the model behavior matched multiple sets of experimental measurements from cat motoneurons innervating the MG muscle (ElBasiouny et al. 2005).

Given that involuntary muscle spasms and exaggerated tendon reflexes associated with spasticity are usually triggered by mild sensory stimulation (e.g., rubbing or cooling of the skin, limb movements, or muscle contraction), activation of the motoneuron by synaptic inputs was simulated in the present model. The synapses were distributed over the dendritic tree based on the realistic distribution of Ia afferent-to-motoneuron contacts from cat FR motoneurons (Burke and Glenn 1996; Burke et al. 1979; Glenn et al. 1982). Activating the Ia-afferent system through tendon vibration was simulated by activating the Ia-afferent synapses asynchronously at 180 Hz while adjusting the synapse conductances to give Ia effective synaptic current (Ia I_N) of 4.8 nA at resting potential (ElBasiouny et al. 2005). To allow for systematic gradation of the Ia-synaptic input, the total number of Ia-synapses was divided into eight nearly equal groups, randomly distributed on the dendrites, which were then activated sequentially (ElBasiouny et al. 2006). This activation pattern resulted in a linear increase in the Ia I_N reaching the soma as more synapses were activated. Given that the distribution of different synaptic inputs appears to be effectively similar to that of the Ia-afferents (for discussion see ElBasiouny et al. (2005)), synaptic input from systems other than the Ia-afferents was simulated by increasing the synapse conductances to generate higher synaptic currents (ElBasiouny et al. 2006). This allowed for the examination of the motoneuronal firing behavior in response to different levels of synaptic inputs and the frequency-current (F-I) relationship was constructed (e.g., Fig. 4-5A - upper panel).

4.2.3 Hyperexcitability of motoneurons during spasticity

The goal of the present study was to examine the application of electrical fields for reducing the level of spasticity resulting from the increased excitability of spinal motoneurons after SCI. During spasticity, spinal motoneurons become hyperexcitable and their PIC, which is responsible for the generation of high and sustained motoneuronal firing, long-lasting reflexes, and muscle spasms, becomes fully activated by synaptic inputs (Gorassini et al. 2004; Harvey et al. 2006a, b; Harvey et al. 2006c; Li et al. 2004a; Li et al. 2004b; Thomas and Ross 1997). To simulate this condition, the model motoneuron was synaptically activated at 300% of the strength of the Ia-afferent system (Ia $I_N \approx 14.6$ nA). This level of synaptic input resulted in *full* activation of the Ca^{+2} PIC and generated a high firing rate in the tertiary range of the F-I relationship (Fig. 4-5A – upper panel). We also modified the model electrical and PIC-mediating channel (persistent Na^+ and $Ca_V1.3$ channels) properties to replicate those changes seen following SCI (Fig. 4-6A and B). These changes enhance the excitability of motoneurons following SCI, and contribute to the physiological manifestation of spasticity after injury. Under these conditions, the level of synaptic input required to activate fully the dendritic Ca^{+2} PIC decreased to 100% of the strength of the Ia-afferent system (Ia $I_N \approx 5$ nA). This allowed us to investigate the efficacy of using electrical fields in reducing the excitability of spinal motoneurons after SCI and the emergence of spasticity. Synaptic inputs that caused partial activation of the Ca^{+2} PIC were also investigated (Fig. 4-5A).

To assess the level of activation of the dendritic $Ca_V1.3$ channels and quantify the magnitude of the mediated current, we measured the average dendritic Ca^{+2} PIC (I_{Ca}; e.g., Fig. 4-3A – 2nd trace). This average Ca^{+2} PIC was computed as follows:

$$I_{Ca} = 1/n \times \sum_{i=1}^{n} i_{Ca\,i}$$

where n is the number of compartments that have the $Ca_V1.3$ channels, and i_{Ca_i} is the calcium current mediated by the $Ca_V1.3$ channels located in compartment number i.

4.2.4 Simulation of extracellular stimulation through electrical fields

Electrical fields resulting from current flow between two large parallel plate electrodes and applied in 3D space parallel to the rostrocaudal, dorsoventral, or mediolateral axes of the spinal cord (SC) were simulated. The gray matter was represented as a 3D uniform ohmic, i.e., isotropic, medium (Hounsgaard and Kiehn 1993). The distance between the two plate electrodes was 8 mm. The model motoneuron was placed between the plate electrodes in which the surrounding electrical field was uniform. This was indicated by the linear relationship of the extracellular voltage gradient along the cell axis between the electrode plates, whereas that parallel to the plates was zero (Fig. 4-2B – left panel). The dendritic morphology of the cell was described in 3D coordinate space centered at the soma and parallel to the rostrocaudal, dorsoventral, and mediolateral axes of the SC (Cullheim et al. 1987). The representation of the motoneuron morphology relative to the plate electrodes and the principal axes of the SC allowed for the computation of the extracellular field potential for each compartment in the model. The following equation was used for computing the extracellular field potential generated from the current flow between two parallel plate electrodes:

$$V_e = I \cdot \rho \cdot (x - 0.5D)$$

where V_e is the extracellular field potential for each compartment, I is the current, ρ is the extracellular electrical resistivity of the gray matter, x is the radial distance along the field axis between each compartment and the positive plate electrode, and D is the distance between the two parallel plate electrodes. The effect of electrical fields between two distantly located electrodes (point sources) or between spherical electrodes was also considered (Appendix 2). Direct current (DC) and alternating current (AC) electrical fields of different waveforms (e.g., sinusoidal, rectangular, and trapezoidal) were simulated by varying the shape of the applied current.

In the present study, we placed the myelinated axon, initial segment, and axon hillock of the model motoneuron in the dorsoventral direction of the SC such that electrical fields applied along that axis induced the greatest polarization of their membrane potential and significantly affected the spiking mechanism of the model motoneuron (Fig. 4-1A). Electrical fields applied along the rostrocaudal or mediolateral axes of the SC, i.e.,

orthogonal to the orientation of the myelinated axon, initial segment, and axon hillock, polarized the dendrites and had no effect on the membrane potential of the myelinated axon, initial segment, and axon hillock of the model motoneuron.

4.2.5 Verification of the motoneuronal activation through electrical fields

To verify the effect of electrical fields on the behavior of the model motoneuron, we simulated the experiments conducted by Hounsgaard and Kiehn (1993) on spinal motoneurons of the turtle during the application of an electrical field in the presence of different channel blockers (tetrodotoxin, TTX, and apamin). The effect of TTX and apamin was simulated in the model by blocking the Na^+ and the Ca^{+2}-activated K^+ channels, respectively. As demonstrated experimentally, a sustained depolarization in the somatic membrane (plateau potential) of the model motoneuron was evoked during application of both soma-depolarizing and soma-hyperpolarizing electrical fields due to the activation of the dendritic Ca^{+2} PIC (compare Fig. 4-1B to Fig. 6Bb and c in Hounsgaard and Kiehn (1993)). The dendritic Ca^{+2} PIC was computed in the model as previously mentioned and is indicated as I_{Ca} in Fig. 4-1B.

The firing behavior of the model motoneuron evoked by the application of an electrical field, and in the absence of synaptic activation, was simulated in Fig. 4-1C. A sinusoidal electrical field was applied along the dorsoventral axis of the SC and parallel to the orientation of the axon, initial segment, and axon hillock of the motoneuron (Fig. 4-1A). This field caused depolarization of the somatic transmembrane potential during the cathodic phase of the field and its hyperpolarization during the anodic phase of the field. Cell firing was evoked during the cathodic phase of the imposed field when the field intensity was increased (Fig. 4-1C - 1). Further increase in the intensity of the applied field resulted in high motoneuronal firing rate, and the baseline transmembrane potential became flattened during the high spiking period (arrow in Fig. 4-1C - 2) as seen experimentally (Chan et al. 1988; Delgado-Lezama et al. 1999; Hounsgaard and Kiehn 1993). When an intracellular hyperpolarizing current pulse was injected at the soma during the high spiking phase, cell firing was reduced and terminated early (Fig. 4-1C - 3) and the somatic membrane potential was more hyperpolarized. This demonstrated

qualitatively the independent and additive interaction between the polarization imposed by the electrical field and that induced by the intracellularly-injected current pulse (Chan et al. 1988; Delgado-Lezama et al. 1999).

4.3 RESULTS

The mechanism by which electrical fields affect neuronal activity is shown in Fig. 4-2. The application of a DC electrical field along the mediolateral axis of the SC (Fig. 4-2A - left panel) resulted in the formation of an extracellular voltage gradient along the direction of the field axis (Fig. 4-2B - left panel - red trace). This induced extracellular voltage gradient altered the transmembrane potential of the neuronal elements along the field axis and caused current to flow inwards, *effectively depolarizing*, one half of the cell, and outwards, *effectively hyperpolarizing*, the other half of the cell (Fig. 4-2B - right panel - red trace). The transmembrane potential of neuronal elements oriented orthogonally to the field direction was not affected by the imposed field (Fig. 4-2B - right panel - blue trace). The spatial distribution of the dendritic transmembrane potential resulting from the imposed electrical field is shown in Fig. 4-2A (right panel). The induced change in transmembrane potential varied linearly with distance along the axis of the imposed field indicating that long dendritic extensions will be polarized mostly by the effect of the field (Fig. 4-2B – left panel). This is in agreement with experiments conducted on spinal motoneurons (Hounsgaard and Kiehn 1993), and demonstrates that these neurons are electrotonically short cells (i.e., have a long space constant) since a linear change in the transmembrane potential with no large deflections at the ends of the dendrites is seen. Because of the anatomical location of the soma and initial segment being relatively in the center of the motoneuron (i.e., near the neutral point where no field-induced polarization takes place), these structures experienced the lowest degree of polarization, whereas the long dendritic extensions experienced the largest degree of polarization (Fig. 4-2A – right panel).

Neurons are normally activated through their synaptic inputs. Following SCI, brief sensory stimulation causes full activation of the motoneuronal PIC, which is implicated in the production of involuntary muscle spasms and exaggerated tendon reflexes associated with spasticity (Li et al. 2004a). Therefore, to simulate this condition, the model motoneuron was activated synaptically with Ia I_N of 14.6 nA (nearly three times that of the Ia-afferent system) that caused full activation of the dendritic Ca^{+2} PIC

(ElBasiouny et al. 2006). The effect of DC electrical fields on the behavior of the actively firing motoneuron was then examined (Fig. 4-3). When the DC field was applied along the mediolateral axis of the SC, reduction in firing rate was observed (Fig 4-3A - upper trace). Reduction in firing rate was also associated with a reduction in the magnitude of the dendritic Ca^{+2} PIC (see I_{Ca} in Fig. 4-3A). The amount of reduction in I_{Ca} was comparable to that of the firing rate indicating that the drop in I_{Ca} was the primary factor in reducing the firing rate and not the direct polarization of the soma and initial segment by the imposed field.

The reduction in firing rate observed upon application of the DC field could be explained as follows. Before application of the field, the dendritic Ca^{+2} PIC was fully activated by the effect of the synaptic input. When the DC field was applied, half of the dendritic tree was hyperpolarized whereas the other half was depolarized similar to Fig. 4-2A (right panel). Dendritic $Ca_V1.3$ channels of the hyperpolarized part of the dendritic tree were deactivated resulting in a reduced Ca^{+2} PIC. In contrast, dendritic $Ca_V1.3$ channels of the depolarized part of the dendritic tree were more activated; however, the magnitude of their Ca^{+2} PIC depended on the dendritic membrane potential because of the nonlinear I-V relationship of the $Ca_V1.3$ channels (Fig. 4-3B). Depolarized dendritic segments whose membrane potential was lower than the potential of the turning point (at -15 mV in Fig. 4-3B) experienced an increase in the magnitude of the mediated Ca^{+2} PIC, whereas depolarized dendritic segments whose membrane potential exceeded the potential of the turning point experienced a reduction in the mediated Ca^{+2} PIC. Given that the extended dendritic segments experience higher levels of polarization relative to the soma and initial segment, the net effect of the depolarizing DC field was a reduction in the mediated Ca^{+2} PIC with little effect of direct polarization on the somatic spiking mechanism by the imposed field.

The effect of the applied electrical field on the amplitude of the dendritic Ca^{+2} PIC was confirmed by direct measurements of the PIC (Fig. 4-3D) from dendritic branches aligned parallel to the field (blue dendritic pathway shown in Fig. 4-3C – lower panel).

Prior to the application of the electrical field, the Ca^{+2} PIC was fully activated along these dendritic branches around the soma (Fig. 4-3D – dashed trace). Following the application of the electrical field, the magnitude of the Ca^{+2} PIC was significantly suppressed on the hyperpolarized part of the dendrites, whereas it did not change much on the depolarized half of the dendrites (Fig. 4-3D – solid trace). Because of the nonlinear properties of the I-V relationship of the $Ca_V1.3$ channels, increased membrane depolarization in the depolarized half of the dendrites did not compensate for the reduction of the Ca^{+2} PIC on the hyperpolarized part of the dendrites. In fact, suppression of the Ca^{+2} PIC by the effect of the electrical field was more evident at dendritic compartments distal from the soma due to the strong depolarization experienced by those compartments. The spatial distribution of the Ca^{+2} PIC was also illustrated pictorially during the presence and absence of the electrical field (Fig. 4-3C). Further support for the aforementioned mechanism of the effect of electrical fields on motoneuronal firing was provided by the profile of the activated plateau potential by the applied field in the presence of TTX and apamin (Fig. 4-1B). The measured I_{Ca} during soma-depolarizing and soma-hyperpolarizing DC fields (1^{st} and 3^{rd} phases in Fig. 4-1B) indicated a reduction in the magnitude of the Ca^{+2} PIC relative to that during the period in which the field was removed (2^{nd} phase in Fig. 4-1B).

When the DC field applied along the mediolateral axis was reversed in polarity, reduction in firing rate was achieved as well; however, to a lesser extent (compare conditions E+ to E- in the upper trace of Fig. 4-3A). This variation in the amount of reduction in firing rate based on field polarity could be explained by the imperfect symmetry of the dendritic projections around the soma along the mediolateral axis. That is, more $Ca_V1.3$ channels might be (de)activated in one half of the dendritic tree than in the other half due to the imperfect symmetry of the motoneuronal dendritic projections around the soma, their geometry and orientation relative to the field, and the distribution of the $Ca_V1.3$ channels. Similar results were obtained when a reversed-polarity DC field was applied along the rostrocaudal axis of the SC (not illustrated).

To study the effect of electrical fields on the spiking mechanism of spinal motoneurons, a DC field applied along the dorsoventral axis of the SC and parallel to the orientation of the axon, initial segment, and axon hillock of the model motoneuron was simulated (Fig. 4-4). When the DC field was applied such that the axon, initial segment, and axon hillock were extracellularly hyperpolarized (condition E+ in Fig. 4-4), two active processes occurred that simultaneously reduced the motoneuronal firing rate: (1) The initial segment was directly inhibited by the effect of the applied field causing less activation of the Na^+ channels and generation of action potentials. (2) The net dendritic Ca^{+2} PIC, indicated by I_{Ca}, reaching the soma and initial segment was reduced at a slower rate by the effect of the applied field on the dendrites as explained in Fig. 4-3A. The net effect of these two processes was a rapid and significant reduction in the motoneuronal firing rate (Fig. 4-4 - upper trace - E+ condition). Conversely, when the DC field was applied such that the axon, initial segment, and axon hillock were extracellularly depolarized (condition E- in Fig. 4-4), two counteracting processes occurred simultaneously that affected the firing rate: (1) The initial segment was directly stimulated by the effect of the applied field causing more activation of the Na^+ channels and generation of action potentials. (2) The net dendritic I_{Ca} reaching the soma and initial segment was slowly reduced by the effect of the applied field on the dendrites. The net result of these two processes was an initial rise in firing rate followed by a slow decline (Fig. 4-4 - upper trace - E- condition). The steady-state firing rate was determined mainly by the relative strength of the aforementioned processes. The effect of the applied DC field on the dendrites is evident in the reduction of I_{Ca}. Despite the reduction in I_{Ca} during the E- condition in Fig. 4-4, there was little change in firing rate due to the direct stimulation of the axon, initial segment, and axon hillock by the imposed field.

4.3.1 Effect of DC electrical fields on the excitability of spinal motoneurons

The effect of electrical fields on the F-I relationship of spinal motoneurons was investigated as well. Application of weak DC electrical fields of intensities 8.5 mV/mm and 30 mV/mm along the mediolateral axis of the SC in response to different levels of synaptic input resulted in a linear F-I relationship over the full range of the effective synaptic current reaching the soma (Fig. 4-5A - upper panel). This effect was achieved by

modulating the activation level of the dendritic $Ca_V1.3$ channels, as shown by I_{Ca} in the lower panel of Fig. 4-5A, which resulted in a shallower graded magnitude of the Ca^{+2} PIC in response to an increasing level of synaptic input. This is also supported by the shallower slope of the linear F-I relationship as compared to that of the secondary range before the application of the electrical field. The intensity of the applied field modulated the slope of the linear F-I relationship. Furthermore, application of the DC field suppressed the excitability of spinal motoneurons even when synaptic inputs caused partial activation of the Ca^{+2} PIC. During the secondary range of the F-I relationship, the afterhyperpolarization regulates the activation level of the $Ca_V1.3$ channels resulting in a graded activation of the Ca^{+2} PIC (ElBasiouny et al. 2006). Therefore, application of DC electrical fields acted in tandem with the afterhyperpolarization and resulted in a more potent regulating effect on the magnitude of the Ca^{+2} PIC. In sum, application of DC electrical fields resulted in a reduction in the excitability of spinal motoneurons, and the magnitude of this reduction could be modulated by varying the intensity of the applied field.

Application of a DC electrical field of intensity 30 mV/mm resulted in suppression of the overall excitability of the model motoneuron; however, it facilitated its recruitment (indicated by the horizontal arrow in Fig. 4-5A) and caused an increase, rather than a reduction, in the motoneuronal firing rate in response to low levels of synaptic input (vertical arrow in Fig. 4-5A). That is, at low levels of synaptic input, the Ca^{+2} PIC that was activated by the application of the DC field was higher in magnitude than that originally activated by the synaptic input alone (Fig. 4-5B, Ia I_N = 6 nA). This increase in magnitude of the Ca^{+2} PIC at low levels of synaptic input facilitated the recruitment of the motoneuron. Nevertheless, application of a weaker DC electrical field of intensity 8.5 mV/mm avoided the facilitation of motoneuronal recruitment, but reduced the overall motoneuronal excitability to a lesser extent (open circles in Fig. 4-5A).

The effect of DC field intensity applied along the principal axes of the SC (rostrocaudal, dorsoventral, and mediolateral) on the motoneuronal firing rate in response to a synaptic input of 14.6 nA (three times that of the Ia-afferent system) is shown in Fig. 4-5C.

Generally, there was a linear relationship between the intensity of the applied field and the change in firing rate. Direct current fields applied in some directions were found to be more effective in reducing, or even turning off, cell firing. For instance, DC field applied along the rostrocaudal axis of the SC resulted in a linear reduction of firing rate, but could not turn off firing completely (Fig. 4-5C - filled circles). On the other hand, DC fields applied along the mediolateral axis of the SC were more effective in reducing firing rate (note the higher slope of the filled squares in Fig. 4-5C) and were able to turn off firing completely. This dissimilarity in effect could be explained by the number of dendritic projections (and dendritic $Ca_V1.3$ channels) of the model motoneuron that was polarized by the imposed field along that axis.

Direct current fields that directly polarized the axon and initial segment as well as the dendritic tree (along the dorsoventral axis) had the strongest impact on firing rate. Direct current fields that hyperpolarized the axon and initial segment resulted in the steepest reduction of firing rate until firing was totally blocked at high field intensities (Fig. 4-5C - filled triangles). Conversely, DC fields that depolarized the axon and initial segment resulted in an increase in firing rate (maximum increase was nearly 20%) until inactivation of the Na^+ channels was encountered and firing was then blocked (Fig. 4-5C - open triangles).

4.3.2 Alteration in electrical properties after SCI

The effect of changes in the motoneuronal electrical properties after SCI on the reduction in firing rate of spinal motoneurons during the application of electrical fields was also investigated. These changes contribute to the increased motoneuronal excitability following SCI. The change in the motoneuronal active (e.g., firing threshold, V_{th}) and passive (e.g., resting membrane potential, V_{rest}; specific membrane resistance, R_m) properties were simulated, and the Ia-afferent synapses were activated at 300% to cause full activation of the dendritic PIC. Reduction in the motoneuronal firing rate by the application of a DC electric field along the mediolateral axis of the SC was achieved after the alteration of these electrical properties independently (Fig. 4-6A; conditions B to I in Fig. 4-6B). Moreover, reduction in firing rate was still achieved ($\approx$ 32% reduction;

condition J in Fig. 4-6A and B) even when a combination of changes in electrical properties of the model motoneuron were concurrently implemented to further increase its hyperexcitability (V_{th} was reduced by 5 mV, V_{rest} was depolarized by 5 mV, and R_m at the soma and dendrites was increased by 33%). Importantly, when the combined changes in electrical properties were included, the level of synaptic input required to activate fully the dendritic PIC decreased and full activation of the dendritic PIC was achieved at 100% of the strength of the Ia-afferent system.

Given that the percent change in the PIC amplitude after SCI is not yet determined experimentally, we examined the likelihood of the change in PIC amplitude being a result of the upregulation of the Na^+ and Ca^{+2} PICs in chronic injury. The density of the persistent Na^+ and $Ca_V1.3$ channels was increased such that the amplitude of the Na^+ and Ca^{+2} PICs was increased to 150%. This is the ratio by which the PIC amplitude was increased in response to the administration of the noradrenergic α_1 agonist, methoxamine, to the decerebrate cat preparation (Lee and Heckman 2000). Under this condition, application of a DC electrical field along the mediolateral axis of the SC caused significant reduction in the motoneuronal firing rate ($\approx$ 47% reduction; condition K in Fig. 4-6B). When the combined changes in electrical properties were included in conjunction with the increase in the PIC amplitude, substantial reduction in firing rate was still achieved ($\approx$ 67% reduction; condition L in Fig. 4-6B). Provided that a recent immunohistochemical study reported no change in the density of the $Ca_V1.3$ channels in spinal motoneurons of spastic rats after chronic SCI, we also examined the possibility of the enhancement in PIC amplitude due to changes in channel properties (e.g., hyperpolarization of the half-activation potential of $Ca_V1.3$ channels) following injury. The half-activation potential of the $Ca_V1.3$ channels was hyperpolarized by 5 mV in conjunction with the combined changes in electrical properties. Under these conditions, application of electrical fields resulted in a significant reduction in firing rate ($\approx$ 55% reduction; condition M in Fig. 4-6A and B). Again, a low level of synaptic input (100% of Ia I_N) was required to activate fully the dendritic PIC in conditions K to M in Fig. 4-6B. Thus, our results demonstrate that reduction in firing rate due to the application of

electrical fields is still viable after SCI when changes in the electrical and PIC-mediating channel properties of spinal motoneurons take place.

We also investigated the effect of changes in the distribution or activation pattern of synaptic inputs after SCI on the reduction in firing rate of spinal motoneurons during the application of electrical fields (Fig. 4-6C). This was achieved by simulating the experiments conducted by Delgado-Lezama et al (1999) in which preferential activation of different parts of the dendritic tree (medial versus lateral) was obtained through the activation of different descending tracts (the medial versus the dorsolateral funiculus). In the present study, the medial synapses were preferentially activated at 500%, whereas the lateral synapses were activated at 100% during the application of a DC electrical field along the mediolateral axis of the SC (condition B in Fig. 4-6C). Similarly, preferential activation of lateral, rostral, and caudal synapses were simulated during the application of the same field along the mediolateral axis of the SC (conditions C to E in Fig. 4-6C, respectively). These simulations were compared to the homogenous activation of all synapses during the application of the same field (condition A in Fig. 4-6C). Our results show that reduction in the motoneuronal firing rate was still achieved during preferential activation of synaptic contacts that caused full activation of the dendritic PIC.

4.3.3 Effect of AC electrical fields on the firing behavior of spinal motoneurons

Because long-duration DC electrical fields could potentially cause tissue damage and induce long-term changes in the excitability of neurons (Chan and Nicholson 1986) which in some cases may not be desirable, we investigated the effect of low-frequency AC electrical fields ($\approx$ 0.5 Hz) of different waveforms on the firing behavior of motoneurons (Fig. 4-7). An AC electrical field of square waveform was applied along the mediolateral axis and the motoneuronal firing rate was measured (Fig. 4-7A). Reduction in the motoneuronal firing rate was achieved during the different phases of the applied AC field (Fig. 4-7A - upper trace) and was also accompanied by a comparable reduction in I_{Ca} (Fig. 4-7A - 2nd trace). However, the amount of reduction in both the firing rate and I_{Ca} was variable during the different phases of the applied AC field due to the imperfect symmetry of the model motoneuronal dendritic projections around the soma along the

mediolateral axis. Peaks in firing rate were seen during the abrupt transitions between the different phases of the AC field due to the capacitive property of the membrane (arrows in Fig. 4-7A). To minimize these transitional peaks in firing rate, a trapezoidal-waveform field of the same intensity was examined to allow for a relatively smooth transition between the different phases of the AC field. Peaks in firing rate were minimized and a relatively smoother I_{Ca} was achieved (Fig. 4-7B). The effect of sinusoidal electrical fields on the firing behavior of spinal motoneurons was also simulated as these fields are widely used in experimental setups (Chan and Nicholson 1986; Chan et al. 1988; Hounsgaard and Kiehn 1993). During a sinusoidal field the intensity of the field continuously varies with time and so does the change in field polarity during the different phases of the field. Thus, a variable reduction in firing rate and I_{Ca} was achieved with no sudden peaks due to the smooth variation in the field intensity (Fig. 4-7C - black trace). Sinusoidal electrical fields of higher frequencies (100 Hz) resulted in a steady, but lower, reduction in firing rate (Fig. 4-7C - gray trace).

4.4 DISCUSSION

The goal of the present study was to provide a 'proof of principle' that extracellularly-applied electrical fields can modulate the excitability of spinal motoneurons through regulating the magnitude of their dendritic PIC. Our results demonstrate, for the first time, that DC and AC electrical fields could suppress the excitability of active motoneurons and induce reduction in their firing rate. This reduction is modulated by the intensity of the imposed field. The suppression of motoneuronal excitability suggested by the present study results from the interaction between the field-induced polarization, the relative positional symmetry of the soma with respect to the dendrites, and the activation level of the dendritic voltage-gated channels. The reduction in firing rate was not instantaneous and took hundreds of milliseconds to reach steady-state ($\approx$ 200 to 300 ms). This is due to the distal location of the dendritic $Ca_V1.3$ channels, their slow kinetics, and the capacitive property of the cell membrane (Jefferys et al. 2003).

4.4.1 Comparison to experimental results

Our simulation results are in agreement with previous experimental studies in which the effects of electrical fields were investigated. Application of electrical fields on spinal motoneurons was examined experimentally to demonstrate the dendritic origin of the Ca^{+2} channels responsible for the Ca^{+2} plateau (Hounsgaard and Kiehn 1993). It is evident from their illustrations that there was a reduction in the motoneuronal firing activity when a soma-depolarizing DC field was applied as compared to that when the DC field was removed (see Fig. 6Ab and c in Hounsgaard and Kiehn (1993)). Mid-molecular layer stellate cells of the turtle cerebellum which have dendrites oriented in all directions (similar to motoneurons) were found to be modulated by reversed electrical fields (Chan and Nicholson 1986). Our results are also in concurrence with those of Delgado-Lezama et al. (1999) in which the effect of facilitation of local synaptic inputs on the motoneuronal firing rate and generation of plateau potentials during the application of DC electrical fields was studied. The present study demonstrated that electrical fields could facilitate the recruitment of inactive motoneurons, but suppress the excitability of those already active (particularly motoneurons with fully activated PIC).

Weak electrical fields could avoid the facilitation of motoneuronal recruitment, but are less effective in suppressing the overall motoneuronal excitability. Physiologically, motoneurons appear to fire mostly in the tertiary range of their F-I relationship in which their dendritic PIC is fully activated (ElBasiouny et al. 2006; Hornby et al. 2002). During spasticity, motoneurons are actively firing with their PIC fully activated (Li et al. 2004a; Li et al. 2004b). Application of electrical fields would then effectively suppress the excitability of those motoneurons; thereby, reducing the severity of spasticity.

4.4.2 Effect of electrical fields on ionic channels

One could argue that the present study only included the $Ca_V1.3$ channels on the dendrites of the model motoneuron; however, there are undoubtedly other dendritic voltage-gated conductances that mediate different inward and outward currents. The effect of electrical fields described in the present study for reducing the excitability of motoneurons is ascribed mainly to the differential polarization of the dendritic tree. Hyperpolarization of the membrane potential of one part of the dendritic tree would result in reducing all ionic (inward and outward) currents mediated by the dendritic channels. Alternatively, depolarization of the membrane potential of the other part of the dendritic tree would result in increasing all outward currents whereas the magnitude of inward currents would depend on the dendritic membrane potential relative to that of the turning point of the channel I-V relationship, as explained in Fig. 4-3B. Our simulations of the dendritic $Ca_V1.3$ channels demonstrated that the net effect is usually a reduction in the mediated current. Therefore, polarization of the dendrites by the applied electrical fields would result in reducing the excitability of motoneurons regardless of the type of the dendritic channels. It is expected that the activation/deactivation of the hyperpolarization-activated mixed cation current (I_h) via the differential depolarization induced by the applied field would have a small effect on the motoneuronal firing rate. This is because the channels mediating the I_h appear to be located at or proximal to the soma as no prolonged tail currents are observed at the termination of the voltage commands used to study this current (Kiehn et al. 2000; Kjaerulff and Kiehn 2001). Therefore, these channels will be minimally affected by the imposed field as they are close to the field's neutral point near the motoneuronal somata.

Furthermore, the dendritic $Ca_V1.3$ channels were distributed in the present study on dendritic segments of path distance 300 to 850 μm from the soma based on the *wide band distribution* previously described in ElBasiouny et al. (2005) in which multiple sets of experimental measurements were matched. If these channels were present on more distal dendritic segments of other neurons, larger reductions in firing rate would be obtained as longer dendritic projections experience higher levels of polarization and their channels are more (de)activated by the applied field (Chan and Nicholson 1986).

4.4.3 Spatial activation of the dendritic PIC

One could contend that the effect of electrical fields in reducing the motoneuronal firing rate is contingent upon the condition of having the *entire* dendritic tree strongly depolarized by synaptic inputs causing full activation of the PIC in all dendritic regions. Thus, motoneurons whose dendrites are partially depolarized by synaptic inputs would experience an increase in their firing activity by the applied field. In the present study, we examined various patterns of synaptic activation that caused either strong depolarization of the whole dendrites or depolarization that was confined to parts of the dendritic tree (Fig. 4-6C). In the latter, synaptic activation resulted in full activation of the dendritic PIC in only the depolarized portions of the dendrites and partial activation of the PIC in the other portions. Under these conditions, the electrical field was still effective in reducing the motoneuronal firing rate. Therefore, the dendritic tree does not need to be entirely depolarized for the suppression of firing rate by electrical fields to be effective. In other words, the effect of the electrical field in suppressing the motoneuronal excitability is independent of the pattern of synaptic activation that activates the dendritic PIC.

4.4.4 Changes following SCI

It has been shown that spinal motoneurons undergo changes in their electrical and morphological properties, and the number and distribution of synaptic inputs after SCI (Bose et al. 2005; Hochman and McCrea 1994a, b, c; Kitzman 2005, 2006, 2007). Morphologically, Kitzman (2005) showed that after SCI and the full development of spasticity there was a reduction in the size of the soma and the number of the primary,

secondary and tertiary dendrites of motoneurons innervating the spastic muscles. The motoneuronal electrical properties, on the other hand, showed a different trend. Some electrical properties were reduced (e.g., time constant, afterhyperpolarization duration), some were increased (e.g., rheobase, voltage-threshold), and others did not change (e.g., resting membrane potential, action potential height, input resistance) (Hochman and McCrea 1994b). For the synaptic inputs, Kitzman (2006; 2007) showed that during spasticity there was a significant increase in the ratio of the excitatory to inhibitory inputs; however, the increase appeared to originate primarily from interneuronal inputs. In the present study, we examined the effects of the change in the motoneuronal electrical properties and the distribution of synaptic activation on the reduction of firing rate induced by the application of electrical fields. Our results demonstrated that application of electrical fields for the suppression of the motoneuronal excitability is still effective after SCI when the motoneuronal electrical properties and the level and distribution of synaptic activation are altered (Fig. 4-6). The change in morphological properties was not examined in the present study as it is not clear from the published data whether the loss of the dendritic branches was equal in all directions (i.e., equal loss of the dendritic branches along the mediolateral, dorsoventral, and rostrocaudal axes of the SC) or biased towards some directions. Motoneurons that exhibit no directional bias in the loss of their dendritic segments would have their soma near to the neutral point of the imposed field, and would experience reduction in their firing rate during fields of reversed polarity (similar to Fig. 4-3A and B). On the other hand, motoneurons that exhibit directional bias in the loss of their dendritic segments would have their soma shifted relative to the neutral point, and would experience a net increase or reduction in their firing rate according to the field polarity. Application of AC fields of high intensity in this case would minimize the effects of the motoneuronal morphological changes after SCI or even of motoneurons with asymmetrical dendrites relative to the soma (e.g., motoneurons on the border of the gray and white matter have dendrites that trail that border; (Brown 1981). The high field intensity would create a steep change in the extracellular voltage gradient along the cell and would inactivate the Na^+ channels during the soma depolarization phase of those motoneurons which would cease their firing (similar to the effect of E- along the dorsoventral axis in Fig. 4-5C). The AC field would also minimize

the directional bias in the loss of the dendritic segments by reversing the field polarity across the cell during the alternating phases of the field.

In the present study, we activated the dendritic PIC fully by activating the synaptic inputs at 300% of the strength of the Ia-afferent system. One could argue that during spasticity muscle spasms are triggered by moderate synaptic inputs that activate the dendritic PIC. Thus, activating the motoneuron with a high level of synaptic input does not simulate the activation of the PIC during spasticity. When the combined changes in electrical and/or PIC properties were included in the model to simulate more realistically spastic motoneurons after SCI, full activation of the dendritic PIC was achieved at a lower level of synaptic input (100%, Ia $I_N \approx 5$ nA), a level that was barely adequate to recruit the motoneuron prior to these changes. Under these conditions, reduction in the motoneuronal firing rate was still obtained through the application of electrical fields (Fig. 4-6). Hence, suppression of the motoneuronal excitability by the applied electrical field is obtained regardless of the level of synaptic input required to cause full activation of the dendritic PIC. One could also argue that the density of the PIC-mediating channels (persistent Na^+ and $Ca_v1.3$ channels) in the present model were based on measurements obtained from motoneurons of animals with no injury (ElBasiouny et al. 2005). Consequently, these densities do not reflect the change in PIC amplitude after injury. It has been shown experimentally that motoneurons obtained from chronic spinal rats have enhanced (nearly two-fold increase) PICs relative to those obtained from acute spinal animals (Harvey et al. 2006c); however, the percent change in the PIC amplitude relative to that with no injury is yet undetermined. Recently, an immunohistchemical report showed no change in the density of $Ca_v1.3$ channels mediating the dendritic PIC in motoneurons of spastic rats after chronic SCI (Anelli et al. 2006). Furthermore, indirect assessment of the motoneuronal PIC amplitude from the firing profile of motor units could be obtained using a paired motor unit analysis technique in which the difference in firing rate at recruitment and derecruitment ($F_{r\text{-}d}$) is proportional to the amplitude of the PIC (Gorassini et al. 2004). This technique showed similar values of $F_{r\text{-}d}$ in healthy volunteers and individuals with chronic SCI indicating similar PIC amplitudes in both populations (Gorassini et al. 2002; Gorassini et al. 2004). Altogether, these observations

indicate that recovery of near-normal levels of PIC amplitude takes place after chronic injury, and that the lack of control of this PIC through the neuromodulatory drive from the brainstem leads to the muscle spasms seen after injury. Nevertheless, we examined in the present model various conditions in which the motoneuronal PIC had similar or upregulated (150%) amplitudes (through either a change in channel densities or channel properties) to those measured from uninjured animals (Fig. 4-6). Under these conditions, suppression of the motoneuronal excitability was still achieved by the application of electrical fields.

4.4.5 Effect of electrical fields on the various neuronal elements in the SC

Applied electrical fields would result in polarizing not only motoneurons in the SC but also other neuronal elements (e.g., sensory and motor axons, descending fibers, and interneurons). For sensory axons, primary afferents will be the most sensitive structures to the imposed field because of their large diameter and low threshold for polarization. Afferents experiencing a depolarizing field would be stimulated resulting in larger synaptic input to the spinal neurons, whereas those experiencing a hyperpolarizing field would be inhibited resulting in lesser synaptic input to the spinal neurons. This polarization in turn would modulate the level of synaptic input reaching the cells. We do not expect this modulation of synaptic inputs to change our findings given that reduction of firing rate was achieved at all levels of synaptic inputs (Fig. 4-5A - upper panel) and under different synaptic activation patterns (Fig. 4-6C). Similarly, motor axons could be polarized as well by the applied field. Hyperpolarization of motor axons would cause reduction in muscle activity, whereas depolarization would cause enhancement of muscle activity. The effect of the latter could be modulated by using high intensity electrical fields that would inactivate the Na^+ channels at nodes of Ranvier and prevent axonal firing (similar to the effect of E- along the dorsoventral axis in Fig. 4-5C). Descending axons could also be activated by the applied electrical field. The resultant effect of their stimulation would be a preferential activation of synaptic inputs to motoneurons. Simulations of Fig. 4-6C illustrated that suppression of the motoneuronal excitability through the application of electrical fields could be achieved even during non-homogenous activation of dendritic synaptic inputs. For interneurons, the effect of the

applied electrical field will depend on their morphology. Previous studies of two classes of spinal interneurons (Renshaw and Ia-interneurons) showed that they have a central soma with dendrites projecting radially in many directions; however, their dendrites are relatively smaller and of simpler structure as compared to those of motoneurons (Bui et al. 2003; Fyffe 1990; Rastad et al. 1990). This implies that spinal interneurons would be similarly polarized by the applied electrical field but to a lesser extent, and motoneurons would experience the largest degree of polarization. However, similar to their proposed effect on motoneurons with asymmetrical dendrites relative to the soma, high intensity electrical fields would suppress the excitability of other interneurons that might have positional asymmetry of their soma relative to the dendrites, by inactivating their Na^+ channels (similar to the effect of E- along the dorsoventral axis described in Fig. 4-5C).

Although the effect of extracellularly-applied electrical fields in the SC was simulated in the present study, our results and the discussed concepts could also be extended to electrical fields applied in the brain. For instance, weak cathodal transcranial DC stimulation (tDCS) has been shown to induce a long-term reduction in cortical excitability, whereas anodal tDCS induced a long-term increase in cortical excitability (Ardolino et al. 2005; Lang et al. 2004). The mechanisms underlying tDCS-induced effects are still unclear, but its action could be explained by the interaction between the neuronal differential polarization induced by the applied field, orientation of the pyramidal neurons relative to the applied field, and the positional asymmetry of the soma with respect to the dendrites in brain neurons. Thus, the neuronal excitability and firing activity would be increased by a soma-depolarizing field (anodal tDCS) and reduced by a soma-hyperpolarizing field (cathodal tDCS) similar to the effects of applied electrical fields on cerebellar Purkinje cells (Chan and Nicholson 1986; Chan et al. 1988).

4.4.6 Feasibility and potential applications

The suppression of motoneuronal excitability for the reduction of spasticity after SCI has been recently suggested through the delivery of extracellularly-injected current pulses of various waveforms (ElBasiouny and Mushahwar 2007). However, electrical fields generated by extracellularly-applied currents between plate electrodes for the reduction of

spasticity may have a number of advantages over those generated by extracellularly-injected current pulses through microelectrodes. First, electrical fields are more feasible and easier to implement as they could be applied less invasively and polarize neural populations distant from the electrodes. Second, electrical fields would polarize all neuronal pools between the plate electrodes (i.e., regional effect) eliminating the need for implanting multiple microelectrodes (with each having a local effect) in order to obtain a functional outcome. Third, given that the applied current is not delivered by local sharp microelectrodes, current density induced in the tissue is low, which minimizes the potential for tissue damage in long-term chronic stimulation applications (Francis et al. 2003). Moreover, the finding of the present study that AC electrical fields could maintain a reduction in the firing rate of motoneurons even during the different opposite phases of the applied field resolves some of the potential drawbacks of DC electrical fields. The amount of reduction in firing rate was found to be dependent on the extension of the dendritic projections and their symmetry around the soma along the axis of the applied field. This dependence could negatively affect the influence of the imposed field if it were permanently applied in a direction that had little impact on the cells or polarize some neurons more than the others based on their orientation relative to the applied field in that direction. AC electrical fields would then minimize this directional bias and allow for more distributed polarization of neurons along that direction and during the different phases of the imposed field. It is also known that application of DC electrical fields produces changes in the extracellular concentration of K^+ ions (Chan and Nicholson 1986) which would affect the long-term excitability of neurons and their firing behavior. Application of AC electrical fields would avoid these long-term changes in spinal neurons while maintaining a reduction in their firing rate.

In the SC, the orientation of the motoneuronal dendrites varies based on the location of their somata (Scheibel and Scheibel 1969; Sterling and Kuypers 1967). Motoneurons with somata in the ventral part of the ventral horn have dendrites that project primarily in the rostrocaudal axis of the SC, whereas those with somata in the dorsal or lateral parts of the motor cell columns have dendrites that project radially (Brown 1981). Therefore, electrical fields applied along the rostrocaudal axis of the SC would be the most effective

in modulating the excitability of spinal motoneurons. Such electrical fields could be practically implemented by passing electrical current between slightly shifted, or even non-overlapping, plate electrodes along the rostrocaudal axis of the SC.

4.4.7 Motoneuronal firing behavior during spasticity

The firing behavior of spinal motoneurons during spasticity could be inferred from that of human motor units after SCI (Thomas and Ross 1997). During muscle spasms, the firing behavior of human motor units was found to be variable. Thomas & Ross (1997) found that the firing rate of the majority of motor units was proportional to the intensity of muscle spasms, other motor units fired in doublets only near the peak intensity of the spasm, whereas the rest of motor units had a relatively constant firing rate. For the second and third groups, muscle spasms may be generated due to synchronous activation of their motoneurons. Reduction of the firing rate as proposed in the present study may suppress muscle spasms by reducing the motoneuronal firing rate of the first group and desynchronizing the motoneuronal spiking of the second and third groups. Furthermore, Zijdewind and Thomas (2003) observed significantly increased motor unit firing activity during muscle spasms that was not seen in the same unit during maximum voluntary contractions in individuals with incomplete SCI. Therefore, the reduction, but not the blockade, of motoneuronal firing rate would allow for reduction of spastic muscle contractions without preventing muscle activation through the residual voluntary drive. Application of electrical fields of *moderate* intensity could facilitate the recruitment of inactive motoneurons, if present, during muscle spasms. This could cause an increase in the level of spasticity. However, the firing rate of those newly recruited motoneurons will be controlled by the applied field. Given the aforementioned desirable properties of electrical field stimulation (e.g., safety, feasibility, and permitting volitional muscle activation), AC electrical fields could be applied prophylactically to avoid spastic seizures. Electrical fields could also be used in the management of bladder dysfunction after SCI by suppressing the hyperactivity of the sphincter motoneurons during urination and preventing co-contraction of the sphincter and the detrusor muscle of the bladder.

In summary, electrical fields were shown to reduce the excitability of spinal motoneurons. This could provide an effective rehabilitation therapy for suppressing the increased excitability of spinal motoneurons and the severity of spasticity following SCI.

4.5 FIGURES

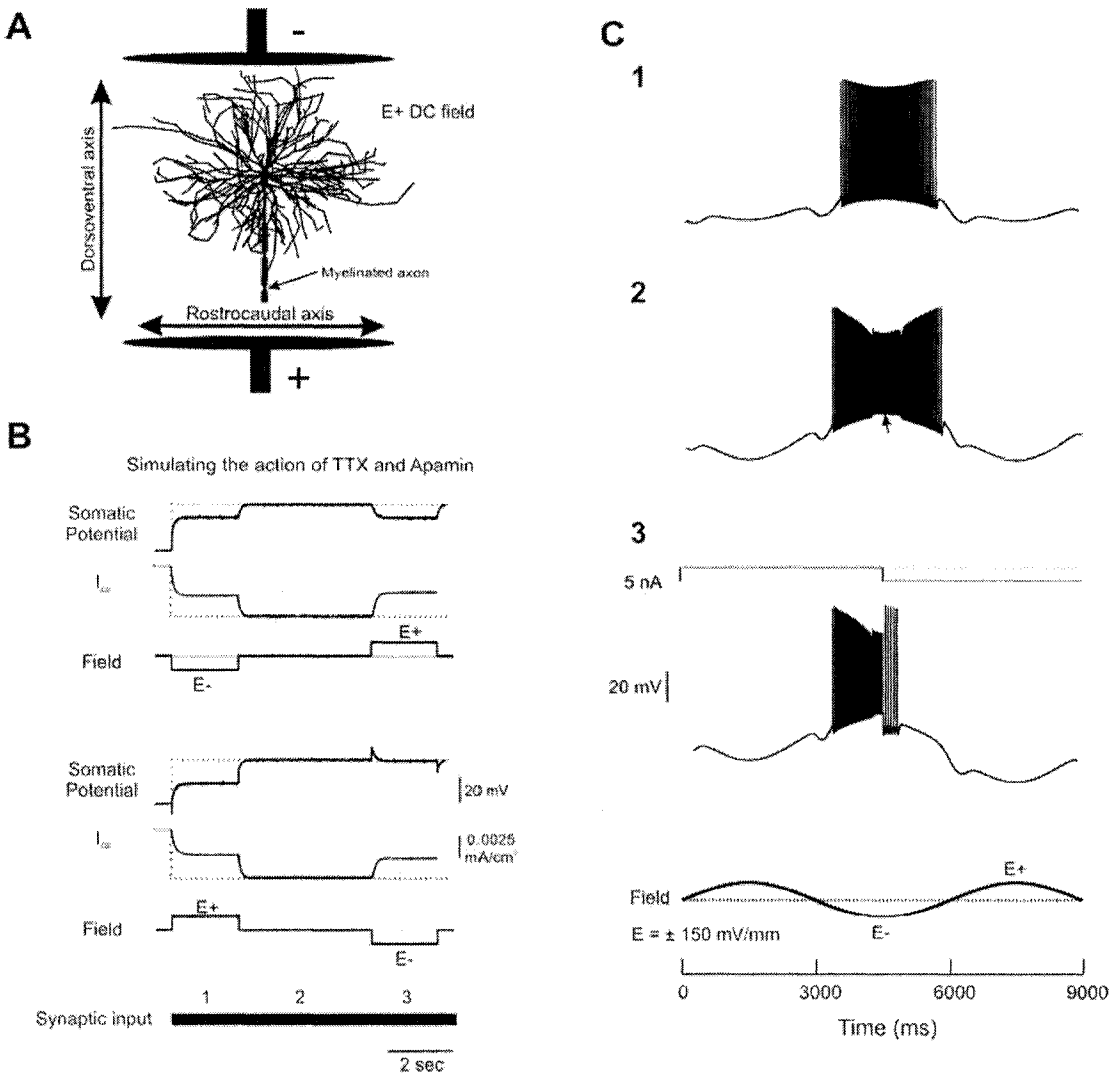

Figure 4-1. Verification of the effect of electrical fields on the behavior of the model motoneuron. **A**: The model motoneuron was placed in an electrical field (E+ orientation) applied along the dorsoventral axis of the SC and parallel to the axon, initial segment, and axon hillock of the motoneuron. Diagram is not to scale. The myelinated axon was magnified to illustrate its orientation relative to the direction of the applied field. **B**: The electrical field was applied during the simulation of the presence of TTX and apamin. The somatic transmembrane potential (upper trace) and I_{Ca} (2nd trace) were measured simultaneously during the application of a DC electrical field along the dorsoventral axis of the SC (3rd trace) and activation of synaptic inputs (lower trace). Dotted lines in the 1st,

2^{nd}, 4^{th}, and 5^{th} traces show the magnitude of the somatic transmembrane potential and I_{Ca}, in response to synaptic activation only. During the application of an E+ DC field, the soma and initial segment were hyperpolarized, whereas they were depolarized during the application of an E- field. **C**: Cell firing evoked by field stimulation along the dorsoventral axis of the SC when no synaptic input was activated. A sinusoidal electrical field (lower trace) was applied as shown in **A** that evoked cell firing during the cathodic phase of the field when the soma was depolarized (1^{st} trace). Higher firing rate and activation of the dendritic Ca^{+2} PIC were evoked when the field intensity was increased (2^{nd} trace). Arrow shows the flat baseline of the somatic transmembrane during activation of the plateau potential (compare to Fig. 3A1 in Chan et al. (1988). Cell firing was interrupted and the somatic membrane potential was lowered when an intracellular hyperpolarizing current pulse (-4.5 nA, 4500 ms) was injected at the soma during the activation of the dendritic plateau potential (3^{rd} trace - compare to Fig. 3A2 in Chan et al. (1988).

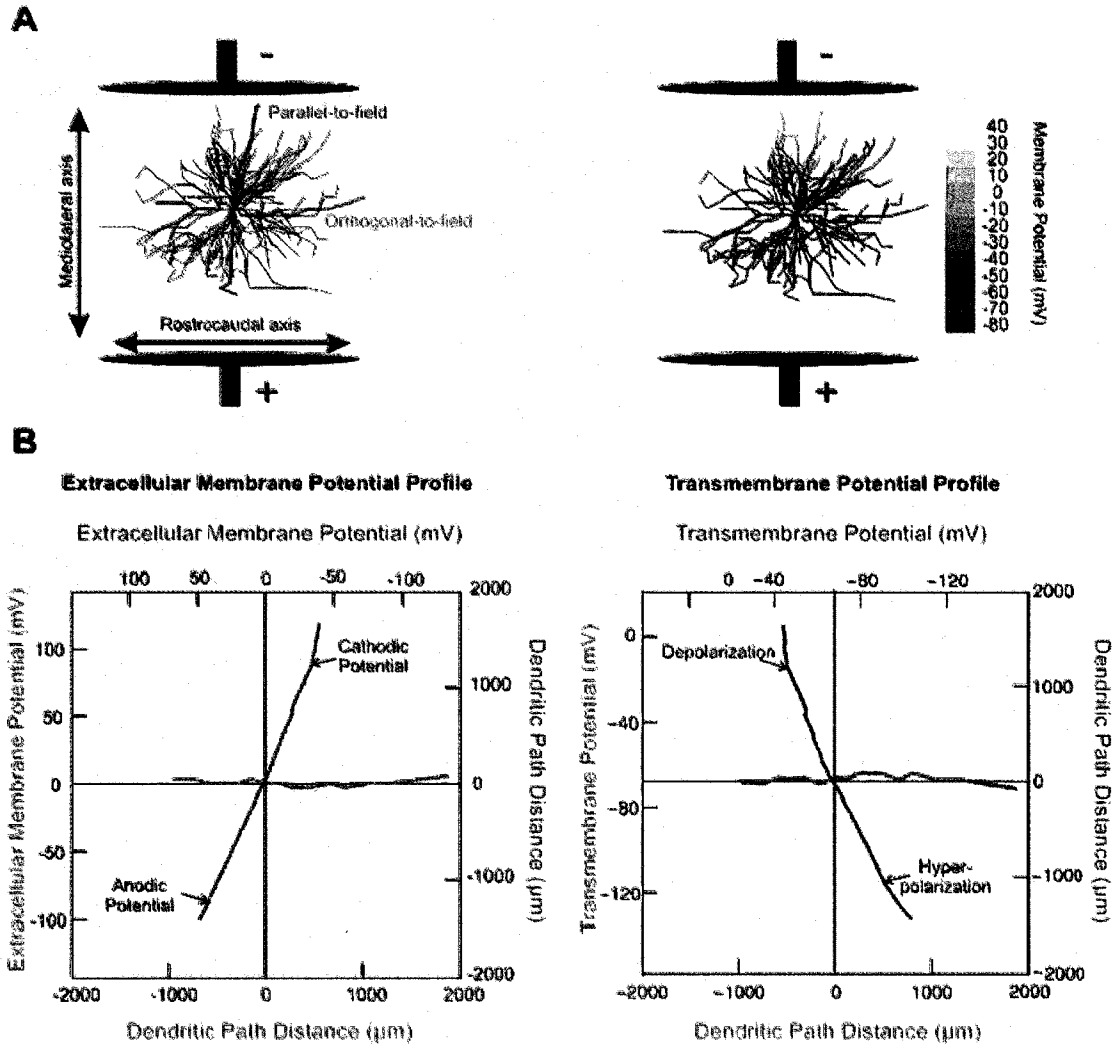

Figure 4-2. Effect of DC electrical field on the membrane potential of the model motoneuron. **A**: Electrical field applied along the mediolateral axis of the SC and generated by current flow between two plate electrodes was simulated (left panel). Dendritic segments aligned orthogonal (blue) and parallel (red) to the field axis are shown. Spatial distribution of the dendritic transmembrane potential caused by the imposed field (right panel). **B**: The extracellular membrane potential (left panel) and transmembrane potential (right panel) profiles formed by the imposed electrical field along the dendritic segments shown in A are presented at steady-state and during no activation of synaptic input. The spatial arrangement of the dendritic segments is preserved relative to the imposed field. Labels of the abscissa and the ordinate have the same color as the trace. Soma location is at the origin.

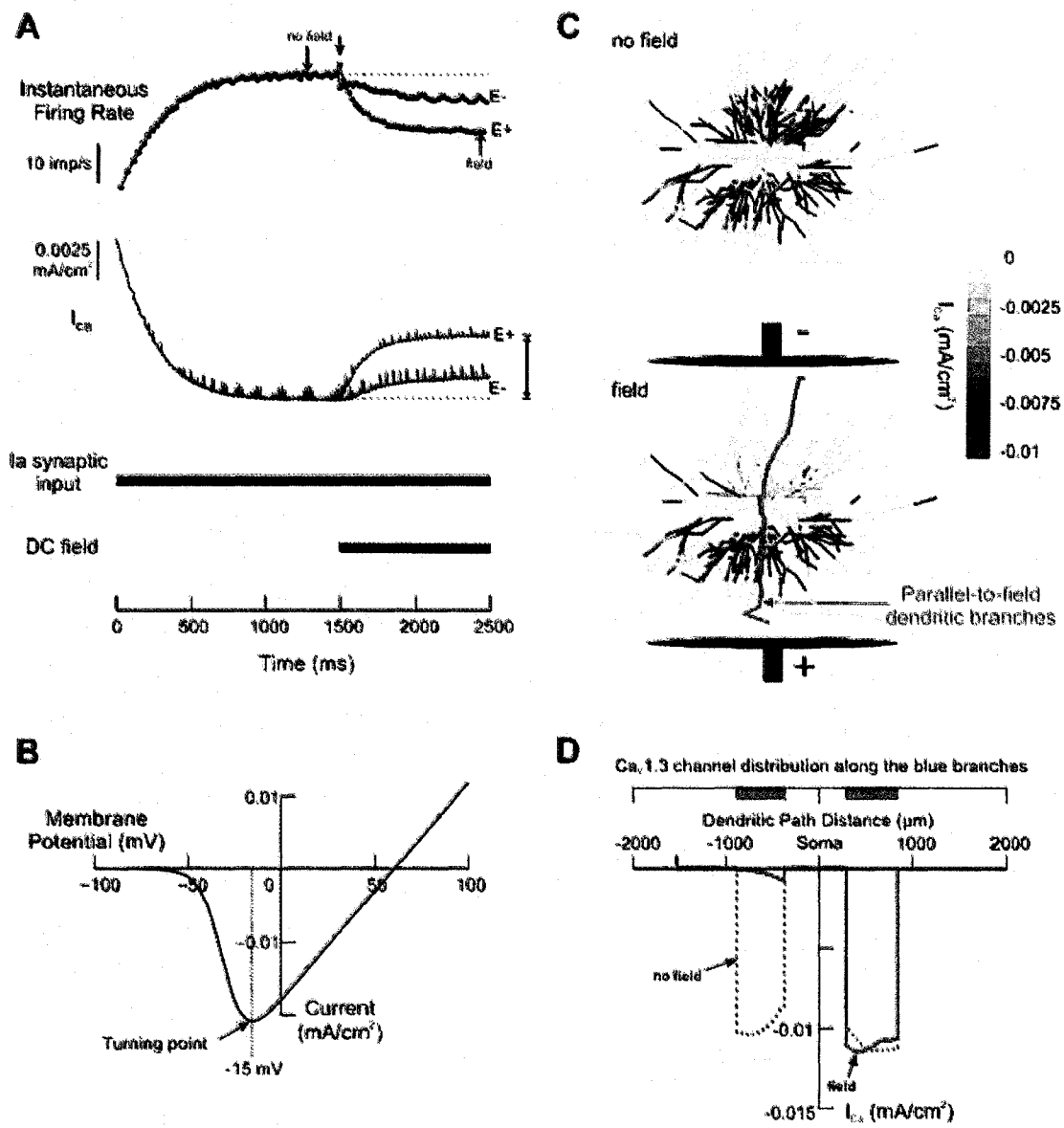

Figure 4-3. Effect of DC electrical fields on the firing behavior of the model motoneuron. **A**: The somatic firing rate (upper trace) and I_{Ca} (2nd trace) during activation of synaptic inputs (300% that of the Ia-afferent system, 3rd trace). After steady-state firing was reached, a DC field (lower trace) of either polarity (E+ or E-) was applied along the mediolateral axis of the SC (as shown in Fig. 4-2). The arrow shows the instantaneous increase in firing rate at the onset of the electrical field. The thin dotted lines in the upper and 2nd traces illustrate the steady-state level of firing rate and I_{Ca}, respectively. The amount of reduction in I_{Ca} is also indicated by the arrow in the 2nd trace. **B**: The I-V

relationship of the dendritic $Ca_V1.3$ channels. The vertical dotted line illustrates the membrane potential at which the inward current starts to decrease (turning point). **C**: Spatial distribution of I_{Ca} mediated through the dendritic $Ca_V1.3$ channels before (upper panel) and after (lower panel) the application of the electrical field. Current flowing axially through the model dendritic compartments towards the soma is not shown. **D**: The amplitude of I_{Ca} flowing through the dendritic segments aligned parallel to the imposed field (shown in blue in **C**) before (dashed line) and after (solid line) the application of the electrical field in A. The distribution of the $Ca_V1.3$ channels along the dendritic (blue) branches is indicated by the horizontal blue bars.

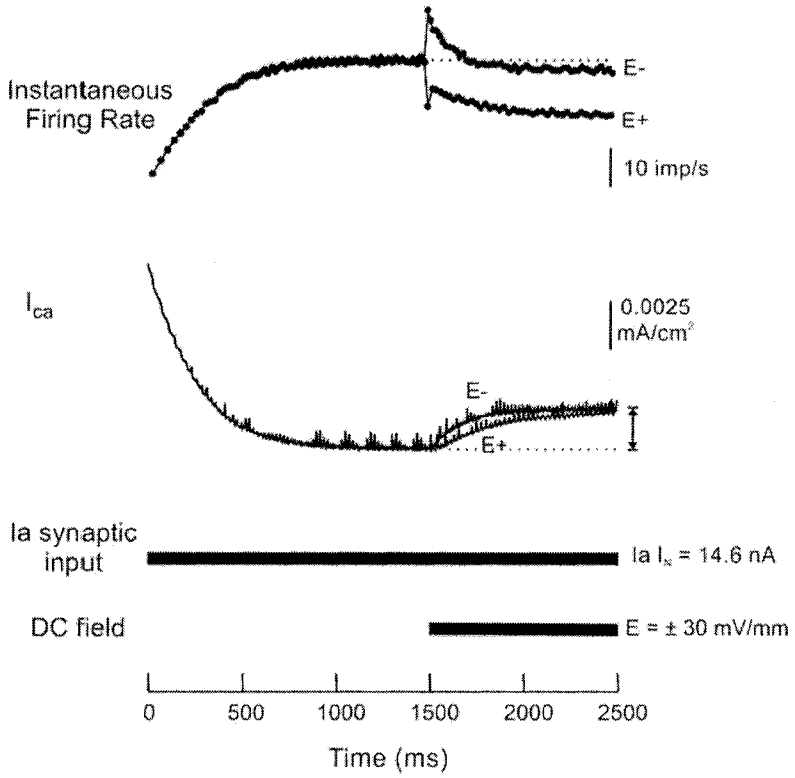

Figure 4-4. Effect of DC electrical fields that caused direct polarization of the axon, initial segment, and axon hillock. The motoneuronal firing rate (upper trace) and I_{Ca} (2nd trace) during activation of synaptic inputs (300% that of the Ia-afferent system, 3rd trace). After steady-state firing was reached, a DC field (lower trace) of either polarity (E+ or E-) was applied along the dorsoventral axis of the SC (as shown in Fig. 4-1A). The thin dotted lines in the upper and 2nd traces illustrate the steady-state level of firing rate and I_{Ca}, respectively. The amount of reduction in I_{Ca} is also indicated by the arrow in the 2nd trace.

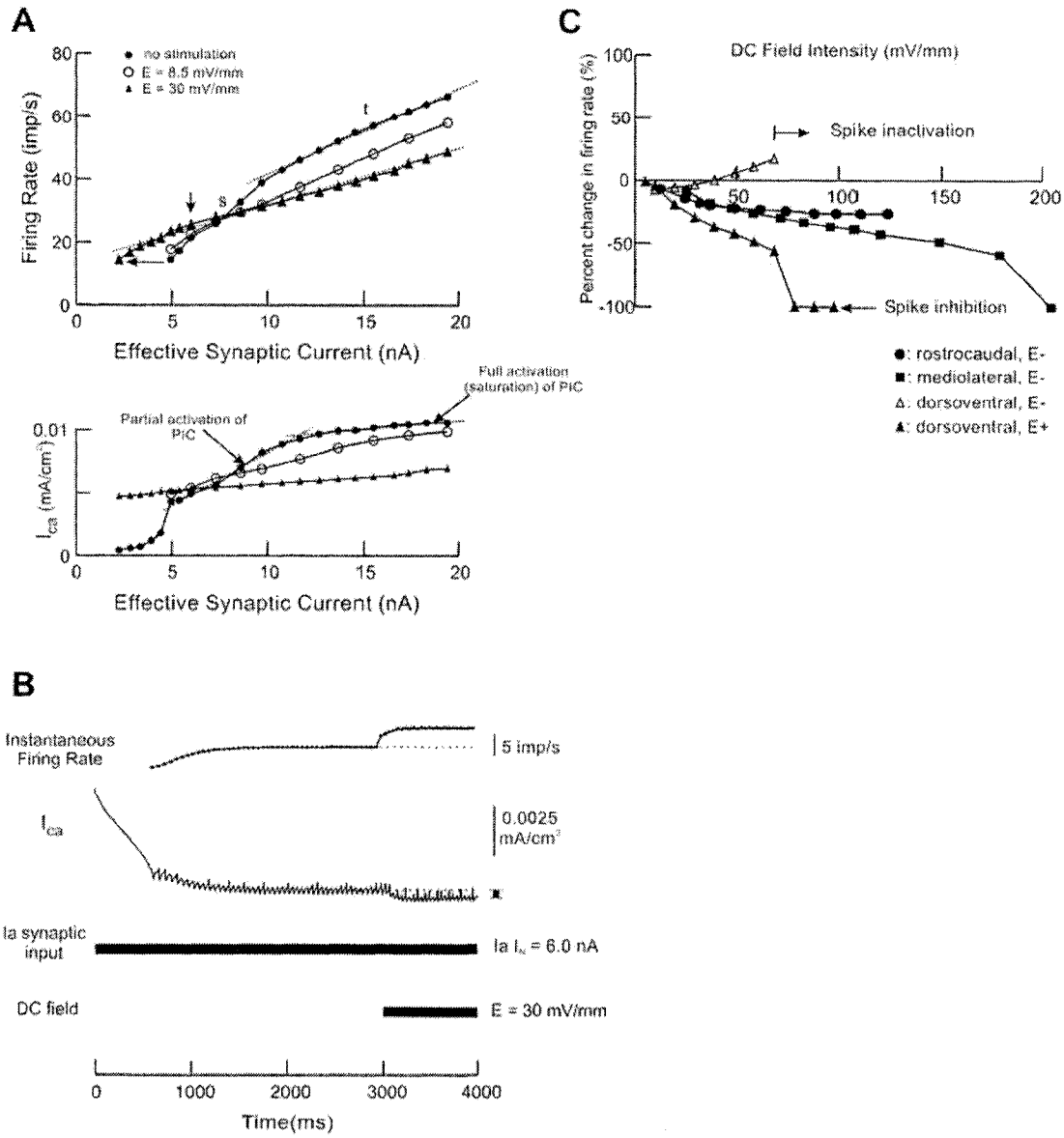

Figure 4-5. Effect of DC electrical fields on the excitability of the model motoneuron. **A**: The F-I relationship (upper panel) and I_{Ca} (lower panel) before (filled circles) and after (open circles and filled triangles) application of DC electrical fields of intensities 8.5 mV/mm and 30 mV/mm, respectively, along the mediolateral axis of the SC. *s* (4.95 Hz/nA, r^2= 0.995) and *t* (2.73 Hz/nA, r^2= 0.996) denote the secondary and tertiary ranges of the original F-I relationship. After stimulation, the F-I relationship and I_{Ca} became linear (2.72 Hz/nA, r^2= 0.997 for a field of 8.5 mV/mm and 1.84 Hz/nA, r^2= 0.989 for a field of 30 mV/mm). Arrows show early recruitment (horizontal arrow) and increase of

firing rate (vertical arrow) in response to electrical field stimulation of intensity 30 mV/mm at low levels of synaptic input. **B**: Increase in firing rate in response to DC electrical field stimulation of intensity 30 mV/mm at low levels of synaptic input indicated by the vertical arrow in **A**. Somatic firing rate (upper trace) and I_{Ca} (2^{nd} trace) during synaptic activation (3^{rd} trace) of Ia I_N = 6.0 nA and application of a DC electrical field (lower trace). Black bar illustrates the increase in magnitude of I_{Ca}. **C**: Relation between the intensity of the applied DC field and the percent change in firing rate in response to field application along different axes of the SC.

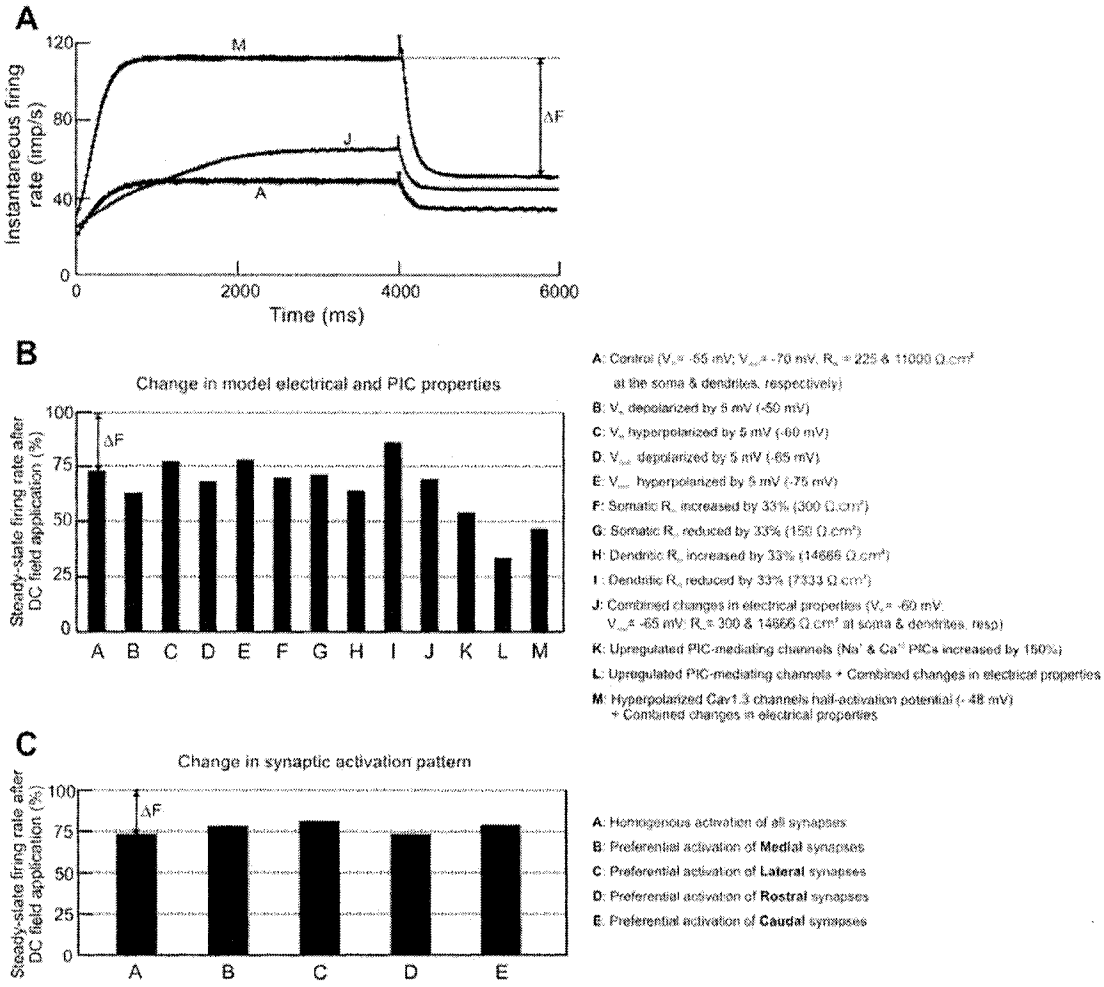

Figure 4-6. Effect of changes in electrical and PIC properties and patterns of synaptic activation on the reduction in the motoneuronal firing rate induced by application of a DC electrical field. **A**: Examples of reduction in the model motoneuron firing rate induced by the application of a DC electrical field along the mediolateral axis of the SC (similar to E+ condition in Fig. 4-3A) under conditions (A, J, and M) explained in **B**. Note the difference in the level of steady-state firing rate achieved before the application of the electrical field and the time course of its development due to the change in excitability of the model motoneuron under these conditions. The black bars in **B** represent the steady-state motoneuronal firing rate after application of the DC electrical field and after the alteration in different electrical and PIC properties of the model motoneuron. The bars in **C** represent the steady-state motoneuronal firing rate after the application of the DC field

and during homogenous and preferential activation of different synapses. The double arrow indicates the amount of reduction in firing rate (ΔF) relative to the steady-state motoneuronal firing rate before application of the DC field. The dendritic PIC was fully activated through synaptic activation under all conditions of panels **A**, **B**, and **C**.

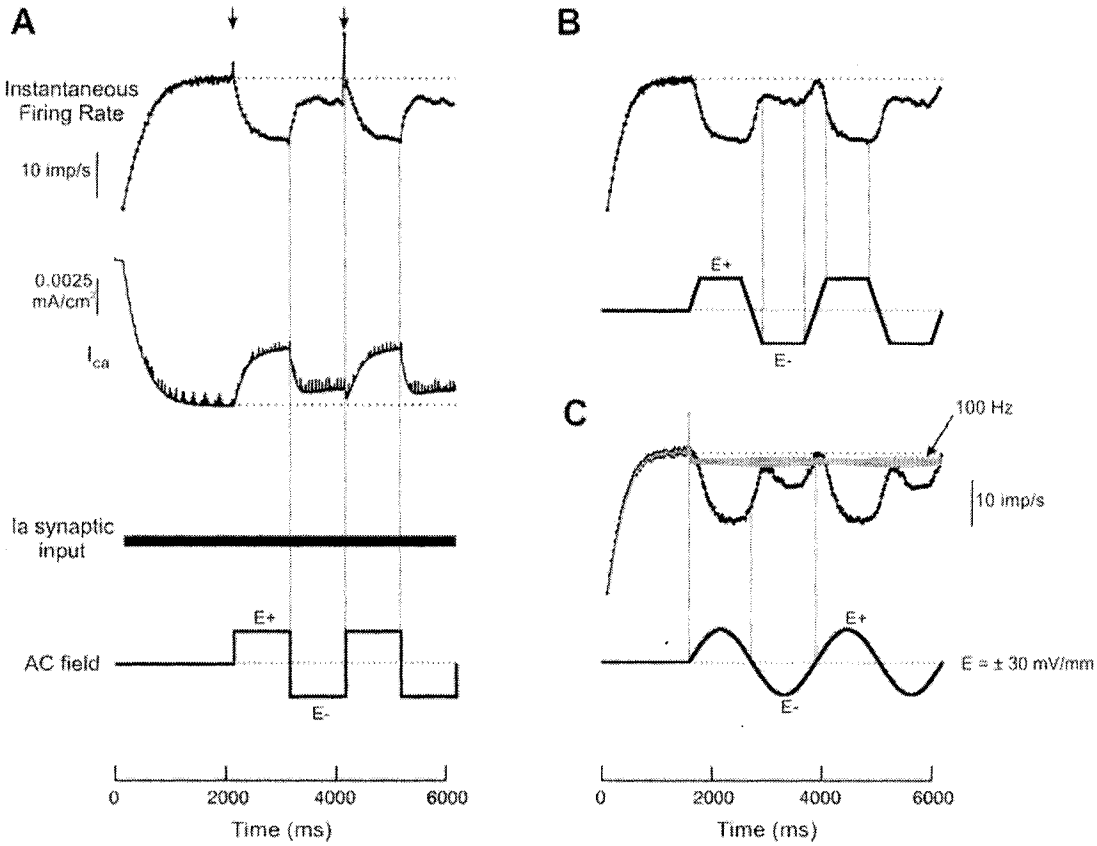

Figure 4-7. Effect of AC electrical fields on the firing behavior of the model motoneuron Effect of a square-waveform (**A**), trapezoidal-waveform (**B**), and sinusoidal (**C**) low-frequency AC electrical fields on the firing behavior of the model motoneuron. In A, somatic firing rate (upper trace) and I_{Ca} (2nd trace) during synaptic activation (3rd trace) and application of a square AC electrical field (lower trace) along the mediolateral axis of the SC are shown. Arrows in **A** show the abrupt jumps in firing rate due to the capacitance of the membrane. In **B** and **C**, somatic firing rate (upper trace) and AC electrical field (lower trace) along the mediolateral axis of the SC are shown. Maximum field intensity (E) was 30 mV/mm. Gray trace in **C** shows cell firing rate in response to sinusoidal electrical field stimulation of 100 Hz and same field intensity.

4.6 REFERNECES

Anelli R, Sanelli L, Bennett DJ, and Heckman CJ. Expression of L-type calcium channel [alpha]1-1.2 and [alpha]1-1.3 subunits on rat sacral motoneurons following chronic spinal cord injury. *Neuroscience* In Press, doi: 10.1016/j.neuroscience.2006.12.043, 2006.

Ardolino G, Bossi B, Barbieri S, and Priori A. Non-synaptic mechanisms underlie the after-effects of cathodal transcutaneous direct current stimulation of the human brain. *J Physiol (Lond)* 568: 653-663, 2005.

Baginskas A, Gutman A, and Svirskis G. Bi-stable dendrite in constant electric field: A model analysis. *Neuroscience* 53: 595-603, 1993.

Bikson M, Inoue M, Akiyama H, Deans JK, Fox JE, Miyakawa H, and Jefferys JGR. Effects of uniform extracellular DC electric fields on excitability in rat hippocampal slices in vitro. *J Physiol (Lond)* 557: 175-190, 2004.

Bose P, Parmer R, Reier PJ, and Thompson FJ. Morphological changes of the soleus motoneuron pool in chronic midthoracic contused rats. *Experimental Neurology* 191: 13-23, 2005.

Brown A. *Organization in the spinal cord. The anatomy and physiology of identified neurones*. Berlin Heidelberg New York: Springer-Verlag, 1981.

Bui TV, Cushing S, Dewey D, Fyffe RE, and Rose PK. Comparison of the Morphological and Electrotonic Properties of Renshaw Cells, Ia Inhibitory Interneurons, and Motoneurons in the Cat. *J Neurophysiol* 90: 2900-2918, 2003.

Burke RE and Glenn LL. Horseradish peroxidase study of the spatial and electrotonic distribution of group Ia synapses on type-identified ankle extensor motoneurons in the cat. *J Comp Neurol* 372: 465-485., 1996.

Burke RE, Walmsley B, and Hodgson JA. HRP anatomy of group Ia afferent contacts on alpha motoneurones. *Brain Res* 160: 347-352., 1979.

Carlin KP, Jones KE, Jiang Z, Jordan LM, and Brownstone RM. Dendritic L-type calcium currents in mouse spinal motoneurons: implications for bistability. *Eur J Neurosci* 12: 1635-1646, 2000.

Chan C and Nicholson C. Modulation by applied electric fields of Purkinje and stellate cell activity in the isolated turtle cerebellum. *J Physiol* 371: 89-114, 1986.

Chan CY, Hounsgaard J, and Nicholson C. Effects of electric fields on transmembrane potential and excitability of turtle cerebellar Purkinje cells in vitro. *J Physiol* 402: 751-771, 1988.

Cullheim S, Fleshman JW, Glenn LL, and Burke RE. Membrane area and dendritic structure in type-identified triceps surae alpha motoneurons. *J Comp Neurol* 255: 68-81, 1987.

Delgado-Lezama R, Perrier J-F, and Hounsgaard J. Local facilitation of plateau potentials in dendrites of turtle motoneurones by synaptic activation of metabotropic receptors. *J Physiol (Lond)* 515: 203-207, 1999.

Delgado-Lezama R, Perrier J-F, Nedergaard S, Svirskis G, and Hounsgaard J. Metabotropic synaptic regulation of intrinsic response properties of turtle spinal motoneurones. *J Physiol* 504: 97-102, 1997.

ElBasiouny SM, Bennett DJ, and Mushahwar VK. Simulation of Ca+2 Persistent Inward Currents in Spinal Motoneurons: Mode of Activation and Integration of Synaptic Inputs. *J Physiol (Lond)* 570: 355-374, 2006.

ElBasiouny SM, Bennett DJ, and Mushahwar VK. Simulation of Dendritic Cav1.3 Channels in Cat Lumbar Motoneurons: Spatial Distribution. *J Neurophysiol* 94: 3961-3974, 2005.

ElBasiouny SM and Mushahwar VK. Modulation of Motoneuronal Firing Behavior after Spinal Cord Injury using Intraspinal Microstimulation Current Pulses: A Modeling Study. *J Appl Physiol* In Press, doi: 10.1152/japplphysiol.01222.2006, 2007.

ElBasiouny SM and Mushahwar VK. Suppressing the excitability of spinal motoneurons by extracellularly applied electrical fields and current pulses: A modeling study. *2006 Abstract Viewer/Itinerary Planner, Washington, DC: Society for Neuroscience, Online* Session Number: 55, 2006.

Fleshman J, Segev I, and Burke R. Electrotonic architecture of type-identified alpha-motoneurons in the cat spinal cord. *J Neurophysiol* 60: 60-85, 1988.

Francis JT, Gluckman BJ, and Schiff SJ. Sensitivity of Neurons to Weak Electric Fields. *J Neurosci* 23: 7255-7261, 2003.

Fyffe REW. Evidence for separate morphological classes of Renshaw cells in the cat's spinal cord. *Brain Research* 536: 301-304, 1990.

Glenn L, Burke R, Fleshman J, and Lev-Tov A. Estimates of electrotonic distance of group Ia contacts on cat a-motoneurons: An HRP-morphological study. *Soc Neurosci Abstr* 8: 995, 1982.

Gorassini M, Yang JF, Siu M, and Bennett DJ. Intrinsic Activation of Human Motoneurons: Possible Contribution to Motor Unit Excitation. *J Neurophysiol* 87: 1850-1858, 2002.

Gorassini MA, Knash ME, Harvey PJ, Bennett DJ, and Yang JF. Role of motoneurons in the generation of muscle spasms after spinal cord injury. *Brain* 127: 2247-2258, 2004.

Harvey PJ, Li X, Li Y, and Bennett DJ. 5-HT2 Receptor Activation Facilitates a Persistent Sodium Current and Repetitive Firing in Spinal Motoneurons of Rats With and Without Chronic Spinal Cord Injury. *J Neurophysiol* 96: 1158-1170, 2006a.

Harvey PJ, Li X, Li Y, and Bennett DJ. Endogenous Monoamine Receptor Activation Is Essential for Enabling Persistent Sodium Currents and Repetitive Firing in Rat Spinal Motoneurons. *J Neurophysiol* 96: 1171-1186, 2006b.

Harvey PJ, Li Y, Li X, and Bennett DJ. Persistent Sodium Currents and Repetitive Firing in Motoneurons of the Sacrocaudal Spinal Cord of Adult Rats. *J Neurophysiol* 96: 1141-1157, 2006c.

Hines M and Carnevale T. The NEURON simulation environment. *Neural Comput* 9: 1179-1209, 1997.

Hochman S and McCrea D. Effects of chronic spinalization on ankle extensor motoneurons. I. Composite monosynaptic Ia EPSPs in four motoneuron pools. *J Neurophysiol* 71: 1452-1467, 1994a.

Hochman S and McCrea D. Effects of chronic spinalization on ankle extensor motoneurons. II. Motoneuron electrical properties. *J Neurophysiol* 71: 1468-1479, 1994b.

Hochman S and McCrea D. Effects of chronic spinalization on ankle extensor motoneurons. III. Composite Ia EPSPs in motoneurons separated into motor unit types. *J Neurophysiol* 71: 1480-1490, 1994c.

Hornby T, McDonagh J, Reinking R, and Stuart D. Motoneurons: A preferred firing range across vertebrate species? *Muscle Nerve* 25: 632-648, 2002.

Hounsgaard J, Hultborn H, Jespersen B, and Kiehn O. Bistability of alpha-motoneurones in the decerebrate cat and in the acute spinal cat after intravenous 5-hydroxytryptophan. *J Physiol* 405: 345-367., 1988.

Hounsgaard J and Kiehn O. Calcium spikes and calcium plateaux evoked by differential polarization in dendrites of turtle motoneurones in vitro. *J Physiol* 468: 245-259, 1993.

Jefferys JGR, Deans J, Bikson M, and Fox J. Effects of weak electric fields on the activity of neurons and neuronal networks. *Radiat Prot Dosimetry* 106: 321-323, 2003.

Kiehn O, Kjaerulff O, Tresch MC, and Harris-Warrick RM. Contributions of intrinsic motor neuron properties to the production of rhythmic motor output in the mammalian spinal cord. *Brain Research Bulletin* 53: 649-659, 2000.

Kitzman P. Alteration in axial motoneuronal morphology in the spinal cord injured spastic rat. *Experimental Neurology* 192: 100-108, 2005.

Kitzman P. Changes in vesicular glutamate transporter 2, vesicular GABA transporter and vesicular acetylcholine transporter labeling of sacrocaudal motoneurons in the spastic rat. *Experimental Neurology* 197: 407-419, 2006.

Kitzman P. VGLUT1 and GLYT2 labeling of sacrocaudal motoneurons in the spinal cord injured spastic rat. *Experimental Neurology* In Press, Corrected Proof, 2007.

Kjaerulff O and Kiehn O. 5-HT Modulation of Multiple Inward Rectifiers in Motoneurons in Intact Preparations of the Neonatal Rat Spinal Cord. *J Neurophysiol* 85: 580-593, 2001.

Lang N, Nitsche M, Paulus W, Rothwell J, and Lemon R. Effects of transcranial direct current stimulation over the human motor cortex on corticospinal and transcallosal excitability. *Exp Brain Res* 156: 439-443, 2004.

Lee RH and Heckman CJ. Adjustable Amplification of Synaptic Input in the Dendrites of Spinal Motoneurons In Vivo. *J Neurosci* 20: 6734-6740, 2000.

Lee RH and Heckman CJ. Influence of voltage-sensitive dendritic conductances on bistable firing and effective synaptic current in cat spinal motoneurons in vivo. *J Neurophysiol* 76: 2107-2110., 1996.

Li Y, Gorassini MA, and Bennett DJ. Role of Persistent Sodium and Calcium Currents in Motoneuron Firing and Spasticity in Chronic Spinal Rats. *J Neurophysiol* 91: 767-783, 2004a.

Li Y, Harvey PJ, Li X, and Bennett DJ. Spastic Long-Lasting Reflexes of the Chronic Spinal Rat Studied In Vitro. *J Neurophysiol* 91: 2236-2246, 2004b.

McIntyre CC and Grill WM. Extracellular Stimulation of Central Neurons: Influence of Stimulus Waveform and Frequency on Neuronal Output. *J Neurophysiol* 88: 1592–1604, 2002.

Rastad J, Gad P, Jankowska E, McCrea D, and Westman J. Light microscopical study of dendrites and perikarya of interneurones mediating la reciprocal inhibition of cat lumbar alpha-motoneurones. *Anatomy and Embryology* 181: 381-388, 1990.

Scheibel M and Scheibel A. Terminal patterns in cat spinal cord. 3. Primary afferent collaterals. *Brain Res* 13: 417-443, 1969.

Simon M, Perrier J-F, and Hounsgaard J. Subcellular distribution of L-type Ca²⁺ channels responsible for plateau potentials in motoneurons from the lumbar spinal cord of the turtle. *Eur J Neurosci* 18: 258-266, 2003.

Sterling P and Kuypers H. Anatomical organization of the brachial spinal cord of the cat. II. The motoneuron plexus. *Brain Res* 4: 16-32, 1967.

Svirskis G, Baginskas A, Hounsgaard J, and Gutman A. Electrotonic measurements by electric field-induced polarization in neurons: theory and experimental estimation. *Biophys J* 73: 3004-3015, 1997a.

Svirskis G, Gutman A, and Hounsgaard J. Detection of a Membrane Shunt by DC Field Polarization During Intracellular and Whole Cell Recording. *J Neurophysiol* 77: 579-586, 1997b.

Thomas CK and Ross BH. Distinct Patterns of Motor Unit Behavior During Muscle Spasms in Spinal Cord Injured Subjects. *J Neurophysiol* 77: 2847-2850, 1997.

Zijdewind I and Thomas CK. Motor Unit Firing During and After Voluntary Contractions of Human Thenar Muscles Weakened by Spinal Cord Injury. *J Neurophysiol* 89: 2065-2071, 2003.

Chapter 5: Modulation of Motoneuronal Firing Behavior after Spinal Cord Injury using Intraspinal Microstimulation Current Pulses: A Modeling Study †

5.1 INTRODUCTION

Spasticity is a neurological impairment that usually develops after an upper motor neuron lesion (e.g. stroke or spinal cord injury, SCI). It is characterized by velocity-dependent muscle hypertonus and exaggerated tendon jerks resulting from the hyperexcitability of the stretch reflex (Lance 1980). Clinical consequences of spasticity involve general weakness and loss of dexterity (Barnes and Johnson 2001). Spasticity also interferes with volitional muscle activation and reduces the functional outcome of the residual voluntary drive after SCI. Current treatments of spasticity involve oral or intrathecal administration of non-specific pharmacological agents (e.g. baclofen and clonidine) which cause general suppression of the neuronal activity in a patient already suffering from a reduced voluntary drive (Anderson et al. 1982; Hudgson and Weightman 1971).

The mechanisms underlying spasticity remain unclear. It is currently thought that the increased excitability of spinal motoneurons during spasticity could be partly due to changes in the intrinsic membrane properties of α-motoneurons causing full activation of voltage-dependent dendritic persistent inward currents (PICs) after the injury (for review see Eken et al. 1989 and Powers and Binder 2001). After SCI, the activation and deactivation of the dendritic PIC are no longer under the control of the descending drive (e.g. presynaptic inhibition) leading to increased motoneuronal excitability and firing rate, muscle spasms, and long-lasting reflexes in response to afferent inputs (Li et al. 2004a; Thomas and Ross 1997).

† A revised version of this chapter has been accepted for publication (ElBasiouny SM and Mushahwar VK, *J. Applied Physiol.*, in press, 2007 'used with permission').

In most of its applications, electrical stimulation has been commonly used to modulate the excitability of neuronal elements to generate functional body movements, alleviate motor disorders, and restore sensory function, e.g. intraspinal microstimulation (ISMS), deep brain stimulation (DBS), and visual and cochlear prostheses (Dostrovsky et al. 2000; Eckhorn et al. 2006; McCreery et al. 2000; Mushahwar et al. 2000). In the present study, we simulated the effects of applying focal electrical current pulses to the central nervous system to inhibit, rather than activate, neuronal elements and reduce their activity. This would be beneficial in situations where reduction of the neuronal excitability in general is desired to alleviate motor disorders. One of these applications is the reduction of the hyperexcitability of spinal motoneurons which contributes to the emergence of spasticity after SCI (Bennett et al. 2001; Eken et al. 1989). Therefore, we investigated electrical stimulation in the spinal cord as our model, and spasticity as the motor disorder to be reduced. More specifically, our goal was to reduce the hyperexcitability, and increased firing rate, of spinal motoneurons following SCI *without* prohibiting muscle activation through the residual volitional drive. Using intraspinal microwires implanted in the spinal cord after the injury to restore limb movements, the developed paradigms could be delivered to reduce the severity of spasticity as well. To achieve this goal, three waveforms of electrical current pulses were examined in a motoneuron computer model: 1) High-frequency sinusoidal and rectangular current pulses, 2) Low-frequency biphasic charge-balanced rectangular pulses, and 3) Biphasic charge-imbalanced pulses.

A morphologically-detailed computer model of a cat spinal α-motoneuron was developed to examine the effect of these pulses on the excitability and firing behavior of motoneurons. Our results suggest that suprathreshold high-frequency sinusoidal and rectangular current pulses (> 7xThreshold, 7T, > 5 kHz) could inactivate Na^+ channels and prohibit the propagation of action potentials (APs) through the axon. Subthreshold biphasic charge-imbalanced pulses (< 0.4T, 1 – 3 kHz, net DC < 5 μA) were able to reduce the axonal firing rate significantly (up to ≈ 25% reduction). The motoneuronal firing rate was reduced by the charge-imbalanced pulses at all levels of synaptic input resulting in a reduction in the slope of the frequency-current (F-I) relationship.

Conversely, subthreshold high-frequency sinusoidal and rectangular current pulses and low-frequency biphasic charge-balanced (subthreshold and suprathreshold) pulses were ineffective in inducing reduction in the motoneuronal firing rate. The former pulses did not provide adequate levels of sustained depolarization to inactivate Na^+ channels in the soma and initial segment (IS) of the motoneuron, whereas the latter did not induce adequate levels of hyperpolarization in the IS or first node of Ranvier to reduce the motoneuronal firing rate. Results of the present study provide potential electrical stimulation paradigms that could be used as clinical interventions after SCI. In addition to using ISMS for restoring limb movements after the injury, the paradigms discussed here could be also used to reduce spasticity. Our results and the discussed concepts could also be extended to other applications were focal electrical microstimulation in the central nervous system is used (e.g. DBS and the management of bladder dysfunction). Part of this work was previously presented in abstract form (ElBasiouny and Mushahwar 2006).

5.2 MATERIALS AND METHODS

A three-dimensional (3D) morphologically-detailed computer model of a cat α-motoneuron was developed to examine the effect of different extracellularly-injected current pulses on the excitability and firing behavior of motoneurons. This model incorporated realistic motoneuronal morphology and dendritic distribution of synaptic input. The model also included a distribution of dendritic channels that allowed it to reproduce a wide variety of motoneuronal behaviors (ElBasiouny et al. 2005).

5.2.1 Model structure

Full description of the model morphology, biophysical properties, and verification is provided in ElBasiouny *et al.* (ElBasiouny et al. 2005). Briefly, a compartmental cable model of a cat α-motoneuron was developed that had full representation of the motoneuronal structure, consisting of soma, IS, axon hillock (AH), myelinated axon, and a dendritic tree (Fig. 5-1A). The dendritic tree was based on the 3D detailed morphology for type-identified triceps surae motoneurons (fatigue-resistant (FR) type, medial gastrocnemius motoneuron, identified as cell 43/5 in Cullheim et al. 1987). The model was developed using NEURON simulation environment (Hines and Carnevale 1997). The model passive properties were set based on previous studies for the same 43/5 FR motoneuron (Cullheim et al. 1987; Fleshman et al. 1988). Voltage-gated ion channels at the soma, IS, and AH determining the motoneuronal active properties included fast and persistent Na^+, delayed rectifier K^+, Ca^{+2}-activated K^+, and N-type Ca^{+2} channels. Ion channels at nodes of Ranvier included fast and persistent Na^+ and slow K^+ channels. Channel densities were set such that the model active properties were within the 95% confidence range of experimental measurements from cat α-motoneurons, and the model generated APs and afterhyperpolarizations with characteristics similar to experimental measurements (ElBasiouny et al. 2005).

The myelinated axon was based on the model developed by McIntyre and Grill (2002) in which nodes of Ranvier and myelin were electrically represented. The myelinated axon had a fiber diameter of 14 μm, 10 nodes of Ranvier, and conduction velocity of 83 m/s

which is comparable to that of FR motoneurons (Hochman and McCrea 1994). The instantaneous motoneuronal firing rate was measured from the interspike intervals of the last node of Ranvier of the myelinated axon (≈10 mm from the soma) which represents the firing rate seen by the muscle fiber of that motor unit.

5.2.2 Dendritic channels and synaptic input

The dendritic low voltage-activated L-type calcium ($Ca_V1.3$ type) channels that mediate Ca^{+2} PIC were distributed over an intermediate region between 300 μm and 850 μm from the soma. With this dendritic distribution, the model behavior matched multiple sets of experimental measurements from cat motoneurons innervating the MG muscle (ElBasiouny et al. 2005).

Given that involuntary muscle spasms and exaggerated tendon reflexes associated with spasticity are usually triggered by mild sensory stimulation (e.g. rubbing or cooling of the skin, limb movements, or muscle contraction), activation of the motoneuron by synaptic input was simulated in the present model. The synapses were distributed over the dendritic tree based on the realistic distribution of Ia afferent-to-motoneuron contacts from cat FR motoneurons (Burke and Glenn 1996; Burke et al. 1979; Glenn et al. 1982). For synaptic activation of the motoneuron, tendon vibration was simulated by activating the Ia-afferent synapses asynchronously at 180 Hz while adjusting the synapse conductances to give Ia effective synaptic current (Ia I_N) equal to that measured experimentally at resting potential (ElBasiouny et al. 2005). This is the current that effectively reaches the soma due to synaptic activation (Heckman and Binder 1988).To allow for systematic gradation of the synaptic input, the total number of Ia-synapses was divided into groups, randomly distributed on the dendrites, which were then activated sequentially (ElBasiouny et al. 2006). This activation pattern resulted in a linear increase in the Ia I_N reaching the soma as more synapses were activated. Given that the distribution of different synaptic inputs appears to be effectively similar to that of the Ia-afferents (for discussion see ElBasiouny et al. 2005), synaptic input from systems other than the Ia-afferents was simulated by increasing the synapse conductances to generate higher synaptic currents (ElBasiouny et al. 2006). This allowed for the examination of the

motoneuronal firing behavior in response to different levels of synaptic input and the F-I relationship was constructed (e.g. Fig. 5-5 – filled circles).

5.2.3 Hyperexcitability of motoneurons during spasticity

The goal of the present study was to examine the efficacy of various electrical current pulses in suppressing the motoneuronal firing activity; thereby, the level of spasticity after SCI. During spasticity, spinal motoneurons become hyperexcitable and their dendritic PIC, which is responsible for the generation of high firing rates, long-lasting reflexes, and muscle spasms, becomes fully activated by synaptic input (Gorassini et al. 2004; Li et al. 2004a; Li et al. 2004b; Thomas and Ross 1997). To simulate this condition, the model motoneuron was synaptically activated at 300% of the strength of the Ia-afferent system (Ia $I_N \approx 14.6$ nA). The generated motoneuronal firing rate was described using the classical nomenclature that depicts the different linear ranges (primary, secondary and tertiary ranges) of the F-I relationship (Kernell 1965a, b). The delivered level of synaptic input resulted in *full* activation of the Ca^{+2} PIC and generated a high firing rate in the tertiary range of the F-I relationship (Fig. 5-5A – filled circles). Synaptic input that caused partial activation of the Ca^{+2} PIC, in the secondary range of the F-I relationship (Fig. 5-5B), were also investigated.

To assess the level of activation of the dendritic $Ca_V1.3$ channels and quantify the magnitude of the mediated current, we measured the average dendritic Ca^{+2} PIC (I_{Ca}; e.g. Fig. 5-2 – 5th trace). This average Ca^{+2} PIC was computed as follows:

$$I_{Ca} = 1/n \times \sum_{i=1}^{n} i_{Ca\,i}$$

where n is the number of compartments that have the $Ca_V1.3$ channels, and $i_{Ca\,i}$ is the calcium current mediated by the $Ca_V1.3$ channels located in compartment number i.

5.2.4 Simulation of electrical stimulation through extracellular current pulses

The model motoneuron was stimulated with a monopolar extracellular point source electrode (similar to intraspinal microwires implanted in the spinal cord to restore limb movements after SCI (Mushahwar and Horch 2000; Saigal et al. 2004)) positioned at

X_e, Y_e, Z_e (Fig. 5-1A). The gray matter was represented as a 3D ohmic isotropic medium (Hounsgaard and Kiehn 1993). The extracellular resistivity (ρ) of the gray matter was adjusted to replicate the current-distance relationship from Gustafsson and Jankowska (1976) (Fig. 5-1B), and was set to 2000 Ω.cm. Given that the value of ρ was significantly higher than that used in previous models, sensitivity analysis was performed to study the effect of variation in the value of ρ on the model results (section 5.3.6; Table 5-2). The dendritic morphology of the motoneuron was described in 3D coordinate space centered at the soma and parallel to the rostrocaudal (X), dorsoventral (Y), and mediolateral (Z) axes of the spinal cord (Cullheim et al. 1987). The representation of the motoneuronal morphology relative to the source electrode and the principal axes of the spinal cord allowed for the computation of the extracellular field potential at each compartment in the model resulting from current injection at the electrode site using the following equation:

$$V_e = \frac{I \cdot \rho}{4 \cdot \pi \cdot r}\ ,\ r = \sqrt{(\ (x - X_e)^2 + (y - Y_e)^2 + (z - Z_e)^2\ )} \qquad \text{(McIntyre and Grill 2000)}$$

where V_e is the extracellular field potential at each compartment, I is the amplitude of the injected current pulse, ρ is the extracellular electrical resistivity of the gray matter, and r is the radial distance between each compartment (located at x,y,z) and the source electrode.

5.2.5 Verification of motoneuronal activation through extracellular current pulses

Activation of the model motoneuron by extracellular injection of current pulses was compared to experimental data from Gustafsson and Jankowska (1976). The model had current-distance relationship that matched experimental data (Fig. 5-1B). Similar to the experimental conditions, threshold currents were measured using an extracellular cathodic current pulse 200 μs in duration that caused activation of the cell. Threshold currents were measured along a track 50 μm lateral to the IS, and along the dorsoventral direction of the electrode position that provided the lowest threshold. Simulations were conducted with passive dendritic tree, i.e. no dendritic voltage-gated channels were present, as experimental measurements were obtained from anaesthetized cats (Gustafsson and Jankowska 1976). Anesthesia suppresses the L-type calcium channels

mediating the PIC in spinal motoneurons (Guertin and Hounsgaard 1999) and significantly reduces the availability of monoaminergic inputs to motoneurons (Hultborn and Kiehn 1992). Therefore, the behavior of the motoneuronal dendrites in anesthetized preparations is dominated by their passive properties (Powers and Binder 2001).

5.2.6 Electrical stimulation paradigms

The effect of three different waveforms of electrical current pulses on the firing rate of a spinal motoneuron was examined:

A) High-frequency sinusoidal and rectangular current pulses

Suprathreshold high-frequency sinusoidal and rectangular current pulses were tested in the model (Fig. 5-2 – bottom trace). The pulse amplitude ranged between 50 μA (1.1T) and 500 μA (10T), and stimulation frequency ranged between 5 kHz and 20 kHz.

B) Biphasic charge-balanced rectangular pulses

Symmetrical and asymmetrical biphasic charge-balanced rectangular pulses were examined in the model (Fig. 5-3A). The pulse amplitude ranged between 0.1T and 10T; pulse width ranged between 100 μs to 500 μs (for the short phase) and 1000 μs to 1500 μs (for the long phase); and stimulation frequency ranged between 50 Hz and 1000 Hz.

C) Biphasic charge-imbalanced pulses

Subthreshold biphasic charge-imbalanced current pulses with a 4:1 ratio of the cathodic to anodic phases were tested in the model (Fig. 5-4 – bottom trace). The cathodic pulse amplitude ranged between 0.1T and 1T; cathodic pulse width ranged between 50 μs and 500 μs; stimulation frequency ranged between 1 kHz and the highest stimulation frequency possible (when no delay was present between the pulses); and net DC current ranged between 0.5 μA and 6 μA.

5.3 RESULTS

5.3.1 Extracellular electrical stimulation of high-frequency sinusoidal and rectangular current pulses

The effect of extracellular injection of high-frequency sinusoidal and rectangular current pulses on the firing behavior of motoneurons was simulated in Fig. 5-2. High-frequency sinusoidal and rectangular current pulses were examined because they are safe (i.e. charge-balanced pulses) to apply in chronic applications. The extracellular stimulating electrode was moved freely in 3D space around the model motoneuron in order to investigate the effect of electrode location on the motoneuronal firing behavior. The stimulating electrode was initially placed relatively distal from the soma and IS (within the dendritic tree) at which location the motoneuronal firing threshold was 45 μA. The model motoneuron was activated in response to a synaptic input of 14.6 nA (nearly three times that of the Ia-afferent system) that caused full activation of the dendritic Ca^{+2} PIC (Fig. 5-2 – 4th trace). After steady-state motoneuronal firing was reached, extracellular injection of suprathreshold high-frequency (5 kHz, 300 μA, ≈ 7T) sinusoidal pulses was applied (Fig. 5-2 – bottom trace). The delivered pulses produced a state of sustained depolarization primarily in the first node of Ranvier as it is the nearest structure to the stimulating electrode with the highest density of Na^+ channels, and caused inactivation of the Na^+ channels. The sustained depolarization of the first node of Ranvier was illustrated by the profile of the activation gating particle (m) of the Na^+ channels in response to the delivered pulses in which a high and sustained activation level was achieved (Fig. 5-2 – 2nd trace). The sustained depolarization at the first node of Ranvier, in turn, resulted in inactivation of the APs propagating through the axon and hyperpolarization of the soma, IS, and dendrites (Fig. 5-2 – 3rd trace),. The change in axonal membrane potential was reduced from 110 mV (height of the axonal APs) before stimulation to less than 30 mV after stimulation. The motoneuronal firing rate in response to the delivered pulses was then reduced to zero (Fig. 5-2 – upper trace). The delivered pulses also resulted in reduction of the dendritic Ca^{+2} PIC (indicated by I_{Ca} in Fig. 5-2 – 4th trace) due to the hyperpolarization induced in the dendrites in response to the intense depolarization in the soma and IS. Similar results were obtained when the extracellular stimulating electrode

was placed at locations relatively near to the soma and IS structures (activation thresholds as low as 5 μA), or when suprathreshold rectangular current pulses were simulated. However, at those near locations inactivation of Na^+ channels was achieved in the IS and the first node of Ranvier (structures with the highest density of Na^+ channels). Generally, axonal APs were inactivated in response to high-frequency sinusoidal or rectangular current pulses of amplitude seven times the motoneuronal activation threshold and larger ($\geq$ 7T). Conversely, subthreshold high-frequency or suprathreshold low-frequency ($<$ 3 kHz) sinusoidal and rectangular current pulses were unable to provide adequate levels of sustained depolarization to inactivate Na^+ channels in the soma and IS; hence, firing rate was increased rather than reduced (not illustrated).

5.3.2 Extracellular electrical stimulation of biphasic charge-balanced current pulses

The application of low-frequency biphasic charge-balanced pulses to reduce the motoneuronal firing rate was also examined in the model. Biphasic charge-balanced pulses were chosen because they do not cause tissue damage and electrode corrosion (Mortimer 1981). Different pulse parameters such as pulse shape (symmetrical and asymmetrical), amplitude (subthreshold and suprathreshold), pulse width (100 to 500 μs and 1000 to 1500 μs for the short and long phases, respectively), and stimulation frequency (50 to 1000 Hz) were tested in the model (Fig. 5-3A). Biphasic charge-balanced pulses were ineffective in inducing reductions in the firing rate of the model motoneuron (Fig. 5-3B). Because of their relative low-frequency, these pulses were incapable of maintaining an adequate level of hyperpolarization in the membrane potential of the IS or first node of Ranvier. This was especially difficult to achieve during the strong depolarization of the motoneuronal membrane by the full activation of the dendritic PIC and enhanced synaptic input as is expected during spasticity.

5.3.3 Extracellular electrical stimulation of biphasic charge-imbalanced current pulses

Given that biphasic charge-balanced pulses could not reduce firing rate and high-frequency sinusoidal and rectangular current pulses completely inactivated the axonal APs which would result in a relaxed (i.e. paralyzed) muscle, we investigated the application of biphasic charge-imbalanced pulses to reduce, rather than block, the

motoneuronal firing rate reaching the muscle (Fig. 5-4). These pulses have been shown to have higher safe limits than those for monophasic pulses with equivalent net DC current (Scheiner et al. 1990). Biphasic charge-imbalanced pulses of 4:1 (cathodic to anodic phase proportion) were used (Fig. 5-4C – bottom trace – inset). This proportion allowed for the injection of charge-imbalanced pulses with a wide range of net DC current and pulse amplitudes within the subthreshold range for motoneuronal firing (< 1T). The short duration of the anodic phase (half that of the cathodic phase) was chosen to allow for fast partial recovery of the injected charge in the tissue which minimizes irreversible electrochemical reactions at the electrode-tissue interface (Mortimer 1981). Extracellular injection of high-frequency, subthreshold, biphasic charge-imbalanced pulses (5 μA and 200 μs for the cathodic phase, 2.5 μA and 100 μs for the anodic phase, stimulation frequency of 3333 Hz, net DC = 2.5 μA) resulted in an initial rise followed by a drop in the motoneuronal firing rate (≈ 20%, Fig. 5-4B – trace 1). The effective low DC current generated by the charge-imbalanced pulses produced subthreshold and sustained depolarization of the soma and IS which caused the initial increase in firing rate (Fig. 5-4A – yellow color). Conversely, a sustained hyperpolarization was generated in the proximal dendrites and nodes of Ranvier in response to the subthreshold depolarization of the soma and IS by the imbalanced pulses (Fig. 5-4A – purple color). The induced axonal hyperpolarization reduced the resultant firing rate that propagated through the axon (Fig. 5-4B – trace 1), whereas the dendritic hyperpolarization reduced the dendritic PIC (Fig. 5-4B – 2nd trace). The stimulating electrode was moved at various locations relative to the model motoneuron (i.e. near to and far from the IS) to examine the effectiveness of charge-imbalanced pulse stimulation in the reduction of the motoneuronal firing rate at different electrode locations (Table 5-1). Generally, pulse amplitudes lower than 40% of the motoneuronal activation threshold (< 0.4T) were efficient in inducing reduction in axonal firing rate. Higher pulse amplitudes (> 0.4T) caused direct activation of the IS and/or first node of Ranvier, and resulted in higher axonal firing rate.

To examine the effect of the charge-imbalanced pulse amplitude on the extent of the initial rise in the motoneuronal firing rate, we simulated the delivery of charge-imbalanced pulses of lower net DC current (2 μA and 200 μs for the cathodic phase, 1 μA

and 100 μs for the anodic phase, stimulation frequency of 3333 Hz, net DC = 1 μA). The initial rise in firing rate at the onset of stimulation was reduced significantly (Fig. 5-4B – trace 2). This demonstrates that the initial rise in firing rate is an instantaneous response to the direct stimulation of the IS, and is dependent on the level of stimulation (i.e. net DC current).

Because APs could obscure observing steady-state alterations in the membrane potential, we verified the effect of high-frequency, subthreshold, biphasic charge-imbalanced pulses on the membrane potential during the blockade of Na^+ channels in the model motoneuron (Fig. 5-4C). This is similar to the effect of adding sodium channel blockers tetrodotoxin (TTX) or lidocaine derivative QX-314 to motoneurons to block the sodium spikes (Hounsgaard and Kiehn 1989; Lee and Heckman 1999; Li and Bennett 2003). In response to synaptic activation, the membrane potential of the IS showed strong membrane depolarization, whereas that of the last node of Ranvier showed weak membrane depolarization due to its distal location (≈ 10 mm) from the dendrites (Fig. 5-4C – upper panel). Upon the delivery of the subthreshold biphasic charge-imbalanced pulses, differential polarization of the motoneuronal membrane potential was induced. The membrane potential of the IS was further depolarized, whereas those of the nodes of Ranvier and the dendrites were hyperpolarized by the effect of the charge-imbalanced pulses (Fig. 5-4C – upper panel). Hyperpolarization of the dendritic membrane potential is illustrated by the reduction in the magnitude of the dendritic PIC reaching the soma (Fig. 5-4C – bottom trace), which resulted in subsequent gradual decrease in the membrane potential of the IS (Fig. 5-4C – upper panel). Therefore, measurements from simulations in the presence and absence of motoneuronal firing confirmed the differential polarization effect induced in the motoneuronal membrane by the charge-imbalanced pulses and the hyperpolarization of the axonal membrane.

The effect of extracellular stimulation with biphasic charge-imbalanced current pulses on the F-I relationship of spinal motoneurons was investigated (Fig. 5-5). The F-I relationship was constructed by plotting the steady-state firing rate evoked in response to different levels of synaptic input versus the effective synaptic current reaching the soma

at each level of synaptic activation. The injection of biphasic charge-imbalanced current pulses resulted in a linear F-I relationship (Fig. 5-5A, slope after stimulation = 3.1 impulse/s/nA; $r^2 = 0.99$). There was a reduction in the firing rate at all levels of synaptic input indicating an overall reduction in the motoneuronal excitability even when the dendritic Ca^{+2} PIC was fully activated (during the tertiary range of cell firing; Fig. 5-5B). Furthermore, the injection of biphasic charge-imbalanced current pulses caused a right shift in the F-I relationship indicating an increase in the recruitment threshold of the motoneuron (horizontal arrow in Fig. 5-5A).

5.3.4 Effect of change in pulse parameters

Because of the nonlinear time- and voltage-dependent properties of the motoneuronal membrane potential and channel dynamics, the amount of reduction in firing rate by charge-imbalanced pulses is sensitive to variations in pulse parameters. To obtain charge-imbalanced pulses (of 4:1 cathodic to anodic phase ratio) of the lowest net DC current and largest induced reduction in firing rate, the effect of pulse parameters on the firing behavior of the model motoneuron was investigated (Fig. 5-6). The pulse shape (ratio between the anodic and cathodic phases) was not changed during these simulations. The net DC current of the charge-imbalanced pulses was varied through changing either the pulse amplitude (amplitude modulation) or the pulse frequency (frequency modulation) when other pulse parameters were kept constant (Fig. 5-6A). Reduction in the motoneuronal firing rate was obtained with net DC current as low as 0.5 μA (≈ 5%). The increase in the net DC current (0.5 to 3 μA) resulted in larger reductions in firing rate (5% to 22%). Further increase in the net DC current (>3 μA) caused an increase in the firing rate due to direct activation of the IS and/or the first node of Ranvier. Interestingly, net DC current produced through amplitude modulation showed higher efficacy in inducing reduction in firing rate than that produced through frequency modulation (at 1 μA compare open squares to filled circles in Fig. 5-6A).

To obtain the largest reduction in firing rate for the same net DC level, we studied the effect of pulse width on the firing behavior of the model motoneuron (Fig. 5-6B). The charge-imbalanced pulses were delivered at the highest frequency (i.e. no delay between

pulses). Short pulse widths ($\leq$ 100 μs) were more efficient in reducing the motoneuronal firing rate, whereas longer pulse widths ($\geq$ 200 μs) resulted in lower reduction in firing rate (Fig. 5-6B).

5.3.5 Alteration in electrical properties after SCI

The effect of changes in the motoneuronal electrical properties after SCI on the reduction in the motoneuronal firing rate achieved through the delivery of the proposed electrical current pulses was also investigated. Changes in electrical properties after SCI such as the reduction in the motoneuronal firing threshold (V_{th}) and the depolarization of the resting membrane potential (V_{rest}) were simulated. Each of these changes caused an increase in the excitability of the model motoneuron. Blockage of motoneuronal firing was achieved through the delivery of high-frequency sinusoidal pulses even after the alteration of these electrical properties (gray bars of conditions B and C in Fig. 5-7). The effect of Na^+ channel inactivation properties on the efficacy of the high-frequency current pulses in blocking motoneuronal firing was also examined. We found that blockade of motoneuronal firing was still achieved even after increasing and decreasing the Na^+ channel inactivation time constant by a factor of 2 (gray bars of conditions D and E in Fig. 5-7).

The effect of changes in the electrical properties of the motoneuron after SCI and the Na^+ channel inactivation properties on the efficacy of biphasic charge-imbalanced pulses was also investigated. Reduction in the motoneuronal firing rate was still achieved by the delivery of charge-imbalanced pulses even after the alteration of these properties (black bars of conditions B to E in Fig. 5-7).

5.3.6 Sensitivity analysis of the gray matter extracellular resistivity (ρ)

The value of the extracellular resistivity of the gray matter required to replicate the experimentally measured current-distance relationship (Fig. 5-1B) in the model was significantly higher than that used in previous modeling studies. Therefore, we investigated the effect of variation in the value of ρ on the model results (Table 5-2). When the value of ρ was varied over that range that is commonly used (500 to 1000

Ω.cm), the amplitude of the high-frequency AC pulses and charge-imbalanced pulses required to block axonal firing and produce the same amount of reduction in motoneuronal firing rate, respectively, varied inversely with ρ. However, the amplitude of these pulses relative to the activation threshold of the model motoneuron was the same.

5.4 DISCUSSION

The main goal of the present study was to develop extracellular electrical current pulses that could be delivered focally through microwires implanted in the central nervous system to reduce the excitability of neurons. The particular example we focused on was reducing the increased motoneuronal excitability and firing activity; thereby, level of spasticity, through electrical stimulation of the spinal cord using microwires implanted for restoring limb movements after SCI. Results of the present study propose various electrical current pulses for reducing the motoneuronal firing behavior that range from graded reduction (through subthreshold charge-imbalanced pulses) to full blockade (through suprathreshold high-frequency sinusoidal or rectangular current pulses) of motoneuronal firing rate. Subthreshold biphasic charge-imbalanced pulses reduced the motoneuronal firing rate through deactivation of Na^+ channels in the first node of Ranvier, whereas suprathreshold high-frequency sinusoidal or rectangular current pulses blocked motoneuronal firing rate through inactivation of Na^+ channels in the soma, IS, and first node of Ranvier. Our results also demonstrated that high-frequency sinusoidal pulses and biphasic charge-imbalanced pulses were still effective even after changing the motoneuronal electrical properties (which increased the motoneuronal excitability) and after changing the inactivation properties of the Na^+ channels (Fig. 5-7). Suppression of the motoneuronal firing rate was maintained throughout the delivery of the charge-imbalanced pulses or high-frequency pulses. It is expected that the dendritic distribution of Na^+ channels, which is still unknown, would not affect our results as the differential polarization induced by the high-frequency stimulation or the charge-imbalanced pulses is generated primarily in the first node of Ranvier and IS which are the structures with the highest density of Na^+ channels.

Electrical stimulation, both in the peripheral and central nervous system, has been previously used for the reduction of spasticity. This included stimulation of the spastic muscles (Vodovnik et al. 1984), muscles antagonistic to the spastic ones (Alfieri 1982), and stimulation of the dorsal columns of the spinal cord through epiduarlly placed electrodes (Kanaka and Kumar 1990). In the first case, reduction of spasticity could be

due to the electrical stimulation of the cutaneous afferents (Bajd et al. 1985; Dewald et al. 1996) which is thought to induce synaptic plasticity (e.g. long-term potentiation and depression) in the spinal circuitry (Dewald and Given 1994; Dewald et al. 1996). The reduction in spasticity persisted for at least 30 min after stimulation (Dewald et al. 1996). In the second case, reduction of spasticity could be attributed to the reduction in the motoneuronal PIC by the effect of Ia-reciprocal inhibition (Kuo et al. 2003), whereas in the third case reduction of spasticity could be due to the increase in presynaptic inhibition by the effect of electrical stimulation (Hunter and Ashby 1994). Conduction block of unwanted motor nerve activity was examined as well. This block was achieved using either DC stimulation (Bhadra and Kilgore 2004) or high-frequency sinusoidal stimulation (Bhadra and Kilgore 2005; Kilgore and Bhadra 2004; Williamson and Andrews 2005). In the present study, we investigated various electrical stimulation pulses that could be delivered through intraspinal microwires implanted in the spinal cord to restore limb movements after SCI. These pulses would reduce the level of spasticity through the suppression of the increased motoneuronal excitability and firing behavior after the injury. This reduction was achieved either through the inactivation of Na^+ channels in the IS by suprathreshold high-frequency sinusoidal or rectangular current pulses or through the deactivation of Na^+ channels in the initial nodes of Ranvier by subthreshold charge-imbalanced pulses.

5.4.1 High-frequency sinusoidal and rectangular current pulses

High-frequency sinusoidal and rectangular current pulses were examined in the present study because they are charge-balanced, and their charge density and charge per phase are within the safe limits (710 $\mu C/cm^2$ and 0.02 μC/phase for pulse parameters described in Fig. 5-2) (Agnew and McCreery 1990). These pulses were previously investigated in the peripheral nervous system to induce a conduction block of motor nerves (Bhadra and Kilgore 2005; Kilgore and Bhadra 2004; Williamson and Andrews 2005), or to obtain normal recruitment order through activation of small to large nerve fibers (Solomonow 1984) (for a detailed review see Kilgore and Bhadra, 2004). These authors suggested that high-frequency sinusoidal stimulation blocks nerve conduction by producing a region of sustained depolarization of the nerve fiber membrane potential despite that there is no net

charge injected into the tissue (Kilgore and Bhadra 2004; Williamson and Andrews 2005). To the best of our knowledge, the present study is the first to investigate injection of high-frequency sinusoidal or rectangular current pulses in the central nervous system. Our results also confirm effective depolarization blockade as the mechanism of action of high-frequency sinusoidal current pulses. This is supported by the behavior of the activation gating particle (*m*) during high-frequency sinusoidal current pulses (Fig. 5-2 – 2nd trace) and the reduction in the dendritic PIC by stimulation-induced hyperpolarization generated in structures distal to the stimulating electrode (Fig. 5-2 – 2nd trace). Noteworthy, the slow recovery of Na^+ channels from their inactivation after the cessation of high-frequency stimulation would make the cell refractory for some time following the cessation of stimulation.

5.4.2 Biphasic charge-imbalanced pulses

The design of stimulating protocols is usually challenged by the compromise between the efficacy of the stimulation paradigm, the safety of the tissue, and the integrity of the stimulating electrode (Merrill et al. 2005). A monophasic stimulating waveform is the most efficacious, but the most unsafe paradigm with regards to tissue damage, whereas a charge-balanced biphasic stimulating waveform with very short interpulse intervals is the safest, but the least efficacious paradigm (Merrill et al. 2005). Charge-imbalanced biphasic waveforms are considered the best in terms of the balance between efficiency, safety of the tissue, and maintenance of the integrity of the stimulating electrode (Merrill et al. 2005). It has experimentally been shown that DC current stimulation (i.e. *not* through monophasic or charge-imbalanced pulses) up to 3 μA in the rat spinal cord can be safe (Hurlbert et al. 1993). Furthermore, charge-imbalanced biphasic current pulses were found to have higher safe limits for tissue damage than those for monophasic (3.5 times higher safe limits than monophasic pulses with equivalent net DC current) or charge-balanced biphasic current pulses (Scheiner et al. 1990). Therefore, application of biphasic charge-imbalanced pulses is a safer alternative than DC or monophasic stimulation of an equivalent DC current. It also implies that biphasic charge-imbalanced pulses of net DC up to 10 μA could be tolerated safely by the spinal cord. In the present study, the efficacy of the stimulation paradigm was assessed by the amount of induced

reduction in firing rate in response to the injected current pulses. Charge-imbalanced pulses as low as 0.5 μA and up to 3 μA were shown to reduce the motoneuronal firing rate (Fig. 5-6A). Given that the amplitude of the proposed pulses is small, the charge density, charge per phase, and current density per phase (35.3 $\mu C/cm^2$, 1 nC/phase, and 0.18 A/cm^2 for pulse parameters described in Fig. 5-4, and assuming an electrode stimulating surface area of 2830 μm^2) are far lower than the safety limits for electrical stimulation in the central nervous system (Agnew and McCreery 1990). Because very little information is available in the literature on biphasic charge-imbalanced pulses, we investigated the effect of different pulse parameters on the evoked behavior of motoneurons. We noted that due to the time- and voltage-dependent intrinsic membrane properties, we could enhance the efficacy of the charge-imbalanced pulses (i.e. increase the amount of reduction in firing rate), or reduce the net DC current while achieving the same reduction in firing rate, by varying the pulse parameters (e.g. short pulse widths, amplitude modulation).

The net DC current injected into the tissue by the charge-imbalanced current pulses could affect the integrity of the stimulating electrodes (Merrill et al. 2005). To overcome this problem, several approaches could be employed. First, electrode materials that have high resistivity to corrosion (e.g. platinum-iridium alloys) would be used (Merrill et al. 2005; Mortimer 1981). Second, the delivery of the charge-imbalanced pulses could also be limited to the time of the spastic syndrome. That is, the charge-imbalanced pulses would be delivered only when the uncontrolled muscle spasms and long-lasting reflexes are activated. This strategy has been experimentally shown to minimize effectively microstimulation-induced tissue damage (McCreery et al. 2004). Third, electrical stimulation could be rotated among the intraspinal microwires (electrode rotation; in which current pulses are delivered separately and consecutively through each electrode) implanted in the spinal cord for restoring movement of the legs following SCI. The aforementioned techniques for minimizing electrode corrosion would also be beneficial in reducing any potential tissue damage that could result from the delivered pulses.

Our results showed that biphasic charge-imbalanced pulses with low net DC current were able to reduce the motoneuronal firing rate; however, an initial rise in firing rate was encountered at the onset of stimulation (Fig. 5-4B – upper trace). This initial increase in firing rate could then generate a muscle spasm or increase the level of an existing spasm. The initial increase in firing rate was shown to be an instantaneous response to the direct stimulation of the IS by the delivered pulses. Increasing the amplitude of the delivered pulses gradually (i.e. ramp) would reduce the initial rise in the motoneuronal firing rate and would prevent the generation of a muscle spasm at the onset of stimulation.

For the same net DC level, we found that charge-imbalanced pulses with short pulse durations ($\leq$ 100 μs) induced greater reduction in firing rate than those with long pulse durations ($\geq$ 200 μs; Fig. 5-6B). This dissimilarity in effect could be explained by the effect of the pulse duration on the dynamics of Na^+ channels at the first node of Ranvier. The conductance of Na^+ channels (G_{Na}; where $G_{Na} = \bar{G}_{Na} \cdot m^3 \cdot h$) depends primarily on a fast activation gating particle (m) and to a lesser extent on a relatively slow inactivation gating particle (h). That is, the m particle has a short time constant (τ_m) relative to that of the h particle (τ_h differs by two orders of magnitude than τ_m), making m more sensitive to rapid variation in membrane potential than h (Grill and Mortimer 1995). Therefore, current pulses with short durations that correspond to τ_m and much shorter than τ_h ($<<\tau_h \approx$ 600 μs) would have their primary effect exerted on the m particle while minimally affecting the h particle, and would have greater influence on the conductance of Na^+ channels. Conversely, current pulses with long durations would affect both the m and h particles of Na^+ channels (i.e. long hyperpolarization of the membrane potential would reduce m, which reduces G_{Na}, and increase h, which increases G_{Na}). Therefore, the counteracting effects of m and h by the induced hyperpolarization at the first node of Ranvier by long imbalanced pulses would reduce the efficiency of the delivered pulses in suppressing the conductance of axonal Na^+ channels.

5.4.3 General discussion

The present model considered only the effect of the proposed current pulses on the firing behavior of a single motoneuron; however, the effect on other neuronal elements could be predicted. For suprathreshold high-frequency sinusoidal and rectangular current waveforms, these pulses had large amplitudes ($\geq$ 7T) which would cause inactivation of APs in sensory and motor axons. Therefore, relaxation in muscle activity would result in response to this stimulation. This is similar to the conduction block of APs in motor nerves produced experimentally by high-frequency sinusoidal stimulation in the peripheral nervous system (Bhadra and Kilgore 2005; Kilgore and Bhadra 2004; Williamson and Andrews 2005). However, high-frequency sinusoidal or rectangular current pulses would prevent the residual voluntary drive after incomplete SCI from activating the muscle. Subthreshold biphasic charge-imbalanced pulses would have their effects primarily on the IS and nodes of Ranvier (structures with the lowest activation threshold). Given the low amplitude of these pulses ($<$ 0.4T), the affected structures would be depolarized, but not activated, and the induced hyperpolarization in adjacent nodes of Ranvier would reduce the axonal firing rate. Sensory axon terminals in the gray matter become small in diameter and most likely would not be activated by the delivered pulses. Even though activated, stimulation of those axons would minimally affect the motoneuronal firing through their subsequent excitatory synaptic actions on the motoneurons due to the large reduction in the dendritic PIC which is responsible for the enhancement of synaptic current. The effectiveness of charge-imbalanced pulses in reducing the motoneuronal firing rate was found to be sensitive to the net DC current (i.e. amplitude of stimulation) and the stimulating electrode location relative to the motoneuron. That is, pulses that would be subthreshold to some motoneurons (probably those far from the stimulating electrode) might be suprathreshold to other motoneurons (probably those closer to the stimulating electrode). The amplitude of the delivered pulses should then be adjusted to avoid activation of a large number of motoneurons that could generate a muscle spasm. Therefore, the amplitude of stimulation, number of intraspinal microwires, and degree of electrode rotation required to obtain a functional reduction in the overall muscle activity would need to be determined experimentally. Our results could also be beneficial in situations where suppression of the motoneuronal excitability

in general is desired to provoke muscle relaxation. For instance, the proposed paradigms could be effective in the management of bladder dysfunction after SCI by reducing the hyperexcitability of external urethral sphincter motoneurons in Onuf's nucleus during micturition and preventing the concomitant contraction of the sphincter and the detrusor muscle of the bladder.

Although extracellular electrical stimulation in the spinal cord was simulated in the present study, our results and the discussed concepts could also be extended to electrical stimulation in the brain. For instance, our results could be beneficial in understanding the mechanisms underlying deep brain stimulation (DBS). Electrical stimulation causes differential polarization of the stimulated neuronal elements and results in regions of depolarization and hyperpolarization. The spatial distribution and magnitude of these regions depend on the electrode geometry, orientation relative to the stimulating electrode, and morphology of the neuronal elements (Chan and Nicholson 1986; Rattay 1986). Recently, McIntyre et al. (2004) showed that DBS produces complex patterns of excitation and inhibition in neurons in the vicinity of the electrode, and that the somatic activity of these neurons could be entirely different from their axonal activity, which represents the functional output of the stimulated nuclei. Understanding this decoupling of the somatic and axonal activity during DBS could resolve the discrepancy in neural recordings regarding the mechanism(s) of action of DBS (McIntyre et al. 2004). Therefore, comprehending the effects of extracellular electrical microstimulation on the firing behavior of axons and cell bodies is crucial in uncovering the mechanisms underlying the therapeutic effects of DBS. The present study discusses the same concepts of stimulation-induced differential polarization in response to electrical microstimulation in the spinal cord. We took advantage of the induced differential polarization to reduce the axonal activity despite the depolarization of the somatic membrane (Fig. 5-4).

In summary, extracellular electrical stimulation of suprathreshold high-frequency sinusoidal or rectangular current pulses, or subthreshold biphasic charge-imbalanced pulses through intraspinal microwires were shown to reduce the increased excitability and firing activity of spinal motoneurons after SCI. The proposed stimulation paradigms

applied through ISMS microwires used for restoring standing and walking after SCI could also provide a potential clinical therapy for reducing the severity of spasticity, in addition to the restoration of limb movements, following the injury.

5.5 TABLES

Table 5-1. Efficacy of biphasic charge-imbalanced pulses in reducing the motoneuronal firing rate at various distances from the IS of the model motoneuron. Pulse parameters were 0.3T and 200 μs for the cathodic phase; 0.15T and 100 μs for the anodic phase; 3333.3 Hz (i.e. no delay between pulses).

Distance from the IS (μm)	**Threshold (μA)**	**Percent reduction in firing rate (%)**
100	5.1	15.6
150	9.45	18.8
200	19	20.6
250	27.6	20.7
300	42.3	18.1

Table 5-2. Sensitivity analysis to study the effect of variation in the value of the gray matter extracellular resistivity (ρ) on model results.

ρ (Ω.cm)	Model activation threshold (μA)	Pulse amplitude (μA)	Percent pulse amplitude (xT)	Effect on firing of the model motoneuron	Pulse type
2000	45 μA	300 μA	≈ 7 T	Firing block	High-freq AC Stim
	19 μA	5 μA*	≈ 0.26 T	Reduction in firing rate (≈ 22%)	Charge-imbalanced
1000	90 μA	600 μA	≈ 7 T	Firing block	High-freq AC Stim
	38 μA	10 μA*	≈ 0.26 T	Reduction in firing rate (≈ 22%)	Charge-imbalanced
500	180 μA	1200 μA	≈ 7 T	Firing block	High-freq AC Stim
	76 μA	20 μA*	≈ 0.26 T	Reduction in firing rate (≈ 22%)	Charge-imbalanced

*: Amplitude of the cathodic phase of the biphasic charge-imbalanced pulses. Cathodic pulse width (200 μs) and pulse shape (ratio 4:1) were kept constant.

5.6 FIGURES

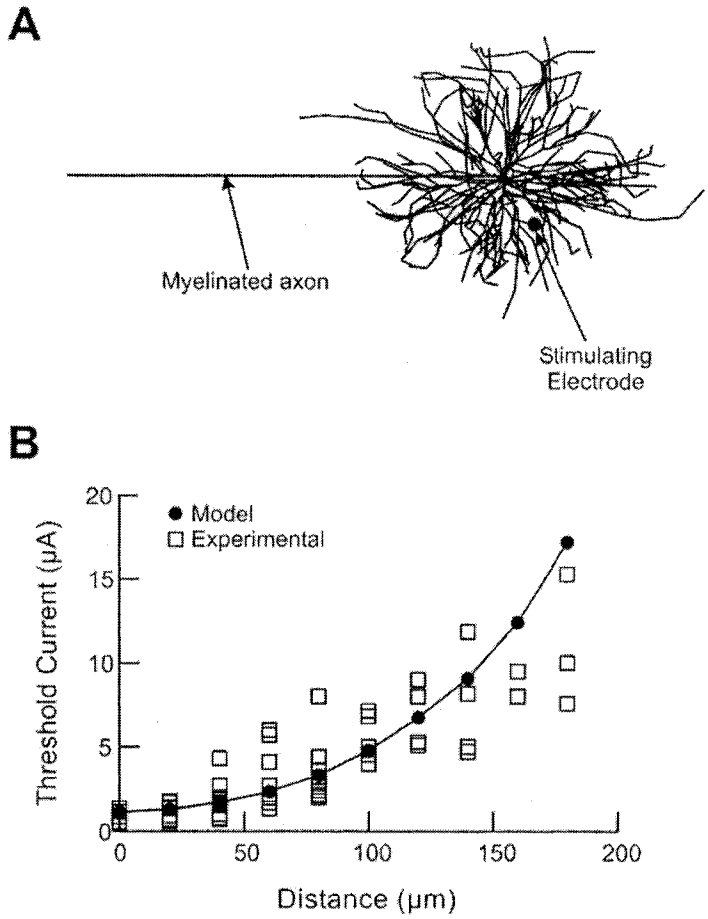

Figure 5-1. Model properties. **A:** Model morphology indicating the location of the stimulating electrode (black dot) relative to the motoneuron. Cell firing was measured from the membrane potential of the last node of Ranvier. **B:** Verification of the motoneuronal activation by extracellular injection of current pulses. Threshold-distance relationship of the model motoneuron (filled circles) compared to experimental data (open squares) from Gustafsson and Jankowska (1976). Threshold current was measured by using an extracellular cathodic current pulse of 200 μs in duration.

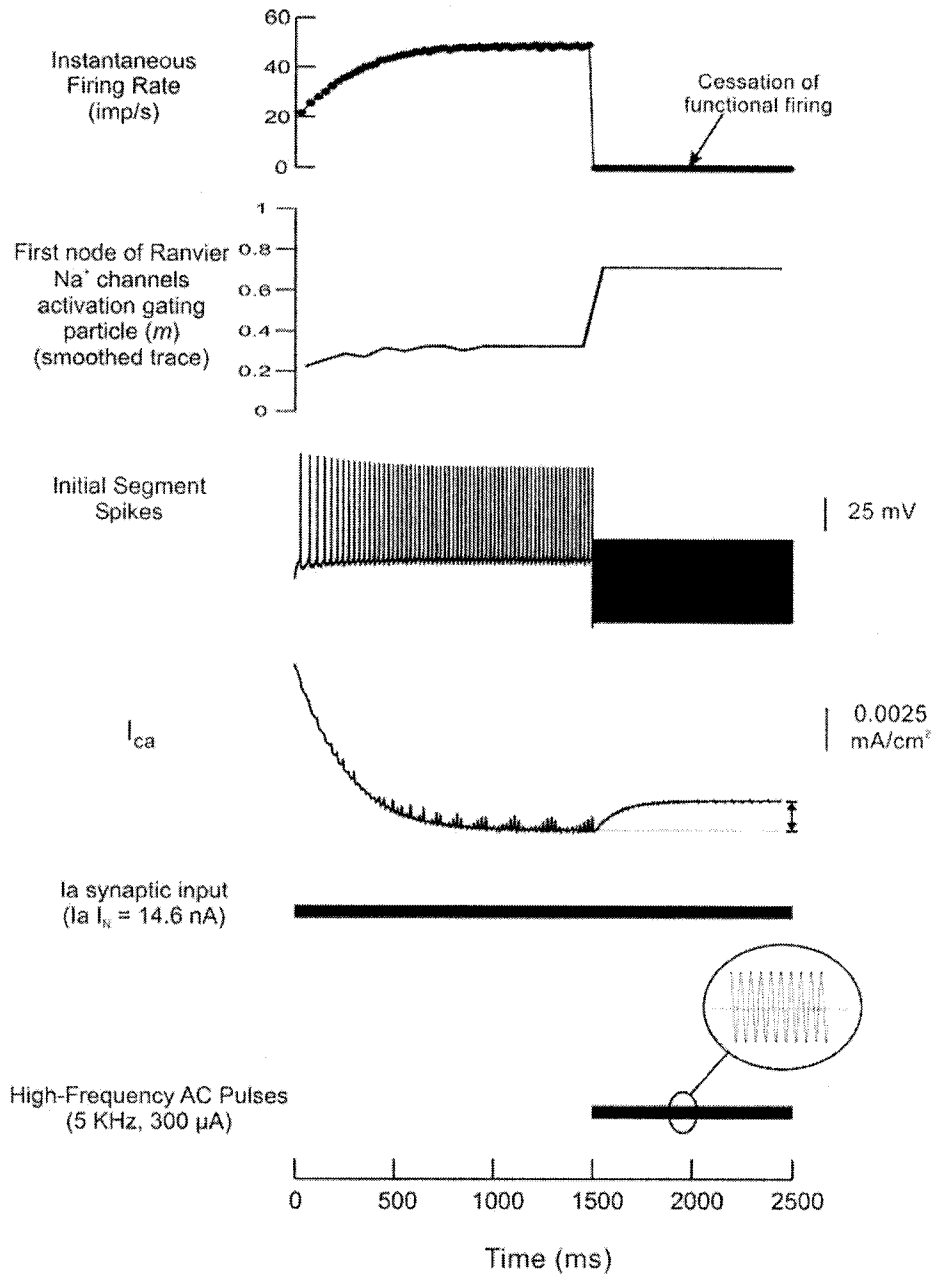

Figure 5-2. Effect of high-frequency sinusoidal current pulses on the firing behavior of spinal motoneurons. Shown are the motoneuronal firing rate measured from the last node of Ranvier (upper trace), the behavior (low pass filtered at 10 Hz) of the activation gating particle (*m*) of Na^+ channels in the first node of Ranvier (2^{nd} trace), IS spikes (3^{rd} trace), and the dendritic I_{Ca} (4^{th} trace) during synaptic activation at 300% of Ia-synaptic input (5^{th} trace) and extracellular electrical stimulation of high-frequency sinusoidal current

pulses (bottom trace). The amount of reduction in the dendritic PIC is indicated by the arrow in the 4th trace. Pulse parameters were 5 kHz and 300 μA (≈ 7T) sinusoidal pulses. A similar effect could be obtained by high-frequency rectangular current pulses.

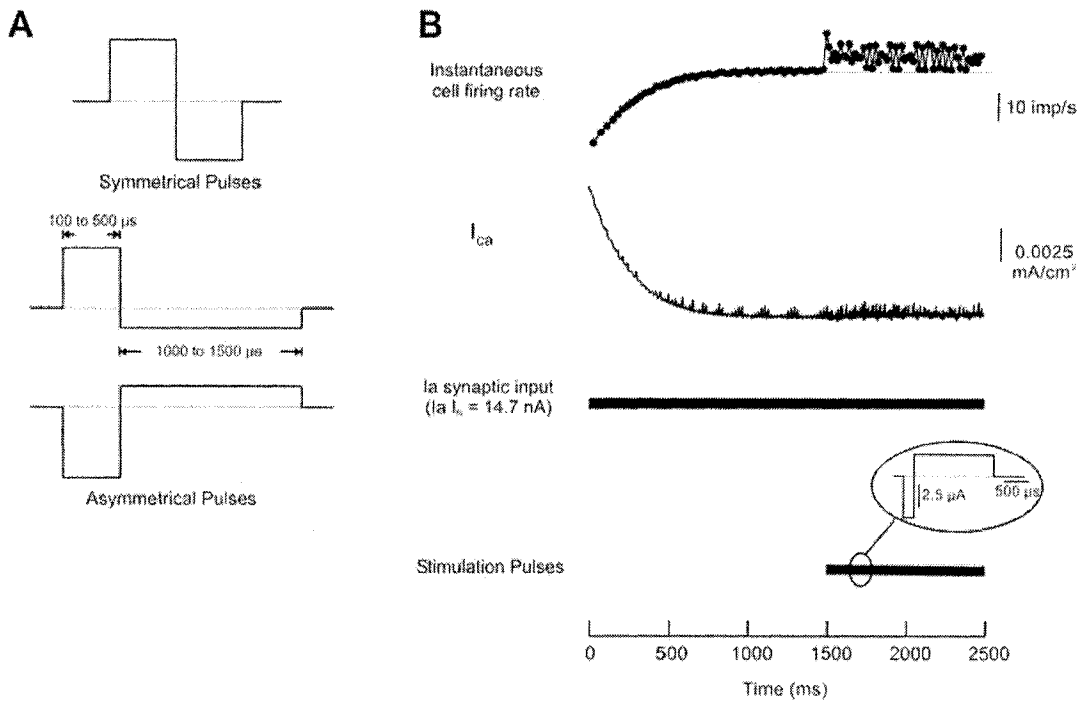

Figure 5-3. Effect of low-frequency biphasic charge-balanced pulses on the firing behavior of spinal motoneurons. **A:** Symmetrical and asymmetrical pulses examined in the model to induce reduction in firing rate. Different pulse parameters were tested (subthreshold and suprathreshold amplitudes; 100 to 1500 µs pulse phase duration; 50 - 1000 Hz). **B:** Shown are the cell firing rate measured from the last node of Ranvier (upper trace) and dendritic I_{Ca} (2^{nd} trace) during synaptic activation at 300% of Ia-synaptic input (3^{rd} trace) and extracellular electrical stimulation of biphasic charge-balanced pulses (bottom trace). Pulses caused increase in cell firing rate. Pulse parameters were 5 µA and 200 µs for the cathodic phase; 0.67 µA and 1500 µs for the anodic phase; 588 Hz (i.e. no delay between pulses).

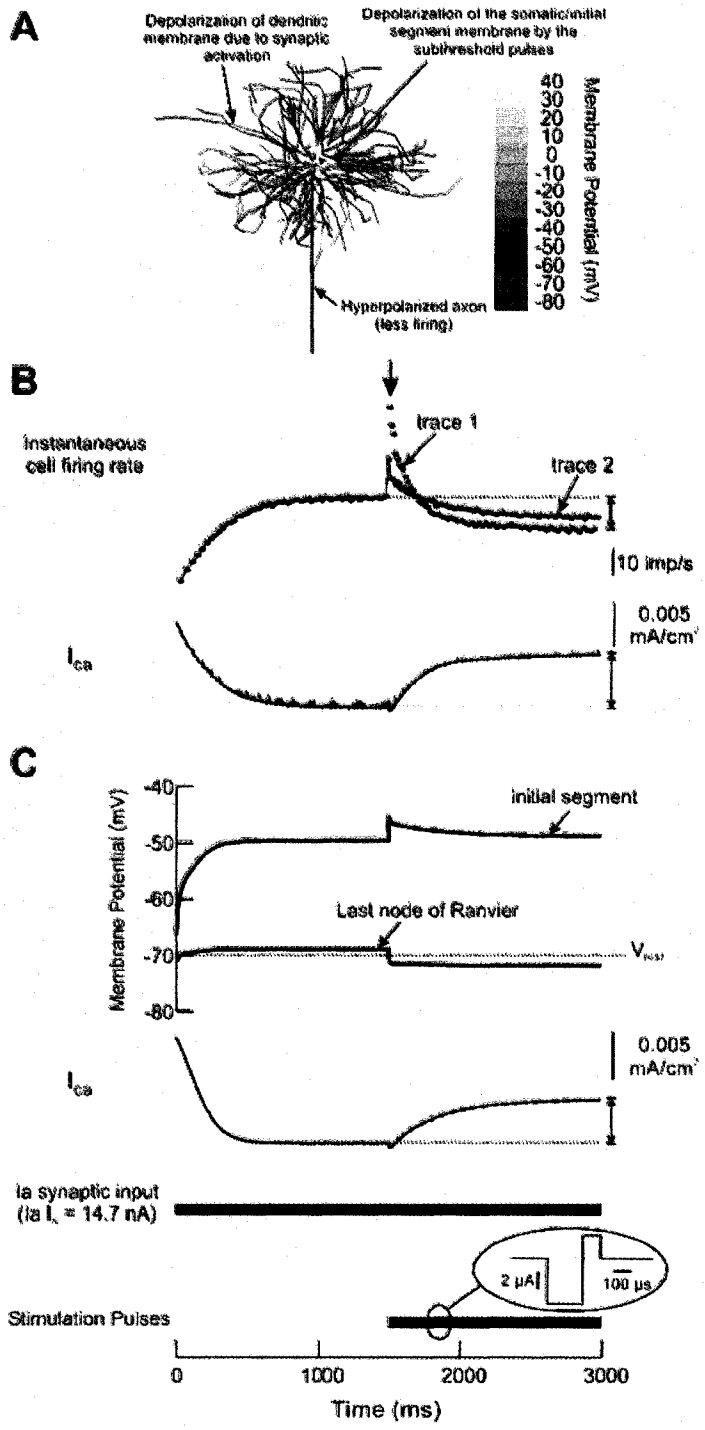

Figure 5-4. Effect of biphasic charge-imbalanced current pulses on the firing behavior of spinal motoneurons. **A:** Membrane potential of different elements of the model motoneuron in response to extracellular electrical stimulation of subthreshold imbalanced pulses and 300% of synaptic activation. **B:** Motoneuronal firing rate measured from the

last node of Ranvier in response to charge-imbalanced pulses of net DC current 2.5 μA (trace 1) and 1.0 μA (trace 2) and dendritic I_{Ca} (2nd trace). **C:** Membrane potential of the IS and last node of Ranvier (upper panel) and dendritic I_{Ca} (2nd trace) during blockade of Na^+ channels in the model motoneuron. Data in **B** and **C** were measured during synaptic activation at 300% of Ia-synaptic input and extracellular electrical stimulation of subthreshold biphasic charge-imbalanced pulses of net DC current 2.5 μA (bottom traces). Pulse parameters were 5 μA and 200 μs for the cathodic phase; 2.5 μA and 100 μs for the anodic phase; net DC ≈ 2.5 μA; 3333.3 Hz (i.e. no delay between pulses). Motoneuronal activation threshold was 19 μA. Steady-state firing rate and dendritic PIC are indicated by the dotted lines in the upper and 3rd traces of **B**, respectively. Cell firing rate was reduced by ≈ 11 impulse/s (22%). The amount of reduction in firing rate and the dendritic PIC are indicated by the thin arrows in the upper and 3rd traces of **B**, respectively. An initial rise in firing rate in response to electrical stimulation is indicated by the left arrow (upper trace of **B**). Charge-imbalanced pulses of smaller net DC current (1 μA) caused less initial rise in firing rate (trace 2). During blockade of Na^+ channels in the model motoneuron, membrane potential of the IS showed depolarization, whereas that of the last node of Ranvier showed hyperpolarization in response to the electrical stimulation (upper panel of **C**). The resting membrane potential (V_{rest}) is indicated by the dotted line in the upper panel of **C**. The gradual reduction in the membrane potential of the IS is due to the reduction in magnitude of the PIC reaching the soma (2nd trace of **C**).

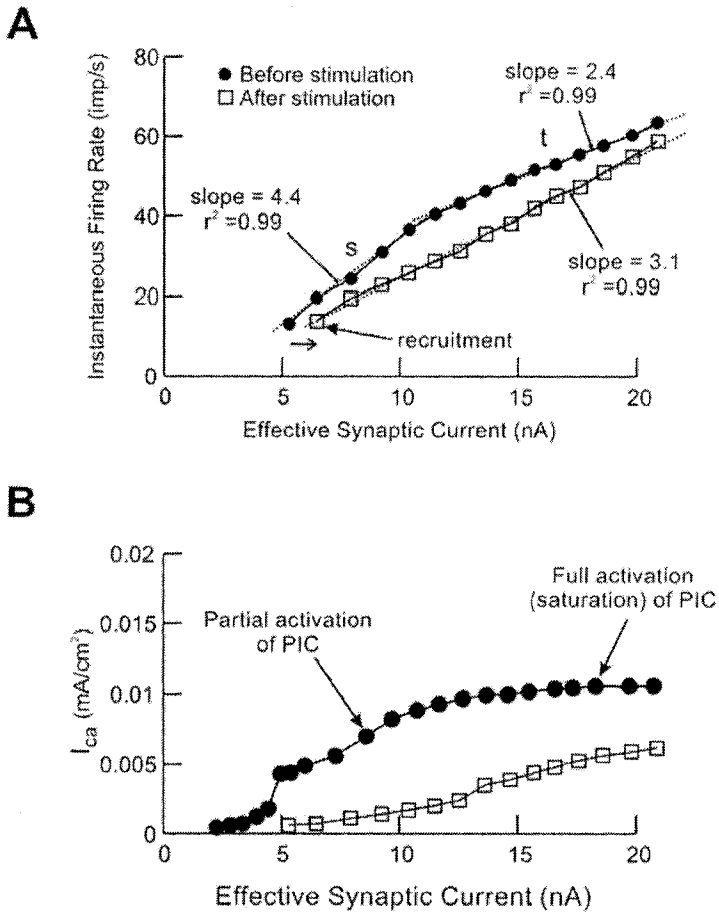

Figure 5-5. Effect of biphasic charge-imbalanced current pulses on the F-I relationship of spinal motoneurons. The F-I relationship (**A**) and I_{Ca} (**B**) before (filled circles) and after (open squares) electrical stimulation. Reduction in firing rate was exhibited at all levels of synaptic input. Before electrical stimulation, the F-I relationship consisted of a secondary (slope = 4.4 impulse/s/nA; $r^2 = 0.99$) and tertiary (slope = 2.4 impulse/s/nA; $r^2 = 0.99$) ranges. After electrical stimulation, the F-I relationship became linear in shape with shallower slope (slope = 3.1 impulse/s/nA; $r^2 = 0.99$). The dotted lines represent the best linear fit for the different ranges of the F-I relationship before and after electrical stimulation. The horizontal arrow shows the shift in motoneuron recruitment in response to the applied charge-imbalanced pulses. Pulse parameters were the same as mentioned in Fig. 5-4.

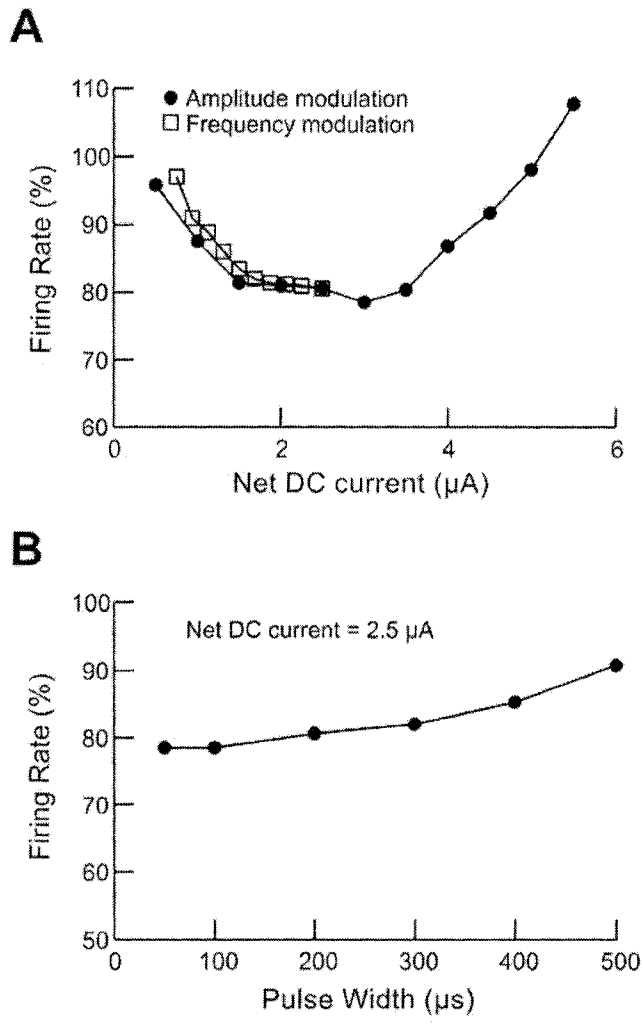

Figure 5-6. Effect of charge-imbalanced pulse parameters on the firing behavior of spinal motoneurons. **A:** Relationship between the net DC current and the resultant motoneuronal firing rate. Net DC current was obtained by varying either pulse amplitude (amplitude modulation) or stimulation frequency (frequency modulation) when other pulse parameters were kept constant. Pulse shape (ratio between the anodic and cathodic phases) was preserved. **B:** Effect of pulse width on the resultant motoneuronal firing rate. For the same net DC current (2.5 μA), short pulse phases (anodic and cathodic with preserved proportion) result in the largest reduction in firing rate. The charge-imbalanced pulses were delivered at the highest stimulating frequency possible (i.e. no delay between pulses).

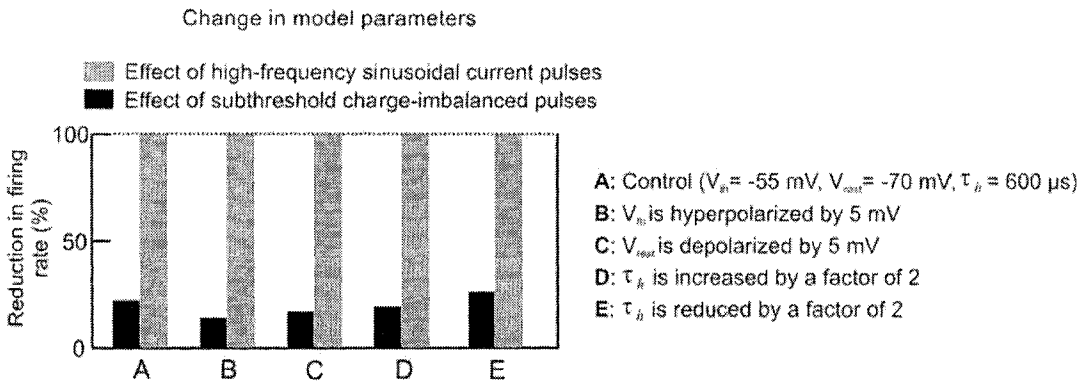

Figure 5-7. The effect of model parameters on the efficacy of high-frequency sinusoidal pulses and biphasic charge-imbalanced pulses in suppressing motoneuronal firing rate.

5.7 REFERENCES

Agnew W and McCreery D. *Neural Prostheses: Fundamental Studies*: Englewood Cliffs, NJ: Prentice Hall, 1990.

Alfieri V. Electrical treatment of spasticity. Reflex tonic activity in hemiplegic patients and selected specific electrostimulation. *Scand J Rehabil Med* 14: 177-182, 1982.

Anderson R, Brigham P, Cady W, and Kellar K. Role of alpha-2 adrenergic affinity in the action of a non-sedative antispasticity agent. *Acta Neurol Scand* 66: 248-258, 1982.

Bajd T, Gregoric M, Vodovnik L, and Benko H. Electrical stimulation in treating spasticity resulting from spinal cord injury. *Arch Phys Med Rehabil* 66: 515-517, 1985.

Barnes MP and Johnson GR. *Upper Motor Neurone Syndrome and Spasticity. Clinical Management and Neurophysiology*: Cambridge University Press, 2001.

Bennett DJ, Li Y, and Siu M. Plateau Potentials in Sacrocaudal Motoneurons of Chronic Spinal Rats, Recorded In Vitro. *J Neurophysiol* 86: 1955-1971, 2001.

Bhadra N and Kilgore KL. Block of mammalian motor nerve conduction using high frequency alternating current. *10th Annual conference of the international FES society*: 165-167, 2005.

Bhadra N and Kilgore KL. Direct current electrical conduction block of peripheral nerve. *IEEE Trans Neural Syst Rehabil Eng* 12: 313-324, 2004.

Burke RE and Glenn LL. Horseradish peroxidase study of the spatial and electrotonic distribution of group Ia synapses on type-identified ankle extensor motoneurons in the cat. *J Comp Neurol* 372: 465-485., 1996.

Burke RE, Walmsley B, and Hodgson JA. HRP anatomy of group Ia afferent contacts on alpha motoneurones. *Brain Res* 160: 347-352., 1979.

Chan C and Nicholson C. Modulation by applied electric fields of Purkinje and stellate cell activity in the isolated turtle cerebellum. *J Physiol* 371: 89-114, 1986.

Cullheim S, Fleshman JW, Glenn LL, and Burke RE. Membrane area and dendritic structure in type-identified triceps surae alpha motoneurons. *J Comp Neurol* 255: 68-81, 1987.

Dewald J and Given J. Electrical stimulation and spasticity reduction: fact or fiction? *Phys Med Rehab - State of the art reviews* 8: 507-522, 1994.

Dewald J, Given J, and Rymer W. Long-lasting reductions of spasticity induced by skin electrical stimulation. *IEEE Trans Rehabil Eng* 4: 231-242, 1996.

Dostrovsky JO, Levy R, Wu JP, Hutchison WD, Tasker RR, and Lozano AM. Microstimulation-Induced Inhibition of Neuronal Firing in Human Globus Pallidus. *J Neurophysiol* 84: 570-574, 2000.

Eckhorn R, Wilms M, Schanze T, Eger M, Hesse L, Eysel UT, Kisvarday ZF, Zrenner E, Gekeler F, and Schwahn H. Visual resolution with retinal implants estimated from recordings in cat visual cortex. *Vision Research* 46: 2675-2690, 2006.

Eken T, Hultborn H, and Kiehn O. Possible functions of transmitter-controlled plateau potentials in alpha motoneurones. *Prog Brain Res* 80: 257-267; discussion 239-242, 1989.

ElBasiouny SM, Bennett DJ, and Mushahwar VK. Simulation of Ca+2 Persistent Inward Currents in Spinal Motoneurons: Mode of Activation and Integration of Synaptic Inputs. *J Physiol (Lond)* 570: 355-374, 2006.

ElBasiouny SM, Bennett DJ, and Mushahwar VK. Simulation of Dendritic Cav1.3 Channels in Cat Lumbar Motoneurons: Spatial Distribution. *J Neurophysiol* 94: 3961-3974, 2005.

ElBasiouny SM and Mushahwar VK. Suppressing the excitability of spinal motoneurons by extracellularly applied electrical fields and current pulses: A modeling study. *2006 Abstract Viewer/Itinerary Planner, Washington, DC: Society for Neuroscience, Online* Session Number: 55, 2006.

Fleshman J, Segev I, and Burke R. Electrotonic architecture of type-identified alpha-motoneurons in the cat spinal cord. *J Neurophysiol* 60: 60-85, 1988.

Glenn L, Burke R, Fleshman J, and Lev-Tov A. Estimates of electrotonic distance of group Ia contacts on cat a-motoneurons: An HRP-morphological study. *Soc Neurosci Abstr* 8: 995, 1982.

Gorassini MA, Knash ME, Harvey PJ, Bennett DJ, and Yang JF. Role of motoneurons in the generation of muscle spasms after spinal cord injury. *Brain* 127: 2247-2258, 2004.

Grill WM and Mortimer J. Stimulus waveforms for selective neural stimulation. *Engineering in Medicine and Biology Magazine, IEEE* 14: 375-385, 1995.

Guertin PA and Hounsgaard J. Non-volatile general anaesthetics reduce spinal activity by suppressing plateau potentials. *Neuroscience* 88: 353-358, 1999.

Gustafsson B and Jankowska E. Direct and indirect activation of nerve cells by electrical pulses applied extracellularly. *J Physiol* 258: 33-61., 1976.

Heckman C and Binder MD. Analysis of effective synaptic currents generated by homonymous Ia afferent fibers in motoneurons of the cat. *J Neurophysiol* 60: 1946-1966., 1988.

Hines M and Carnevale T. The NEURON simulation environment. *Neural Comput* 9: 1179-1209, 1997.

Hochman S and McCrea D. Effects of chronic spinalization on ankle extensor motoneurons. III. Composite Ia EPSPs in motoneurons separated into motor unit types. *J Neurophysiol* 71: 1480-1490, 1994.

Hounsgaard J and Kiehn O. Calcium spikes and calcium plateaux evoked by differential polarization in dendrites of turtle motoneurones in vitro. *J Physiol* 468: 245-259, 1993.

Hounsgaard J and Kiehn O. Serotonin-induced bistability of turtle motoneurones caused by a nifedipine-sensitive calcium plateau potential. *J Physiol* 414: 265-282., 1989.

Hudgson P and Weightman D. Baclofen in the treatment of spasticity. *Br Med J* 4: 15-17, 1971.

Hultborn H and Kiehn O. Neuromodulation of vertebrate motor neuron membrane properties. *Curr Opin Neurobiol* 2: 770-775, 1992.

Hunter JP and Ashby P. Segmental effects of epidural spinal cord stimulation in humans. *J Physiol* 474: 407-419, 1994.

Hurlbert R, Tator C, and Theriault E. Dose-response study of the pathological effects of chronically applied direct current stimulation on the normal rat spinal cord. *J Neurosurg* 79: 905-916, 1993.

Kanaka T and Kumar M. Neural stimulation for spinal spasticity. *Paraplegia* 28: 399-405, 1990.

Kernell D. The adaptation and the relation between discharge frequency and current strength of cat lumbosacral motoneurones stimulated by long-lasting injected currents. *Acta Physiol Scand* 65: 65-73, 1965a.

Kernell D. Synaptic Influence On The Repetitive Activity Elicited In Cat Lumbosacral Motoneurones By Long-Lasting Injected Currents. *Acta Physiol Scand* 63: 409-410, 1965b.

Kilgore K and Bhadra N. Nerve conduction block utilising high-frequency alternating current. *Med Biol Eng Comput* 42: 394-406, 2004.

Kuo JJ, Lee RH, Johnson MD, Heckman HM, and Heckman C. Active Dendritic Integration of Inhibitory Synaptic Inputs In Vivo. *J Neurophysiol* 90: 3617-3624, 2003.

Lance J. Pathophysiology of spasticity and clinical experience with Baclofen. In: *Spasticity: Disordered motor control*, edited by Lance J, Feldman R, Young R and Koella W. Chicago: Year Book, 1980, p. 185 – 204.

Lee RH and Heckman CJ. Paradoxical Effect of QX-314 on Persistent Inward Currents and Bistable Behavior in Spinal Motoneurons In Vivo. *J Neurophysiol* 82: 2518-2527, 1999.

Li Y and Bennett DJ. Persistent Sodium and Calcium Currents Cause Plateau Potentials in Motoneurons of Chronic Spinal Rats. *J Neurophysiol* 90: 857-869, 2003.

Li Y, Gorassini MA, and Bennett DJ. Role of Persistent Sodium and Calcium Currents in Motoneuron Firing and Spasticity in Chronic Spinal Rats. *J Neurophysiol* 91: 767-783, 2004a.

Li Y, Harvey PJ, Li X, and Bennett DJ. Spastic Long-Lasting Reflexes of the Chronic Spinal Rat Studied In Vitro. *J Neurophysiol* 91: 2236-2246, 2004b.

McCreery D, Pikov V, Lossinsky A, Bullara L, and Agnew W. Arrays for chronic functional microstimulation of the lumbosacral spinal cord. *IEEE Trans Neural Syst Rehabil Eng* 12: 195-207, 2004.

McCreery DB, Yuen TGH, and Bullara LA. Chronic microstimulation in the feline ventral cochlear nucleus: physiologic and histologic effects. *Hearing Research* 149: 223-238, 2000.

McIntyre C and Grill W. Selective Microstimulation of Central Nervous System Neurons. *Annals of Biomedical Engineering* 28: 219-233, 2000.

McIntyre CC and Grill WM. Extracellular Stimulation of Central Neurons: Influence of Stimulus Waveform and Frequency on Neuronal Output. *J Neurophysiol* 88: 1592–1604, 2002.

McIntyre CC, Savasta M, Kerkerian-Le Goff L, and Vitek JL. Uncovering the mechanism(s) of action of deep brain stimulation: activation, inhibition, or both. *Clinical Neurophysiology* 115: 1239-1248, 2004.

Merrill DR, Bikson M, and Jefferys JGR. Electrical stimulation of excitable tissue: design of efficacious and safe protocols. *Journal of Neuroscience Methods* 141: 171-198, 2005.

Mortimer J. Motor Prostheses. In: *Section 1: The Nervous System*, edited by Brookhart JM and Mountcastle VB. Bethesda, MD: American Physiological Society, 1981, p. 155-187.

Mushahwar V and Horch K. Selective activation of muscle groups in the feline hindlimb through electrical microstimulation of the ventral lumbo-sacral spinal cord. *IEEE Trans Rehabil Eng* 8: 11-21, 2000.

Mushahwar VK, Collins DF, and Prochazka A. Spinal Cord Microstimulation Generates Functional Limb Movements in Chronically Implanted Cats. *Experimental Neurology* 163: 422-429, 2000.

Powers RK and Binder MD. Input-output functions of mammalian motoneurons. *Rev Physiol Biochem Pharmacol* 143: 137-263, 2001.

Rattay F. Analysis of models for external stimulation of axons. *IEEE Trans Biomed Eng* 33: 974-977, 1986.

Saigal R, Renzi C, and Mushahwar V. Intraspinal microstimulation generates functional movements after spinal-cord injury. *IEEE Trans Neural Syst Rehabil Eng* 12: 430-440, 2004.

Scheiner A, Mortimer J, and Roessmann U. Imbalanced biphasic electrical stimulation: muscle tissue damage. *Ann Biomed Eng* 18: 407-425, 1990.

Solomonow M. External control of the neuromuscular system. *IEEE Trans Biomed Eng* 31: 752-763, 1984.

Thomas CK and Ross BH. Distinct Patterns of Motor Unit Behavior During Muscle Spasms in Spinal Cord Injured Subjects. *J Neurophysiol* 77: 2847-2850, 1997.

Vodovnik L, Bowman B, and Hufford P. Effects of electrical stimulation on spinal spasticity. *Scand J Rehabil Med* 16: 29-34, 1984.

Williamson R and Andrews B. Localized electrical nerve blocking. *IEEE Trans Biomed Eng* 52: 362-370, 2005.

Chapter 6: General Discussion and Conclusions

6.1 ROLE OF PICs IN SPASTICITY

The role of the motoneuronal persistent inward currents (PICs) in spasticity has been suggested especially through the work of the Bennett group. Immediately after injury, the loss of the monoaminergic drive to spinal motoneurons results in disinhibition of the dorsal horn and removal of excitatory drive to the ventral horn. Therefore, the excitatory post synaptic potentials (EPSPs) produced by the dorsal horn become increased immediately after spinal cord injury (SCI). These prolonged EPSPs do not activate long-lasting reflexes in acute injury due to the loss of the motoneuronal PICs. However, in chronic injury, long-lasting reflexes could be activated by the prolonged EPSPs due to the recovery of the motoneuronal PICs and the elevated sensitivity of motoneurons to monoamines.

The work of the present thesis led to the development of the first morphologically-detailed computer model of a spiking spinal motoneuron with the PIC mechanism implemented. This model allowed for studying the properties of the dendritic PIC (distribution of channels, mode of activation, and role in dendritic processing of synaptic inputs) under various conditions (cell firing, current clamp, voltage clamp). Direct measurements of the PIC from the motoneuron dendrites are difficult to be performed experimentally. The developed model allowed also for the design of new electrical stimulation-based therapies to suppress the elevated motoneuronal excitability after injury and reduce the intensity of spasticity.

Our simulations have shown that the dendritic $Ca_V1.3$ channels mediating the dendritic Ca^{+2} PIC have similar distribution to that of dendritic synaptic contacts delivering sensory inputs to motoneurons. The overlap of $Ca_V1.3$ channels and synaptic contacts explains the high efficiency of brief sensory stimuli of various modalities (e.g., muscle stretch, touch, etc) in activating the restored dendritic Ca^{+2} PIC after SCI and triggering

long-lasting reflexes and muscle spasms. Our simulations also revealed that under physiological conditions where normal cell firing occurs, the Ca^{+2} PIC is not activated in an all-or-none manner as was previously predicted. Instead, the Ca^{+2} PIC is activated in a graded manner with increasing synaptic input until it reaches its full activation level. These results allowed for the reconciliation of several conflicting experimental reports on the PIC mode of activation and its role in dendritic processing of synaptic inputs (enhancement of individual inputs and integration of multiple inputs). The graded activation of the dendritic PIC also suggested that modulation of this current to regulate the motoneuronal firing behavior; hence, modulating the level of spasticity may be feasible.

Electrical stimulation provided a tool to modulate the motoneuronal membrane potential and the gating of voltage-sensitive channels through the induced differential polarization. Although suppression of the motoneuronal excitability was achieved using various modalities of electrical stimulation, the underlying mechanisms were different. Diffuse electrical stimulation, through the application of electrical fields between plate electrodes, allowed for the modulation of the dendritic Ca^{+2} PIC to regulate the motoneuronal firing, thereby influencing muscle activity after SCI. On the other hand, focal electrical stimulation, through the delivery of electrical current pulses via microelectrodes, allowed for the hyperpolarization of the first node of Ranvier and reduction of the axonal firing. With both modalities, the motoneuronal excitability was reduced. These electrical stimulation-based techniques could provide clinical therapies to alleviate spasticity after SCI.

6.2 RECENT SUPPORT FOR MODEL PREDICTIONS

6.2.1 Distribution of $Ca_V1.3$ channels

A recent study by Ballou et al. (2006) showed that the dendritic spatial distribution of the $Ca_V1.3$ channels along a number of dendritic branches of cat spinal motoneurons using immunohistochemical labeling of these channels. Their illustrations support our modeling

predictions regarding the presence of the $Ca_V1.3$ channels in dendritic bands at distances of 400 μm to 900 μm away from the soma.

6.2.2 Graded activation of the PIC

In another recent study by Cope et al. (2006), the mode of activation of the PIC was studied through the discharge pattern of motor units in decerebrate cats. Evidence for graded activation of the PICs was inferred from 1) the linear relationship between the difference in firing rate at recruitment and derecruitment (ΔF) and the magnitude of firing rate modulation of the test unit, and 2) the near-linear summation of ΔFs in response to different sensory stimuli (muscle stretch and pinch). These results support our model predictions regarding the graded activation of PICs during normal cell firing.

Our computer simulations demonstrated that the afterhyperpolarization (AHP) effectively acts as a voltage clamp that limits the depolarization of the cell during firing; hence, graded activation of PICs is achieved. A recent study by Shapiro and Lee (2006) supported our predictions by showing that the AHP conductance effectively provides partial clamp of the somatic voltage.

6.3 FUTURE DIRECTIONS

The developed motoneuron model helped in studying the PICs and their activation properties; however, a more accurate motoneuron model for the condition of spasticity could be developed by including the changes in motoneuronal electrical and morphological properties after injury. Such a model could assist in understanding the biophysical and ionic basis underlying the changes in passive and active properties of motoneurons after injury.

Our results have provided specifications for electrical stimulation-based interventions to suppress the elevated motoneuronal excitability and the intensity of muscle spasms after SCI. Verification of the model predictions in animal models of spasticity after chronic SCI would be essential for the assessment of the efficacy of those proposed therapies in

reducing the intensity of spasticity. The proposed electrical stimulation paradigms would enhance the functional outcome of the residual voluntary drive in incomplete SC injured individuals by avoiding the general suppression of their neural activity by current nonspecific antispastic drugs.

6.4 CLINICAL APPLICATIONS

Clinically, electrical field stimulation has numerous attractive properties (e.g., feasibility, safety, and permitting volitional muscle activation) and may be a promising technique for reducing spasticity. During spasticity prolonged exaggerated reflexes are activated, which involve contraction of numerous synergistic muscles around multiple joints (e.g., the flexed position of the arm that involves the activation of the flexors around the wrist and the elbow joints). Application of electrical fields would cause general suppression in the activity of those muscles through the spread of the field-evoked responses via their spinal connections. Application of alternating current electrical fields could be introduced prophylactically to avoid spastic seizures. Metal plates used clinically to provide mechanical support for the cord after spinal injury could be used to deliver the electrical field. On the other hand, the proposed stimulation paradigms of current pulses could be delivered through intraspinal microstimulation microwires used for restoring standing and walking after SCI. Those pulses could relieve spasticity, in addition to restoring limb movements following the injury. For both electrical stimulation paradigms, adaptive adjustment of the stimulation amplitude to the intensity of muscle spasms could be incorporated by allowing the patient to change the intensity of the applied electrical stimulation. This would allow for the reduction of muscle spasms without prohibiting muscle activation through the residual voluntary drive.

In the present thesis work, the behavior of a single motoneuron in response to the application of the proposed electrical stimulation paradigms was studied. Although motoneurons represent the output of the spinal network and their firing behavior governs the activity of the innervated muscle, these paradigms can also modulate the behavior of spinal networks by acting on various neuronal elements in the spinal cord (e.g., sensory

and motor axons, descending tracts, and interneurons). These effects involve changes in the levels of excitation and inhibition mediated by spinal circuits (e.g., Ia-reciprocal inhibition, recurrent inhibition, presynaptic inhibition, interneuronal polysynaptic pathways) that converge on reflexes and regulate their gain. Nonetheless, the success of the proposed paradigms is also contingent upon several factors. For the application of electrical fields, electrode properties (e.g., size and shape) and their orientation and alignment on the spinal column are critical factors for effective application of an electrical field with the minimum stimulating intensity. Some orientations might provide inadequate functional reduction in the level of spasticity, or may cause large initial spasms that could be harmful. For the injection of current pulses, the number of stimulating microwires and the distance between them are critical factors for obtaining a functional reduction in the intensity of muscle spasms. Furthermore, the intensity of the stimulation could result in suppressing the residual volitional drive in individuals with incomplete SCI, in addition to muscle spasms.

6.5 REFERENCES

Ballou EW, Smith WB, Anelli R, and Heckman CJ. Measuring dendritic distribution of membrane proteins. *Journal of Neuroscience Methods* 156: 257-266, 2006.

Cope T, Powers R, and Nardelli P. Graded amplification of synaptic inputs: evidence from paired motor axon recordings. *2006 Neuroscience Meeting Planner Atlanta, GA: Society for Neuroscience, 2006 Online* Program number: 637.22, 2006.

Shapiro N and Lee R. Implications of active dendrites on motoneuron current and voltage properties. *2006 Neuroscience Meeting Planner Atlanta, GA: Society for Neuroscience, 2006 Online* Program number: 55.5, 2006.

Appendix 1: Model Parameters †

7.1 INTRODUCTION

The model was implemented in the NEURON simulation environment (Hines and Carnevale 1997), version 5.7. A variable integration time step was used with error of 0.001 %. This method ensured capturing fine details in the measurements even during fast simulations. The membrane dynamics were simulated to represent neural activity at 36 degrees Celsius and the resting membrane potential was -70 mV. Times were in milliseconds (ms), currents were in milliampere per square centimeter (mA/cm^2), voltages were in millivolts (mV), and concentrations were in millimolar (mM).

The ionic currents, I_{ion}, of different channels can be described by the following general expression

$$I_{ion} = g_{ion} \times (V_m - E_{ion}) \qquad (A1)$$

$$g_{ion} = \bar{g}_{ion} \times m^n \times h^l \qquad (A2)$$

where g_{ion} is the varying conductance of the ion channel; $\bar{g}_{ion}$ is the maximum conductance of the ion channel listed in Table 2-1; m and h are the activation and inactivation gating variables (states), respectively, ranging between 0 and 1; n and l are the order of activation and inactivation, respectively.

For each membrane state variable (η), the time and voltage dependence is given by:

$$d\eta/dt = \alpha_\eta(1-\eta) - \beta_\eta\eta \qquad (A3)$$

$$\tau_\eta = 1/(\alpha_\eta + \beta_\eta) \qquad (A4)$$

† A version of this appendix has been published (ElBasiouny SM, Bennett DJ, and Mushahwar VK, *J. Neurophysiol.* 94: 3961-74, 2005 'used with permission').

7.2 SOMA CHANNELS

7.2.1 Fast $Na^{\pm}$ channels

$$I_{Naf} = \bar{g}_{Naf} \times m^3 \times h \times (V_m - E_{Na}) \quad \text{(A5)}$$

$$\bar{g}_{Naf} = 0.06\ S/cm^2 \qquad E_{Na} = 50\,mV \quad \text{(A6)}$$

$$\alpha_m = [-0.4 \times (V_m + 49)] / [e^{(-(V_m+49)/5)} - 1] \quad \text{(A7)}$$

$$\beta_m = [0.4 \times (V_m + 25)] / [e^{((V_m+25)/5)} - 1] \quad \text{(A8)}$$

$$\tau_h = 30 / [e^{((V_m+60)/15)} + e^{(-(V_m+60)/16)}] \quad \text{(A9)}$$

$$h_\infty = 1 / [e^{((V_m+58)/7)} + 1] \quad \text{(A10)}$$

7.2.2 Delayed rectifier $K^{\pm}$ channels

$$I_{Kdr} = \bar{g}_{Kdr} \times n^4 \times (V_m - E_K) \quad \text{(A11)}$$

$$\bar{g}_{Kdr} = 0.8\ S/cm^2 \qquad E_K = -80\,mV \quad \text{(A12)}$$

$$\tau_n = 5 / [e^{((V_m+50)/40)} + e^{(-(V_m+50)/50)}] \quad \text{(A13)}$$

$$n_\infty = 1 / [e^{((V_m+31)/-15)} + 1] \quad \text{(A14)}$$

7.2.3 Calcium dynamics

The intracellular Ca^{+2} concentration (measured in mM) in the soma depends on the total compartmental Ca^{+2} current, I_{Ca} according to the following balance equation (Booth et al. 1997; McIntyre and Grill 2002).

$$d[Ca]_i/dt = f \times [-\alpha \times I_{Ca} - k_{Ca} \times [Ca]_i] \quad \text{(A15)}$$

$$f = 0.01 \qquad \alpha = 1\ mol/mC/cm^2 \qquad k_{Ca} = 8\ ms^{-1} \quad \text{(A16)}$$

$$[Ca^{+2}]_o = 2\ mM \qquad [Ca^{+2}]_i|_{t=0} = 0.0001\ mM \quad \text{(A17)}$$

where f is the percent of free to bound Ca^{+2} (set to 0.01 based on report from Helmchen et al. (1996). The parameter α converts the total I_{Ca} to Ca^{+2} concentration. k_{Ca} is the Ca^{+2}

removal rate, where Ca^{+2} is removed by uptake into internal stores or by pump extrusion (Booth et al. 1997). In the soma, the total Ca^{+2} current is mediated by the N-type Ca^{+2} channels. $[Ca^{+2}]_o$ is the extracellular Ca^{+2} concentration, and $[Ca^{+2}]_i\ |_{t=0}$ is the intracellular Ca^{+2} concentration at time =0.

The reversal potential for Ca^{+2} channels was calculated from Nernst equation as follows:

$$E_{Ca} = [(R \times T)/(Z \times F)] \times \ln([Ca^{+2}]_o / [Ca^{+2}]_i)$$
$$= [(1000 \times R \times 309.15)/(2 \times F)] \times \ln([Ca^{+2}]_o / [Ca^{+2}]_i) \qquad (A18)$$

$$R = 8.31441\ V\,C\,mol^{-1}\,K^{-1} \qquad T = 36\,°C + 273.15 \qquad (A19)$$

$$Z = 2 \qquad F = 96485.309\ C\,mol^{-1} \qquad (A20)$$

where R is the gas constant, T is the absolute temperature on the Kelvin scale, Z is the valence for Ca^{+2}, and F is Faraday's constant. The factor 1000 is used to convert E_{Ca} to mV.

7.2.4 Ca^{+2}-dependent K^{+} channels

The calcium-dependent potassium channel ($K(Ca^{+2})$) is activated according to the following Hill expression (Booth et al. 1997):

$$I_{K(Ca^{+2})} = \bar{g}_{K(Ca^{+2})} \times [[Ca^{+2}]_i / ([Ca^{+2}]_i + K_d)] \times (V_m - E_K) \qquad (A21)$$

$$\bar{g}_{K(Ca^{+2})} = 0.02\ S/cm^2 \qquad K_d = 0.0005\ mM \qquad E_K = -80\ mV \qquad (A22)$$

where $[Ca^{+2}]_i$ is the intracellular calcium concentration, and K_d is the half-saturation level.

7.2.5 N-type Ca^{+2} channels

$$I_{CaN} = \bar{g}_{CaN} \times m^2 \times h \times (V_m - E_{Ca}) \qquad (A23)$$

$$\bar{g}_{CaN} = 0.01\ S/cm^2 \qquad (A24)$$

$$\tau_m = 15\ ms \qquad (A25)$$

$$m_\infty = 1/\left[e^{((V_m+25)/-5)}+1\right] \quad (A26)$$

$$\tau_h = 50\ ms \quad (A27)$$

$$h_\infty = 1/\left[e^{((V_m+43)/5)}+1\right] \quad (A28)$$

7.3 INITIAL SEGMENT AND AXON HILLOCK CHANNELS

7.3.1 Fast $Na^{\pm}$ channels

$$I_{Naf} = \bar{g}_{Naf} \times m^3 \times h \times (V_m - E_{Na}) \quad (A29)$$

$$\bar{g}_{Naf} = 1.34\ S/cm^2 \qquad E_{Na} = 50\,mV \quad (A30)$$

$$\alpha_m = \left[-0.4 \times (V_m + 53)\right]/\left[e^{(-(V_m+53)/5)} - 1\right] \quad (A31)$$

$$\beta_m = \left[0.4 \times (V_m + 33)\right]/\left[e^{((V_m+33)/5)} - 1\right] \quad (A32)$$

$$\tau_h = 30/\left[e^{((V_m+60)/15)} + e^{(-(V_m+60)/16)}\right] \quad (A33)$$

$$h_\infty = 1/\left[e^{((V_m+58)/7)}+1\right] \quad (A34)$$

7.3.2 Persistent $Na^{\pm}$ channels

$$I_{Nap} = \bar{g}_{Nap} \times m^3 \times (V_m - E_{Na}) \quad (A35)$$

$$\bar{g}_{Nap} = 0.033\,mS/cm^2 \qquad E_{Na} = 50\,mV \quad (A36)$$

$$\alpha_m = \left[-0.0353 \times (V_m + 21.4)\right]/\left[e^{(-(V_m+21.4)/5)} - 1\right] \quad (A37)$$

$$\beta_m = \left[0.000883 \times (V_m + 25.7)\right]/\left[e^{((V_m+25.7)/5)} - 1\right] \quad (A38)$$

7.3.3 Delayed rectifier $K^{\pm}$ channels

$$I_{Kdr} = \bar{g}_{Kdr} \times n^4 \times (V_m - E_K) \quad (A39)$$

$$\bar{g}_{Kdr} = 0.17\ S/cm^2 \qquad E_K = -80\,mV \quad (A40)$$

$$\tau_n = 5/\left[e^{((V_m+50)/40)} + e^{(-(V_m+50)/50)}\right] \quad (A41)$$

$$n_{\infty} = 1/\left[e^{((V_m+31)/-15)} + 1\right] \quad \text{(A42)}$$

7.4 DENDRITIC CHANNELS

7.4.1 LVA L-type Ca^{+2} ($Ca_V1.3$) channels

$$I_{CaL} = \bar{g}_{CaL} \times l \times (V_m - E_{Ca}) \quad \text{(A43)}$$

$\bar{g}_{CaL}$ = see Results (chapter 2) for values of each distribution $E_{Ca} = 60\,mV$ (A44)

$$\tau_l = 60\ ms \quad \text{(A45)}$$

$$l_{\infty} = 1/\left[e^{((V_m+43)/-6)} + 1\right] \quad \text{(A46)}$$

7.5 DENDRITIC SYNAPTIC INPUTS

The synaptic current, I_{syn}, resulting from the activation of individual synapses of different systems was modeled as a battery, E_{syn}, representing the equilibrium potential of the synapse, in series with a time varying conductance, g_{syn}. This conductance was described by an alpha function (Rall 1967; Segev et al. 1990; Jones and Bawa 1997) with time-to-peak (τ_{syn}) as follows:

$$I_{syn}(t) = g_{syn}(t) \times (V_m - E_{syn}) \quad \text{(A47)}$$

$$g_{syn}(t) = \bar{g}_{syn} \times \left[t/\tau_{syn}\right] \times e^{(1-(t/\tau_{syn}))} \quad \text{(A48)}$$

$\tau_{syn} = 0.2\ ms$ $\qquad \bar{g}_{syn} = 0.0033\ \mu S$ $\qquad E_{syn} = 0.0\ mV$ (A49)

7.6 REFERENCES

Booth V, Rinzel J, and Kiehn O. Compartmental Model of Vertebrate Motoneurons for Ca2+-Dependent Spiking and Plateau Potentials Under Pharmacological Treatment. *J Neurophysiol* 78: 3371-3385, 1997.

Helmchen F, Imoto K, and Sakmann B. Ca2+ buffering and action potential-evoked Ca2+ signaling in dendrites of pyramidal neurons. *Biophys J* 70: 1069-1081., 1996.

Hines M and Carnevale T. The NEURON simulation environment. *Neural Comput* 9: 1179-1209, 1997.

Jones KE and Bawa P. Computer Simulation of the Responses of Human Motoneurons to Composite 1A EPSPS: Effects of Background Firing Rate. *J Neurophysiol* 77: 405-420, 1997.

McIntyre CC and Grill WM. Extracellular Stimulation of Central Neurons: Influence of Stimulus Waveform and Frequency on Neuronal Output. *J Neurophysiol* 88: 1592–1604, 2002.

Rall W. Distinguishing theoretical synaptic potentials computed for different soma-dendritic distributions of synaptic input. *J Neurophysiol* 30: 1138-1168, 1967.

Segev I, Fleshman JW, and Burke RE. Computer simulation of group Ia EPSPs using morphologically realistic models of cat alpha-motoneurons. *J Neurophysiol* 64: 648-660, 1990.

Appendix 2: Electrical Fields of Point Source or Spherical Electrodes

8.1 INTRODUCTION

The electrical field generated from current flow between two electrodes depends on the electrode shape and configuration (Fig. 8-1). In chapter 4, we examined the effect of an electrical field generated from the current flow between two *parallel plate* electrodes (Fig. 4-1; Fig. 8-1A). The extracellular field potential (V_e) for this configuration is described by the following relationship:

$$V_e = I \cdot \rho \cdot (x - 0.5D)$$

where V_e is the extracellular field potential for each compartment, I is the current, ρ is the extracellular electrical resistivity of the gray matter, x is the radial distance along the field axis between each compartment and the positive plate electrode, and D is the distance between the two parallel plate electrodes.

Given that practical implementation of electrical fields to the spinal cord could involve the deployment of electrodes of different shapes and sizes (i.e., other than parallel plate electrodes), we examined the effect of uniform electrical fields generated between two *distantly located (point source)* electrodes or *spherical* electrodes on the firing behavior of motoneurons. In this case, the uniform electrical field will be only valid in the central region when the two electrodes are placed far away from each other. The extracellular field potential for this configuration (Fig. 8-1B) could be described by the following formula:

$$V_e = \frac{I \cdot \rho}{4 \cdot \pi}\left(\frac{1}{r_+} - \frac{1}{r_-}\right)$$

where V_e is the extracellular field potential for each compartment, I is the current, ρ is the extracellular electrical resistivity of the gray matter, r_+ and r_- are the radial distances

between each compartment and the positive and negative plate electrodes along the field axis, respectively.

For the same field intensity, uniform electrical fields generated from current flow between either parallel plate electrodes or distantly located spherical electrodes had identical effects on the motoneuronal firing behavior and resulted in reduction of firing rate of similar amounts (Fig. 8-2). This indicates that uniform electrical fields generated in the spinal cord using electrodes of different shapes would be effective in reducing the motoneuronal excitability in the stimulated region of the cord.

8.2 FIGURES

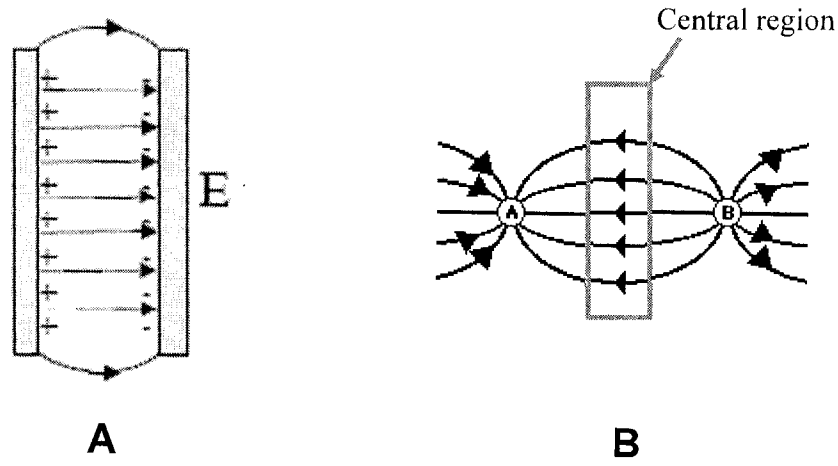

Figure 8-1. Electrical field lines generated from current flow between two parallel plate electrodes (**A**) and two point source or spherical electrodes (**B**). Note that when the point source or spherical electrodes are placed far from each other, the central region of the field becomes uniform.

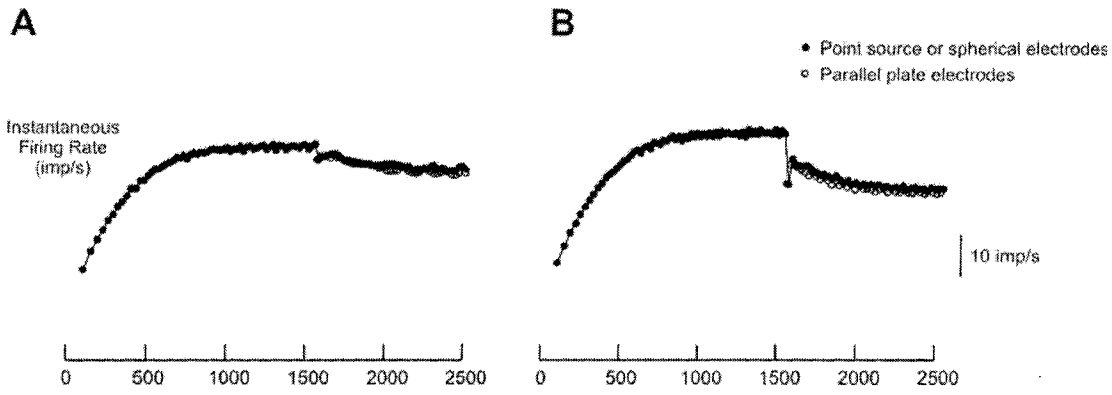

Figure 8-2. Comparison of the model motoneuronal firing rates after the application of DC electrical fields along the mediolateral (**A**) and dorsoventral (**B**) axes of the spinal cord.

Appendix 3: Program Code

The model was implemented in the NEURON simulation environment.

9.1 MAIN PROGRAM

```
load_file("nrngui.hoc")                    // - Load Neuron
load_file("GlobalVariables.hoc")           // - Define global variables for the model
// Morphology and Biophysical Files
load_file("Axon.hoc")                      // - Define the morphology and
                                           // biophysical properties of the Axon
load_file("TreeMorphology.hoc")            //- Define the morphology of dendritic tree,
                                           // soma, axon hillock and Initial segment
                                           // with connection to the axon
load_file("TreeBiophysics.hoc")            // - Define the passive properties and ion
                                           // channels of the dendrites, soma, axon
                                           // hillock and initial segment
load_file("Dendritic Channels.hoc")        // - Define dendritic ion channels and their
                                           // properties
load_file("Gca Computation.hoc")           // - Compute the overall conductance and Ica
                                           // of the CaV1.3 channels

// Synapses Files
load_file("IaAfferentSynapses.hoc")        // - Activate groups of the Ia afferent
                                           // synapses (from 13.7% to 100%)

// Extracellular Stimulation Files
load_file("Record Field Potentials.hoc")   // - Record extracellular field potentials from
                                           // all segments in the model
                                           // - Interpolate nodes to form the mesh
load_file("CustomizedInit.hoc")            // - Customized NEURON procedures init(),
                                           // advance())

// Electrode Configuration
load_file("MonopolarExtracellStim.hoc")    // - Compute Resistance between nodes and
                                           // Extracellular Stimulation/Recording elect.

// Extracellular Waveforms
load_file("Trapezoidal Pulse.hoc")         // - Design of the Extracellular Stimulus –
                                           // 3 part Trapezoidal waveform
load_file("SinWavePulse.hoc")              // - Design of the Extracellular Stimulus –
                                           // Sin Waveform

// Extracellular Fields
load_file("Extracellular DC Field.hoc")    // - Apply a homogenous extracellular DC field
load_file("Extracellular AC Field-SinWave.hoc")          // - Apply a homogenous
                                                         // extracellular AC field
load_file("Extracellular AC Field-SquareWave.hoc")       // - Apply a homogenous
                                                         // extracellular AC field
```

9.2 GLOBAL VARIABLES

```
// Settings for extracellular stimulation through injected pulses
Isotropic_Medium = 1            // Flag for extracellular stimulation/recording  mechanism
                                // = 0  means anisotropic medium
                                // = 1  means isotropic medium
proc model_globels() {
  if (Isotropic_Medium == 1){   // Isotropic medium
```

```
        rho = 2000              // ohm cm, the approximate extracellular resistivity
                                // (isotropic medium) of spinal cord grey matter in
                                // the cat.
    } else {                    // Anisotropic medium
        rho_x = 2000            // ohm cm, the approximate extracellular resistivity
                                // (x-direction) of spinal cord grey matter in cat.
        rho_y = 2000            // ohm cm, the approximate extracellular resistivity
                                // (y-direction) of spinal cord grey matter in cat.
        rho_z = 2000            // ohm cm, the approximate extracellular resistivity
                                // (z-direction) of spinal cord grey matter in cat.
    }
// Define Variables and Flags
IaAFFERENTSFLAG = 0             // Flag for creation of the Ia-Afferents synapses, OFF by default
IaINHIBITIONFLAG = 0            // Flag for creation of the Ia-Inhibitory synapses, OFF by default
Select_IaAFFERENTSFLAG = 0      // Flag for creation of selected groups of the Ia-afferents synapses,
                                // OFF by default
celsius = 36
v_init= -70                     // mV, resting membrane potential
}
model_globels()
```

9.3 AXON

Model is adapted from McIntyre CC, Richardson AG, and Grill WM. Journal of Neurophysiol 87:995-1006, 2002.
The Shiftvalue is added to center the soma at point (0,0,0).
shiftvalue = 0.5*Length of Soma + Length of the Initial Segment + Total Length of the Axon Hillock Structure + Total Length of the Axon Structure
Total Length of the Axon Structure= Number_ShortAxonNodes x Short_Segment + (axonnodes-Number_ShortAxonNodes) x Long_Segment

```
// Topological parameters
axonnodes=10
Number_ShortAxonNodes=5
paranodes1=20
paranodes2=20
axoninter=60
axontotal=110
// Morphological Parameters
fiberD= 14                      // For FR motoneuron, diam is 14 um. This give CV of 91
                                // m/s, measured between nodes 9 and 8,
                                // measured with current injected at the iseg of 0.5 ms, and
                                // 20 nA pulse. Passive tree.
paralength1=3
nodelength=1.0
space_p1=0.002
space_p2=0.004
space_i=0.004
// Biophysical Properties of the Axon Structure
// Electrical parameters
rhoa_Axnodes=0.7e6              // Ohm-um
mycm=0.1                        // uF/cm2/lamella membrane
mygm=0.001                      // S/cm2/lamella membrane
proc ChooseAxonDiam() {
        if (fiberD==10.0) {g=0.690 axonD=6.9 nodeD=3.3 paraD1=3.3 paraD2=6.9 deltax=1150
paralength2=46 nl=120}
```

```
        if (fiberD==11.5) {g=0.700 axonD=8.1 nodeD=3.7 paraD1=3.7 paraD2=8.1 deltax=1250
paralength2=50 nl=130}
        if (fiberD==12.8) {g=0.719 axonD=9.2 nodeD=4.2 paraD1=4.2 paraD2=9.2 deltax=1350
paralength2=54 nl=135}
        if (fiberD==14.0) {g=0.739 axonD=10.4 nodeD=4.7 paraD1=4.7 paraD2=10.4 deltax=1400
paralength2=56 nl=140}
        if (fiberD==15.0) {g=0.767 axonD=11.5 nodeD=5.0 paraD1=5.0 paraD2=11.5 deltax=1450
paralength2=58 nl=145}
        if (fiberD==16.0) {g=0.791 axonD=12.7 nodeD=5.5 paraD1=5.5 paraD2=12.7 deltax=1500
paralength2=60 nl=150}
        interlength=(deltax-nodelength-(2*paralength1)-(2*paralength2))/6
        Long_Segment= (nodelength + 2*paralength1 + 2*paralength2 + 6*interlength)
        Short_Segment= (nodelength + 2*paralength1 + 2*paralength2 + 6*interlength/3)
        shiftvalue= 0.5*48.8 + 50 + Number_ShortAxonNodes*Short_Segment +
      (axonnodes-Number_ShortAxonNodes)*Long_Segment

        Rpn0=(rhoa_Axnodes*.01)/(PI*((((nodeD/2)+space_p1)^2)-((nodeD/2)^2)))
        Rpn1=(rhoa_Axnodes*.01)/(PI*((((paraD1/2)+space_p1)^2)-((paraD1/2)^2)))
        Rpn2=(rhoa_Axnodes*.01)/(PI*((((paraD2/2)+space_p2)^2)-((paraD2/2)^2)))
        Rpx=(rhoa_Axnodes*.01)/(PI*((((axonD/2)+space_i)^2)-((axonD/2)^2)))
}
ChooseAxonDiam()
// Define the electrical properties for each compartment of the axon structure
create node[axonnodes], MYSA[paranodes1], FLUT[paranodes2], STIN[axoninter]
access node[0]
proc initialize(){
        for i=0,axonnodes-1 {
                node[i]{
                        insert ax
//                      gnabar_ax = 0.0                 // to see the changes in membrane
                                                        // potential at the 1st node of Ranvier
//                      gnapbar_ax = 0.0
                        insert extracellular  xraxial=Rpn0     xg=1e10     xc=0
                        insert xtra
                        insert pas                g_pas = 0.007     e_pas = -80
                        Ra=rhoa_Axnodes/10000
                        cm=2
                        }
                }
        for i=0, paranodes1-1 {
                MYSA[i]{
                        insert pas          g_pas=0.001*paraD1/fiberD    e_pas= v_init
                        insert extracellular  xraxial=Rpn1     xg=mygm/(nl*2)
                        xc=mycm/(nl*2)
                        insert xtra
                        Ra=rhoa_Axnodes*(1/(paraD1/fiberD)^2)/10000
                        cm=2*paraD1/fiberD
        }}
        for i=0, paranodes2-1 {
                FLUT[i]{
                        insert pas          g_pas=0.0001*paraD2/fiberD   e_pas= v_init
                        insert extracellular  xraxial=Rpn2          xg=mygm/(nl*2)
                        xc=mycm/(nl*2)
                        insert xtra

                        Ra=rhoa_Axnodes*(1/(paraD2/fiberD)^2)/10000
```

```
                    cm=2*paraD2/fiberD
                    }
        }
        for i=0, axoninter-1 {
                STIN[i]{
                insert pas          g_pas=0.0001*axonD/fiberD    e_pas= v_init
                        insert extracellular   xraxial=Rpx              xg=mygm/(nl*2)
                        xc=mycm/(nl*2)
                        insert xtra
                        Ra=rhoa_Axnodes*(1/(axonD/fiberD)^2)/10000
                        cm=2*axonD/fiberD
                        } }}
initialize()
// Define 3D-data for each compartment of the structure
// Nodes (5 nodes, n0 to end of n4) away from the initial segment. They have Long segments
for i=0, axonnodes-Number_ShortAxonNodes-1 {
        access node[i]
        pt3dadd(0,(Long_Segment*i)-shiftvalue,0,nodeD)
        pt3dadd(0,(Long_Segment*i)+nodelength-shiftvalue,0,nodeD)
        access MYSA[2*i]
        pt3dadd(0,(Long_Segment*i)+nodelength-shiftvalue,0,fiberD)
        pt3dadd(0,(Long_Segment*i)+nodelength+paralength1-shiftvalue,0,fiberD)
        access FLUT[2*i]
        pt3dadd(0,(Long_Segment*i)+nodelength+paralength1-shiftvalue,0,fiberD)
        pt3dadd(0,(Long_Segment*i)+nodelength+paralength1+paralength2-
        shiftvalue,0,fiberD)
        access STIN[6*i]
        pt3dadd(0,(Long_Segment*i)+nodelength+paralength1+paralength2-
        shiftvalue,0,fiberD)
        pt3dadd(0,(Long_Segment*i)+nodelength+paralength1+paralength2+interlength-
        shiftvalue,0,fiberD)
        access STIN[6*i+1]
        pt3dadd(0,(Long_Segment*i)+nodelength+paralength1+paralength2+interlength-
        shiftvalue,0,fiberD)
        pt3dadd(0,(Long_Segment*i)+nodelength+paralength1+paralength2+
        2*interlength-shiftvalue,0,fiberD)
        access STIN[6*i+2]
        pt3dadd(0,(Long_Segment*i)+nodelength+paralength1+paralength2+
        2*interlength-shiftvalue,0,fiberD)
        pt3dadd(0,(Long_Segment*i)+nodelength+paralength1+paralength2+
        3*interlength-shiftvalue,0,fiberD)
        access STIN[6*i+3]
        pt3dadd(0,(Long_Segment*i)+nodelength+paralength1+paralength2+
        3*interlength-shiftvalue,0,fiberD)
        pt3dadd(0,(Long_Segment*i)+nodelength+paralength1+paralength2+
        4*interlength-shiftvalue,0,fiberD)
        access STIN[6*i+4]
        pt3dadd(0,(Long_Segment*i)+nodelength+paralength1+paralength2+
        4*interlength-shiftvalue,0,fiberD)
        pt3dadd(0,(Long_Segment*i)+nodelength+paralength1+paralength2+
        5*interlength-shiftvalue,0,fiberD)
        access STIN[6*i+5]
        pt3dadd(0,(Long_Segment*i)+nodelength+paralength1+paralength2+
        5*interlength-shiftvalue,0,fiberD)
        pt3dadd(0,(Long_Segment*i)+nodelength+paralength1+paralength2+
        6*interlength-shiftvalue,0,fiberD)
```

```
        access FLUT[2*i+1]
         pt3dadd(0,(Long_Segment*i)+nodelength+paralength1+paralength2+
         6*interlength-shiftvalue,0,fiberD)
         pt3dadd(0,(Long_Segment*i)+nodelength+paralength1+2*paralength2+
         6*interlength-shiftvalue,0,fiberD)
        access MYSA[2*i+1]
         pt3dadd(0,(Long_Segment*i)+nodelength+paralength1+2*paralength2+
         6*interlength-shiftvalue,0,fiberD)
         pt3dadd(0,(Long_Segment*i)+nodelength+2*paralength1+2*paralength2+
         6*interlength-shiftvalue,0,fiberD)
  }
// Nodes (5 nodes, n5 to end of n9) close to the initial segment. They have Short Segments.
for i=axonnodes-Number_ShortAxonNodes, axonnodes-1 {
  access node[i]
  pt3dadd(0,(Long_Segment*(axonnodes-4))+(Short_Segment*(i-axonnodes+4))-
  shiftvalue,0,nodeD)
  pt3dadd(0,(Long_Segment*(axonnodes-4))+(Short_Segment*(i-
  axonnodes+4))+nodelength-shiftvalue,0,nodeD)
  access MYSA[2*i]
  pt3dadd(0,(Long_Segment*(axonnodes-4))+(Short_Segment*(i-
  axonnodes+4))+nodelength-shiftvalue,0,fiberD)
  pt3dadd(0,(Long_Segment*(axonnodes-4))+(Short_Segment*(i-
  axonnodes+4))+nodelength+paralength1-shiftvalue,0,fiberD)
  access FLUT[2*i]
  pt3dadd(0,(Long_Segment*(axonnodes-4))+(Short_Segment*(i-
  axonnodes+4))+nodelength+paralength1-shiftvalue,0,fiberD)
  pt3dadd(0,(Long_Segment*(axonnodes-4))+(Short_Segment*(i-
  axonnodes+4))+nodelength+paralength1+paralength2-shiftvalue,0,fiberD)
  access STIN[6*i]
  pt3dadd(0,(Long_Segment*(axonnodes-4))+(Short_Segment*(i-
  axonnodes+4))+nodelength+paralength1+paralength2-shiftvalue,0,fiberD)
  pt3dadd(0,(Long_Segment*(axonnodes-4))+(Short_Segment*(i-
  axonnodes+4))+nodelength+paralength1+paralength2+(interlength/3)-
  shiftvalue,0,fiberD)
  access STIN[6*i+1]
  pt3dadd(0,(Long_Segment*(axonnodes-4))+(Short_Segment*(i-
  axonnodes+4))+nodelength+paralength1+paralength2+(interlength/3)-
  shiftvalue,0,fiberD)
  pt3dadd(0,(Long_Segment*(axonnodes-4))+(Short_Segment*(i-
  axonnodes+4))+nodelength+paralength1+paralength2+2*(interlength/3)-
  shiftvalue,0,fiberD)
  access STIN[6*i+2]
  pt3dadd(0,(Long_Segment*(axonnodes-4))+(Short_Segment*(i-
  axonnodes+4))+nodelength+paralength1+paralength2+2*(interlength/3)-
  shiftvalue,0,fiberD)
  pt3dadd(0,(Long_Segment*(axonnodes-4))+(Short_Segment*(i-
  axonnodes+4))+nodelength+paralength1+paralength2+3*(interlength/3)-
  shiftvalue,0,fiberD)
  access STIN[6*i+3]
  pt3dadd(0,(Long_Segment*(axonnodes-4))+(Short_Segment*(i-
  axonnodes+4))+nodelength+paralength1+paralength2+3*(interlength/3)-
  shiftvalue,0,fiberD)
  pt3dadd(0,(Long_Segment*(axonnodes-4))+(Short_Segment*(i-
  axonnodes+4))+nodelength+paralength1+paralength2+4*(interlength/3)-
  shiftvalue,0,fiberD)
  access STIN[6*i+4]
```

```
  pt3dadd(0,(Long_Segment*(axonnodes-4))+(Short_Segment*(i-
  axonnodes+4))+nodelength+paralength1+paralength2+4*(interlength/3)-
  shiftvalue,0,fiberD)
  pt3dadd(0,(Long_Segment*(axonnodes-4))+(Short_Segment*(i-
  axonnodes+4))+nodelength+paralength1+paralength2+5*(interlength/3)-
  shiftvalue,0,fiberD)
  access STIN[6*i+5]
  pt3dadd(0,(Long_Segment*(axonnodes-4))+(Short_Segment*(i-
  axonnodes+4))+nodelength+paralength1+paralength2+5*(interlength/3)-
  shiftvalue,0,fiberD)
  pt3dadd(0,(Long_Segment*(axonnodes-4))+(Short_Segment*(i-
  axonnodes+4))+nodelength+paralength1+paralength2+6*(interlength/3)-
  shiftvalue,0,fiberD)
  access FLUT[2*i+1]
  pt3dadd(0,(Long_Segment*(axonnodes-4))+(Short_Segment*(i-
  axonnodes+4))+nodelength+paralength1+paralength2+6*(interlength/3)-
  shiftvalue,0,fiberD)
  pt3dadd(0,(Long_Segment*(axonnodes-4))+(Short_Segment*(i-
  axonnodes+4))+nodelength+paralength1+2*paralength2+6*(interlength/3)-
  shiftvalue,0,fiberD)
  access MYSA[2*i+1]
  pt3dadd(0,(Long_Segment*(axonnodes-4))+(Short_Segment*(i-
  axonnodes+4))+nodelength+paralength1+2*paralength2+6*(interlength/3)-
  shiftvalue,0,fiberD)
  pt3dadd(0,(Long_Segment*(axonnodes-4))+(Short_Segment*(i-
  axonnodes+4))+nodelength+2*paralength1+2*paralength2+6*(interlength/3)-
  shiftvalue,0,fiberD)
 }
// Connect the compartments together to form the axon structure
for i=0, axonnodes-2 {
                connect MYSA[2*i](0), node[i](1)
                connect FLUT[2*i](0), MYSA[2*i](1)
                connect STIN[6*i](0), FLUT[2*i](1)
                connect STIN[6*i+1](0), STIN[6*i](1)
                connect STIN[6*i+2](0), STIN[6*i+1](1)
                connect STIN[6*i+3](0), STIN[6*i+2](1)
                connect STIN[6*i+4](0), STIN[6*i+3](1)
                connect STIN[6*i+5](0), STIN[6*i+4](1)
                connect FLUT[2*i+1](0), STIN[6*i+5](1)
                connect MYSA[2*i+1](0), FLUT[2*i+1](1)
                connect node[i+1](0), MYSA[2*i+1](1)
    }
    i=axonnodes-1
                connect MYSA[2*i](0), node[i](1)
                connect FLUT[2*i](0), MYSA[2*i](1)
                connect STIN[6*i](0), FLUT[2*i](1)
                connect STIN[6*i+1](0), STIN[6*i](1)
                connect STIN[6*i+2](0), STIN[6*i+1](1)
                connect STIN[6*i+3](0), STIN[6*i+2](1)
                connect STIN[6*i+4](0), STIN[6*i+3](1)
                connect STIN[6*i+5](0), STIN[6*i+4](1)
                connect FLUT[2*i+1](0), STIN[6*i+5](1)
                connect MYSA[2*i+1](0), FLUT[2*i+1](1)
// Create a list of all segments of the axon structure
objref AxonList
AxonList = new SectionList() // Create a section list for the names of the axon elements
```

```
for i=0, axonnodes-1 {
    access node[i]
    AxonList.append()          // add the currently accessed axon section to the Axonlist
    access MYSA[2*i]
    AxonList.append()          // add the currently accessed axon section to the Axonlist
    access FLUT[2*i]
    AxonList.append()          // add the currently accessed axon section to the Axonlist
    access STIN[6*i]
    AxonList.append()          // add the currently accessed axon section to the Axonlist
    access STIN[6*i+1]
    AxonList.append()          // add the currently accessed axon section to the Axonlist
    access STIN[6*i+2]
    AxonList.append()          // add the currently accessed axon section to the Axonlist
    access STIN[6*i+3]
    AxonList.append()          // add the currently accessed axon section to the Axonlist
    access STIN[6*i+4]
    AxonList.append()          // add the currently accessed axon section to the Axonlist
    access STIN[6*i+5]
    AxonList.append()          // add the currently accessed axon section to the Axonlist
    access FLUT[2*i+1]
    AxonList.append()          // add the currently accessed axon section to the Axonlist
    access MYSA[2*i+1]
    AxonList.append()          // add the currently accessed axon section to the Axonlist
}
access MYSA[19]                // confirm that the last compartment is added to the list
AxonList.append()              // add the last part of the axon structure to the Axonlist
AxonList.unique()              // confirm that there is no multiples of compartments in the
                               // list.
```

9.4 TREE MORPHOLOGY

```
// This code reads the anatomy files format (for the Soma, Ah, IS in 3D-SISAH-Morphology.ant) and (for
Dendrites in DT3DMorphology.ant)
// and then creates the appropriate NEURON morphology and connection.
// The structure iseg organized such that:
// DendritesList (proximal, distal) - Soma - AHList (tapered Axon Hillock) - IS - Axon.
objref den, ord, br, seg, type
strdef tstr, tstr2, tstr3, rr
objref f
objref DendritesList, AHList, ProxDendList, DistDendList
DendritesList = new SectionList()          // Create a section list for the names of the dendrites in the tree
AHList = new SectionList()                 // Create a section list for the names of the AH segments
ProxDendList = new SectionList()           // Create a section list for the names of the Proximal Dendrites
DistDendList = new SectionList()           // Create a section list for the names of the Distal Dendrites
proc r() { local x1, y1, z1, x2, y2, z2, diam, i
    den = new Vector()
    ord = den.c  br = den.c  seg = den.c  type = den.c
    f = new File()
    f.ropen("FR43-5MorphANDaxon_Y.ant")    // Open file for the 3D Morphology of Dendrites
    for (i = 0; !f.eof ; i += 1) {         // i is the order of dendrite segment in the table
        den.append(f.scanvar())
        ord.append(f.scanvar())
        br.append(f.scanvar())
        seg.append(f.scanvar())
        type.append(f.scanvar())
```

```
            x1 = f.scanvar()
            y1 = f.scanvar()
            z1 = f.scanvar()
            x2 = f.scanvar()
            y2 = f.scanvar()
            z2 = f.scanvar()
            f.scanvar()                          // skip seg length. it is inconsistent with 3-d
            diam = f.scanvar()

            sname(tstr, i)                       // give a name to this section
            sprint(tstr2, "create %s", tstr)     // create this segment
            execute(tstr2)
            sprint(tstr2, "access %s", tstr)     // access this segment
            execute(tstr2)
            pt3dadd(x1, y1, z1, diam)            // add morphology info to this segment
            pt3dadd(x2, y2, z2, diam)
            con(i)                               // connect this segment to the previous segment
        }
}
proc sname() {
        if (numarg() > 2) {
            sprint($s1, "den%do%db%ds%dt%d", $2, $3, $4, $5, $6)
        }else{
            sprint($s1, "den%do%db%ds%dt%d", den.x[$2], ord.x[$2], br.x[$2], seg.x[$2],
            type.x[$2])
        }
        if ($2 == 0)  $s1="iseg"
        if ($2 == 1)  $s1="ah1"
        if ($2 == 2)  $s1="ah2"
        if ($2 == 3)  $s1="ah3"
        if ($2 == 4)  $s1="ah4"
        if ($2 == 5)  $s1="ah5"
        if ($2 == 6)  $s1="ah6"
        if ($2 == 7)  $s1="ah7"
        if ($2 == 8)  $s1="ah8"
        if ($2 == 9)  $s1="ah9"
        if ($2 == 10) $s1="ah10"
        if ($2 == 11) $s1="ah11"
        if ($2 == 12) $s1="soma"
}
proc sname1() {
        if (numarg() > 2) {
            sprint($s1, "den%do%db%ds%dt%d", $2, $3, $4, $5, $6)
        }else{
            sprint($s1, "den%do%db%ds%dt%d", den.x[$2], ord.x[$2], br.x[$2], seg.x[$2], type.x[$2])
        }
        if ($2 == 0)    $s1="iseg"
        if ($2 == 1)  { $s1="ah1"
                AHList.append()                  }
        if ($2 == 2)  { $s1="ah2"
                AHList.append()                  }
        if ($2 == 3)  { $s1="ah3"
                AHList.append()
                }
        if ($2 == 4)  { $s1="ah4"
                AHList.append()                  }
```

```
    if ($2 == 5)  { $s1="ah5"
            AHList.append()                 }
    if ($2 == 6)  { $s1="ah6"
            AHList.append()                 }
    if ($2 == 7)  { $s1="ah7"
            AHList.append()                 }
    if ($2 == 8)  { $s1="ah8"
            AHList.append()                 }
    if ($2 == 9)  { $s1="ah9"
            AHList.append()                 }
```

9.5 TREE BIOPHYSICS

```
// This code is used to assign the active and passive properties to the Soma, AH, IS, and
//  the Dentritic Tree of the model.
// The specific membrane conductance is in S/cm^2, the reversal potential in mV,
// specific axial resistivity in Ohm*cm and specific membrane capacitance in
// microF/cm^2.
// The values of Ra, Cm,and Rm are according to Fleshman J, Segev I, and Burke R,
// "Electronic Architecture of Type-Identified alpha-motoneurons in the // cat spinal
// cord," J Neurophysiol, 60(1):60-85, 1988.
// The system tau= 7 ms, and input Resistance (Rin)=1.32 M Ohm
soma {
        insert extracellular
        insert xtra
        insert NafSm                            // Fast Na Channels
        insert KdrSm                            // Delayed Rectifier Channels
        insert CaSm                             // Calcium-activated K Channels +
                                                // Calcium Channels (L-type, N-
                                                // type) + Calcium Dynamics
        insert pas              g_pas=(1/225)   // S/cm2
                                e_pas= v_init   // mv
        Ra=70                                   // ohm.cm
        cm=1                                    // uf/cm2
}
iseg {
        insert extracellular
        insert xtra
        insert NafIs                            // Fast Na Channels
        insert NapIs                            // Persistent Na Channels
        insert KdrIs                            // Delayed Rectifier K Channels
        insert pas              g_pas=(1/225)   // S/cm2
                                e_pas= v_init   // mv
        Ra=70                                   // ohm.cm
        cm=1                                    // uf/cm2
}
forsec AHList {
        insert extracellular
        insert xtra
        insert NafIs                            // Fast Na Channels
        insert NapIs                            // Persistent Na Channels
        insert KdrIs                            // Delayed Rectifier K Channels
        insert pas              g_pas=(1/225)   // S/cm2
                                e_pas= v_init   // mv
        Ra=70                                   // ohm.cm
```

```
        cm=1                                    // uf/cm2
}
forsec DendritesList {
        insert extracellular
        insert xtra
        insert info
        insert pas              g_pas=(1/11000)         // S/cm2
```

9.6 DENDRITIC CHANNELS

```
// Define nseg in every segment according to d_lambda
proc segments_numbers() {
        D_LAMBDA = 0.1
        forall { nseg = int((L/(D_LAMBDA*lambda_f(100))+0.9)/2)*2 + 1 }
} // End of Procedure
// Procedure for getting the parent of a compartment
strdef string, CompName
proc GetParent(){                       // The procedure has a string input, which is the
                                        // compartment name
        sprint(string, "access %s", $s1)
        execute(string)
        A=x3d(0)                B=y3d(0)                C=z3d(0)
        if((A!=0) && (B!=0) && (C!=0)){
                forsec DendritesList {
        if((x3d(1)==A) && (y3d(1)==B)  && (z3d(1)==C)) {
        LengthCounter = LengthCounter + L
        SpaceCounter = SpaceCounter + sqrt(10000*diam/4/Ra/g_pas(0.5))
        ElectrotonicCounter  = ElectrotonicCounter +
        L/sqrt(10000*diam/4/Ra/g_pas(0.5))

        XElectrotonicCounter = XElectrotonicCounter + sqrt( (x3d(0)-x3d(1))^2
        )/sqrt(10000*diam/4/Ra/g_pas(0.5))
        YElectrotonicCounter = YElectrotonicCounter + sqrt( (y3d(0)-y3d(1))^2
        )/sqrt(10000*diam/4/Ra/g_pas(0.5))
        ZElectrotonicCounter = ZElectrotonicCounter + sqrt( (z3d(0)-z3d(1))^2
        )/sqrt(10000*diam/4/Ra/g_pas(0.5))
        GetParent(secname())                                                    }
                }
        }
} // End of procedure
proc FindDendLoc(){
        LengthCounter = 0
        SpaceCounter = 0
        ElectrotonicCounter = 0
        XElectrotonicCounter = 0
        YElectrotonicCounter = 0
        ZElectrotonicCounter = 0
        CompName = $s1
        sprint(string, "access %s", CompName)
        execute(string)
        LengthCounter = L/2
        SpaceCounter = sqrt( 10000*diam/4/Ra/g_pas(0.5) )
        ElectrotonicCounter = L/sqrt(10000*diam/4/Ra/g_pas(0.5))
        XElectrotonicCounter = sqrt( (x3d(0)-x3d(1))^2
        )/sqrt(10000*diam/4/Ra/g_pas(0.5))          // no units, both in um
```

```
        YElectrotonicCounter = sqrt( (y3d(0)-y3d(1))^2
        )/sqrt(10000*diam/4/Ra/g_pas(0.5))          // no units, both in um
        ZElectrotonicCounter = sqrt( (z3d(0)-z3d(1))^2
        )/sqrt(10000*diam/4/Ra/g_pas(0.5))          // no units, both in um
        GetParent(CompName)
        sprint(string, "%s.DendDist_info=%f",CompName,LengthCounter)
        execute(string)
        sprint(string, "%s.SpaceConstant_info=%f",CompName,SpaceCounter)
        execute(string)
        sprint(string, "%s.ElectroL_info=%f",CompName,ElectrotonicCounter)
        execute(string)
        sprint(string, "%s.ElectroLx_info=%f",CompName,XElectrotonicCounter)
        execute(string)
        sprint(string, "%s.ElectroLy_info=%f",CompName,YElectrotonicCounter)
        execute(string)
        sprint(string, "%s.ElectroLz_info=%f",CompName,ZElectrotonicCounter)
        execute(string)
} // End of procedure
proc GetInfo() {
        forsec DendritesList {
                LengthCounter = 0
                SpaceCounter = 0
                ElectrotonicCounter = 0
                XElectrotonicCounter = 0
                YElectrotonicCounter = 0
                ZElectrotonicCounter = 0
                FindDendLoc(secname())
        }
} // End Procedure
proc GetXYZ() {
        CompName = $s1
        sprint(string, "access %s", CompName)
        execute(string)
        print DendDist_info
        printf("X=%.2f   \t Y=%.2f \t Z=%.2f\n",(x3d(0)+x3d(1))/2,(y3d(0)+y3d(1))/2,(z3d(0)+z3d(1))/2)
} // End of procedure
proc AdjustIsegAH() {
        forsec AHList {
                gnabar_NafIs = iseg.gnabar_NafIs        // AH is the same as Iseg
                gnapbar_NapIs = iseg.gnapbar_NapIs      // AH is the same as Iseg
                gkbar_KdrIs = iseg.gkbar_KdrIs          // AH is the same as Iseg
        }
} // End of Procedure
proc UpdateChannels() {
        soma.gnabar_NafSm = 0.06
        soma.gkdrbar_KdrSm = 0.80048
        soma.gkcabar_CaSm = 0.02
        soma.gcanbar_CaSm = 0.01
        // Calcium Dynamics
        f_CaSm = 0.01
        alpha_CaSm = 1
        kca_CaSm = 8
        kd_CaSm = 0.0005
        nexp_CaSm = 1
        // Channels for the Iseg and AH
        iseg.gnabar_NafIs = 1.3392
```

```
        iseg.gnapbar_NapIs = 3.2971e-5
        iseg.gkbar_KdrIs = 0.16552
        AdjustIsegAH()
} // End of Procedure
proc ShiftThreshold() {
        // Channels for the soma
        amA_NafSm = 14 + $1
        bmA_NafSm = 38 + $1
        theta_h_NafSm = 55 - $1
        theta_n_KdrSm = 28 - $1
        thetamn_CaSm = 22 - $1
        thetahn_CaSm = 40 - $1
        amA_NafIs = 10 + $1
        bmA_NafIs = 30 + $1
        theta_h_NafIs = 55 - $1
        theta_n_KdrIs = 28 - $1
        ampB_NapIs = 38.4 - $1
        bmpB_NapIs = 42.7 - $1
} // End of Procedure
segments_numbers()
UpdateChannels()
ShiftThreshold(7)
GetInfo()
access soma                                          // access the origin
distance()                                           // define soma as the origin
forsec DendritesList {
    for (x) if ((x>0) && (x<1)) {
                DendPathDist_info(x) = distance(x) - soma.L/2
                                }
}
// Define the distribution of LVA L-type Calcium channels over the motoneuron dendritic tree
objref PICsList
PICsList = new SectionList()            // Create a section list for the names of the
                                        // compartments that hold the Ca+2 L-type channels
forsec DendritesList {
        if((300<=DendDist_info) && (DendDist_info<=850)){
                insert Llva
                theta_m_Llva = -43
                tau_m_Llva = 60
                kappa_m_Llva = -6
                gcaLlvabar_Llva = 0.00014
                PICsList.append()
        }
}
objref ColorPICs
proc Display_PICs() {
        ColorPICs= new Shape()                  // Create a shape plot
        ColorPICs.color_list(PICsList,2)        // Color the compartments that hold
                                                // the L-type Ca+2 channels, RED
} // End of Procedure
Display_PICs()
```

9.7 GCA COMPUTATION

```
// This file is loaded to compute the overall conductance (Gca) of the CaV1.3 channels
// over the dendritic tree during the // simulation time. Calculation of the Gca is controlled
// by:
// START: which determines the time at which the calculation of Gca starts
// STEP: which determines the time interval after which the calculation of Gca is done
// during the simulation
// END: which determines the time at which the calculation of Gca ends
// Gca: represents the overall conductance of ALL CaV1.3 channels (between 300 to
// 850 um)
// Ica: represents the overall Ca current mediated by the CaV1.3 channels (between
// 300 to 850 um)
START = 0
STEP = 5
END = 50000
objref SampleTime
objref SigmaGcaVec, SigmaProxGcaVec, SigmaDistGcaVec, SimTimeVec
objref SigmaIcaVec
SigmaGcaVec = new Vector()                    // vector to hold the SigmaGca data
SimTimeVec = new Vector()                     // vector to hold the time
SigmaIcaVec = new Vector()                    // vector to hold the SigmaIca data
proc GetConductance() {
        SigmaGca = 0                          // reset the counter
        SigmaIca = 0                          // reset the counter
        forsec PICsList {
                SigmaGca = SigmaGca + gcaLlva_Llva    // compute the Gca
                SigmaIca = SigmaIca + ica_Llva        // compute the Ica
        }
        SigmaGcaVec.append(SigmaGca/356)
        SigmaIcaVec.append(SigmaIca/356)
        SimTimeVec.append(t)
        SigmaGca = 0
        SigmaIca = 0
        if (t+STEP <= END) {
                cvode.event(t+STEP, "GetConductance()")
        }
} // End of Procedure
objref Ggca, Gica
proc GcaPlot(){
        Ggca=new Graph()
        Gica=new Graph()
        SigmaGcaVec.plot(Ggca,SimTimeVec)
        Ggca.label(0.7,0.7,"Gca Normalized")
        SigmaIcaVec.plot(Gica,SimTimeVec)
        Gica.label(0.7,0.7,"Ica Normalized")
} // End of Procedure
SampleTime = new FInitializeHandler("cvode.event(START,\"GetConductance()\")")
```

9.8 IA AFFERENT SYNAPSES

```
// HELP
// This file is used to grade creating the Ia synapses over the dendritic tree. The compartment names that
hold synapses are read from the
```

```
// external file, and these synapses are located at the middle of these compartments.
//-------------------------------------------------------------------------------------------------------
// Ia-Afferents Synapses Parameters
IaVibrationFreq = 180              // [Hz], muscle vibration frequency
IaTimeofVibration = 50000          // [ms], how long the synapses will be activated
IaSyn_tau = 0.2                    // [ms], time constant of synapse.
                                   // Note: an alpha conductance as tau1=tau2
IaSyn_Erev = 0                     // [mV], the reversal potential of the glutamenargic
                                   // synapses is 70 mV over the resting potential
IaSyn_gmax = 0.0099                // [uS], the peak conductance of the synapse
IaSyn_Delay = 0                    // [ms], the delay before activating the synapses
IaSynNumber_GrA = 78               // Number of Ia synapses - Group A
IaSynNumber_GrB = 76               // Number of Ia synapses - Group B
IaSynNumber_GrC = 74               // Number of Ia synapses - Group C
IaSynNumber_GrD = 72               // Number of Ia synapses - Group D
TotalIaSynNumber = IaSynNumber_GrA + IaSynNumber_GrB + IaSynNumber_GrC +
IaSynNumber_GrD
IaSynActivation = 4                        // Pattern of activation of the Ia-synapses, Choose
                                           // one of the following:
                                           // 0: for All-group activation, all synapses are
                                           // activated at the same time.
                                           // 2: for 2-group activation, synapses are divided
                                           // into 2 groups activated with 50% phase shift
                                           // 4: for 4-group activation, synapses are divided
                                           // into 4 groups activated with 25% phase shift

// Number of Gr A:    11   21   31   41   51   60   69   78
// Number of Gr B:    10   20   30   40   49   58   67   76
// Number of Gr C:    10   20   30   40   49   58   66   74
// Number of Gr D:    10   20   29   38   47   56   64   72
// For 100% => IaSyn_gmax = 0.0033
//    150% => IaSyn_gmax = 0.00495
//    200% => IaSyn_gmax = 0.0066
//    250% => IaSyn_gmax = 0.00825
//    300% => IaSyn_gmax = 0.0099
// Pattern of activation of the Ia-synapses is by 4-group activation, where synapses are
// divided into 4 groups (A, B, C, and D) activated with 25% phase shift.
strdef name, ssA
objref fileA, fileB, fileC, fileD
sprint(ssA, "objref IaAfferentSyn[%d]",TotalIaSynNumber)
execute(ssA)
sprint(ssA, "objref IaAfferentNC[%d]",TotalIaSynNumber)
execute(ssA)
objref IaAfferentNS_A, IaAfferentNS_B, IaAfferentNS_C, IaAfferentNS_D
// Create a section list to hold the compartments names that will contain the synapses
objref DendSynapsesList
DendSynapsesList = new SectionList()
// Create a section list for the names of the compartments that contain the synapses
proc CreateIaAfferentsSyn() { local i
    fileA = new File()
    fileA.ropen("IaAffSynGradeGrA.ant")        // Open file for synapses of Group A
    for i=0,(IaSynNumber_GrA-1) {
        fileA.scanstr(name)                    // Read compartment from Group A
        sprint(ssA, "access %s", name)         // access this compartment
        execute(ssA)
          DendSynapsesList.append()            // Add compartment to the  Synapses List
```

```
            IaAfferentSyn[i] = new Exp2Syn(0.5)      // Add a synapse to compartment
        }
        fileA.close()
        fileB = new File()
        fileB.ropen("IaAffSynGradeGrB.ant")          // Open file for synapses of Group B
        for i=IaSynNumber_GrA, (IaSynNumber_GrA+IaSynNumber_GrB-1) {
            fileB.scanstr(name)                      // Read compartment from Group B
            sprint(ssA, "access %s", name)           // access this compartment
            execute(ssA)
              DendSynapsesList.append()              // Add compartment to the  Synapses List
               IaAfferentSyn[i] = new Exp2Syn(0.5)   // Add a synapse to compartment
        }
        fileB.close()
        fileC = new File()
        fileC.ropen("IaAffSynGradeGrC.ant")          // Open file for synapses of Group C
        for i=(IaSynNumber_GrA+IaSynNumber_GrB),
(IaSynNumber_GrA+IaSynNumber_GrB+IaSynNumber_GrC-1) {
            fileC.scanstr(name)                      // Read compartment from Group C
            sprint(ssA, "access %s", name)           // access this compartment
            execute(ssA)
              DendSynapsesList.append()              // Add compartment to the  Synapses List
              IaAfferentSyn[i] = new Exp2Syn(0.5)    // Add a synapse to compartment
        }
        fileC.close()
        fileD = new File()
        fileD.ropen("IaAffSynGradeGrD.ant")  // Open file for synapses of Group D
        for i=(IaSynNumber_GrA+IaSynNumber_GrB+IaSynNumber_GrC),
(IaSynNumber_GrA+IaSynNumber_GrB+IaSynNumber_GrC+IaSynNumber_GrD-1) {
            fileD.scanstr(name)                      // Read compartment from Group D
            sprint(ssA, "access %s", name)           // access this compartment
            execute(ssA)
            DendSynapsesList.append()                // Add compartment to the  Synapses List
        IaAfferentSyn[i] = new Exp2Syn(0.5)          // Add a synapse to compartment
        }
        fileD.close()
        IaAFFERENTSFLAG = 1                          // Turn flag ON
Display_Synapses()                                   // Display the synapses on the shape plot
} // End of Procedure
// Procedure to activate Ia-Afferents Excitatory Synapses
proc IaAfferents_ON() { local i
            if (IaAFFERENTSFLAG){
            // Check if the Ia-Afferents synapses have been created or not
            // Create 4 sources of stimulation to each group of the Ia-Afferents Synapses
            IaAfferentNS_A = new NetStim(0.5)  // creates the NetStim that drive Group A
            IaAfferentNS_A.interval = 1000/IaVibrationFreq                  // Periodic time
            IaAfferentNS_A.number = IaTimeofVibration*IaVibrationFreq/1000     // time of
                                                                                    // stimulation
            IaAfferentNS_B = new NetStim(0.5)  /// creates the NetStim that drive Group B
            IaAfferentNS_B.interval = 1000/IaVibrationFreq
            IaAfferentNS_B.number = IaTimeofVibration*IaVibrationFreq/1000
            IaAfferentNS_C = new NetStim(0.5)
            IaAfferentNS_C.interval = 1000/IaVibrationFreq
            IaAfferentNS_C.number = IaTimeofVibration*IaVibrationFreq/1000
            IaAfferentNS_D = new NetStim(0.5)
            IaAfferentNS_D.interval = 1000/IaVibrationFreq
            IaAfferentNS_D.number = IaTimeofVibration*IaVibrationFreq/1000
```

```
        // Determine the pattern of activation
        if (IaSynActivation == 0) {
                IaAfferentNS_A.start = 0
        IaAfferentNS_B.start = 0
                IaAfferentNS_C.start = 0
                IaAfferentNS_D.start = 0
                } else    if (IaSynActivation == 2) {
                IaAfferentNS_A.start = 0
                        IaAfferentNS_B.start = 1000/IaVibrationFreq/2
                        IaAfferentNS_C.start = 0
                        IaAfferentNS_D.start = 1000/IaVibrationFreq/2
                } else    if (IaSynActivation == 4) {
                        IaAfferentNS_A.start = 0
                        IaAfferentNS_B.start = 1000/IaVibrationFreq/4
                        IaAfferentNS_C.start = 1000/IaVibrationFreq/2
                        IaAfferentNS_D.start = 1000/IaVibrationFreq/4*3
                }
            for i=0, (IaSynNumber_GrA-1) {
                        IaAfferentSyn[i].tau1 = IaSyn_tau
                        IaAfferentSyn[i].tau2 = IaSyn_tau
                        IaAfferentSyn[i].e = IaSyn_Erev
                        IaAfferentNC[i] = new NetCon(IaAfferentNS_A, IaAfferentSyn[i])
            IaAfferentNC[i].weight = IaSyn_gmax
                        IaAfferentNC[i].delay = IaSyn_Delay
                }
            for i=IaSynNumber_GrA, (IaSynNumber_GrA+IaSynNumber_GrB-1) {
                        IaAfferentSyn[i].tau1 = IaSyn_tau
IaAfferentSyn[i].tau2 = IaSyn_tau
                        IaAfferentSyn[i].e = IaSyn_Erev
                        IaAfferentNC[i] = new NetCon(IaAfferentNS_B, IaAfferentSyn[i])
            IaAfferentNC[i].weight = IaSyn_gmax
IaAfferentNC[i].delay = IaSyn_Delay
                }
            for i=(IaSynNumber_GrA+IaSynNumber_GrB),
(IaSynNumber_GrA+IaSynNumber_GrB+IaSynNumber_GrC-1) {
                        IaAfferentSyn[i].tau1 = IaSyn_tau
IaAfferentSyn[i].tau2 = IaSyn_tau
                        IaAfferentSyn[i].e = IaSyn_Erev
                        IaAfferentNC[i] = new NetCon(IaAfferentNS_C, IaAfferentSyn[i])
            IaAfferentNC[i].weight = IaSyn_gmax
IaAfferentNC[i].delay = IaSyn_Delay
                }
            for i=(IaSynNumber_GrA+IaSynNumber_GrB+IaSynNumber_GrC),
(IaSynNumber_GrA+IaSynNumber_GrB+IaSynNumber_GrC+IaSynNumber_GrD-1) {
                        IaAfferentSyn[i].tau1 = IaSyn_tau
            IaAfferentSyn[i].tau2 = IaSyn_tau
                        IaAfferentSyn[i].e = IaSyn_Erev
                        IaAfferentNC[i] = new NetCon(IaAfferentNS_D, IaAfferentSyn[i])
            IaAfferentNC[i].weight = IaSyn_gmax
                        IaAfferentNC[i].delay = IaSyn_Delay
                }
        } else{
                print "Create the Ia-Afferents synapses first using the command CreateIaAfferentsSyn()"
        }
} // End of Procedure
// Procedure that displays the synapses on the model morphology
```

```
objref Gsynapses
Gsynapses = new Shape(0)
Gsynapses.view(-3000, -1000, 5000, 500, 0, 519, 206.1, 200.8)  Gsynapses.label(0.233193, 0.932963,
"Synapses", 2, 1, 0, 0, 6)
// Draw xyz scale bars
create xScale, yScale, zScale
proc anatscale() {
        if ($4>0) {  // if length arg is <= 0 then do nothing
                xScale {
                        pt3dclear()
                        pt3dadd($1, $2, $3, 1)
                        pt3dadd($1+$4, $2, $3, 1)
                }
                yScale {
                        pt3dclear()
                        pt3dadd($1, $2, $3, 1)
                        pt3dadd($1, $2+$4, $3, 1)
                }
                zScale {
                        pt3dclear()
                        pt3dadd($1, $2, $3, 1)
                        pt3dadd($1, $2, $3+$4, 1)
                }}}
proc Display_Synapses() {
// Display the Ia-Afferents synapses if they have been created
        if (IaAFFERENTSFLAG){
            for i=0,(TotalIaSynNumber-1) {
                        Gsynapses.point_mark(IaAfferentSyn[i],6)
        // make it brown
                }}
        anatscale(1500,0,0,100)
        // origin of xyz scale bars and length of 100 um
} // End of Procedure
// Procedure to activate medial synapses only
objref SynapseNames
SynapseNames = new Vector()
proc Medial_Synapses() {
        SynapseID = 0                                           // IDs between 0 to 299
        forsec DendSynapsesList {
                SynapseNames.append(SynapseID)
                SynapseLocation = (z3d(0)+z3d(1))/2
                if ( SynapseLocation >= 0 ){
                        IaAfferentNC[SynapseID].weight = 0.0165                 }
                        SynapseID = SynapseID + 1
}
} // End of Procedure
// Procedure to activate lateral synapses only
proc Lateral_Synapses() {
        SynapseID = 0                                           // IDs between 0 to 299
        forsec DendSynapsesList {
                SynapseNames.append(SynapseID)
                SynapseLocation = (z3d(0)+z3d(1))/2
                if ( SynapseLocation < 0 ){
                        IaAfferentNC[SynapseID].weight = 0.0165                 }
                        SynapseID = SynapseID + 1
}
```

```
} // End of Procedure
// Procedure to activate dorsal synapses only
proc Rostral_Synapses() {
        SynapseID = 0                                   // IDs between 0 to 299
        forsec DendSynapsesList {
                SynapseNames.append(SynapseID)
                SynapseLocation = (x3d(0)+x3d(1))/2
                if ( SynapseLocation >= 0 ){
                        IaAfferentNC[SynapseID].weight = 0.0165          }
                        SynapseID = SynapseID + 1
}
} // End of Procedure
// Procedure to activate caudal synapses only
proc Caudal_Synapses() {
        SynapseID = 0                                   // IDs between 0 to 299
        forsec DendSynapsesList {
                SynapseNames.append(SynapseID)
        SynapseLocation = (x3d(0)+x3d(1))/2
                if ( SynapseLocation < 0 ){
                        IaAfferentNC[SynapseID].weight = 0.0165
        }
                SynapseID = SynapseID + 1
}
} // End of Procedure
////////////////////////////////////// Calling Procedures ////////////////////////////////////////////////////
CreateIaAfferentsSyn()          // Create the Ia-Afferent Synapses, but not activated
IaAfferents_ON()                // Activate the Ia-Afferent Synapses
Display_Synapses()              // Display the synapses on the shape plot
//Rostral_Synapses()            // Activate MEDIAL synapses only
//Caudal_Synapses()             // Activate MEDIAL synapses only
//Medial_Synapses()             // Activate MEDIAL synapses only
//Lateral_Synapses()            // Activate LATERAL synapses only
```

9.9 RECORD FIELD POTENTIALS

```
// Procedure that computes the total potential recorded by the Extracellular Recording Electrodes #1 and #2
vrec1 = 0                       // extracellularly recorded potential
vrec2 = 0                       // extracellularly recorded potential
proc fieldrec() {
        sum1 = 0
        sum2 = 0
        forall {
                if (ismembrane("xtra")) {
                        for (x) if (x!=0 && x!=1) {sum1 += er1_xtra(x)}
                // for (x) if ((x>0) && (x<1))
                        for (x) if (x!=0 && x!=1) {sum2 += er2_xtra(x)}
                }}
} // End of Procedure
objref xx, yy, zz, length
objref xint, yint, zint, range
proc Interpolate() { local ii, nn, kk, xr
        forall {
          if ( (ismembrane("xtra"))  ) {
                nn = n3d()
                xx = new Vector(nn)
```

```
yy = new Vector(nn)
zz = new Vector(nn)
length = new Vector(nn)
for ii = 0,nn-1 {
        xx.x[ii] = x3d(ii)
        yy.x[ii] = y3d(ii)
        zz.x[ii] = z3d(ii)
        length.x[ii] = arc3d(ii)
}
range = new Vector(nseg+2)
range.indgen(1/nseg)
range.sub(1/(2*nseg))
range.x[0]=0
range.x[nseg+1]=1
xint = new Vector(nseg+2)
yint = new Vector(nseg+2)
zint = new Vector(nseg+2)
xint.interpolate(range, length, xx)
yint.interpolate(range, length, yy)
zint.interpolate(range, length, zz)
for ii = 1, nseg {
        xr = range.x[ii]
if (ismembrane("xtra")) {
                x_xtra(xr) = xint.x[ii]
                y_xtra(xr) = yint.x[ii]
                z_xtra(xr) = zint.x[ii]
        }}}
```

9.10 CUSTOMIZED INITIALIZATION

```
// Override the original init() procedure to:
// 1- compute the total potential recorded by the Extracellular Recording Electrodes #1
// and #2 at the begining of the Run.
// In this procedure, code is executed only once at the beginning of the run
proc init() {
    finitialize(v_init)
    fcurrent()
    fieldrec()              // Function to compute the extracellular potentials for all
                            // segments for recording.
    vrec1 = sum1            // Recorded extracellular potential for Electrode #1
    vrec2 = sum2            // Recorded extracellular potential for Electrode #2
} // End of Procedure

// Override the original advance() procedure to:
// 1- compute the total potential recorded by the Extracellular Recording Electrodes #1
// and #2 in each time step during the Run.
// In this procedure, code is executed every time step during the run
proc advance() {
    fadvance()
    fieldrec()              // Function to compute the extracellular potentials for all
                            // segments for recording.
    vrec1 = sum1            // Recorded extracellular potential for Electrode #1
    vrec2 = sum2            // Recorded extracellular potential for Electrode #2
} // End of Procedure
```

9.11 MONOPOLAR EXTRACELLULAR STIMULATION

```
// Resistance between each node and the Extracellular Stimulation/Recording electrodes
ElectrodesPosition = 1
// Monopolar Stimulating Electrode
XEstim = 200                    // um
YEstim = -59.4
ZEstim = 0
XErec1 = 0                      // um
YErec1 = 0
ZErec1 = 132

XErec2 = 300                    // um
YErec2 = 300
ZErec2 = 300
create sElec                    // bogus section to show extracell Stim electrode location
create rElec1, rElec2           // bogus section to show extracell Rec electrodes location
objref psElec                   // bogus PointProcess just to show Stim location
objref prElec1, prElec2         // bogus PointProcess just to show Rec location

objref gElec                    // Figure that shows extracellular electrode location
gElec = new Shape(0)            // create it but don't map it to the screen yet
gElec.view(-3000, -1000, 5000, 500, 0, 519, 206.1, 200.8)
gElec.label(0.233193, 0.932963, "Extracellular Electrodes", 2, 1, 0, 0, 6)
gElec.label(0.158957, 0.882963, "Stim(Red) - Record (Blue/Green)", 2, 1, 0, 0, 6)

// Procedure that computes the resistance between each node and the Extracellular
// Stimulating Electrode
proc setRstim() {  local r
 forall {
  if (ismembrane("xtra")) {
   for (x) if ((x>0) && (x<1)) {
        if (Isotropic_Medium  == 1){
        // Isotropic medium, 0.01 converts rho's cm to um and ohm to megohm
        r = sqrt((x_xtra(x) - XEstim)^2 + (y_xtra(x) - YEstim)^2 + (z_xtra(x) –
          ZEstim)^2)
        Rstim_xtra(x) = 0.01*(rho / 4 / PI)*(1/r)
        } else {
        // Anisotropic medium, 0.01 converts rho's cm to um and ohm to megohm
        r_x = (x_xtra(x) - XEstim)^2
        r_y = (y_xtra(x) - YEstim)^2
        r_z = (z_xtra(x) - ZEstim)^2
        Rstim_xtra(x) = 0.01 * (1 / 4 / PI) * ( (r_x/rho_y/rho_z) + (r_y/rho_x/rho_z) +
                        (r_z/rho_x/rho_y) )^-0.5
                }}}}
} // End of Procedure
// Resistance between each node and the Extracellular Recording Electrode #1
proc setRrec1() {  local r
 forall {
  if (ismembrane("xtra")) {
   for (x) if ((x>0) && (x<1)) {
          if (Isotropic_Medium  == 1){
                        // Isotropic medium
            r = sqrt((x_xtra(x) - XErec1)^2 + (y_xtra(x) - YErec1)^2 + (z_xtra(x) –
          ZErec1)^2)
            Rrec1_xtra(x) = (rho / 4 / PI)*(1/r)*0.01
```

```
        } else {
                                // Anisotropic medium
                        r_x = (x_xtra(x) - XEstim)^2
                        r_y = (y_xtra(x) - YEstim)^2
                        r_z = (z_xtra(x) - ZEstim)^2
                Rrec1_xtra(x) = 0.01 * (1 / 4 / PI) * ( (r_x/rho_y/rho_z) +
                                (r_y/rho_x/rho_z) + (r_z/rho_x/rho_y) )^-0.5
        }}}}
} // End of Procedure
// Resistance between each node and the Extracellular Recording Electrode #2
proc setRrec2() {  local r
 forall {
  if (ismembrane("xtra")) {
   for (x) if ((x>0) && (x<1)) {
        if (Isotropic_Medium  == 1){
                // Isotropic medium
                r = sqrt((x_xtra(x) - XErec2)^2 + (y_xtra(x) - YErec2)^2 + (z_xtra(x) –
                        ZErec2)^2)
                Rrec2_xtra(x) = (rho / 4 / PI)*(1/r)*0.01
        } else {
                // Anisotropic medium
                r_x = (x_xtra(x) - XEstim)^2
                r_y = (y_xtra(x) - YEstim)^2
                r_z = (z_xtra(x) - ZEstim)^2
                Rrec2_xtra(x) = 0.01 * (1 / 4 / PI) * ( (r_x/rho_y/rho_z) +
                                        (r_y/rho_x/rho_z) + (r_z/rho_x/rho_y) )^-0.5
        }}}}
} // End of Procedure
// Procedure that draws the location of the Extracellular Stimulating Electrode
proc drawelecstim() {
        sElec {
                // make it 0.5 um long
                pt3dclear()
                pt3dadd($1-0.25, $2, $3, 1)
                pt3dadd($1+0.25, $2, $3, 1)
                psElec = new IClamp(0.5)
        }
        gElec.point_mark(psElec, 2)  // make it Red
} // End of Procedure
// Procedure that draws the location of the Extracellular Recording Electrode #1
proc drawelecrec1() {
        rElec1 {
                // make it 0.5 um long
                pt3dclear()
                pt3dadd($1-0.25, $2, $3, 1)
                pt3dadd($1+0.25, $2, $3, 1)
                prElec1 = new IClamp(0.5)
        }
        gElec.point_mark(prElec1, 3)  // make it Blue
} // End of Procedure
// Procedure that draws the location of the Extracellular Recording Electrode #2
proc drawelecrec2() {
        rElec2 {
                // make it 0.5 um long
                pt3dclear()
                pt3dadd($1-0.25, $2, $3, 1)
```

```
                pt3dadd($1+0.25, $2, $3, 1)
                prElec2 = new IClamp(0.5)
        }
        gElec.point_mark(prElec2, 4)  // make it Green
} // End of Procedure
////////////////////////////////////////////// Setting the Electrodes ////////////////////////////////////////////////
// Procedure that set the Extracellular Stimulating Electrode
proc SetStimElec() {
        XEstim = $1
        YEstim = $2
        ZEstim = $3
        if(ElectrodesPosition==1){
                setRstim(XEstim, YEstim, ZEstim)
                drawelecstim(XEstim, YEstim, ZEstim)
        }
} // End of Procedure
// Procedure that set the Extracellular Recording Electrode #1
proc SetRecElec1() {
        XErec1 = $1
        YErec1 = $2
        ZErec1 = $3
        if(ElectrodesPosition==1){
                setRrec1(XErec1, YErec1, ZErec1)
                drawelecrec1(XErec1, YErec1, ZErec1)
        }
} // End of Procedure
// Procedure that set the Extracellular Recording Electrode #2
proc SetRecElec2() {
        XErec2 = $1
        YErec2 = $2
        ZErec2 = $3
        if(ElectrodesPosition==1){
                setRrec2(XErec2, YErec2, ZErec2)
                drawelecrec2(XErec2, YErec2, ZErec2)
        }
} // End of Procedure
// Current locations of all Extracellular Stimulating and Recording Electrodes
proc ElecLocations() {
printf("\t The Stimulating Electrode (Red): (%d,%d,%d) \n",XEstim,YEstim,ZEstim)
printf("\t The Recording Electrode #1 (Blue): (%d,%d,%d) \n",XErec1,YErec1,ZErec1)
printf("\t The Recording Electrode #2 (Green): (%d,%d,%d) \n",XErec2,YErec2,ZErec2)
} // End of Procedure
// Re-compute all resistances based on the new value of rho
proc Update_rho(){
SetStimElec(XEstim, YEstim, ZEstim)   // Put Extra Stimulating Electrode at (x, y, z)
SetRecElec1(XErec1, YErec1, ZErec1)   // Put Extra Recording Electrode #1 at (x, y, z)
SetRecElec2(XErec2, YErec2, ZErec2)   // Put Extra Recording Electrode #2 at (x, y, z)
} // End of Procedure
Update_rho()
```

9.12 TRAPEZOIDAL PULSES

```
// This file designs the Extracellular Stimulating Waveform - 3 part trapezoidal pulses
/*The stimulus is constructed from a waveform template that is copied to a Vector.
For each section that has the xtra mechanism, this Vector is used to drive is_xtra.
```

```
The transfer resistance rx_xtra takes care of the amplitude and sign of the local extracellular field.*/
// create basic stimulus waveform (a simple rectangular pulse)
// default values
//----------------
AMP1 = -5.0             // uA, amplitude of phase 1
PW1 = 200               // us, pulse width of phase 1
Tramp1 = 0              // us, ramp time (before and after) of phase 1
AMP2 = 2.5              // uA, amplitude of phase 2
PW2 = 100               // us, pulse width of phase 2
Tramp2 = 0              // us, ramp time (before and after) of phase 2
AMP3 = 0                // uA, amplitude of phase 3
BTramp3 = 0             // us, BEFORE ramp time of phase 3
PW3 = 0                 // us, pulse width of phase 3
ATramp3 = 0             // us, AFTER ramp time of phase 3
FREQ = 3333.3           // Hz, frequency of stimulation pulse
EndTime = 10000         // ms, End time for stimulation
DEL = 1500              // ms, delay. Time after which stimulation starts
objref TimeVector, StimVector      // create vectors
TimeVector = new Vector()
StimVector = new Vector()
// Procedure to design the stimulation waveform
proc Design_Waveform() {local del, pw_1, amp_1, freq, endtime, pw_2, amp_2, pw_3, amp_3, Tperiodic,
tramp_1, tramp_2, btramp_3, atramp_3, t_rem
del   = $1
pw_1  = $2
amp_1 = $3
freq  = $4
endtime = $5
amp_2 = $6
pw_2  = $7
amp_3 = $8
pw_3  = $9
tramp_1 = $10
tramp_2 = $11
btramp_3 = $12
atramp_3 = $13
Tperiodic = 1000/freq
// Remaining time. This is to fill the difference between the periodic time (1000/freq)
// and the sum of PW1, 2*Tramp1, PW2, 2*Tramp2, BTramp3, PW3, and ATramp3
t_rem = Tperiodic - (pw_1 + 2*tramp_1 + pw_2 + 2*tramp_2 + pw_3 + atramp_3 + btramp_3)
Tstim = endtime - del
nn = int(Tstim/Tperiodic)          // compute how many cycles of stimulation
cycle = 10                         // space required for stimulation cycle of a 3 part
                                   // trapezoidal waveform and remaining time
                                   // Note: dupilcation of time is NOT required for non sharp-edge pulses
 PreAndPost = 3                    // space required for pre and post stimulation cycle
TimeVector.resize(PreAndPost + nn*cycle)        // resize Timevector for the required space
StimVector.resize(PreAndPost + nn*cycle)        // resize Stimulationvector for required space
StimVector.fill(0)                              // reset the stimulation vector - no pulses
// Fill the pre space with the delay information before stimulation
TimeVector.x[0] = 0
StimVector.x[0] = 0
TimeVector.x[1] = del
StimVector.x[1] = 0
// Design the stimulation waveform
for (i=0;i<nn;i+=1) {                           // For every stimulation cycle
```

```
      TimeVector.x[i*cycle+2] = Tperiodic * i + del + tramp_1
      StimVector.x[i*cycle+2] = amp_1
      TimeVector.x[i*cycle+3] = Tperiodic * i + del + tramp_1 + pw_1
      StimVector.x[i*cycle+3] = amp_1
      TimeVector.x[i*cycle+4] = Tperiodic * i + del + tramp_1 + pw_1 + tramp_1
      StimVector.x[i*cycle+4] = 0
      TimeVector.x[i*cycle+5] = Tperiodic * i + del + tramp_1 + pw_1 + tramp_1 + tramp_2
      StimVector.x[i*cycle+5] = amp_2
      TimeVector.x[i*cycle+6] = Tperiodic * i + del + tramp_1 + pw_1 + tramp_1 + tramp_2 + pw_2
      StimVector.x[i*cycle+6] = amp_2
      TimeVector.x[i*cycle+7] = Tperiodic * i + del + tramp_1 + pw_1 + tramp_1 + tramp_2 + pw_2 +
tramp_2
      StimVector.x[i*cycle+7] = 0
      TimeVector.x[i*cycle+8] = Tperiodic * i + del + tramp_1 + pw_1 + tramp_1 + tramp_2 + pw_2 +
tramp_2 + btramp_3
      StimVector.x[i*cycle+8] = amp_3
      TimeVector.x[i*cycle+9] = Tperiodic * i + del + tramp_1 + pw_1 + tramp_1 + tramp_2 + pw_2 +
tramp_2 + btramp_3 + pw_3
      StimVector.x[i*cycle+9] = amp_3
      TimeVector.x[i*cycle+10] = Tperiodic * i + del + tramp_1 + pw_1 + tramp_1 + tramp_2 + pw_2 +
tramp_2 + btramp_3 + pw_3 + atramp_3
      StimVector.x[i*cycle+10] = 0
      TimeVector.x[i*cycle+11] = Tperiodic * i + del + tramp_1 + pw_1 + tramp_1 + tramp_2 + pw_2 +
tramp_2 + btramp_3 + pw_3 + atramp_3 + t_rem
      StimVector.x[i*cycle+11] = 0
   }
// Fill the post space with the end information after stimulation
   TimeVector.x[PreAndPost+nn*cycle-1]= endtime
   StimVector.x[PreAndPost+nn*cycle-1]= 0
}// End Procedure
// Procedure to play the stimulation waveform
Attach_Stimulation = 0                    // set flag to 0
proc Deliver_Waveform() {
   forall {
      if (Attach_Stimulation == 0) {                  // check if is_xtra is attached to the stim vector
         if (ismembrane("xtra")) {
            StimVector.play(&is_xtra,TimeVector,1)
            Attach_Stimulation = 1                    // set flag to 1 to stop further iterations
         }}}
} // End Procedure
// Procedure to set the stimulation parameters
proc Set_Stim_Parameters() {
  del = $1
  pw_1 = $2/1000          // To convert from micro to milli
  amp_1 = $3/1000         // To convert from micro to milli
  freq = $4
  endtime =$5
  amp_2 = $6/1000         // To convert from micro to milli
  pw_2 = $7/1000          // To convert from micro to milli
  amp_3 = $8/1000         // To convert from micro to milli
  pw_3 = $9/1000          // To convert from micro to milli
  tramp_1 = $10/1000      // To convert from micro to milli
  tramp_2 = $11/1000      // To convert from micro to milli
  Btramp_3 = $12/1000     // To convert from micro to milli
  Atramp_3 = $13/1000     // To convert from micro to milli
```

```
 Design_Waveform(del, pw_1, amp_1, freq, EndTime, amp_2, pw_2, amp_3, pw_3, tramp_1, tramp_2,
Btramp_3, Atramp_3)
 Deliver_Waveform()
}// End Procedure
// Check the values of the Extracellular settings to make sure that they are correct
// Conditions for correct settings are:
// EndTime > Delay
// PW < T (1/freq)
// If there is wrong setting, the error message will be displayed and the amplitude will be set to zero.
proc Check_Values(){
if ( (EndTime >= DEL) &&  (((PW1+2*Tramp1+PW2+2*Tramp2+PW3+ATramp3+BTramp3)/1000) <=
(1000/FREQ)) ) {
     Set_Stim_Parameters(DEL, PW1, AMP1, FREQ, EndTime, AMP2, PW2, AMP3, PW3, Tramp1,
Tramp2, BTramp3, ATramp3)
     printf("Extracellular Settings Accepted \n")
   }else {
     printf(" Incorrect Extracellular Settings. Errors may be: \n")
     printf(" End Time is shorter than Delay AND/OR \n")
     printf(" Sum of (PW1+2*Tramp1+PW2+2*Tramp2+PW3+2*Tramp3) is larger than T (Periodic
Time) \n")
     AMP1 = 0
     AMP2 = 0
     AMP3 = 0
   }
} // End Procedure
```

9.13 SIN WAVE PULSES

```
// Extracellular Stimulating Waveform - sin pulses
// Create a dummy compartment that has the pointprocess SinIClamp
create Dummy
access Dummy
L = 1
diam = 1
objref SinI                    // Define the pointprocess SinIClamp
SinI= new SinIClamp(0.5)       // Place the pointprocess SinIClamp in Dummy
// create basic stimulus waveform (a sin wave pulse)
// default values
//----------------
AMP = 400                      // uA, amplitude of stimulus
FREQ = 5000                    // Hz, freq of stimulus
TSTIM = 50000                  // ms, time for electrical stimulation
DEL = 1500                     // ms, delay before applying the stimulation
SinI.amp = AMP
SinI.freq = FREQ
SinI.dur = TSTIM
SinI.del = DEL
// Settings for changing the properties of the Sin wave during simulation time
STARTTIME = 2000               // ms, change settings when simulation time reaches STARTTIME ms
INTERVAL = 500                 // ms, change settings every INTERVAL ms
LASTTIME = 20250               // ms, time of last change
AMPSTEP = 10                   // uA, step increase in amplitude  or
FREQSTEP = 50                  // Hz, step increase in frequency
// Link the SinI pointprocess to is_xtra
// override the init() procedure
```

```
proc init() {
 finitialize(v_init)
 fcurrent()
 fieldrec()                  // Function to compute the extracellular potentials for all segments for recording.
 vrec1 = sum1                // Recorded extracellular potential for Electrode #1
 vrec2 = sum2                // Recorded extracellular potential for Electrode #2
 is_xtra = (SinI.i)/1000     // play values of SinIClamp.i pointprocess into is_xtra
                  // divide by 1000 to convert the delivered current to mA to be compatible with xtra
 if (cvode.active()) {
  cvode.re_init()
 } else {
  fcurrent()
 }
} // End of Procedure
// override the advance() procedure
proc advance() {
 fadvance()
 fieldrec()                  // Function to compute the extracellular potentials for all segments for recording.
 vrec1 = sum1                // Recorded extracellular potential for Electrode #1
 vrec2 = sum2                // Recorded extracellular potential for Electrode #2
 is_xtra = (SinI.i)/1000     // play values of SinIClamp.i pointprocess into is_xtra
        // divide by 1000 to convert the delivered current to mA to be compatible with xtra
 if (cvode.active()) {
  cvode.re_init()
 } else {
  fcurrent()
 }
} // End of Procedure
// Update the settings of the Sin wave
objref Sinfih                           // Define the FInitializeHandler varaibles
proc UpdateSinSettings(){
        // Update properties
        SinI.amp += AMPSTEP             // Increase the amplitude of stimulation by 5 uA
//      SinI.freq += FREQSTEP           // Increase the frequency of stimulation by 1 Hz
        // Reset the CVODE integrator - a required step for variable time step simulations
        if (cvode_active()) {
                cvode.re_init()
        }
        // Determine when the next event will occur
        if (t+INTERVAL <= LASTTIME) {
                cvode.event(t+INTERVAL, "UpdateSinSettings()")
        }
} // End of Procedure
////////////////////////////////////// Calling  Procedures ////////////////////////////////////////////////////
// Change the parameters of the Sin wave during the run time
//Sinfih = new FInitializeHandler("cvode.event(STARTTIME,\"UpdateSinSettings()\")")  // Set the times
for changing the settings of the Sin wave
```

9.14 EXTRACELLULAR DC FIELD

```
// - This code simulates the application of a homogenous extracellular field potential for stimulation
// - Should be used in conjunction with the 'xtra' mechanism
// User Settings
Start_Time_Field = 1500                 // Time after which the extracellular field is turned ON
End_Time_Field = 20000                  // Time after which the extracellular field is turned OFF
```

```
AMP = -0.25                             // applied DC current to generate the field
Field_Direction = 3                     // Direction of the field
                                        // 1 = along the x-axis (rostrocaudal direction)
                                // 2 = along the y-axis (dorsoventral direction)
                                // 3 = along the z-axis (mediolateral direction)

Electrode_A_Position = -4000    // Positions of the electrode plates (A and B) that generate the field
Electrode_B_Position = 4000     // Position is described in terms of 3d location along (parallel to) the
                                // direction of the field
// Based on the previous electrode positions, the distance between electrodes in um:
Field_Distance = abs(Electrode_A_Position - Electrode_B_Position)
// This procedure sets the Rstim resistance for every compartment subjected to the DC field
proc Set_Field_Resistance() {  local rA, rB
    // Apply the field to all segments in the model
    forall {
                if (ismembrane("xtra")) {
                for (x) if ((x>0) && (x<1)) {
                                if (Field_Direction == 1) {
                                        // 0.01 converts rho's cm to um and ohm to megohm
                                        Rstim_xtra(x) = 0.01 * rho * (x_xtra(x) –
                                        Electrode_A_Position - 0.5*Field_Distance)
                                }

                                if (Field_Direction == 2) {
                                        // 0.01 converts rho's cm to um and ohm to megohm
                                        Rstim_xtra(x) = 0.01 * rho * (y_xtra(x) –
                                        Electrode_A_Position - 0.5*Field_Distance)
                                }

                                if (Field_Direction == 3) {
                                        // 0.01 converts rho's cm to um and ohm to megohm
                                        Rstim_xtra(x) = 0.01 * rho * (z_xtra(x) –
                                        Electrode_A_Position - 0.5*Field_Distance)
                                }}}}
} // End of Procedure
// This procedure draw the electrode configuration relative to the modeled cell
create Elec_A                   // bogus section to show the extracell Stim electrode A location
create Elec_B                   // bogus section to show the extracell Stim electrode B location
proc Display_Field() {
        Elec_A {
                // make the electrode 30 um in width, and 2 mm in diameter
                pt3dclear()
                if(Field_Direction == 1) {
                        pt3dadd(Electrode_A_Position-15, 0, 0, 2000)
                        pt3dadd(Electrode_A_Position+15, 0, 0, 2000)
                } else if (Field_Direction == 2) {
                        pt3dadd(0, Electrode_A_Position-15, 0, 2000)
                        pt3dadd(0, Electrode_A_Position+15, 0, 2000)
                } else if (Field_Direction == 3) {
                        pt3dadd(0, 0, Electrode_A_Position-15, 2000)
                        pt3dadd(0, 0, Electrode_A_Position+15, 2000)
                }}
        Elec_B {
                // make the electrode 5 um in width, and 5 um in diameter
                pt3dclear()
                if(Field_Direction == 1) {
```

```
                pt3dadd(Electrode_B_Position-15, 0, 0, 2000)
                pt3dadd(Electrode_B_Position+15, 0, 0, 2000)
        } else if (Field_Direction == 2) {
                pt3dadd(0, Electrode_B_Position-15, 0, 2000)
                pt3dadd(0, Electrode_B_Position+15, 0, 2000)
        } else if (Field_Direction == 3) {
                pt3dadd(0, 0, Electrode_B_Position-15, 2000)
                pt3dadd(0, 0, Electrode_B_Position+15, 2000)
        }}
} // End of Procedure
// Procedure to design the stimulation waveform
objref TimeVector, StimVector                                   // create vectors
TimeVector = new Vector()
StimVector = new Vector()
proc Design_Waveform() { local start_time, end_time, amp
 start_time = $1
 end_time  = $2
 amp = $3
TimeVector.resize(5)      // resize the Time vector for the required number of vector elements
StimVector.resize(5)      // resize the Stimulation vector for the required number of vector elements
 // Fill the vectors with the stimulation information
 TimeVector.x[0] = 0
 StimVector.x[0] = 0
 TimeVector.x[1] = start_time
 StimVector.x[1] = 0
 TimeVector.x[2] = start_time
 StimVector.x[2] = amp
 TimeVector.x[3] = end_time
 StimVector.x[3] = amp
 TimeVector.x[4] = end_time
 StimVector.x[4] = 0
}       // End Procedure
// Procedure to play the stimulation waveform
Attach_Stimulation = 0                  // set flag to 0
proc Deliver_Waveform() {
  forall {
    if (Attach_Stimulation == 0) {      // check if is_xtra is attached to the stim vector
      if (ismembrane("xtra")) {
        StimVector.play(&is_xtra,TimeVector,1)
        Attach_Stimulation = 1          // set flag to 1 to stop further iterations
      }}}
} // End Procedure
// This procedure checks the values of the Extracellular settings
proc Check_Values(){
    Design_Waveform(Start_Time_Field, End_Time_Field, AMP)   // Design the stimulation profile
        Deliver_Waveform()                                  // Link the waveform to is
        Set_Field_Resistance()                              // Update the field parameters
        Display_Field()
        // Based on the previous electrode positions, the distance between electrodes in um:
        Field_Distance = abs(Electrode_A_Position - Electrode_B_Position)
    printf("Extracellular Settings Updated \n")
}       // End Procedure
// Display the panel for Extracellular field stimulation parameters
xpanel("Extracellular DC Field")
        xvalue("Start Time (ms)", "Start_Time_Field", 1, "", 1)
        xvalue("End Time (ms)", "End_Time_Field", 1, "", 1)
```

```
        xvalue("Direction of Field", "Field_Direction", 1, "", 1)
        xvalue("Position of Electrode A (um)", "Electrode_A_Position", 1, "", 1)
        xvalue("Position of Electrode B (um)", "Electrode_B_Position", 1, "", 1)
        xvalue("Applied Current (mA)", "AMP", 1, "", 1)
    xbutton("Accept Parameters","Check_Values()")
xpanel(0,550)
////////////////////////////////////// Calling Procedures ////////////////////////////////////////////////////////////////////////////
// Display the applied field relative to the modeled cell
Display_Field()
Check_Values()
```

9.15 EXTRACELLULAR AC FIELD – SIN WAVE

```
// - This code simulates the application of a homogenous extracellular field potential for stimulation
// - The applied field is an AC field of sin wave shape
// - Should be used in conjunction with the 'xtrafield' mechanism, which can be adapted for extracellular
recording
// - This code applies a homogenous field which implies an isotropic medium
// Create a dummy compartment that has the pointprocess SinIClamp
create Dummy
access Dummy
L = 1
diam = 1
objref SinI                     // Define the pointprocess SinIClamp
SinI= new SinIClamp(0.5)        // Place the pointprocess SinIClamp in Dummy
// User Settings
Start_Time_Field = 0            // Time after which the extracellular field is turned ON
End_Time_Field = 10000          // Time after which the extracellular field is turned OFF
AMP = 0.64                      // Amplitude of the applied AC current to generate the field
FREQ = 0.16667                  // Hz, freq of AC field
Field_Direction = 2             // Direction of the field
                                // 1 = along the x-axis (rostrocaudal direction)
                                // 2 = along the y-axis (dorsoventral direction)
                                // 3 = along the z-axis (mediolateral direction)
Electrode_A_Position = -4000    // Positions of the electrode plates (A and B) that generate the field
Electrode_B_Position = 4000     // Position is descriped in terms of 3d location along (parallel to) the
                                // direction of the field
// Based on the previous electrode positions, the distance between electrodes in um:
Field_Distance = abs(Electrode_A_Position - Electrode_B_Position)
SinI.amp = AMP
SinI.freq = FREQ
SinI.del = Start_Time_Field
SinI.dur = Start_Time_Field + End_Time_Field
// This procedure sets the Rstim resistance for every compartment subjected to the DC field
proc Set_Field_Resistance() {  local rA, rB
// Apply the field to all segments in the model
    forall {
                if (ismembrane("xtra")) {
                for (x) if ((x>0) && (x<1)) {
                if (Field_Direction == 1) {
                // 0.01 converts rho's cm to um and ohm to megohm
                Rstim_xtra(x) = 0.01 * rho * (x_xtra(x) - Electrode_A_Position - 0.5*Field_Distance)
                                }
                if (Field_Direction == 2) {
                // 0.01 converts rho's cm to um and ohm to megohm
```

```
                Rstim_xtra(x) = 0.01 * rho * (y_xtra(x) - Electrode_A_Position - 0.5*Field_Distance)
                                }
                if (Field_Direction == 3) {
                // 0.01 converts rho's cm to um and ohm to megohm
                Rstim_xtra(x) = 0.01 * rho * (z_xtra(x) - Electrode_A_Position - 0.5*Field_Distance)
                                }}}}
} // End of Procedure
// This procedure draw the electrode configuration relative to the modeled cell
create Elec_A                                                   // bogus section to show the
extracell Stim electrode A location
create Elec_B                                                   // bogus section to show the
extracell Stim electrode B location
proc Display_Field() {
        Elec_A {
                // make the electrode 30 um in width, and 2 mm in diameter
                pt3dclear()
                if(Field_Direction == 1) {
                        pt3dadd(Electrode_A_Position-15, 0, 0, 2000)
                        pt3dadd(Electrode_A_Position+15, 0, 0, 2000)
                } else if (Field_Direction == 2) {
                        pt3dadd(0, Electrode_A_Position-15, 0, 2000)
                        pt3dadd(0, Electrode_A_Position+15, 0, 2000)
                } else if (Field_Direction == 3) {
                        pt3dadd(0, 0, Electrode_A_Position-15, 2000)
                        pt3dadd(0, 0, Electrode_A_Position+15, 2000)
                }
        }
        Elec_B {
                // make the electrode 5 um in width, and 5 um in diameter
                pt3dclear()
                if(Field_Direction == 1) {
                        pt3dadd(Electrode_B_Position-15, 0, 0, 2000)
                        pt3dadd(Electrode_B_Position+15, 0, 0, 2000)
                } else if (Field_Direction == 2) {
                        pt3dadd(0, Electrode_B_Position-15, 0, 2000)
                        pt3dadd(0, Electrode_B_Position+15, 0, 2000)
                } else if (Field_Direction == 3) {
                        pt3dadd(0, 0, Electrode_B_Position-15, 2000)
                        pt3dadd(0, 0, Electrode_B_Position+15, 2000)
                }
        }
} // End of Procedure
// This procedure checks the values of the Extracellular settings
proc Check_Values(){
          SinI.amp = AMP
                // Update properties of the Sin wave
          SinI.freq = FREQ
          SinI.del = Start_Time_Field
          SinI.dur = Start_Time_Field + End_Time_Field
          Set_Field_Resistance()                                // Update the field parameters
          // Based on the previous electrode positions, the distance between electrodes in um:
          Field_Distance = abs(Electrode_A_Position - Electrode_B_Position)
             printf("Extracellular Settings Updated \n")
} // End Procedure
// Display the panel for Extracellular field stimulation parameters
xpanel("Extracellular AC Field - Sin Wave")
```

```
        xvalue("Start Time (ms)", "Start_Time_Field", 1, "", 1)
        xvalue("End Time (ms)", "End_Time_Field", 1, "", 1)
        xvalue("Direction of Field", "Field_Direction", 1, "", 1)
        xvalue("Position of Electrode A (um)", "Electrode_A_Position", 1, "", 1)
        xvalue("Position of Electrode B (um)", "Electrode_B_Position", 1, "", 1)
        xvalue("Applied Current (mA)", "AMP", 1, "", 1)
        xvalue("Field Frequency (Hz)", "FREQ", 1, "", 1)
    xbutton("Accept Parameters","Check_Values()")
xpanel(0,550)
// Link the SinI pointprocess to is_xtra
// override the init() procedure
proc init() {
 finitialize(v_init)
 fcurrent()
 fieldrec()              // Function to compute the extracellular potentials for all segments for recording.
 vrec1 = sum1            // Recorded extracellular potential for Electrode #1
 vrec2 = sum2            // Recorded extracellular potential for Electrode #2
 is_xtra = (SinI.i)      // play values of SinIClamp.i pointprocess into is_xtra
 if (cvode.active()) {
  cvode.re_init()
 } else {
  fcurrent()
 }
} // End of Procedure
// override the advance() procedure
proc advance() {
 fadvance()
 fieldrec()              // Function to compute the extracellular potentials for all segments for recording.
 vrec1 = sum1            // Recorded extracellular potential for Electrode #1
 vrec2 = sum2            // Recorded extracellular potential for Electrode #2
 is_xtra = (SinI.i)      // play values of SinIClamp.i pointprocess into is_xtra
 if (cvode.active()) {
  cvode.re_init()
 } else {
  fcurrent()
 }
} // End of Procedure
////////////////////////////////////// Calling  Procedures ////////////////////////////////////////////////////////////////////////////
// Display the applied field relative to the modeled cell
Display_Field()
```

9.16 EXTRACELLULAR AC FIELD – SQUARE WAVE

```
// - This code simulates the application of a homogenous extracellular field potential for stimulation
// - The applied field is an AC field of square wave shape
// - Should be used in conjunction with the 'xtrafield' mechanism, which can be adapted for extracellular
recording
// - This code applies a homogenous field which implies an isotropic medium
 // User Settings
Start_Time_Field = 2000  // Time after which the extracellular field is turned ON
End_Time_Field = 20000  // Time after which the extracellular field is turned OFF
AMP1 = -0.25             // Amplitude of the applied AC current to generate the field - Phase 1
PW1 = 1000               // ms, duration of the applied AC current to generate the field - Phase 1
AMP2 = 0.25              // Amplitude of the applied AC current to generate the field - Phase 2
PW2 = 1000               // ms, duration of the applied AC current to generate the field - Phase 2
```

```
AMP3 = 0                    // mA, amplitude of the applied AC current to generate the field - Phase 3
PW3 = 0                     // ms, duration of the applied AC current to generate the field - Phase 3
FREQ = 500                  // Hz, freq of AC field
Field_Direction = 3                 // Direction of the field
                                    // 1 = along the x-axis (rostrocaudal direction)
                                    // 2 = along the y-axis (dorsoventral direction)
                                    // 3 = along the z-axis (mediolateral direction)
Electrode_A_Position = -4000        // Positions of the electrode plates (A and B) that generate the field
Electrode_B_Position = 4000         // Position is descriped in terms of 3d location along (parallel to) the
                                    // direction of the field
// Based on the previous electrode positions, the distance between electrodes in um:
Field_Distance = abs(Electrode_A_Position - Electrode_B_Position)
//  This procedure set the Rstim resistance for every compartment subjected to the DC field
proc Set_Field_Resistance() {  local rA, rB
    // Apply the field to all segments in the model
    forall {
                if (ismembrane("xtra")) {
                for (x) if ((x>0) && (x<1)) {
                if (Field_Direction == 1) {
                // 0.01 converts rho's cm to um and ohm to megohm
                Rstim_xtra(x) = 0.01 * rho * (x_xtra(x) - Electrode_A_Position - 0.5*Field_Distance)
                                    }
                if (Field_Direction == 2) {
                // 0.01 converts rho's cm to um and ohm to megohm
                Rstim_xtra(x) = 0.01 * rho * (y_xtra(x) - Electrode_A_Position - 0.5*Field_Distance)
                                    }
                if (Field_Direction == 3) {
                // 0.01 converts rho's cm to um and ohm to megohm
                Rstim_xtra(x) = 0.01 * rho * (z_xtra(x) - Electrode_A_Position - 0.5*Field_Distance)
                                    }}}}
} // End of Procedure
// This procedure draw the electrode configuration relative to the modeled cell
create Elec_A                       // bogus section to show the extracell Stim electrode A location
create Elec_B                       // bogus section to show the extracell Stim electrode B location
proc Display_Field() {
        Elec_A {
                // make the electrode 30 um in width, and 2 mm in diameter
                pt3dclear()
                if(Field_Direction == 1) {
                        pt3dadd(Electrode_A_Position-15, 0, 0, 2000)
                        pt3dadd(Electrode_A_Position+15, 0, 0, 2000)
                } else if (Field_Direction == 2) {
                        pt3dadd(0, Electrode_A_Position-15, 0, 2000)
                        pt3dadd(0, Electrode_A_Position+15, 0, 2000)
                } else if (Field_Direction == 3) {
                        pt3dadd(0, 0, Electrode_A_Position-15, 2000)
                        pt3dadd(0, 0, Electrode_A_Position+15, 2000)
                }}
        Elec_B {
                // make the electrode 5 um in width, and 5 um in diameter
                pt3dclear()
                if(Field_Direction == 1) {
                        pt3dadd(Electrode_B_Position-15, 0, 0, 2000)
                        pt3dadd(Electrode_B_Position+15, 0, 0, 2000)
                } else if (Field_Direction == 2) {
                        pt3dadd(0, Electrode_B_Position-15, 0, 2000)
```

```
                pt3dadd(0, Electrode_B_Position+15, 0, 2000)
            } else if (Field_Direction == 3) {
                pt3dadd(0, 0, Electrode_B_Position-15, 2000)
                pt3dadd(0, 0, Electrode_B_Position+15, 2000)
            }}} // End of Procedure
// Procedure to design the stimulation waveform
objref TimeVector, StimVector                    // create vectors
TimeVector = new Vector()
StimVector = new Vector()
proc Design_Waveform() { local start_time, end_time, amp1, pw1, amp2, pw2, amp3, pw3, freq,
Tperiodic, Tstim, trem
start_time = $1
end_time  = $2
amp1 = $3
pw1 = $4
amp2 = $5
pw2 = $6
amp3 = $7
pw3 = $8
freq = $9
Tperiodic = 1000/freq                            // in ms
Tstim = (end_time - start_time)                  // in ms
 // Remaining time. This is to fill the difference between the periodic time (1000/freq)
 // and the sum of PW1, PW2, and PW3
 trem = Tperiodic - (pw1 + pw2 + pw3)
 nn = int(Tstim/Tperiodic)                       // compute how many cycles of stimulation
 cycle = 8              // vector elements required for stimulation cycle of a 3 part rectangular waveform
                        // Note: dupilcation of time is required for sharp-edge pulses
 PreAndPost = 3         // vector elements required for pre and post stimulation information
 TimeVector.resize(PreAndPost + nn*cycle  //resize Timevector for the required number of vectorelements
 StimVector.resize(PreAndPost + nn*cycle) //resize Stimulationvector for the required number of vector
 StimVector.fill(0)                              // reset the stimulation vector - no pulses
 // Fill the pre space with the delay information before stimulation
 TimeVector.x[0] = 0
 StimVector.x[0] = 0
 TimeVector.x[1] = start_time
 StimVector.x[1] = 0
 // Design the stimulation waveform
 for (i=0;i<nn;i+=1) {                           // For every stimulation cycle
     TimeVector.x[i*cycle+2] = Tperiodic * i + start_time
     StimVector.x[i*cycle+2] = amp1
     TimeVector.x[i*cycle+3] = Tperiodic * i + start_time + pw1
     StimVector.x[i*cycle+3] = amp1
     TimeVector.x[i*cycle+4] = Tperiodic * i + start_time + pw1
     StimVector.x[i*cycle+4] = amp2
     TimeVector.x[i*cycle+5] = Tperiodic * i + start_time + pw1 + pw2
     StimVector.x[i*cycle+5] = amp2
     TimeVector.x[i*cycle+6] = Tperiodic * i + start_time + pw1 + pw2
     StimVector.x[i*cycle+6] = amp3
     TimeVector.x[i*cycle+7] = Tperiodic * i + start_time + pw1 + pw2 + pw3
     StimVector.x[i*cycle+7] = amp3
     TimeVector.x[i*cycle+8] = Tperiodic * i + start_time + pw1 + pw2 + pw3
     StimVector.x[i*cycle+8] = 0
     TimeVector.x[i*cycle+9] = Tperiodic * i + start_time + pw1 + pw2 + pw3 + trem
     StimVector.x[i*cycle+9] = 0
 }
```

```
 // Fill the post space with the end information after stimulation
    TimeVector.x[PreAndPost+nn*cycle-1] = end_time
    StimVector.x[PreAndPost+nn*cycle-1] = 0
} // End Procedure
// Procedure to play the stimulation waveform
Attach_Stimulation = 0                    // set flag to 0
proc Deliver_Waveform() {
  forall {
    if (Attach_Stimulation == 0) {        // check if is_xtra is attached to the stim vector
      if (ismembrane("xtra")) {
        StimVector.play(&is_xtra,TimeVector,1)
        Attach_Stimulation = 1            // set flag to 1 to stop further iterations
      }}}
}// End Procedure
// This procedure checks the values of the Extracellular settings
proc Check_Values(){
if ( (End_Time_Field - Start_Time_Field) >= (1000/FREQ) ) {
Design_Waveform(Start_Time_Field, End_Time_Field, AMP1, PW1, AMP2, PW2, AMP3, PW3, FREQ)
                  // Design the stimulation profile
                  Deliver_Waveform()          // Link the waveform to is
                  Set_Field_Resistance()      // Update the field parameters
                  Display_Field()
                  // Based on the previous electrode positions, the distance between electrodes in um:
                  Field_Distance = abs(Electrode_A_Position - Electrode_B_Position)
        printf("Extracellular Settings Updated \n")
         } else {
        printf("Error in Extracellular Settings \n")
        printf("Stimulation time is short than one stimulating cycle \n")
        printf("Change either End_Time_Field or FREQ \n")
         }
} // End Procedure
// Display the panel for Extracellular field stimulation parameters
xpanel("Extracellular AC Field - Square Wave")
        xvalue("Start Time (ms)", "Start_Time_Field", 1, "", 1)
        xvalue("End Time (ms)", "End_Time_Field", 1, "", 1)
        xvalue("Direction of Field", "Field_Direction", 1, "", 1)
        xvalue("Position of Electrode A (um)", "Electrode_A_Position", 1, "", 1)
        xvalue("Position of Electrode B (um)", "Electrode_B_Position", 1, "", 1)
        xvalue("Current Amplitude - 1 (mA)", "AMP1", 1, "", 1)
        xvalue("Current Duration - 1 (ms)", "PW1", 1, "", 1)
        xvalue("Current Amplitude - 2 (mA)", "AMP2", 1, "", 1)
        xvalue("Current Duration - 2 (ms)", "PW2", 1, "", 1)
        xvalue("Current Amplitude - 3 (mA)", "AMP3", 1, "", 1)
        xvalue("Current Duration - 3 (ms)", "PW3", 1, "", 1)
        xvalue("Field Frequency (Hz)", "FREQ", 1, "", 1)
   xbutton("Accept Parameters","Check_Values()")
xpanel(0,550)
Display_Field()
```